GREEN'S FUNCTIONS FOR MULTI-LAYERED POROELASTIC MEDIA AND AN INDIRECT BOUNDARY ELEMENT METHOD

BY

TEERAPONG SENJUNTICHAI

A Dissertation
Submitted to The University of Manitoba
in Partial Fulfillment of the Requirements
for the Degree of

DOCTOR OF PHILOSOPHY

Department of Civil and Geological Engineering
University of Manitoba
Winnipeg, Manitoba, Canada

ISBN 0-315-98977-7

Name TEERAPONG SENJUNTICHAI

Dissertation Abstracts International is arranged by broad, general subject categories. Please select the one subject which most nearly describes the content of your dissertation. Enter the corresponding four-digit code in the spaces provided.

Civil Engineering

SUBJECT TERM

0	5	4	3

SUBJECT CODE

U·M·I

Subject Categories

THE HUMANITIES AND SOCIAL SCIENCES

COMMUNICATIONS AND THE ARTS
- Architecture 0729
- Art History 0377
- Cinema 0900
- Dance 0378
- Fine Arts 0357
- Information Science 0723
- Journalism 0391
- Library Science 0399
- Mass Communications 0708
- Music 0413
- Speech Communication 0459
- Theater 0465

EDUCATION
- General 0515
- Administration 0514
- Adult and Continuing 0516
- Agricultural 0517
- Art 0273
- Bilingual and Multicultural 0282
- Business 0688
- Community College 0275
- Curriculum and Instruction 0727
- Early Childhood 0518
- Elementary 0524
- Finance 0277
- Guidance and Counseling 0519
- Health 0680
- Higher 0745
- History of 0520
- Home Economics 0278
- Industrial 0521
- Language and Literature 0279
- Mathematics 0280
- Music 0522
- Philosophy of 0998
- Physical 0523
- Psychology 0525
- Reading 0535
- Religious 0527
- Sciences 0714
- Secondary 0533
- Social Sciences 0534
- Sociology of 0340
- Special 0529
- Teacher Training 0530
- Technology 0710
- Tests and Measurements 0288
- Vocational 0747

LANGUAGE, LITERATURE AND LINGUISTICS
- Language
  - General 0679
  - Ancient 0289
  - Linguistics 0290
  - Modern 0291
- Literature
  - General 0401
  - Classical 0294
  - Comparative 0295
  - Medieval 0297
  - Modern 0298
  - African 0316
  - American 0591
  - Asian 0305
  - Canadian (English) 0352
  - Canadian (French) 0355
  - English 0593
  - Germanic 0311
  - Latin American 0312
  - Middle Eastern 0315
  - Romance 0313
  - Slavic and East European 0314

PHILOSOPHY, RELIGION AND THEOLOGY
- Philosophy 0422
- Religion
  - General 0318
  - Biblical Studies 0321
  - Clergy 0319
  - History of 0320
  - Philosophy of 0322
- Theology 0469

SOCIAL SCIENCES
- American Studies 0323
- Anthropology
  - Archaeology 0324
  - Cultural 0326
  - Physical 0327
- Business Administration
  - General 0310
  - Accounting 0272
  - Banking 0770
  - Management 0454
  - Marketing 0338
- Canadian Studies 0385
- Economics
  - General 0501
  - Agricultural 0503
  - Commerce-Business 0505
  - Finance 0508
  - History 0509
  - Labor 0510
  - Theory 0511
- Folklore 0358
- Geography 0366
- Gerontology 0351
- History
  - General 0578
  - Ancient 0579
  - Medieval 0581
  - Modern 0582
  - Black 0328
  - African 0331
  - Asia, Australia and Oceania 0332
  - Canadian 0334
  - European 0335
  - Latin American 0336
  - Middle Eastern 0333
  - United States 0337
- History of Science 0585
- Law 0398
- Political Science
  - General 0615
  - International Law and Relations 0616
  - Public Administration 0617
- Recreation 0814
- Social Work 0452
- Sociology
  - General 0626
  - Criminology and Penology 0627
  - Demography 0938
  - Ethnic and Racial Studies 0631
  - Individual and Family Studies 0628
  - Industrial and Labor Relations 0629
  - Public and Social Welfare 0630
  - Social Structure and Development 0700
  - Theory and Methods 0344
- Transportation 0709
- Urban and Regional Planning 0999
- Women's Studies 0453

THE SCIENCES AND ENGINEERING

BIOLOGICAL SCIENCES
- Agriculture
  - General 0473
  - Agronomy 0285
  - Animal Culture and Nutrition 0475
  - Animal Pathology 0476
  - Food Science and Technology 0359
  - Forestry and Wildlife 0478
  - Plant Culture 0479
  - Plant Pathology 0480
  - Plant Physiology 0817
  - Range Management 0777
  - Wood Technology 0746
- Biology
  - General 0306
  - Anatomy 0287
  - Biostatistics 0308
  - Botany 0309
  - Cell 0379
  - Ecology 0329
  - Entomology 0353
  - Genetics 0369
  - Limnology 0793
  - Microbiology 0410
  - Molecular 0307
  - Neuroscience 0317
  - Oceanography 0416
  - Physiology 0433
  - Radiation 0821
  - Veterinary Science 0778
  - Zoology 0472
- Biophysics
  - General 0786
  - Medical 0760

EARTH SCIENCES
- Biogeochemistry 0425
- Geochemistry 0996
- Geodesy 0370
- Geology 0372
- Geophysics 0373
- Hydrology 0388
- Mineralogy 0411
- Paleobotany 0345
- Paleoecology 0426
- Paleontology 0418
- Paleozoology 0985
- Palynology 0427
- Physical Geography 0368
- Physical Oceanography 0415

HEALTH AND ENVIRONMENTAL SCIENCES
- Environmental Sciences 0768
- Health Sciences
  - General 0566
  - Audiology 0300
  - Chemotherapy 0992
  - Dentistry 0567
  - Education 0350
  - Hospital Management 0769
  - Human Development 0758
  - Immunology 0982
  - Medicine and Surgery 0564
  - Mental Health 0347
  - Nursing 0569
  - Nutrition 0570
  - Obstetrics and Gynecology 0380
  - Occupational Health and Therapy 0354
  - Ophthalmology 0381
  - Pathology 0571
  - Pharmacology 0419
  - Pharmacy 0572
  - Physical Therapy 0382
  - Public Health 0573
  - Radiology 0574
  - Recreation 0575
  - Speech Pathology 0460
  - Toxicology 0383
- Home Economics 0386

PHYSICAL SCIENCES

Pure Sciences
- Chemistry
  - General 0485
  - Agricultural 0749
  - Analytical 0486
  - Biochemistry 0487
  - Inorganic 0488
  - Nuclear 0738
  - Organic 0490
  - Pharmaceutical 0491
  - Physical 0494
  - Polymer 0495
  - Radiation 0754
- Mathematics 0405
- Physics
  - General 0605
  - Acoustics 0986
  - Astronomy and Astrophysics 0606
  - Atmospheric Science 0608
  - Atomic 0748
  - Electronics and Electricity 0607
  - Elementary Particles and High Energy 0798
  - Fluid and Plasma 0759
  - Molecular 0609
  - Nuclear 0610
  - Optics 0752
  - Radiation 0756
  - Solid State 0611
- Statistics 0463

Applied Sciences
- Applied Mechanics 0346
- Computer Science 0984
- Engineering
  - General 0537
  - Aerospace 0538
  - Agricultural 0539
  - Automotive 0540
  - Biomedical 0541
  - Chemical 0542
  - Civil 0543
  - Electronics and Electrical 0544
  - Heat and Thermodynamics 0348
  - Hydraulic 0545
  - Industrial 0546
  - Marine 0547
  - Materials Science 0794
  - Mechanical 0548
  - Metallurgy 0743
  - Mining 0551
  - Nuclear 0552
  - Packaging 0549
  - Petroleum 0765
  - Sanitary and Municipal 0554
  - System Science 0790
- Geotechnology 0428
- Operations Research 0796
- Plastics Technology 0795
- Textile Technology 0994

PSYCHOLOGY
- General 0621
- Behavioral 0384
- Clinical 0622
- Developmental 0620
- Experimental 0623
- Industrial 0624
- Personality 0625
- Physiological 0989
- Psychobiology 0349
- Psychometrics 0632
- Social 0451

GREEN'S FUNCTIONS FOR MULTI-LAYERED POROELASTIC MEDIA AND AN INDIRECT BOUNDARY ELEMENT METHOD

BY

TEERAPONG SENJUNTICHAI

A Thesis submitted to the Faculty of Graduate Studies of the University of Manitoba in partial fulfillment of the requirements for the degree of

DOCTOR OF PHILOSOPHY

ABSTRACT

Several problems encountered in geomechanics, energy resource explorations, seismology, biomechanics, etc. involve the study of deformations and stresses in a medium composed of a solid skeleton with fluid-saturated pore spaces. Such a medium is commonly known as a poroelastic material. Although, the theoretical foundations to describe the behaviour of poroelastic materials have been in existence for many years, their applications to analyze complex problems encountered in engineering practice, especially under dynamic loadings, have been attempted only in recent years. Motivated by the relevance of theory of poroelasticity to the modelling of practical problems encountered in several disciplines, this thesis presents Green's functions (fundamental solutions) and a boundary element solution scheme as effective tools for analysis of quasi-static, time-harmonic and transient problems involving homogeneous and multi-layered poroelastic media.

A set of analytical general solutions for governing equations of a poroelastic medium with compressible constituents are presented explicitly for 3-D quasi-static and 2-D dynamic (time-harmonic and transient) problems by using appropriate integral transform techniques. These general solutions are used to derive Green's functions corresponding to quasi-static and dynamic loads, and fluid sources applied at a finite depth below the surface of a homogeneous poroelastic half-space. An exact stiffness matrix method based on analytical general solutions of a homogeneous poroelastic medium is presented to compute 3-D quasi-static and 2-D dynamic Green's functions of a multi-layered poroelastic half-space. Explicit solutions for stiffness matrices of a layer with a finite thickness and an underlying half-space are presented in appropriate integral transform domains. Displacements and pore pressure at layer interfaces are considered as the basic unknowns in the present stiffness method whereas the layer arbitrary coefficients are chosen as basic unknowns in the conventional methods. The significant advantages of the present stiffness matrix scheme over the existing solution schemes are discussed. Selected numerical results for homogeneous and multi-layered poroelastic half-spaces subjected to surface/buried loadings and fluid sources are presented to portray the influence of poroelastic material parameters and other governing parameters on the

response.

An accurate indirect boundary integral equation scheme involving Green's functions derived in this thesis is presented to analyze boundary value problems involving homogeneous and layered poroelastic infinite and semi-infinite media. The present indirect boundary element scheme is developed on the basis of loadings and a fluid source applied on an auxiliary surface defined interior to the surface on which the boundary conditions are prescribed. The analysis is conducted in the Laplace domain for quasi-static and transient problems, and in the frequency domain for time-harmonic problems, respectively. The numerical implementation of the boundary element scheme is presented. The accuracy and the numerical stability of the present scheme are verified by considering a set of boundary value problems (quasi-static, time-harmonic and transient) for which analytical solutions are available. The consolidation of a rigid spheroidal anchor and the dynamic response of a semi-circular tunnel with a rigid wall are investigated to demonstrate the applicability of the present scheme to analyze practical problems.

ACKNOWLEDGEMENTS

The author wishes to express his profound gratitude and sincere appreciation to his advisor Prof. R. K. N. D. Rajapakse. During the last three years, Prof. Rajapakse has always been available and accessible for discussion and guidance up to the completion of this thesis. This study could not be completed without his encouragement and support.

Grateful acknowledgements are conveyed to Prof. A. H. Shah and Prof. Q. Zhang for providing helpful comments and serving in the advisory committee. Sincere thanks are extended to Prof. A. H.-D. Cheng, an internationally renowned authority on the topic of this thesis, for devoting his time to serve as the external examiner.

The author deeply appreciates the support and encouragement of his colleagues, Dr. Y. M. Desai, Dr. U. G. A. Puswewala, Dr. P. Charnvanichborikarn, Dr. Y. Wang, Dr. N. Rattanawangcharoen and Dr. R. Zhang, during graduate work at The University of Manitoba. Thanks are also extended to all of his friends who helped and supported him during his stay in Winnipeg. Special thanks are due to Manit Sujumnong and his family for their help and encouragement.

The author acknowledges the financial support given to him in the form of a research assistantship from NSERC research grant of Prof. Rajapakse and a teaching assistantship from the Department of Civil and Geological Engineering to support his study.

The influence of Prof. Pisidhi Karasudhi of The Asian Institute of Technology in developing author's interest in research is greatly appreciated.

The author is greatly indebted to his parents of many sacrifices they made in educating him and for their continuous encouragement during his entire education. Their inexhaustible love and support helped him to reach this stage of his career. Finally and lovingly, the author would like to thank his wife Tarntip for her patience, understanding and encouragement throughout the course of his study especially during the period when little progress was made. Her contributions to this thesis are invaluable and, without her support, he could not come this far.

TABLE OF CONTENTS

LIST OF TABLES

LIST OF FIGURES

LIST OF SYMBOLS

a = radius or half-width of a loading strip,
and a nondimensionalizing factor for length;

Δa = distance between surfaces $\bar{S}$ and S';

$\mathbf{B}$ = vector whose elements are the specified boundary conditions at node points on $\bar{S}$;

B = Skempton's pore pressure coefficient;

b = parameter accounting for the internal friction of the medium;

c = generalized consolidation coefficient;

$\mathbf{F}$ = vector whose elements are the unknown quantities applied at node points on S';

$\mathbf{F}^{(n)}$ = generalized force vector for the nth layer;

f_0 = intensity of applied loading;

f_i = unknown force in the i-direction applied on surface S';

G_{ij}, G_{iq} = displacement Green's functions;

G_{qj}, G_{qq} = Green's functions for fluid discharge;

$H(\ )$ = Heaviside unit step function;

$H_0^{(1)}(\ )$ = Hankel function of the first kind of order zero;

$H_0^{(2)}(\ )$ = Hankel function of the second kind of order zero;

H_{ij}, H_{iq} = traction Green's functions;

H_{pj}, H_{pq} = Green's functions for pore pressure;

$J_m(\ )$ = Bessel function of the first kind of order m;

$\mathbf{K}^{(n)}$ = stiffness matrix of the nth layer;

$K_m(\ )$ = modified Bessel function of the second kind of order m;

K_H = nondimensional horizontal impedance;

K_M = nondimensional rocking impedance;

K_V = nondimensional vertical impedance;

K_{HM}, K_{MH} = nondimensional coupled impedance;

M = Biot's parameter accounting for compressibility of the medium;

m = density-like parameter;

N = number of node points on surface $\bar{S}$;

N' = number of node points on surface S';

p = excess pore pressure;

p_0 = intensity of applied fluid pressure;

$\mathbf{Q}$ = matrix whose elements are the Green's functions;

q_0 = intensity of applied fluid sink;

q_i = fluid discharge in the i-direction;

r = radial coordinate;

$\bar{S}$ = surface on which boundary conditions are specified;

S' = auxiliary surface on which unknown quantities are applied;

s = Laplace transform parameter;

$\mathbf{T}^{(n)}$ = external force vector at the nth interface;

T_i = traction in the i-direction;

t = time variable;

t^* = nondimensional time for quasi-static problems;

$\mathbf{U}^{(n)}$ = generalized displacement vector for the nth layer;

u_i = displacement of the solid matrix in the i-direction;

w_i = fluid displacement relative to the solid matrix in the i-direction;

x, y, z = Cartesian coordinate;

α = Biot's parameter accounting for compressibility of the medium;

δ = nondimensional frequency;

$\delta(\ )$ = Dirac's delta function;

δ_{ij} = Kronecker delta;

ϵ = dilatation of the solid matrix;

ϵ_{ij} = strain component of the solid matrix;

ζ = variation of fluid volume;

θ = circumferential coordinate;

κ = coefficient of permeability;

λ = Lamé constant;

μ = shear modulus;

ν = drained Poisson's ratio;

ν_u = undrained Poisson's ratio;

ξ = Hankel Fourier transform parameter for 3-D problems
and Fourier transform parameter for 2-D problems;

ρ = mass density of the bulk material;

ρ_f = mass density of the pore fluid;

σ_{ij} = total stress component of the bulk material;

ω = circular frequency;

τ = nondimensional time for transient dynamic problems;

τ_1, τ_2 = nondimensional time for quasi-statics of multi-layered media;

Γ = unknown fluid source applied on surfaceS';

$\bar{\mathcal{H}}_m$ = Laplace-mth order Hankel transform operator.

Chapter 1

INTRODUCTION

1.1 General

The classical theory of elasticity has been used extensively in the past to analyze elastostatic and elastodynamic problems in geomechanics (Poulos and Davis, 1974; Gibson, 1974; Selvadurai, 1979; Luco, 1982; Gazetas, 1983 and Wolf, 1985). Traditionally, field equations have been formulated on the assumption that the soil medium is a single-phased elastic solid. However, geomaterials are often two-phased materials consisting of a solid skeleton with voids filled with water. Such materials are commonly known as *poroelastic materials* (see Fig. 1.1) and widely considered as a much more realistic representation for soils and rocks than ideal elastic materials.

Naturally, water-saturated soils under an externally applied load settle gradually with time. At the instant of application, the load is almost totally carried by the pore water since the water is nearly incompressible when compared to the soil skeleton. The pressure that increases in the pore water due to the externally applied load is called *excess pore pressure* because it is in excess of the initial pore water pressure under *in situ* conditions. Thereafter, the excess pore pressure becomes gradually dissipated as the pore water starts escaping from the voids. This results in an increment in stresses in the soil skeleton and a reduction in the volume of soil mass. This phenomenon is known as *soil consolidation* and it is completed when the excess pore pressure is equal to zero. When the volume reduction in a material under an applied load is equal to the volume of pore fluid drained out it is called a material with incompressible constituents. The incompressible constituent model is a good approximation for consolidation of water-saturated soils (e.g. clay and sand) but for the case of porous rocks, the compressibility of the pore fluid as well as the solid constituent should be considered. In recent years, considerable attention has been directed toward the development of advanced theories and solution algorithms (analytical and numerical) for stress analysis of poroelastic materials since idealizations adopted to study several problems encountered in geomechanics,

energy resource explorations, earthquake engineering and biomechanics often lead to boundary value problems involving poroelastic media.

1.2 Theoretical Foundations of Poroelasticity

The theory of poroelasticity has its origin in the one-dimensional theory of soil consolidation proposed by Terzaghi (1923) concerned with the vertical compression of loaded clay layers. In his work, Terzaghi introduced the *effective stress concept* which states that stress in the soil mass (effective stress) is equal to the total applied stress minus the pore water pressure. Later, Biot (1941a, 1955) presented the general theory of three-dimensional consolidation by adopting Terzaghi's concepts. Biot's theory takes into account the coupling between the solid and fluid stresses and strains based on the classical theory of linear elasticity and Darcy's law. In addition to material constants in classical elasticity, Biot included two parameters accounting for compressibility of a two-phased material, and the coefficient of permeability of a medium in his theory. The physical interpretation of these coefficients as well as the methods of measurements were provided by Biot and Willis (1957) and Yew *et al.* (1978, 1979).

The first theory of elastic wave propagation in a fluid-saturated porous medium was also established by Biot (1956 a,b) by adding inertia terms to his quasi-static theory (Biot, 1941a). Biot revealed that there are two dilatational waves and one rotational wave propagating in a fluid-saturated poroelastic medium instead of two body waves (one dilatational and one rotational) for the case of an ideal elastic material. It is also noted that the body waves in a poroelastic medium are dispersive and dissipative due to the presence of the viscous coupling between the solid matrix and the pore fluid. Later, Biot extended his elastodynamic theory to the cases of anisotropic and viscoelastic porous media (Biot, 1962). After the introduction of theory of mixtures (Truesdell and Toupin, 1960 and Green and Naghdi, 1965), several attempts have been made to obtain generalized theories of porous media following mixture theory concepts (Morland, 1972; Bowen, 1976, 1982; Katsube and Carroll, 1987a,b and others). However, these general theories based on theory of mixtures often result in equations involving coefficients which are obstinate in engineering practice.

Over the last four decades, Biot's theory has been the basis for analysis of a variety of practical problems encountered in geomechanics, geophysics, earthquake engineering and energy resource explorations. The present study is concerned with the quasi-static and dynamic stress analysis of homogeneous and multi-layered poroelastic media. In the following sections, a review of literature related to stress analysis of poroelastic materials is presented in order to define the objectives and the scope of this thesis.

1.3 Literature Review

1.3.1 Solutions for Homogeneous Poroelastic Materials

Biot (1941b) and Biot and Clingan (1941, 1942) presented the earliest solution for the consolidation settlements of poroelastic media under surface loadings by using a method of solution based on the application of Laplace transform with respect to the time variable and a series representation of solutions and boundary conditions. Later, McNamee and Gibson (1960a,b) presented a solution for plane strain and axially symmetric problems through the application of two displacement functions and the appropriate integral transforms (Laplace/Fourier for plane strain problems and Laplace/Hankel for axially symmetric problems), and then obtained solutions for a uniform strip load and a uniform circular patch load applied at the top surface of a semi-infinite clay stratum. Schiffman and Fungaroli (1965) extended the displacement functions to the case of asymmetric problems and studied the consolidation of a homogeneous poroelastic half-space due to a uniform horizontal patch load at the surface. Puswewala and Rajapakse (1988) derived Green's functions for semi-infinite and infinite poroelastic media subjected to axisymmetric internal loadings and a fluid source. Solutions corresponding to a poroelastic half-space with a point sink was also presented by Kanok-Nukulchai and Chau (1990). Rajapakse (1993) presented a stress analysis of a borehole in a poroelastic medium.

The above studies are concerned with the special case involving incompressible constituents which is valid mainly for soils but not for porous rocks. Biot's quasi-static equations for poroelasticity were reformulated by Rice and Cleary (1976) in terms of material constants which are more easily identifiable. In their paper, Rice

and Cleary replaced Biot's two poroelastic parameters accounting for compressibility of poroelastic materials by Skempton's pore pressure coefficient B (Skempton, 1954) and the undrained Poisson's ratio of the bulk material. The formulation of Rice and Cleary (1976) has been widely used to study the quasi-static response of porous elastic solids containing compressible constituents since late seventies. Cleary (1977) presented a set of fundamental solutions for an infinite poroelastic solid. Rudnicki (1986a) rederived Cleary's results for a suddenly applied point force, a fluid mass source and a fluid mass dipole. Problems related to a slip on a fault in a poroelastic medium were also considered by Rudnicki (1986b, 1987). Plane strain problems related to a borehole in a poroelastic medium were studied by Detournay and Cheng (1988). Detournay *et al.* (1989) considered problems related to hydraulic fracturing in fluid-saturated rocks.

In addition to above studies related to quasi-statics of poroelastic materials, many researchers have employed Biot's poroelastodynamic theory to study some basic elastodynamic problems. For example, the propagation of Rayleigh waves in a fluid-saturated poroelastic half-space was studied by Jones (1961) and Deresiewicz (1962). Geertsma and Smith (1961) studied the reflection and transmission of dilatational waves in poroelastic solids. Deresiewicz and Rice (1962) also studied the reflection of body waves from a plane, traction-free boundary of a porous solid. The characteristics of waves propagating in an infinite fluid-saturated poroelastic medium due to an instantaneous point load were investigated by Burridge and Vargas (1979) using Laplace transforms. Norris (1985) derived time-harmonic solution for a point force applied in an unbounded poroelastic medium and obtained a closed form solution for an impulsive point load applied in a nondissipative medium by using Fourier transforms. The solutions for time-harmonic concentrated loads and fluid source applied in an infinite poroelastic medium were presented by Bonnet (1987) by using an analogy between poroelasticity and thermoelasticity in the frequency domain. Boutin *et al.* (1987) considered the Green's functions for infinite poroelastic media due to time-harmonic point forces and a fluid source and discussed the construction of synthetic seismograms from the Green's functions. The poroelastic counterpart of the classical Lamb's problem (Lamb, 1904) was first considered by Paul (1976a,b) by assuming the nondissipative behaviour

of the half-space. Recently, several studies have considered the vibrations due to time-harmonic loads acting at the surface of saturated (Halpern and Christiano, 1986a,b and Philippacopoulos, 1988a) and partially saturated (Philippacopoulos, 1988b, 1989) poroelastic half-spaces.

Based on the above review, it is noted that Green's functions corresponding to quasi-static and dynamic loadings and fluid sources applied at a finite depth below the free surface of a poroelastic half-space with compressible constituents have not been reported in the literature. These Green's functions can be used in the analysis of anchors, buried footings, piles and underground structures (e.g. subway tunnels and pipelines) and also in the development of computer codes based on the boundary integral equation methods for analysis of a variety of complicated problems related to poroelastic media.

1.3.2 Solutions for Layered Poroelastic Media

An important class of problems in practical engineering applications is concerned with the study of mechanical response of a multi-layered medium since it represents a closer approximation to most physical systems such as natural soil profiles, which are normally layered in character. It is noted that studies related to quasi-statics and dynamics of multi-layered poroelastic media are very limited despite their relevance to many useful practical problems encountered in geomechanics, geophysics, earthquake engineering and energy resource explorations. On the other hand, the response of layered *ideal elastic* media has received wide attention in the past. In view of this observation, a review of existing methods for evaluation of static and dynamic response of layered *ideal elastic* media is presented with the assumption that these methods can be extended to study the response of layered poroelastic media.

The study of wave propagation in multi-layered ideal elastic media has received more attention when compared to elastostatic problems due to extensive applications found in earthquake engineering, geophysics and nondestructive characterization of sites. A review of literature indicates that existing methods for determination of static and dynamic responses of a layered ideal elastic medium can be grouped

into two main categories. In the first approach, general solutions, which rigorously satisfy the governing equations, of each layer expressed in terms of a set of arbitrary functions in Fourier or Hankel transform space are used to establish a linear simultaneous equation system with arbitrary functions as the unknowns by considering the boundary conditions at the top surface and continuity conditions at layer interfaces. Thereafter, the equation system is solved numerically for discrete values of the integral transform parameter (alternatively a dimensionless wave number in the dynamic case) and the response is computed by applying numerical quadrature to evaluate the inverse transform integrals. Thomson (1950) and Haskell (1953, 1960, 1962) pioneered the above approach. The Thomson-Haskell approach has significant drawbacks in the numerical implementation due to the presence of mis-matching exponential terms in layer matrices. Improved formulations were developed later by Knopoff (1964), Gilbert and Backus (1966), Watson (1970), Schwab(1970) and others. Studies by Apsel (1979), Luco and Apsel (1983) and Apsel and Luco (1983) present a comprehensive review of previous investigations, and present a computationally efficient and accurate algorithm based on generalized reflection and transmission coefficients (Kennett, 1974) to compute the three-dimensional dynamic response of a multi-layered medium due to buried sources.

The second category of solutions for dynamics of layered media is based on finite element concepts. In this approach, a layered medium is divided into a number of thin layers within which displacements have prescribed variations (e.g. linear in the vertical direction and a suitable form of outgoing waves in the horizontal/radial directions). The governing equations are solved approximately in the finite element sense by using the assumed displacement representation and an approximate stiffness matrix relating boundary displacements and stresses of a typical thin layer is obtained. The assembly of layer stiffness matrices yields the global stiffness equation of the layered system for a given wave number. Numerical solution of the global stiffness equation results in the displacements at thin layer interfaces and subsequent application of numerical quadrature to evaluate integrals over the wave-number domain yields the response of the layered medium. The origin of this method can be traced back to the studies by Lysmer and Waas (1972), Waas (1972) and Dong and Nelson (1972). In addition to the approximate nature of the solution, this method

also has the disadvantage that the presence of an underlying half-space cannot be taken into consideration in a consistent manner. Studies by Kausel *et al.* (1975), Waas (1980), Kausel and Peek (1982), Kausel and Seale (1987), Oner and Dong (1988) and Seale and Kausel (1989) present further developments and applications of the approximate stiffness method for ideal elastic and anisotropic layered media.

As mentioned previously, very limited studies have considered problems related to layered poroelastic media. The Thomson-Haskell approach was used by Vardoulakis and Harnpattanapanich (1986) to evaluate the quasi-static response of a layered poroelastic medium with incompressible constituents. In a subsequent paper (Harnpattanapanich and Vardoulakis, 1987), these authors studied the consolidation of a finite inhomogeneous soil layer whose shear modulus increases linearly with depth (Gibson soil layer) under rectangular surface loads. The application of this scheme to an N-layered poroelastic system results in an unsymmetric matrix of order $8N \times 8N$ which needs to be repetitively solved in the numerical evaluation of the response. The numerical effort involved in the analysis is substantially high due to the presence of Laplace inversion in addition to the Fourier transform inversion in the case of poroelastic media. In addition, the elements of the coefficient matrix involve both negative and positive exponentials of the Fourier transform parameter which results in numerically ill-conditioned matrices for increasing values of the transform parameter. The approximate stiffness matrix method (Lysmer and Waas, 1972 and Waas, 1972) was employed only recently by Bougacha *et al.* (1993b) to study two-dimensional vibrations of fluid-saturated layered poroelastic media. Bougacha *et al.* (1993a) also extended their scheme to evaluate the static and dynamic stiffnesses of rigid strip and circular foundations on a homogeneous poroelastic medium with rigid base.

1.3.3 Numerical Methods for Poroelasticity

All of the studies mentioned in Sections 1.3.1 and 1.3.2 are concerned with problems under simplified boundary and loading conditions (i.e. surface and internal loadings in a homogeneous or multi-layered half-space). However, in practical situations, one encounters more complicated problems such as embedded foundations, pile groups, anchors, underground openings, hydraulic fracture, etc. which

cannot be solved by using standard analytical procedures. In view of this, numerical solutions schemes such as finite and boundary element methods have emerged as powerful tools to analyze various problems encountered in engineering practice.

A finite element scheme was first proposed by Sandhu (1968), and Sandhu and Wilson (1969) for the analysis of consolidation problems. Their solution was based on a variational principle by Gurtin (1964) in which displacement and pore pressure are considered as the basic unknowns. Later, several attempts have been made to improve the Sandhu and Wilson scheme (Hwang *et al.*, 1971; Yokoo *et al.*, 1971a,b; Ghaboussi and Wilson, 1973). Krause (1978) presented a finite element scheme based on the virtual work principle. The combination of a finite element type approximation in spatial coordinates and the application of the Laplace transform to the time coordinate was proposed by Kanok-Nukulchai and Suaris (1982) to study the consolidation process in poroelastic materials by using variational principles based on Biot's theory. Although the finite element method has been extensively applied to the consolidation problems including nonlinear material behaviour, it has drawbacks in some special cases such as the modelling of far-field radiation conditions for wave propagation problems and in the simulation of field singularities in hydraulic fracture problems. The finite element method also becomes inefficient when applied to some problems involving infinite and semi-infinite layered media (Muki and Dong, 1980) since a large discretization of volume is required.

In recent years, the boundary element method (Rizzo, 1967; Liggett and Liu, 1983; Kobayashi, 1984 and Beskos, 1987) has emerged as a versatile computational method to analyze complicated stress analysis and fluid flow problems encountered in many disciplines. Boundary element methods are particularly efficient and accurate in the solution of problems involving unbounded media (e.g. problems in geomechanics, geophysics, earthquake engineering and energy resource explorations) since discretization of volume is unnecessary and far-field radiation conditions and layering can be rigorously modelled by using appropriate Green's functions. The development of boundary integral equation methods for poroelasticity has been the focus of interest of several recent studies following the early theoretical foundations presented by Predeleanu (1968) and Cleary (1977). To the author's knowledge, Cheng (1981) and Cheng and Liggett (1984a,b) presented the first formal numerical

implementation of boundary element analysis for quasi-static response of poroelastic domains through the use of Laplace transforms. Later, several papers have been published on the Laplace transform-based boundary element methods for poroelasticity (e.g. Cheng and Detournay, 1988 and Badmus *et at.*, 1993). Predeleanu (1981), Nishimura (1987), Cheng and Predeleanu (1987), Dargush and Banerjee (1989) and Nishimura and Kobayashi (1989) considered the time-domain analysis of quasi-static response of a poroelastic medium by using time-domain Green's functions for an infinite space. Boundary element formulations for poroelastodynamics have been presented recently by Manolis and Beskos (1989), Dominguez (1991, 1992), Cheng *et al.* (1991) and Wiebe and Antes (1991). It is noted that formal numerical implementations of boundary element formulations for poroelasticity have been attempted only for a limited number of quasi-static and time-harmonic problems and numerical studies for transient dynamic problems have not been reported in the literature. On the other hand, boundary element studies of static and dynamic problems encountered in many engineering applications involving *ideal elastic* materials are very well documented.

Boundary element formulations mentioned above are based on reciprocal theorems (Predeleanu, 1968 and Cleary, 1977) and involve integral equations with singular kernels which have to be solved numerically. Alternatively, it is possible to develop a boundary integral equation formulation which involves non-singular kernel functions by considering the distribution of a set of sources on an auxiliary surface. Such indirect formulations have been successfully used in the past to analyze a variety of problems related to ideal elastic media (Ohsaki, 1973; Rajapakse and Shah, 1988; Mossessian and Dravinski, 1989; Wang and Rajapakse, 1990 and others) and serve as an effective alternative to direct formulations. A review of literature reveals that the development of indirect boundary integral equation method for poroelastic media along the direction of Ohsaki's formulation for ideal elasticity has not been reported in the literature.

1.4 Objectives and Scope of the Present Study

Based on the above literature review, it can be concluded that although Biot's theory for poroelasticity provides a much more realistic and effective representation

of the mechanical response of natural soils and rocks, it has not been applied as widely as the ideal elastic theory to solve problems encountered in geomechanics, energy resource explorations, seismology, earthquake engineering, etc.. For example, the influence of consolidation effects on single piles and pile groups under quasi-static and dynamic loadings, on impedances of embedded foundations, on synthetic seismograms for layered media, on seismic wave scattering by surface topographies in porous soils, etc. have not been investigated in the past. Therefore, there exists a necessity to develop efficient computational tools which can be effectively used to analyze problems encountered in geomechanics, energy resource explorations, earthquake engineering, etc. on the basis of Biot's theory for poroelasticity.

This thesis has three main objectives. First, a set of Green's functions (fundamental solutions) corresponding to homogeneous and layered poroelastic half-spaces subjected to internal loadings and fluid sources are presented. These solutions are known to serve as powerful tools in developing solutions for a variety of boundary value problems in several disciplines. Secondly, an indirect boundary integral equation method based on above Green's functions are presented to solve problems involving complicated geometries and boundary conditions. Thirdly, numerical solutions for several boundary value problems (quasi-static and dynamic internal loads and fluid sinks, anchors, tunnels) involving homogeneous and layered poroelastic media are presented to study the influence of poroelastic material parameters and other governing parameters on the response of the medium. It is expected that the basic tools presented in this thesis could be effectively applied to solve a wide range of problems encountered in geomechanics, energy resource explorations, seismology, earthquake engineering, etc..

The organization of this thesis is described in the following. In Chapter 2, explicit analytical solutions for three-dimensional quasi-static Green's functions of a homogeneous poroelastic half-space with compressible constituents due to internal loadings and a fluid source are presented in Laplace domain. The numerical evaluation of Green's functions and the application of numerical Laplace inversion scheme are discussed. The influence of poroelastic material parameters on the response and the features of the consolidation process are also investigated. An exact stiffness matrix method based on the general solutions given in Chapter 2 is pre-

sented in Chapter 3 to compute quasi-static Green's functions of a multi-layered poroelastic half-space subjected to buried loadings and a fluid source. The significant advantages of the present matrix scheme when compared to existing methods are discussed. The derivation of dynamic (time-harmonic and transient) Green's functions corresponding to loadings and fluid sources applied at a finite depth below the surface of a homogeneous poroelastic half-plane is considered in Chapter 4. The accuracy of proposed numerical scheme for evaluation of dynamic Green's functions is verified. Selected numerical results are presented to portray the influence of poroelastic material parameters on the dynamic response of internally loaded poroelastic half-planes.

The stiffness matrix scheme presented in Chapter 3 is extended in Chapter 5 to evaluate Green's functions of a multi-layered poroelastic half-plane due to time-harmonic loadings and fluid sources applied in the interior of a layered medium by using the general solutions presented in Chapter 4. Numerical evaluation of Green's functions for layered media is discussed and selected numerical results corresponding to multi-layered poroelastic half-planes subjected to surface/buried dynamic excitations are presented. In Chapter 6, the development of computer codes based on an indirect boundary integral equation method for the solutions of quasi-static, time-harmonic and transient problems are presented. The numerical accuracy of the present boundary element scheme is demonstrated by considering a set of boundary value problems involving poroelastic materials for which analytical solutions can be developed. The applicability of the present scheme is demonstrated by considering the quasi-static response of a spheroidal anchor and the dynamic response of a semi-circular tunnel in poroelastic soils. Finally, major conclusions of the thesis and recommendations for future work are presented in Chapter 7.

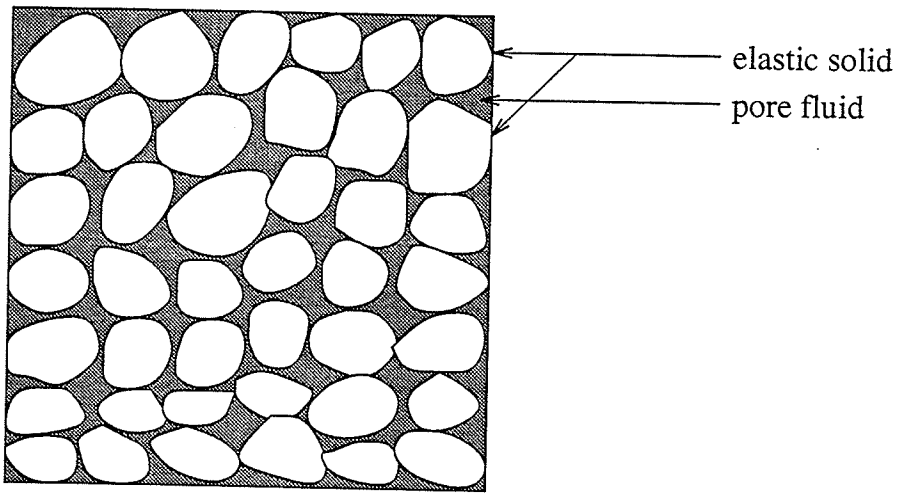

Figure 1.1 poroelastic material

Chapter 2

3-D QUASI-STATIC GREEN'S FUNCTIONS

2.1 General

In this Chapter, explicit solutions for quasi-static Green's functions of a homogeneous poroelastic half-space due to internal loadings and a fluid source are presented. General solutions are derived for equations governing quasi-static deformations of a poroelastic solid with compressible constituents by applying Fourier expansion, Hankel integral transforms and Laplace transforms with respect to the circumferential, radial and time coordinates, respectively. These general solutions are used to derive a set of Green's functions corresponding to circular ring loads (radial, circumferential and vertical) and to a ring fluid source applied at a finite depth below the free surface of a poroelastic half-space. The circumferential variation of the ring loads and the fluid source is described by appropriate trigonometric terms. Complete explicit solutions for Green's functions are presented in the Laplace transform space. The numerical evaluation of Green's functions are also discussed. Selected numerical results for a poroelastic half-space under a set of buried loads and a fluid sink are presented to portray the influence of poroelastic material parameters on the response and the features of the consolidation process.

2.2 Constitutive Equations

Consider a poroelastic medium with a Cartesian coordinate system (x, y, z) and a cylindrical polar coordinate system (r, θ, z) defined such that the z-axis is perpendicular to the free surface as shown in Fig. 2.1. Let u_i denote the average displacement of the solid matrix in the i-direction ($i = x, y, z$ or r, θ, z). Then, the constitutive relations of a homogeneous poroelastic material with compressible constituents can be expressed by using the standard indicial notation as (Biot, 1941)

$$\sigma_{ij} = 2\mu\left[\epsilon_{ij} + \frac{\nu}{1-2\nu}\delta_{ij}\epsilon\right] - \alpha\delta_{ij}p, \qquad i, j = x, y, z \text{ or } r, \theta, z \tag{2.1a}$$

$$p = -\alpha M\epsilon + M\zeta \tag{2.1b}$$

where

$$\zeta = -w_{i,i} \tag{2.2a}$$

$$w_i = \int_0^t q_i dt \tag{2.2b}$$

In the above equations, σ_{ij} is the total stress component of the bulk material; ϵ_{ij} and ϵ are the strain component and the dilatation of the solid matrix, respectively, which are related to the displacement u_i as in ideal elasticity; μ is the shear modulus; ν is the drained Poisson's ratio; δ_{ij} is the Kronecker delta; p is the excess pore fluid pressure (suction is considered negative); ζ is the variation of the fluid volume per unit reference volume; w_i, and q_i denote the average fluid displacement relative to the solid matrix, and the fluid discharge, respectively, in the i-direction ($i = x, y, z$ or r, θ, z). In addition, α and M are Biot's parameters accounting for the compressibility of the two-phased medium. It is noted that $0 \leq \alpha \leq 1$ and $0 \leq M < \infty$ for all poroelastic materials. For a completely dry material, $M \to 0$ whereas for a material with incompressible constituents $\alpha = 1$ and $M \to \infty$. The parameters α and M can be defined alternatively as (Rice and Cleary, 1976)

$$\alpha = \frac{3(\nu_u - \nu)}{B(1-2\nu)(1+\nu_u)} \tag{2.3a}$$

and

$$M = \frac{2\mu B^2 (1-2\nu)(1+\nu_u)^2}{9(\nu_u - \nu)(1-2\nu_u)} \tag{2.3b}$$

where ν_u is the undrained Poisson's ratio and B is Skempton's pore pressure coefficient (Skempton, 1954). For a poroelastic solid, B could vary from zero to one with ν_u varying from ν to 0.5. The limiting cases of a poroelastic material with incompressible constituents and a dry elastic material are obtained when $\nu_u = 0.5$ and $B = 1$, and $\nu_u = \nu$ and $B = 0$, respectively.

2.3 Governing Equations and General Solutions

The quasi-static governing equations (Rice and Cleary, 1976) for a poroelastic medium with compressible constituents, expressed in terms of stresses and pore pressure as the basic variables, can be transformed into Navier equations with coupling terms and a diffusion equation, by treating the displacements and the variation

of fluid volume as the basic unknowns. The governing equations in the absence of body forces (solid and fluid) and a fluid source can be expressed in the cylindrical coordinate system as

$$\nabla^2 u_r + \frac{1}{1-2\nu_u}\frac{\partial \epsilon}{\partial r} - \frac{1}{r}[\frac{2}{r}\frac{\partial u_\theta}{\partial \theta} + \frac{u_r}{r}] - \frac{2B(1+\nu_u)}{3(1-2\nu_u)}\frac{\partial \zeta}{\partial r} = 0 \qquad (2.4a)$$

$$\nabla^2 u_\theta + \frac{1}{1-2\nu_u}\frac{\partial \epsilon}{r\partial \theta} - \frac{1}{r}[\frac{u_\theta}{r} - \frac{2}{r}\frac{\partial u_r}{\partial \theta}] - \frac{2B(1+\nu_u)}{3(1-2\nu_u)}\frac{1}{r}\frac{\partial \zeta}{\partial \theta} = 0 \qquad (2.4b)$$

$$\nabla^2 u_z + \frac{1}{1-2\nu_u}\frac{\partial \epsilon}{\partial z} - \frac{2B(1+\nu_u)}{3(1-2\nu_u)}\frac{\partial \zeta}{\partial z} = 0 \qquad (2.4c)$$

$$\nabla^2 \zeta = \frac{\partial \zeta}{c\partial t} \qquad (2.4d)$$

where

$$\nabla^2 = \frac{\partial^2}{\partial r^2} + \frac{1}{r}\frac{\partial}{\partial r} + \frac{1}{r^2}\frac{\partial^2}{\partial \theta^2} + \frac{\partial^2}{\partial z^2} \qquad (2.5a)$$

$$\epsilon = \frac{\partial u_r}{\partial r} + \frac{u_r}{r} + \frac{1}{r}\frac{\partial u_\theta}{\partial \theta} + \frac{\partial u_z}{\partial z} \qquad (2.5b)$$

$$c = \frac{2\mu\kappa B^2(1-\nu)(1+\nu_u)^2}{9(1-\nu_u)(\nu_u-\nu)} \qquad (2.5c)$$

In the above equations, $u_r(r,\theta,z,t)$, $u_\theta(r,\theta,z,t)$ and $u_z(r,\theta,z,t)$ are the displacements in the r-, θ- and z-direction, respectively; c is the generalized consolidation coefficient and κ is the coefficient of permeability defined as the ratio between the intrinsic permeability of the medium and the fluid viscosity.

At this stage, it is convenient to nondimensionalize all quantities including the coordinate frame with respect to length and time by selecting the radius of a loading area a as a unit length and a^2/c as a unit of time, respectively. All variables will be replaced by appropriate nondimensional variables, but the previous notations will be used for convenience.

Application of Fourier expansion with respect to the circumferential coordinate θ for the displacements and the variation of fluid volume results in

$$u_r(r,\theta,z,t) = \sum_{m=0}^{\infty} u_{rm}(r,z,t)\cos m\theta + \sum_{m=0}^{\infty} \tilde{u}_{rm}(r,z,t)\sin m\theta \qquad (2.6a)$$

$$u_\theta(r,\theta,z,t) = \sum_{m=0}^{\infty} u_{\theta m}(r,z,t)\sin m\theta - \sum_{m=0}^{\infty} \tilde{u}_{\theta m}(r,z,t)\cos m\theta \qquad (2.6b)$$

$$u_z(r,\theta,z,t) = \sum_{m=0}^{\infty} u_{zm}(r,z,t)\cos m\theta + \sum_{m=0}^{\infty} \tilde{u}_{zm}(r,z,t)\sin m\theta \qquad (2.6c)$$

$$\zeta(r,\theta,z,t) = \sum_{m=0}^{\infty} \zeta_m(r,z,t)\cos m\theta + \sum_{m=0}^{\infty} \tilde{\zeta}_m(r,z,t)\sin m\theta \qquad (2.6d)$$

In eqns (2.6), u_{rm}, $u_{\theta m}$, u_{zm} and ζ_m are symmetric components and $\tilde{u}_{rm}$, $\tilde{u}_{\theta m}$, $\tilde{u}_{zm}$ and $\tilde{\zeta}_m$ are antisymmetric components corresponding to the mth harmonic. In the subsequent analysis, only symmetric components are considered without loss of generality. It is noted that the solution corresponding to antisymmetric components can be obtained by making the replacements $\cos m\theta \rightarrow -\sin m\theta$ and $\sin m\theta \rightarrow \cos m\theta$ (Muki, 1960).

The Laplace-mth order Hankel transform of function $\phi(r,z,t)$ with respect to variables t and r, respectively, is defined by (Sneddon, 1951)

$$\bar{\mathcal{H}}_m\{\phi(r,z,t)\} = \int_0^{\infty}\int_0^{\infty} \phi(r,z,t)e^{-st}J_m(\xi r)r\,dr\,dt \qquad (2.7)$$

In eqn (2.7), s and ξ denote the Laplace and Hankel transform parameters, respectively, and J_m denotes the Bessel function of the first kind of order m (Watson, 1944). The inverse relationship is given by

$$\phi(r,z,t) = \frac{1}{2\pi i}\int_{\varrho-i\infty}^{\varrho+i\infty}\int_0^{\infty} \bar{\mathcal{H}}_m\{\phi(r,z,t)\}e^{st}J_m(\xi r)\xi\,d\xi\,ds \qquad (2.8)$$

where ϱ is greater than the real part of all singularities of $\bar{\mathcal{H}}_m\{\phi(r,z,t)\}$ and $i = \sqrt{-1}$.

In view of eqns (2.6)-(2.8), the eqn (2.4d) can be solved directly and the resulting solution can be expressed as

$$\bar{\mathcal{H}}_m(\zeta_m) = A_m(\xi,s)e^{\gamma z} + B_m(\xi,s)e^{-\gamma z} \qquad (2.9)$$

where

$$\gamma = \sqrt{\xi^2 + s} \qquad (2.10)$$

and $A_m(\xi,s)$ and $B_m(\xi,s)$ are arbitrary functions.

Differentiation of eqns (2.4a) to (2.4c) and subsequent manipulations yield

$$\nabla^2\epsilon = \eta\nabla^2\zeta \qquad (2.11)$$

where

$$\eta = \frac{B(1+\nu_u)}{3(1-\nu_u)} \tag{2.12}$$

and ∇^2 is defined as in eqn (2.5a).

Application of Fourier expansion together with Laplace and mth order Hankel integral transforms in eqn (2.11) and the substitution of eqn (2.9) results in

$$\Big[\frac{d^2}{dz^2} - \xi^2\Big]\bar{\mathcal{H}}_m(\epsilon_m) = \eta s\Big(A_m(\xi,s)e^{\gamma z} + B_m(\xi,s)e^{-\gamma z}\Big) \tag{2.13}$$

where

$$\epsilon_m = \frac{\partial u_{rm}}{\partial r} + \frac{u_{rm}}{r} + \frac{m}{r}u_{\theta m} + \frac{\partial u_{zm}}{\partial z} \tag{2.14}$$

The following solution for eqn (2.13) can be obtained by using the method of variation of parameters (Kreider *et al.*, 1966)

$$\bar{\mathcal{H}}_m(\epsilon_m) = \eta\Big(A_m(\xi,s)e^{\gamma z} + B_m(\xi,s)e^{-\gamma z}\Big) + C_m(\xi,s)e^{\xi z} + D_m(\xi,s)e^{-\xi z} \tag{2.15}$$

where $C_m(\xi,s)$ and $D_m(\xi,s)$ are arbitrary functions.

After lengthy manipulations involving eqns (2.4a)-(2.4c), (2.6), (2.9), (2.14) and (2.15), the general solutions for the mth Fourier harmonic of displacement u_i $(i = r,\theta,z)$ in the Laplace-Hankel transform space can be expressed as

$$\begin{aligned}\bar{\mathcal{H}}_{m+1}(u_{rm}+u_{\theta m}) = &-\frac{\xi\eta}{s}\big(A_m e^{\gamma z} + B_m e^{-\gamma z}\big) + a_1 z\big(C_m e^{\xi z} - D_m e^{-\xi z}\big)\\ &+ E_m e^{\xi z} + F_m e^{-\xi z}\end{aligned} \tag{2.16a}$$

$$\begin{aligned}\bar{\mathcal{H}}_{m-1}(u_{rm}-u_{\theta m}) = &\frac{\xi\eta}{s}\big(A_m e^{\gamma z} + B_m e^{-\gamma z}\big) - a_1 z\big(C_m e^{\xi z} - D_m e^{-\xi z}\big)\\ &+ G_m e^{\xi z} + H_m e^{-\xi z}\end{aligned} \tag{2.16b}$$

$$\begin{aligned}\bar{\mathcal{H}}_m(u_{zm}) = &\frac{\gamma\eta}{s}\big(A_m e^{\gamma z} - B_m e^{-\gamma z}\big) - \big(a_1 z - \frac{a_2}{\xi}\big)C_m e^{\xi z} - \big(a_1 z + \frac{a_2}{\xi}\big)D_m e^{-\xi z}\\ &- \big(\frac{E_m - G_m}{2}\big)e^{\xi z} + \big(\frac{F_m - H_m}{2}\big)e^{-\xi z}\end{aligned} \tag{2.16c}$$

where

$$a_1 = \frac{1}{2(1-2\nu_u)}, \qquad a_2 = \frac{(3-4\nu_u)}{2(1-2\nu_u)} \tag{2.17}$$

and $E_m(\xi,s)$, $F_m(\xi,s)$, $G_m(\xi,s)$ and $H_m(\xi,s)$ are arbitrary functions.

Application of Fourier expansion with respect to the circumferential coordinate θ for the stress components and the pore pressure results in

$$\frac{\sigma_{ij}(r,\theta,z,t)}{2\mu} = \sum_{m=0}^{\infty} \sigma_{ijm}(r,z,t)\ f(\theta) \tag{2.18a}$$

$$\frac{p(r,\theta,z,t)}{2\mu} = \sum_{m=0}^{\infty} p_m(r,z,t)\ \cos m\theta \tag{2.18b}$$

In eqns (2.18), σ_{ijm} and p_m are symmetric components corresponding to the mth harmonic and

$$f(\theta) = \begin{cases} \cos m\theta, & i,j \neq \theta \text{ or } i=j=\theta \\ \\ \sin m\theta, & i \text{ or } j = \theta \end{cases} \tag{2.19}$$

Thereafter, the general solutions for the mth Fourier harmonic of the stress components and the pore pressure in the Laplace-Hankel transform space, nondimensionalized with respect to the shear modulus of the medium, can be expressed as

$$\begin{aligned} \bar{\mathcal{H}}_m(\sigma_{rrm} + \frac{u_{rm}}{r} + \frac{m}{r}u_{\theta m}) = &-\frac{\gamma^2\eta}{s}\big(A_m e^{\gamma z} + B_m e^{-\gamma z}\big) \\ &+ \big(a_1\xi z + a_3\big)C_m e^{\xi z} - \big(a_1\xi z - a_3\big)D_m e^{-\xi z} \\ &+ \xi\big(\frac{E_m - G_m}{2}\big)e^{\xi z} + \xi\big(\frac{F_m - H_m}{2}\big)e^{-\xi z} \end{aligned} \tag{2.20a}$$

$$\begin{aligned} \bar{\mathcal{H}}_m(\sigma_{rrm} + \sigma_{\theta\theta m}) = &-\frac{\eta}{s}(\gamma^2 + s)\big(A_m e^{\gamma z} + B_m e^{-\gamma z}\big) \\ &+ \big(a_1\xi z + 2a_3\big)C_m e^{\xi z} - \big(a_1\xi z - 2a_3\big)D_m e^{-\xi z} \\ &+ \xi\big(\frac{E_m - G_m}{2}\big)e^{\xi z} + \xi\big(\frac{F_m - H_m}{2}\big)e^{-\xi z} \end{aligned} \tag{2.20b}$$

$$\begin{aligned} \bar{\mathcal{H}}_{m+1}(\sigma_{zrm} + \sigma_{z\theta m}) = &-\frac{\xi\gamma\eta}{s}\big(A_m e^{\gamma z} - B_m e^{-\gamma z}\big) \\ &+ \big(\frac{2a_1\xi z - 1}{2}\big)C_m e^{\xi z} + \big(\frac{2a_1\xi z + 1}{2}\big)D_m e^{-\xi z} \\ &+ \xi\big(\frac{3E_m - G_m}{4}\big)e^{\xi z} - \xi\big(\frac{3F_m - H_m}{4}\big)e^{-\xi z} \end{aligned} \tag{2.20c}$$

$$\bar{\mathcal{H}}_{m-1}(\sigma_{zrm}-\sigma_{z\theta m}) = \frac{\xi\gamma\eta}{s}\big(A_m e^{\gamma z} - B_m e^{-\gamma z}\big) - \big(\frac{2a_1\xi z-1}{2}\big)C_m e^{\xi z} - \big(\frac{2a_1\xi z+1}{2}\big)D_m e^{-\xi z} - \xi\big(\frac{E_m-3G_m}{4}\big)e^{\xi z} + \xi\big(\frac{F_m-3H_m}{4}\big)e^{-\xi z} \qquad (2.20d)$$

$$\bar{\mathcal{H}}_m(\sigma_{r\theta m}+\frac{m}{r}u_{rm}+\frac{u_{\theta m}}{r}) = \xi\big(\frac{E_m+G_m}{4}\big)e^{\xi z} + \xi\big(\frac{F_m+H_m}{4}\big)e^{-\xi z} \qquad (2.20e)$$

$$\bar{\mathcal{H}}_m(\sigma_{zzm}) = \frac{\xi^2\eta}{s}\big(A_m e^{\gamma z} + B_m e^{-\gamma z}\big) - \big(a_1\xi z - a_4\big)C_m e^{\xi z} + \big(a_1\xi z + a_4\big)D_m e^{-\xi z} - \xi\big(\frac{E_m-G_m}{2}\big)e^{\xi z} - \xi\big(\frac{F_m-H_m}{2}\big)e^{-\xi z} \qquad (2.20f)$$

$$\bar{\mathcal{H}}_m(p_m) = a_5\eta\big(A_m e^{\gamma z} + B_m e^{-\gamma z}\big) - a_4\eta\big(C_m e^{\xi z} + D_m e^{-\xi z}\big) \qquad (2.20g)$$

where

$$a_3 = \frac{\nu_u}{1-2\nu_u}, \qquad a_4 = \frac{(1-\nu_u)}{(1-2\nu_u)}, \qquad a_5 = \frac{B(1-\nu)(1+\nu_u)}{3(\nu_u-\nu)} \qquad (2.21)$$

According to Darcy's law, the fluid discharge in the i-direction is given by

$$q_i = -\kappa\frac{\partial p}{\partial i}, \quad i = r, z, \qquad q_\theta = -\kappa\frac{\partial p}{r\partial\theta} \qquad (2.22)$$

2.4 Solution of Boundary Value Problems

Boundary value problems involving an internally loaded poroelastic half-space are considered in this section to derive the Green's functions. The solutions corresponding to the four basic loading configurations, i.e. a vertical ring load, a radial ring load, a circumferential ring load and a ring fluid source, all of intensity equal to Heaviside unit step function $H(t)$ per unit arc length applied over a circular ring of radius r' at a depth $z = z'$, are presented. The circumferential distribution of the vertical and radial ring loads and the ring fluid source is of the form cos $m\theta$ and that of the circumferential ring load is sin $m\theta$. A solution to the internally

loaded half-space can be derived by considering it as a two-domain boundary value problem (Karasudhi, 1990). A superscript i ($i = 1, 2$) is used to denote the domain number where domain "1" is bounded by $0 \leq z \leq z'$ and domain "2" by $z' \leq z < \infty$. General solutions for each domain are given by eqns (2.16), (2.20) and (2.22) with arbitrary coefficients $A_m^i(\xi, s), B_m^i(\xi, s), ..., H_m^i(\xi, s)$ where a superscript $i = 1, 2$ is used to identify the domain number. Note that for domain "2", arbitrary functions $A_m^2(\xi, s), C_m^2(\xi, s), E_m^2(\xi, s)$ and $G_m^2(\xi, s) \equiv 0$ to ensure the regularity of the solutions at infinity.

In view of the prescribed circumferential distribution of the loading case only the mth Fourier harmonic in eqns (2.6) and (2.18) needs to be considered. Therefore, the boundary and continuity conditions in the Laplace domain can be expressed as

$$\bar{\sigma}_{znm}^1(r, 0, s) = 0, \qquad n = r, \theta, z \qquad (2.23a)$$

$$\bar{p}_m^1(r, 0, s) = 0 \qquad (2.23b)$$

$$\bar{u}_{nm}^1(r, z', s) - \bar{u}_{nm}^2(r, z', s) = 0, \qquad n = r, \theta, z \qquad (2.23c)$$

$$\bar{p}_m^1(r, z', s) - \bar{p}_m^2(r, z', s) = 0 \qquad (2.23d)$$

$$\bar{\sigma}_{znm}^1(r, z', s) - \bar{\sigma}_{znm}^2(r, z', s) = \frac{F_n}{2\mu s}, \qquad n = r, \theta, z \qquad (2.23e)$$

$$\left\{\kappa \frac{\partial \bar{p}_m^1}{\partial z}(r, z', s)\right\} - \left\{\kappa \frac{\partial \bar{p}_m^2}{\partial z}(r, z', s)\right\} = \frac{Q}{2\mu s} \qquad (2.23f)$$

where the superposed bar in eqns (2.23) denotes the Laplace transform of quantities with respect to the time coordinate.

For a vertical ring load,

$$F_z = \delta(r - r'), \qquad F_r = F_\theta = Q = 0 \qquad (2.24)$$

where δ ( ) denotes Dirac's delta function.

For a radial ring load,

$$F_r = \delta(r - r'), \qquad F_\theta = F_z = Q = 0 \qquad (2.25)$$

For a circumferential ring load,

$$F_\theta = \delta(r - r'), \qquad F_r = F_z = Q = 0 \qquad (2.26)$$

For a ring fluid source,

$$Q = \delta(r - r'), \qquad F_r = F_\theta = F_z = 0 \tag{2.27}$$

Substitution of general solutions for displacements, stresses and pore pressure in eqns (2.23) together with eqns (2.24)-(2.27) and the following Hankel transform representation for $\delta(r-r')$ yields a set of linear simultaneous equations to determine arbitrary functions corresponding to the two domains.

$$\delta(r - r') = \int_0^\infty r' J_m(\xi r') J_m(\xi r) \xi d\xi \tag{2.28}$$

The following solutions are obtained for the non-zero arbitrary functions appearing in the general solutions given by eqns (2.16), (2.20) and (2.22) for different loading cases.

2.4.1 Arbitrary Functions for Vertical Ring Loading

$$A_m^1(\xi, s) = \frac{e^{-\gamma z'}}{4a_5 \mu s} r' J_m(\xi r'), \quad B_m^1(\xi, s) = \Big(\frac{b_3 e^{-\xi z'} - b_2 e^{-\gamma z'}}{4a_5 b_1 \mu s}\Big) r' J_m(\xi r') \tag{2.29a}$$

$$B_m^2(\xi, s) = B_m^1(\xi, s) - A_m^1(\xi, s) e^{2\gamma z'} \tag{2.29b}$$

$$C_m^1(\xi, s) = \frac{e^{-\xi z'}}{4a_4 \mu s} r' J_m(\xi r'), \quad D_m^1(\xi, s) = \Big(\frac{b_4 e^{-\xi z'} - 2b_5 \gamma e^{-\gamma z'}}{4a_4 b_1 \mu s}\Big) r' J_m(\xi r') \tag{2.29c}$$

$$D_m^2(\xi, s) = D_m^1(\xi, s) - C_m^1(\xi, s) e^{2\xi z'} \tag{2.29d}$$

$$E_m^1(\xi, s) = \frac{b_6 e^{-\xi z'}}{4a_5 \mu s^2} r' J_m(\xi r') \tag{2.30a}$$

$$F_m^1(\xi, s) = \Big(\frac{b_{10} e^{-\xi z'} - 2b_9 \xi \gamma \eta e^{-\gamma z'}}{4a_5 b_1 \xi \mu s^2}\Big) r' J_m(\xi r') \tag{2.30b}$$

$$F_m^2(\xi, s) = F_m^1(\xi, s) - \frac{b_7 e^{\xi z'}}{4a_5 \mu s^2} r' J_m(\xi r') \tag{2.30c}$$

$$G_m^1(\xi, s) = -E_m^1(\xi, s), \qquad H_m^i(\xi, s) = -F_m^i(\xi, s), \quad i = 1, 2 \tag{2.30d}$$

where

$$b_1 = a_5 s + 2(1-\nu_u)\xi\eta(\xi-\gamma), \quad b_2 = a_5 s + 2(1-\nu_u)\xi\eta(\xi+\gamma) \tag{2.31a}$$

$$b_3 = 4(1-\nu_u)\xi^2\eta - 2(1-2\nu_u)a_5 s - 2a_5\xi s z' \tag{2.31b}$$

$$b_4 = 2(1-\nu_u)\xi\eta(\xi+\gamma) - (3-4\nu_u)a_5 s - 2a_5\xi s z' \tag{2.31c}$$

$$b_5 = 2(1-\nu_u)\xi\eta, \quad b_6 = \xi\eta - \frac{a_5 s z'}{2(1-\nu_u)}, \quad b_7 = \xi\eta + \frac{a_5 s z'}{2(1-\nu_u)} \tag{2.31d}$$

$$b_8 = 2(1-\nu_u)\xi\eta(\xi+\gamma) + (3-4\nu_u)a_5 s, \quad b_9 = 2(1-\nu_u)(\xi^2\eta + a_5 s) \tag{2.31e}$$

$$b_{10} = b_6 b_8 \xi - b_{11}, \quad b_{11} = \frac{a_5 b_9 s}{a_4} \tag{2.31f}$$

2.4.2 Arbitrary Functions for Radial and Circumferential Ring Loadings

$$A_m^1(\xi,s) = \frac{\xi e^{-\gamma z'}}{8a_5\gamma\mu s} r' \Big\{ n J_{m-1}(\xi r') + J_{m+1}(\xi r') \Big\} \tag{2.32a}$$

$$B_m^1(\xi,s) = \Big(\frac{c_1\gamma e^{-\xi z'} - b_2\xi e^{-\gamma z'}}{8a_5 b_1\gamma\mu s} \Big) r' \Big\{ n J_{m-1}(\xi r') + J_{m+1}(\xi r') \Big\} \tag{2.32b}$$

$$B_m^2(\xi,s) = B_m^1(\xi,s) + A_m^1(\xi,s) e^{2\gamma z'} \tag{2.32c}$$

$$C_m^1(\xi,s) = \frac{e^{-\xi z'}}{8a_4\mu s} r' \Big\{ n J_{m-1}(\xi r') + J_{m+1}(\xi r') \Big\} \tag{2.32d}$$

$$D_m^1(\xi,s) = \Big(\frac{c_2 e^{-\xi z'} - 2b_5\xi e^{-\gamma z'}}{8a_4 b_1\mu s} \Big) r' \Big\{ n J_{m-1}(\xi r') + J_{m+1}(\xi r') \Big\} \tag{2.32e}$$

$$D_m^2(\xi,s) = D_m^1(\xi,s) + C_m^1(\xi,s) e^{2\xi z'} \tag{2.32f}$$

$$E_m^1(\xi,s) = \frac{e^{-\xi z'}}{8a_5\xi\mu s^2} r' \Big\{ c_3 n J_{m-1}(\xi r') - c_4 J_{m+1}(\xi r') \Big\} \tag{2.33a}$$

$$F_m^1(\xi,s) = \Big\{ \frac{(b_9 c_3 - c_4 c_5 - b_{11}) n J_{m-1}(\xi r') - (b_9 c_4 - c_3 c_5 + b_{11}) J_{m+1}(\xi r')}{8a_5 b_1 \xi\mu s^2} \Big\} r' e^{-\xi z'}$$

$$- \frac{b_9\xi^2\eta e^{-\gamma z'}}{4a_5 b_1\xi\mu s^2} r' \Big\{ n J_{m-1}(\xi r') + J_{m+1}(\xi r') \Big\} \tag{2.33b}$$

$$F_m^2(\xi,s) = F_m^1(\xi,s) + \frac{e^{\xi z'}}{8a_5\xi\mu s^2} r' \Big\{ c_6 n J_{m-1}(\xi r') - c_7 J_{m+1}(\xi r') \Big\} \tag{2.33c}$$

$$G_m^1(\xi,s) = \frac{e^{-\xi z'}}{8a_5\xi\mu s^2} r' \Big\{ c_4 n J_{m-1}(\xi r') - c_3 J_{m+1}(\xi r') \Big\} \tag{2.33d}$$

$$H_m^1(\xi,s) = \Big\{ \frac{(b_9 c_4 - c_3 c_5 + b_{11}) n J_{m-1}(\xi r') - (b_9 c_3 - c_4 c_5 - b_{11}) J_{m+1}(\xi r')}{8a_5 b_1 \xi\mu s^2} \Big\} r' e^{-\xi z'}$$

$$+ \frac{b_9 \xi^2 \eta e^{-\gamma z'}}{4a_5 b_1 \xi\mu s^2} r' \Big\{ n J_{m-1}(\xi r') + J_{m+1}(\xi r') \Big\} \tag{2.33e}$$

$$H_m^2(\xi,s) = H_m^1(\xi,s) + \frac{e^{\xi z'}}{8a_5\xi\mu s^2} r' \Big\{ c_7 n J_{m-1}(\xi r') - c_6 J_{m+1}(\xi r') \Big\} \tag{2.33f}$$

where

$$c_1 = 4(1-\nu_u)\xi^2\eta + 4(1-\nu_u)a_5 s - 2a_5\xi s z' \tag{2.34a}$$

$$c_2 = 2(1-\nu_u)\xi\eta(\xi+\gamma) + (3-4\nu_u)a_5 s - 2a_5\xi s z' \tag{2.34b}$$

$$c_3 = b_6\xi - \frac{a_5 s}{2(1-\nu_u)}, \quad c_4 = -b_6\xi - \frac{(7-8\nu_u)a_5 s}{2(1-\nu_u)} \tag{2.34c}$$

$$c_5 = (1-2\nu_u)a_5 s + 2(1-\nu_u)\xi\gamma\eta, \quad c_6 = b_7\xi - \frac{a_5 s}{2(1-\nu_u)} \tag{2.34d}$$

$$c_7 = -b_7\xi - \frac{(7-8\nu_u)a_5 s}{2(1-\nu_u)} \tag{2.34e}$$

and

$$n = \begin{cases} -1, & \text{for radial loading,} \\ \\ 1, & \text{for circumferential loading} \end{cases} \tag{2.35}$$

2.4.3 Arbitrary Functions for Ring Fluid Source

$$A_m^1(\xi,s) = \frac{e^{-\gamma z'}}{4a_5\gamma\eta\mu\kappa s} r' J_m(\xi r'), \; B_m^1(\xi,s) = \Big(\frac{2b_5\gamma e^{-\xi z'} - b_2 e^{-\gamma z'}}{4a_5 b_1 \gamma\eta\mu\kappa s} \Big) r' J_m(\xi r') \tag{2.36a}$$

$$B_m^2(\xi,s) = B_m^1(\xi,s) + A_m^1(\xi,s) e^{2\gamma z'} \tag{2.36b}$$

$$C_m^1(\xi,s) = 0, \qquad D_m^1(\xi,s) = b_5 \Big(\frac{e^{-\xi z'} - e^{-\gamma z'}}{2a_4 b_1 \eta\mu\kappa s} \Big) r' J_m(\xi r') \tag{2.36c}$$

$$D_m^2(\xi,s) = D_m^1(\xi,s) \tag{2.36d}$$

$$E_m^1(\xi,s) = \frac{e^{-\xi z'}}{4a_5\mu\kappa s^2} r' J_m(\xi r'), \quad F_m^1(\xi,s) = \Big(\frac{b_8 e^{-\xi z'} - 2b_9 e^{-\gamma z'}}{4a_5 b_1 \mu\kappa s^2}\Big) r' J_m(\xi r') \tag{2.37a}$$

$$F_m^2(\xi,s) = F_m^1(\xi,s) + E_m^1(\xi,s) e^{2\xi z'} \tag{2.37b}$$

$$G_m^1(\xi,s) = -E_m^1(\xi,s), \qquad H_m^i(\xi,s) = -F_m^i(\xi,s), \quad i = 1,2 \tag{2.37c}$$

2.4.4 Special Loading Cases

1)Vertical patch load [Fig. 2.2(a)] and a point load

The deformation fields corresponding to these loadings are axially symmetric about the z-axis and only the terms corresponding to $m = 0$ in eqns (2.6) and (2.18) need to be considered. The arbitrary functions corresponding to a uniform patch loading of radius a and intensity $f_0 H(t)$ as shown in Fig. 2.2(a) are given by eqns (2.29) and (2.30) with the term $r' J_0(\xi r')$ replaced by $f_0 J_1(\xi)/\xi$. In addition, $u_\theta = \sigma_{r\theta} = \sigma_{z\theta} = 0$ for axisymmetric vertical loading.

The arbitrary functions corresponding to a vertical concentrated load of magnitude $P_0 H(t)$ applied at $z = z'$ [poroelastic counterpart of the classical Mindlin's solution for a vertical load (Mindlin, 1936)] is given by eqns (2.29) and (2.30) with $m = 0$ and the term $r' J_0(\xi r')$ replaced by $P_0/2\pi$.

2) Horizontal patch load [Fig. 2.2(b)] and a point load

The deformation fields corresponding to these loading cases are symmetric about $\theta = 0$ and only the symmetric terms corresponding to $m = 1$ in eqns (2.6) and (2.18) need to be considered. The arbitrary functions corresponding to a horizontal patch load can be obtained from eqns (2.32) and (2.33) by replacing the terms $nr' J_0(\xi r')$ and $r' J_2(\xi r')$ by $-2f_0 J_1(\xi)/\xi$ and 0, respectively.

In the case of a concentrated load of magnitude $P_0H(t)$ applied at $z = z'$ [poroelastic counterpart of classical Mindlin's solution for a horizontal load (Mindlin, 1936)], the arbitrary coefficients are once again obtained by replacing the terms $nr'J_0(\xi r')$ and $r'J_2(\xi r')$ in eqns (2.32) and (2.33) by $-P_0/\pi$ and 0, respectively.

3) Patch fluid sink [Fig. 2.2(c)] and a point sink

The deformation fields corresponding to these fluid sinks are axially symmetric about z-axis and only the terms corresponding to $m = 0$ in eqns (2.6) and (2.18) need to be considered. The arbitrary functions corresponding to a circular fluid sink of radius a and uniform intensity $q_0H(t)$ are given by eqns (2.36) and (2.37) with the term $r'J_0(\xi r')$ replaced by $-q_0J_1(\xi)/\xi$. In the case of a point sink of intensity $Q_0H(t)$ applied at $z = z'$, the arbitrary functions are given by eqns (2.36) and (2.37) with $r'J_0(\xi r')$ replaced by $-Q_0/2\pi$. Note that $u_\theta = \sigma_{r\theta} = \sigma_{z\theta} = 0$ for both patch fluid sink and a point sink.

4) Loadings and fluid sources with non-uniform distribution

Arbitrary functions corresponding to loadings and fluid sources with non-uniform intensities applied over an axisymmetric domain (circular or annular) can be obtained by first developing a Fourier expansion of the intensity of applied loads/fluid sources with respect to θ and thereafter integrating with respect to r'. The integration with respect to r' can be obtained numerically or by analytical methods depending on the type of radial distribution of the load/fluid source. In addition, the solutions corresponding to loadings and fluid sources of different configurations (e.g. ring, patch and annular loads) applied in a poroelastic full space can be obtained from the half space solutions by setting z' approaching infinity and replacing $|z' - z|$ by $|z|$ where the origin of the coordinate frame (r, θ, z) is now set at the level of the applied load/source with the z-axis coinciding with the axis of symmetry of the applied load/source.

2.5 Numerical Solutions

2.5.1 Numerical Scheme

The development of an accurate numerical scheme to evaluate the Green's functions due to buried loadings and a fluid source is considered in this section with the intention of eventually using Green's functions in the boundary element analysis. The complete solutions for displacements, stresses, pore pressure and fluid discharge corresponding to each boundary value problem are given by eqns (2.16), (2.20) and (2.22) together with the solutions for arbitrary functions, $A_m^i(\xi, s)$ to $H_m^i(\xi, s)$, given by eqns (2.29)-(2.30), (2.32)-(2.33) and (2.36)-(2.37). The solutions for displacements and stresses at an arbitrary point appear in terms of Lipschitz-Hankel type semi-infinite integrals with respect to Hankel transform parameter ξ and a Bromwich integral with respect to Laplace transform parameter s. It should be noted that the Laplace inversion can be carried out analytically when $z = 0$ and $z' = 0$ (McNamee and Gibson, 1960b). However, the resulting solutions would still involve Lipschitz-Hankel type integrals with respect to ξ which can be evaluated only by numerical quadrature. Given the complexity of the integrands corresponding to the response at an arbitrary point due to a buried load/fluid source, it is proposed to develop an accurate numerical quadrature scheme to evaluate these integrals. The review of literature indicates that the Laplace inversion can be carried out very accurately (Piessen, 1975) by using the numerical inversion method proposed by Stehfest (1970). The formula due to Stehfest is given by

$$f(t) \simeq \frac{\ln 2}{t} \sum_{n=1}^{L} c_n \bar{f}(n\frac{\ln 2}{t}) \qquad (2.38a)$$

where $\bar{f}$ denotes the Laplace transform of $f(t)$ and

$$c_n = (-1)^{n+L/2} \sum_{k=[(n+1)/2]}^{\min(n,L/2)} \frac{k^{L/2}(2k)!}{(L/2-k)!k!(k-1)!(n-k)!(2k-n)!} \qquad (2.38b)$$

and L is even.

The application of eqns (2.38) to evaluate the Green's functions corresponding to internal loadings and a fluid source involves the computation of a series of

Lipschitz-Hankel integrals involving products of Bessel functions at L discrete values of s for each value of t. The semi-infinite integral with respect to ξ can be evaluated accurately by applying an adaptive version of extended trapezoidal formula with $\Delta\xi = 0.1$. This integral possesses a removable singularity at $\xi = 0$ and remains finite for all $\xi > 0$. It is found that accurate time-domain solutions are obtained from eqns (2.38) with $L \geq 6$. The Stehfest method is computationally quite demanding although it is accurate. For example, in the boundary element method the Green's functions need to be computed repetitively at a considerable number of boundary nodes to compute the time-domain solutions. A simpler and computationally more efficient scheme is given by Schapery (1962) which can be expressed as

$$f(t) \simeq [s\bar{f}(s)]_{s=0.5/t} \tag{2.39}$$

where $\bar{f}$ denotes the Laplace transform of $f(t)$ and s is the Laplace transform parameter.

Table 2.1 presents a comparison of nondimensional vertical displacements and pore pressure obtained from Stehfest and Schapery schemes at the point (0,a) due to a uniform vertical patch load applied at a depth $z = a$ as shown in Fig. 2.2(a). A nondimensional time t^*, where $t^* = ct/a^2$, is used in Table 2.1 and hereafter in the discussion of numerical solutions in this Chapter. The two solutions from Table 2.1 agree very closely. Table 2.2 presents solutions for pore pressure at an internal point due to a vertical patch load applied at the surface. Comparison of solutions presented by Schiffman and Fungaroli (1965) with those obtained from Stehfest and Schapery schemes indicate that the pore pressure solutions corresponding to Schapery scheme is less accurate but still acceptable in a practical situation. The suitability of Schapery's scheme for a more complicated situation such as the boundary element method can be assessed only after a detailed numerical study involving a boundary element analysis. Nevertheless, Schapery's scheme is computationally very efficient and it also yields approximate explicit time-domain Green's functions [see eqn (2.39)] which can be useful in the development of direct time-domain solution algorithms.

2.5.2 Numerical Results for Internal Loadings and Fluid Sink

The quasi-static response of poroelastic half-space regions of different material properties to a selected set of internal loading configurations is presented in this section. In the numerical study, time histories of nondimensional displacements and pore pressure due to buried patch loads and a buried patch fluid sink are investigated to study the features of the consolidation process. Stehfest inversion scheme is used to obtain time-domain solutions. The loadings and discharge are assumed to be uniformly distributed over a circular area of radius a with intensity f_0 and q_0, respectively, and acting at a depth a as shown in Figure 2.2. Six different poroelastic materials (Rice and Cleary, 1976), namely, a material with incompressible constituents ($\nu = 0.25, \nu_u = 0.5, B = 1.0$), Ruhr Sandstone ($\nu = 0.12, \nu_u = 0.31, B = 0.88$), Tennessee Marble ($\nu = 0.25, \nu_u = 0.27, B = 0.51$), Berea Sandstone ($\nu = 0.2, \nu_u = 0.33, B = 0.62$), Westerly Granite ($\nu = 0.25, \nu_u = 0.34, B = 0.85$) and Weber Sandstone ($\nu = 0.15, \nu_u = 0.29, B = 0.73$), are considered in the numerical study to investigate the influence of poroelastic material parameters on the response and the features of the consolidation process.

Time histories of nondimensional displacements, $u^*_{zz}[= 2\mu u_z/f_0 a]$, $u^*_{xx}[= 2\mu u_x/f_0 a]$ and $u^*_{zq}[= 2a_5\mu\kappa u_z/q_0 a^2]$, at points O ($r = 0, z = 0$) and B ($r = 0, z = a$) are shown in Figs. 2.3(a), 2.3(b) and 2.3(c) for the uniform patch loadings shown in Figs. 2.2(a), 2.2(b) and 2.2(c), respectively. The trend of the displacement histories are quite similar for both vertical and horizontal loadings and the material with incompressible constituents has the lowest initial solution followed by Westerly Granite, Berea Sandstone, Ruhr Sandstone, Weber Sandstone and Tennessee Marble. Comparison of this behaviour with the material properties indicates that the initial response is mainly governed by the value of the undrained Poisson's ratio. The above dependence of the initial solution for displacements only on the undrained Poisson's ratio can be verified analytically by obtaining the initial ($t = 0^+$) solution through limit procedures. The following initial solutions are obtained for vertical displacement and pore pressure for a vertical patch load [Fig. 2.2(a)]

$$u_z(r,z) = \frac{f_0}{8(1-\nu_u)\mu}\int_0^\infty \left[\left\{(3-4\nu_u)\xi(1+z) + 2\xi^2 z + (3-4\nu_u)^2 - 4(1-\nu_u)(1-2\nu_u)\right\}\right.$$

$$\times e^{-\xi(1+z)} + \Big\{(3-4\nu_u) + \xi|1-z|\Big\}e^{-\xi|1-z|}\Big]\frac{J_1(\xi)J_0(\xi r)}{\xi}d\xi \tag{2.40a}$$

$$p(r,z) = \frac{B(1+\nu_u)f_0}{6(1-\nu_u)}\int_0^\infty \Big[\Big\{(3-4\nu_u) + 2\xi\Big\}e^{-\xi(1+z)} - h^* e^{-\xi|1-z|}\Big] \times J_1(\xi)J_0(\xi r)d\xi \tag{2.40b}$$

where

$$h^* = \begin{cases} 1, & 0 \le z < 1 \\ -1, & 1 < z < \infty \end{cases} \tag{2.41}$$

The initial solutions for horizontal displacement and pore pressure for a horizontal patch load [Fig. 2.2(b)] are given by

$$\begin{aligned} u_x(r,z) = \frac{f_0}{16(1-\nu_u)\mu}\int_0^\infty \Big[\Big\{\Big(-(3-4\nu_u)\xi(1+z) + 2\xi^2 z + 8(1-\nu_u)^2 + 1\Big) \\ \times e^{-\xi(1+z)} + \Big((7-8\nu_u) - \xi|1-z|\Big)e^{-\xi|1-z|}\Big\}J_0(\xi r) \\ + \Big\{\Big((3-4\nu_u)\xi(1+z) - 2\xi^2 z + 8\nu_u(1-\nu_u) - 1\Big) \\ \times e^{-\xi(1+z)} + \Big(1 + \xi|1-z|\Big)e^{-\xi|1-z|}\Big\}J_2(\xi r)\Big]\frac{J_1(\xi)}{\xi}d\xi \end{aligned} \tag{2.42a}$$

$$p(r,z) = \frac{B(1+\nu_u)f_0}{6(1-\nu_u)}\int_0^\infty \Big[\Big\{2\xi - (3-4\nu_u)\Big\}e^{-\xi(1+z)} + e^{-\xi|1-z|}\Big] \times J_1(\xi)J_1(\xi r)d\xi \tag{2.42b}$$

It is interesting to note that the above solutions for displacements are essentially elastic solutions with the Poisson's ratio equal to the undrained Poisson's ratio. In addition, the final solutions ($t \to \infty$) for displacements corresponding to loadings shown in Figs. 2.2(a) and 2.2(b) are given by eqns (2.40a) and (2.42a), respectively, where ν_u replaced by ν. The final solutions for pore pressure are zero for both loading cases. The numerical solutions shown in Figs. 2.3 indicate that the material with the lowest undrained Poisson's ratio has the largest initial displacements. Therefore, the material with incompressible constituents has the lowest initial displacements. On the other hand, the material with the lowest drained Poisson's ratio has the maximum final displacements. In view of eqns (2.40a) and (2.42a), it is evident that the material with incompressible constituents, Tennessee Marble and Westerly Granite have identical final solutions for displacements since the drained

Poisson's ratios of these materials are identical. This fact is also confirmed by the numerical solutions shown in Figs. 2.3(a) and 2.3(b). The order of magnitude of nondimensional final displacements is identical to that of the drained Poisson's ratio.

Naturally, the displacement at point O is always less than that at point B for loadings shown in Figs. 2.2(a) and 2.2(b). The displacement increases slowly when $0 < t^* < 0.1$ and more rapidly during the period $0.1 < t^* < 100$ reaching its final value when $t^* > 1000$ for vertical and horizontal loadings. The displacements shown in Fig. 2.3(c) under a patch fluid sink [Fig. 2.2(c)] have features different to those corresponding to vertical and horizontal loadings. Naturally, the initial displacements are zero for all materials in this case and increase rapidly with time within the period $0.1 < t^* < 100$. Final solutions are reached when $t^* > 1000$ for all six materials. The displacement at point O is found to be higher than that at point B at all time instants. Similar behaviour was also noted in the numerical solutions reported by Kanok-Nukulchai and Chau (1990). The order of the final solutions for a fluid sink is identical to that of ν. Once again the nondimensional final solutions for Tennessee Marble, Westerly Granite and the material with incompressible constituents are identical due to identical drained Poisson's ratios.

Fig. 2.4(a) shows time histories of nondimensional pore pressure, $p_z^*[= p/f_0]$, at point B ($r = 0, z = a$) under a vertical patch load [Fig. 2.2(a)]. Initially ($0 < t^* < 0.1$), excess pore pressure in all materials increase slowly reaching their maximum values near $t^* = 0.1$. This behaviour is called the *Mandel-Cryer effect* (Mandel, 1953). Thereafter, they decrease rapidly with time and become almost negligible after $t^* > 10$. It is noted that the order of magnitude of excess pore pressure developed in all materials under a vertical patch load is identical to that of the Skempton's pore pressure coefficient B. The maximum pore pressure is found in the material with incompressible constituents followed by Ruhr Sandstone, Westerly Granite, Weber Sandstone, Berea Sandstone and Tennessee Marble, respectively. Time histories of nondimensional pore pressure, $p_q^*[= a_5 \kappa p/q_0 a]$, at point B is shown in Fig. 2.4(b) for a fluid sink. The initial pore pressure in all materials are zero and suction is subsequently developed at this point. Thereafter, suction increases more rapidly with time during the period $0.01 < t^* < 1.0$ reaching their final values

when $t^* > 10$.

Figure 2.5 presents the profiles of displacements and pore pressure for Ruhr Sandstone along the r- and z-axis under a vertical patch load [Fig. 2.2(a)] and a fluid sink [Fig. 2.2(c)]. The displacements at all points increase with time and the shape of the displacement profiles remain relatively unchanged with time in the case of vertical loading. Under vertical loading, the highest displacement is observed at the level of loading and it decreases rapidly with the depth below the level of loading. Vertical displacement at the surface level also decreases rapidly with the radial distance and the displacement at $r = 4a$ is about one-fifth of the displacement at $r = 0$. The difference between initial and final surface displacement profiles is about fifteen percent. Pore pressure profiles corresponding to the vertical loadings are shown in Fig. 2.5(c) and these show complicated variation with time. An examination of the explicit solution indicates that at $t^* = 0$ pore pressure is discontinuous within the domain of the loading. It becomes continuous for $t^* > 0$ and undergoes rapid changes with time in the vicinity of loading during the period $0 < t^* < 0.1$. Note that for $t^* < 0.01$ suction is developed in the region $0.5 < z/a < 1.0$. Pore pressure profiles become much smoother when $t^* > 0.1$ and thereafter pore pressure decreases gradually with both the depth and time. Pore pressure within the domain is nearly dissipated when $t^* > 10$.

The variations of vertical displacement along the z-axis and the free surface ($z = 0$) due to a fluid sink are shown in Figs. 2.5(d) and 2.5(e), respectively. These solutions show more dependence on time when compared to those presented in Figs. 2.5(a) and 2.5(b). Maximum displacement is observed near the surface but not at the level of loading and the displacement decreases rapidly near the sink level ($1.0 < z/a < 2.0$). More gradual variation of vertical displacement is noted for $z/a > 2.0$. Maximum surface displacement is noted at the origin ($r = 0, z = 0$) at all times and the surface displacement decreases rapidly with the radial distance. Comparison of numerical solutions for displacements at $t^* = 1000$ and $t^* = 10^6$ indicates that a final equilibrium state is reached when $t^* > 1000$. Similar behaviour was also noted by Kanok-Nukulchai and Chau (1990) for an interior sink in a poroelastic half-space with incompressible constituents. Suction profiles shown in Fig. 2.5(f) indicate that they increase rapidly with time and reaching a final value

when $t^* > 1000$. The initial solution yields zero suction in this case. The maximum value of suction is noted at $z = a$ and a sharp decrease is noted with the depth both above and below the sink level. Naturally, the suction profiles show a singularity at $z = a$ due to the applied sink.

2.6 Conclusions

Green's functions for a poroelastic half-space corresponding to buried circular ring loads acting in the radial, circumferential and vertical directions and to a fluid source are presented. Solutions corresponding to point, circular and annular loadings and fluid sources can be derived from ring load/fluid source solutions. In addition, Green's functions for a poroelastic full space can be obtained by taking certain limits on the corresponding half-space solutions. The Green's functions are expressed in terms of Lipschitz-Hankel integrals involving products of Bessel functions. The complexity of Green's functions hinders any attempts to obtain time-domain solutions by analytical Laplace inversion methods. It is found that accurate time-domain solutions can be obtained by applying the numerical scheme proposed by Stehfest (1970) for Laplace inversion and applying direct numerical quadrature to evaluate the Lipschitz-Hankel integrals. The numerical study also confirms that the simpler and computationally more efficient Schapery's scheme (Schapery, 1962) yields time-domain solutions with reasonable accuracy. The application of Schapery's scheme to the Laplace domain solutions presented in this Chapter results in approximate time-domain Green's functions explicitly.

The response of six different poroelastic half-spaces under buried patch loads and a patch fluid sink is investigated in the numerical study. The nondimensional initial displacements are found to be governed by the undrained Poisson's ratio whereas the final response depends only on the drained Poisson's ratio. In all loading cases it is found that the rate of displacement is higher when $0.1 < t^* < 100$. Final solutions are reached when $t^* > 1000$ for all types of loadings. The difference between the initial and final displacements due to vertical and horizontal loadings is less than twenty percent of the final displacement for all six materials. The initial solutions for pore pressure and displacements are zero due to a fluid sink. Displacements and suction show more dependence and variation with time

under a circular sink when compared to the solutions corresponding to vertical and horizontal loadings. It is also noted that under a sink the highest vertical displacement is not observed at the level of the sink.

An exact stiffness matrix approach based on the general solutions presented in this Chapter is developed in Chapter 3 for the analysis of a multi-layered poroelastic half-space under three-dimensional loadings and fluid sources. The present Green's functions are used in the development of an indirect boundary integral equation method for the analysis of complicated problems related to semi-infinite and infinite poroelastic media in Chapter 6. These Green's functions are equally useful in the application of direct boundary integral equation methods for poroelastic half-space regions. In addition, Green's functions presented in this Chapter can also be used in the analysis of problems encountered in energy resource explorations, groundwater studies and in the development of solutions for anchors, buried footing, piles, etc..

Table 2.1: Comparison of vertical displacement and pore pressure due to a vertical patch load [Fig. 2.2(a)] for a poroelastic material with incompressible constituents ($\nu = 0.25$)

t^*	$2\mu u_z(0,a,t^*)/f_0 a$		$p(0,a,t^*)/f_0$	
(ct/a^2)	Stehfest	Schapery	Stehfest	Schapery
10^{-6}	0.813	0.814	1.424	1.424
10^{-5}	0.814	0.815	1.426	1.427
10^{-4}	0.817	0.819	1.431	1.433
0.001	0.827	0.830	1.448	1.453
0.01	0.853	0.859	1.492	1.497
0.1	0.902	0.905	1.470	1.471
1.0	0.961	0.966	0.045	0.048

Table 2.2: Comparison of pore pressure due to a vertical patch load applied at the top surface for a poroelastic material with incompressible constituents ($\nu = 0.0$)

t^*	$p(0.5,0.1,t^*)/f_0$		
(ct/a^2)	Schiffman and Fungaroli (1965)	Stehfest	Schapery
0.001	0.90	0.894	0.833
0.01	0.48	0.484	0.477
0.1	0.13	0.129	0.166
1.0	0.02	0.015	0.031

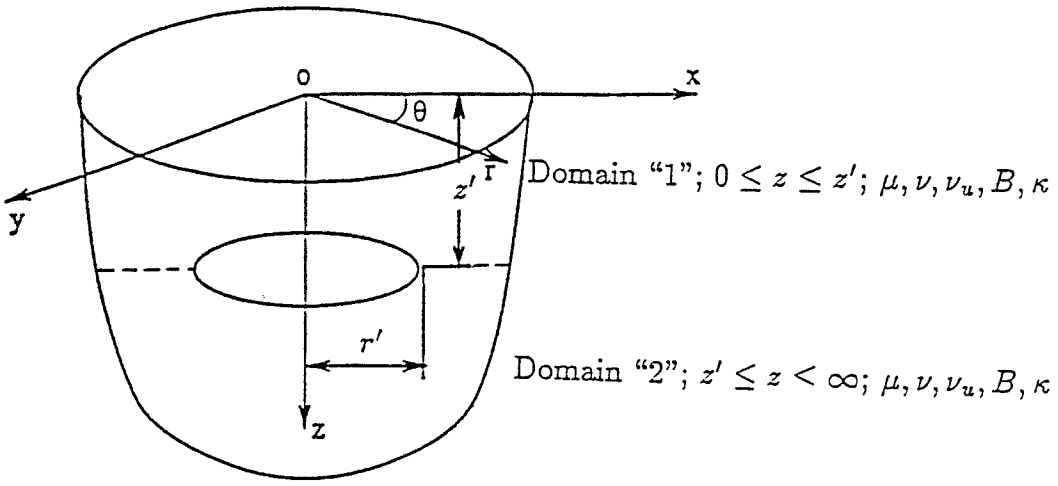

Figure 2.1 Coordinate system and internal ring loading

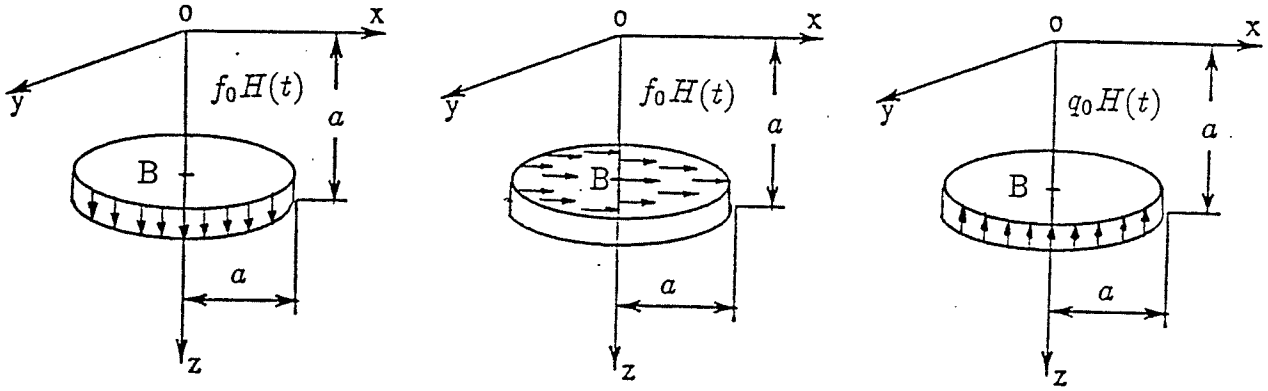

(a) Vertical patch load (b) Horizontal patch load (c) Patch fluid sink

Figure 2.2 Loading configurations considered in numerical study

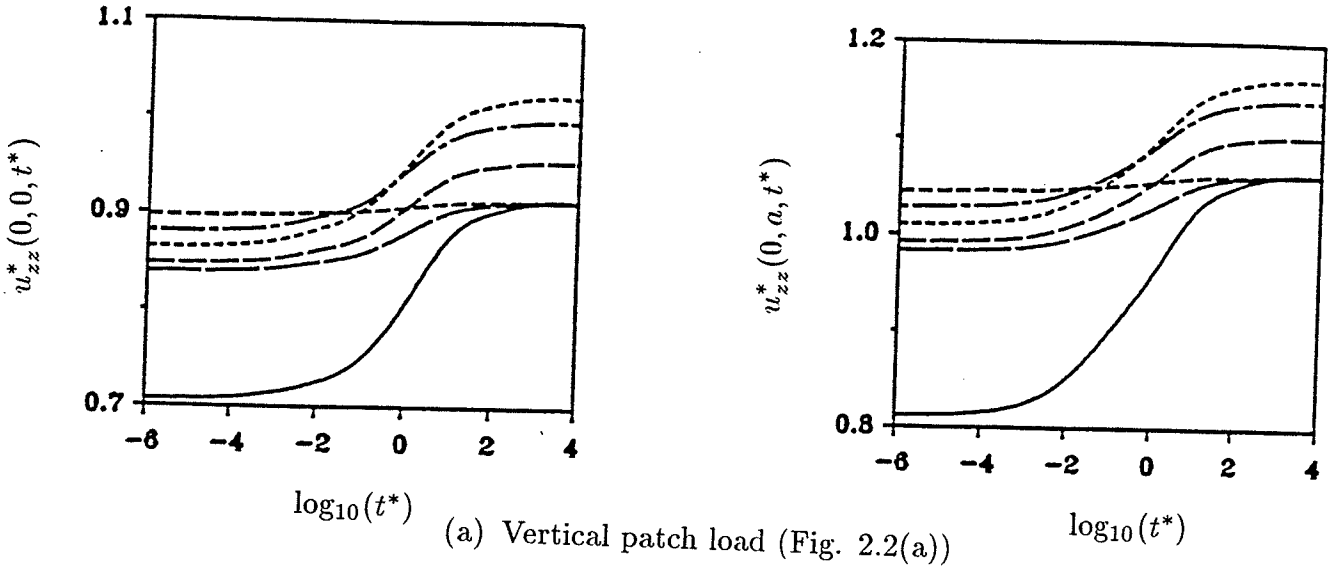

(a) Vertical patch load (Fig. 2.2(a))

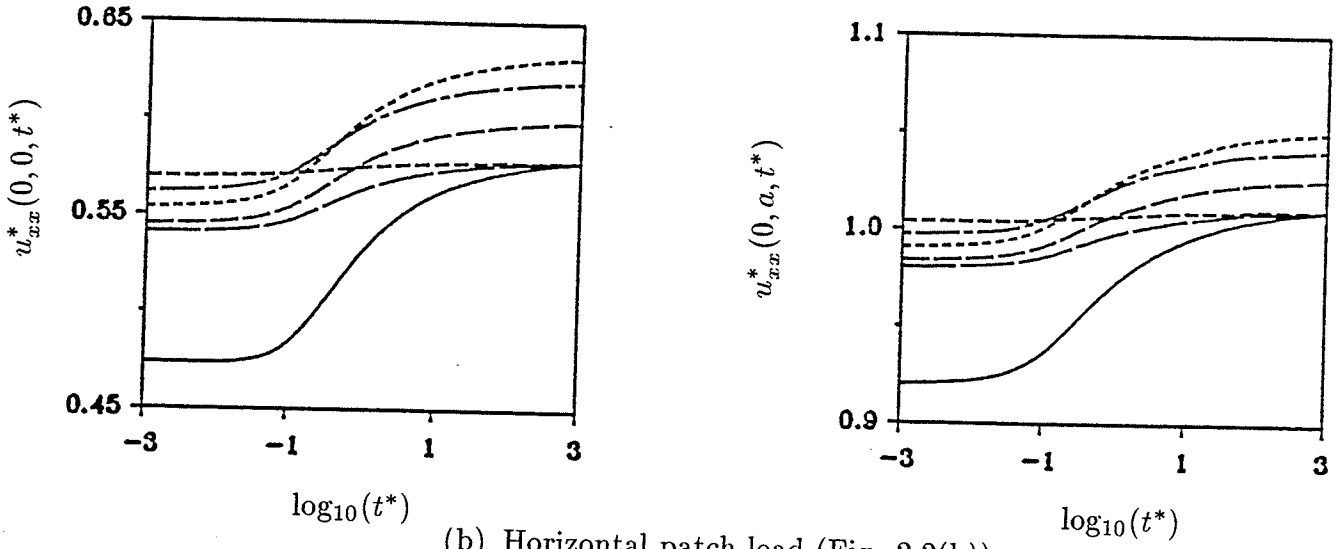

(b) Horizontal patch load (Fig. 2.2(b))

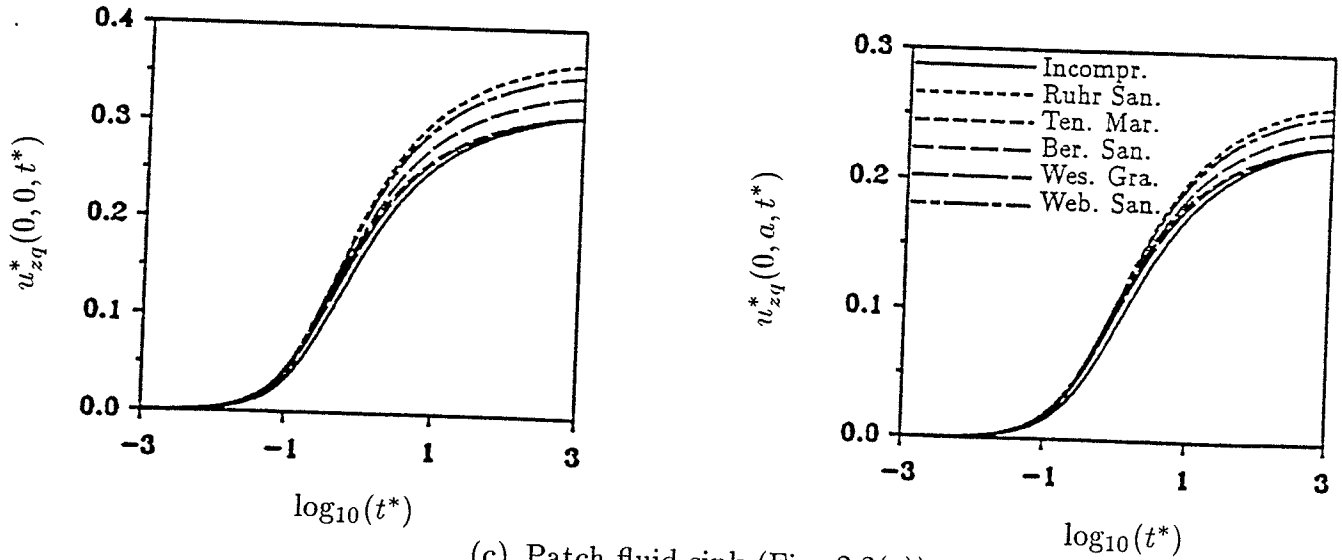

(c) Patch fluid sink (Fig. 2.2(c))

Figure 2.3 Displacement histories at points O ($r = 0, z = 0$) and B ($r = 0, z = a$) for different materials under loadings shown in Figure 2.2

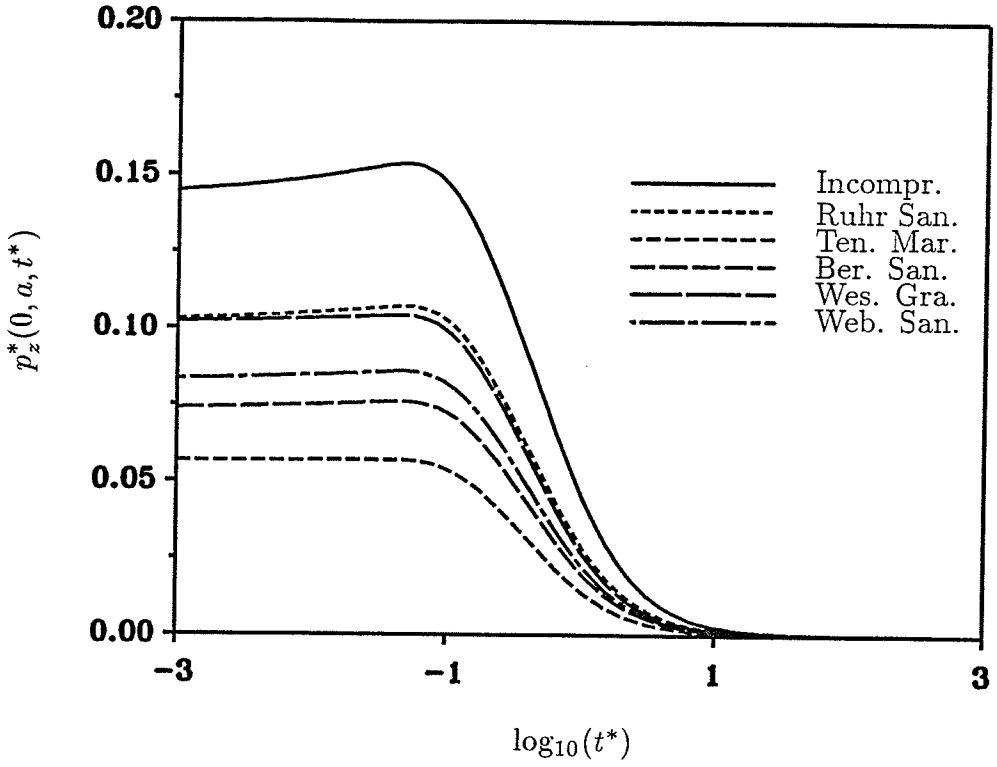

(a) Vertical patch load (Fig. 2.2(a))

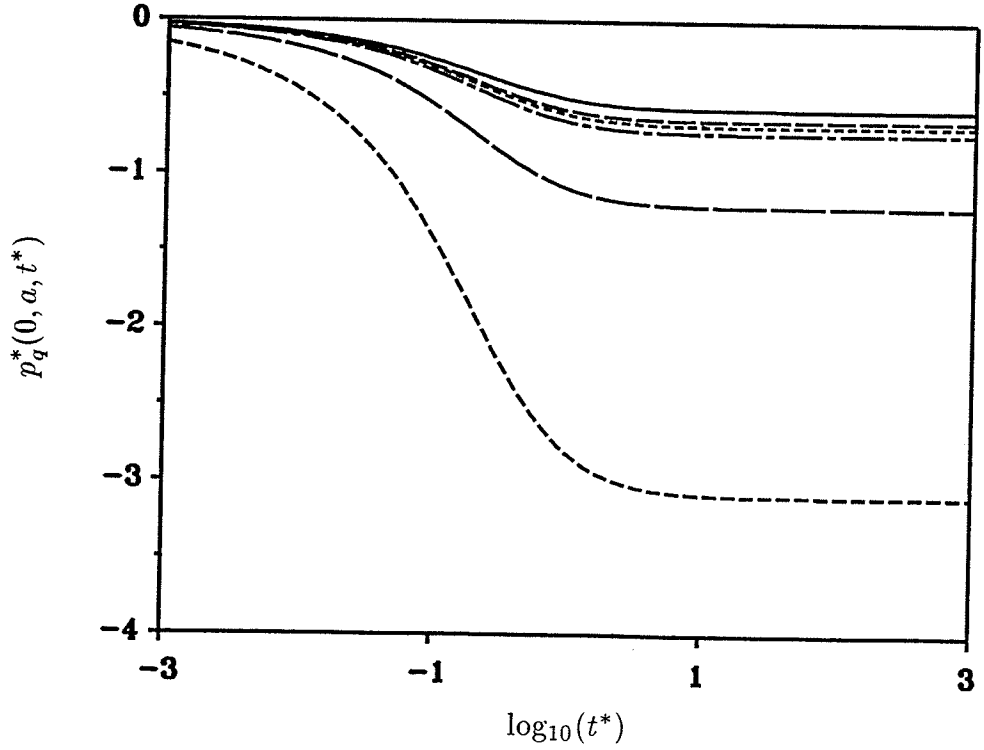

(b) Patch fluid sink (Fig. 2.2(c))

Figure 2.4 Pore pressure histories at point B ($r = 0, z = a$) for different materials under loadings shown in Figs. 2.2(a) and 2.2(c)

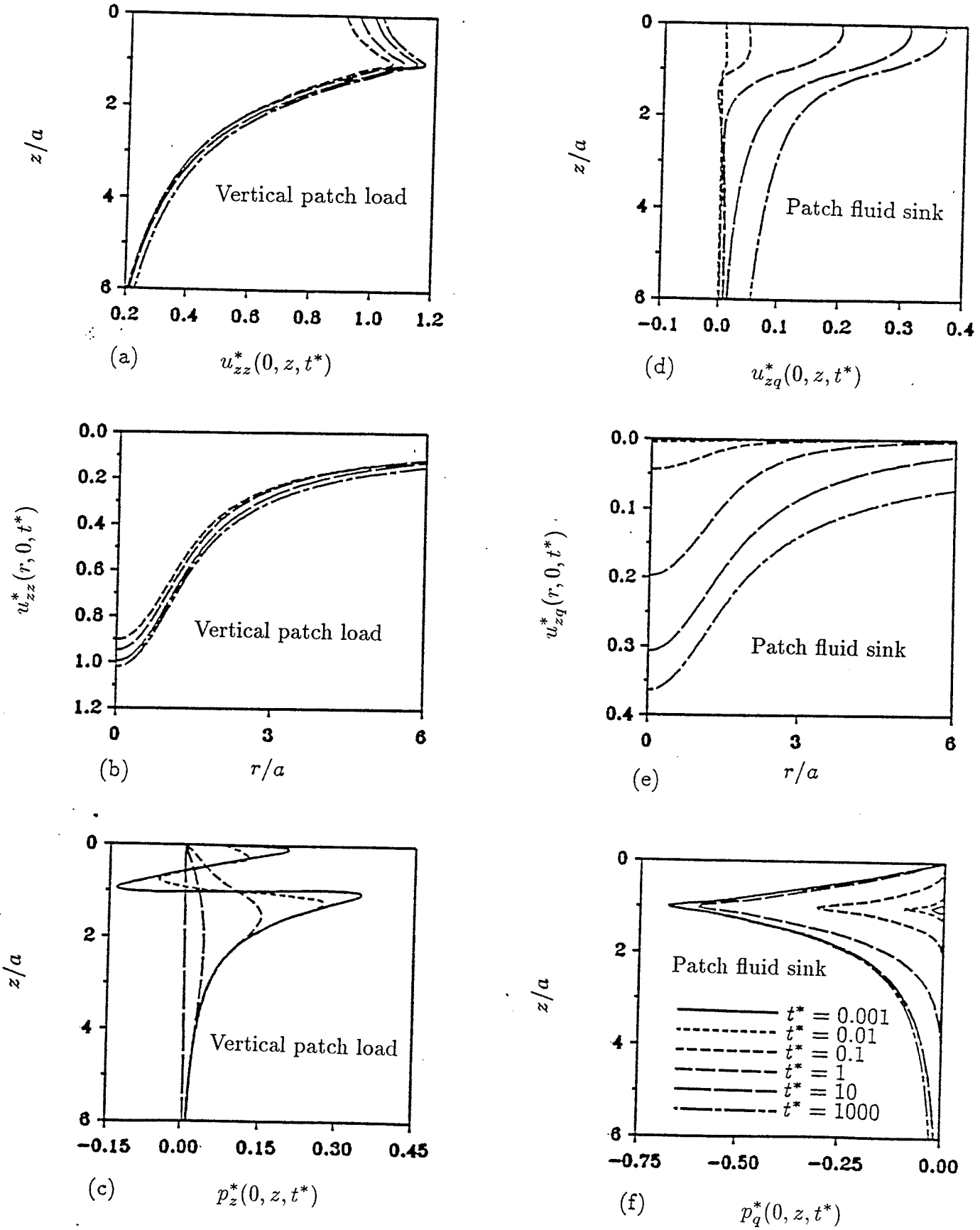

Figure 2.5 Variation of displacements and pore pressure along the z-axis and the surface for Ruhr Sandstone under loadings shown in Figs. 2.2(a) and 2.2(c)

Chapter 3

QUASI-STATIC GREEN'S FUNCTIONS OF A MULTI-LAYERED POROELASTIC HALF-SPACE

3.1 General

An exact stiffness matrix method is presented in this Chapter to compute quasi-static Green's functions of a multi-layered poroelastic half-space with compressible constituents due to buried loadings and a fluid source. The Laplace-Hankel transforms of displacements and pore pressure at layer interfaces are considered as the basic unknowns when compared to the conventional method (Vardoulakis and Harnpattanapanich, 1986) where the layer arbitrary coefficients are chosen as basic unknowns. The three-dimensional analytical general solutions of a homogeneous poroelastic medium presented in Chapter 2 are used to construct explicitly an 8×8 symmetric stiffness matrix which describes the relationship between generalized displacement and force vectors of a layer in the Laplace-Hankel transform space. For an underlying half-space, a 4×4 exact stiffness matrix is also derived explicitly by using the general solutions. The global stiffness matrix of a multi-layered half-space is assembled by considering the continuity conditions of tractions and fluid flow at the interface between the adjacent layers. The numerical solution of the global stiffness equation system for discrete values of Hankel and Laplace transform parameters results in the Laplace-Hankel transforms of displacements and pore pressure at layer interfaces. Thereafter, time-domain solutions for displacements, stresses, pore pressure and fluid discharge are computed by applying a numerical scheme for Laplace inversion and direct numerical quadrature for Hankel transform inversion. Selected numerical results for displacements, pore pressure and fluid discharge corresponding to different poroelastic layered systems are presented in this Chapter to portray the influence of layering and the poroelastic material parameters on the response.

The present method has high numerical efficiency due to the fact that it requires the solution of a banded symmetric stiffness matrix [e.g. $4(N+1) \times 4(N+1)$ for the

system shown in Fig. 3.1] of nearly one-half the size of the unsymmetric coefficient matrix [e.g. $(8N+4)\times(8N+4)$] corresponding to the conventional scheme based on the determination of layer arbitrary coefficients. In addition, the elements of the stiffness matrix involve only numerically stable negative exponential terms of Hankel transform parameters resulting in well-conditioned matrices for all values of transform parameters. The stiffness matrix scheme presented in this Chapter can be used directly to compute the kernel functions required in the application of boundary integral equation methods for layered poroelastic domains.

3.2 Stiffness Matrices

Consider a multi-layered system with a total of N poroelastic layers overlying a poroelastic half-space. Layers and interfaces are numbered as shown in Fig. 3.1. Following Section 2.3, the general solutions for the mth Fourier harmonic of solid and fluid displacements, pore pressure and stresses in the Laplace-Hankel transform space of a homogeneous poroelastic medium can be expressed in the following matrix form:

$$\mathbf{u}(\xi,z,s)=\mathbf{R}(\xi,z,s)\mathbf{C}(\xi,s) \tag{3.1a}$$

$$\mathbf{f}(\xi,z,s)=\mathbf{S}(\xi,z,s)\mathbf{C}(\xi,s) \tag{3.1b}$$

where

$$\mathbf{u}(\xi,z,s)=<u_i(\xi,z,s)>^T, \qquad i=1,2,3,4 \tag{3.2a}$$

$$\mathbf{f}(\xi,z,s)=<f_i(\xi,z,s)>^T, \qquad i=1,2,3,4 \tag{3.2b}$$

$$u_1(\xi,z,s)=\frac{1}{2}\left[\bar{\mathcal{H}}_{m+1}\left(u_{rm}+u_{\theta m}\right)-\bar{\mathcal{H}}_{m-1}\left(u_{rm}-u_{\theta m}\right)\right] \tag{3.3a}$$

$$u_2(\xi,z,s)=\frac{1}{2}\left[\bar{\mathcal{H}}_{m+1}\left(u_{rm}+u_{\theta m}\right)+\bar{\mathcal{H}}_{m-1}\left(u_{rm}-u_{\theta m}\right)\right] \tag{3.3b}$$

$$u_3(\xi,z,s)=\bar{\mathcal{H}}_m\left(u_{zm}\right) \tag{3.3c}$$

$$u_4(\xi,z,s)=\bar{\mathcal{H}}_m\left(p_m\right) \tag{3.3d}$$

$$f_1(\xi,z,s)=\frac{1}{2}\left[\bar{\mathcal{H}}_{m+1}\left(\sigma_{zrm}+\sigma_{z\theta m}\right)-\bar{\mathcal{H}}_{m-1}\left(\sigma_{zrm}-\sigma_{z\theta m}\right)\right] \tag{3.4a}$$

$$f_2(\xi,z,s)=\frac{1}{2}\left[\bar{\mathcal{H}}_{m+1}\left(\sigma_{zrm}+\sigma_{z\theta m}\right)+\bar{\mathcal{H}}_{m-1}\left(\sigma_{zrm}-\sigma_{z\theta m}\right)\right] \tag{3.4b}$$

$$f_3(\xi,z,s)=\bar{\mathcal{H}}_m\left(\sigma_{zzm}\right) \tag{3.4c}$$

$$f_4(\xi, z, s) = \bar{\mathcal{H}}_m(w_{zm}) \tag{3.4d}$$

$$\mathbf{C}(\xi, s) =< A_m \quad B_m \quad C_m \quad D_m \quad E_m \quad F_m \quad G_m \quad H_m >^T \tag{3.5}$$

In the above equations, s and ξ denote the Laplace and Hankel transform parameters, respectively; $\bar{\mathcal{H}}_m$ is the Laplace-mth order Hankel transform operator defined in eqn (2.7) and the arbitrary functions $A_m(\xi, s), B_m(\xi, s), ..., H_m(\xi, s)$ appearing in $\mathbf{C}(\xi, s)$ are to be determined by employing appropriate boundary and/or continuity conditions. In addition, the matrices $\mathbf{R}(\xi, z, s)$ and $\mathbf{S}(\xi, z, s)$ in eqns (3.1) are given by

$$\mathbf{R} = [\mathbf{R}_1 \ \vdots \ \mathbf{R}_2] \tag{3.6a}$$

$$\mathbf{S} = [\mathbf{S}_1 \ \vdots \ \mathbf{S}_2] \tag{3.6b}$$

where

$$\mathbf{R}_1 = \begin{pmatrix} -\xi\eta ce^{\gamma z}/s & -\xi\eta ce^{-\gamma z}/s & a_1 z e^{\xi z} & -a_1 z e^{-\xi z} \\ 0 & 0 & 0 & 0 \\ \gamma\eta ce^{\gamma z}/s & -\gamma\eta ce^{-\gamma z}/s & -(a_1 z - \frac{a_2}{\xi})e^{\xi z} & -(a_1 z + \frac{a_2}{\xi})e^{-\xi z} \\ 2\mu a_5 \eta e^{\gamma z} & 2\mu a_5 \eta e^{-\gamma z} & -2\mu a_4 \eta e^{\xi z} & -2\mu a_4 \eta e^{-\xi z} \end{pmatrix} \tag{3.7a}$$

$$\mathbf{R}_2 = \frac{1}{2}\begin{pmatrix} e^{\xi z} & e^{-\xi z} & -e^{\xi z} & -e^{-\xi z} \\ e^{\xi z} & e^{-\xi z} & e^{\xi z} & e^{-\xi z} \\ -e^{\xi z} & e^{-\xi z} & e^{\xi z} & -e^{-\xi z} \\ 0 & 0 & 0 & 0 \end{pmatrix} \tag{3.7b}$$

$$\mathbf{S}_1 = \mu \begin{pmatrix} -2\xi\gamma\eta ce^{\gamma z}/s & 2\xi\gamma\eta ce^{-\gamma z}/s & (2a_1\xi z - 1)e^{\xi z} & (2a_1\xi z + 1)e^{-\xi z} \\ 0 & 0 & 0 & 0 \\ 2\xi^2\eta ce^{\gamma z}/s & 2\xi^2\eta ce^{-\gamma z}/s & -2(a_1\xi z - a_4)e^{\xi z} & 2(a_1\xi z + a_4)e^{-\xi z} \\ -2a_5\delta_1 e^{\gamma z} & 2a_5\delta_1 e^{-\gamma z} & 2a_4\delta_2 e^{\xi z} & -2a_4\delta_2 e^{-\xi z} \end{pmatrix} \tag{3.7c}$$

$$\mathbf{S}_2 = \frac{\mu}{2}\begin{pmatrix} 2\xi e^{\xi z} & -2\xi e^{-\xi z} & -2\xi e^{\xi z} & 2\xi e^{-\xi z} \\ \xi e^{\xi z} & -\xi e^{-\xi z} & \xi e^{\xi z} & -\xi e^{-\xi z} \\ -2\xi e^{\xi z} & -2\xi e^{-\xi z} & 2\xi e^{\xi z} & 2\xi e^{-\xi z} \\ 0 & 0 & 0 & 0 \end{pmatrix} \tag{3.7d}$$

$$\delta_1 = \frac{\gamma\eta\kappa}{s}, \qquad \delta_2 = \frac{\xi\eta\kappa}{s} \tag{3.7e}$$

and c, γ, η and a_i $(i = 1, 2, 4, 5)$ are defined in eqns (2.5c), (2.10), (2.12), (2.17) and (2.21), respectively, in Section 2.3.

Let a superscript n denote quantities associated with the nth layer ($n = 1, 2, ..., N$). Then, the following relationships can be established for the nth layer of the system shown in Fig. 3.1 by using eqns (3.1a) and (3.1b):

$$\mathbf{U}^{(n)} = \begin{bmatrix} \mathbf{R}^{(n)}(\xi, z_n, s) \\ \cdots\cdots\cdots\cdots \\ \mathbf{R}^{(n)}(\xi, z_{n+1}, s) \end{bmatrix} \mathbf{C}^{(n)} \tag{3.8a}$$

$$\mathbf{F}^{(n)} = \begin{bmatrix} -\mathbf{S}^{(n)}(\xi, z_n, s) \\ \cdots\cdots\cdots\cdots \\ \mathbf{S}^{(n)}(\xi, z_{n+1}, s) \end{bmatrix} \mathbf{C}^{(n)} \tag{3.8b}$$

where

$$\mathbf{U}^{(n)} = < \mathbf{u}^{(n)}(\xi, z_n, s) \quad \mathbf{u}^{(n)}(\xi, z_{n+1}, s) >^T \tag{3.9a}$$

$$\mathbf{F}^{(n)} = < -\mathbf{f}^{(n)}(\xi, z_n, s) \quad \mathbf{f}^{(n)}(\xi, z_{n+1}, s) >^T \tag{3.9b}$$

In eqns (3.8) and (3.9), $\mathbf{U}^{(n)}$ denotes a vector of generalized coordinates for the nth layer whose elements are related to the Laplace-Hankel transforms of the mth Fourier harmonic of displacements and pore pressure of the top and bottom surfaces of the nth layer. Similarly, $\mathbf{F}^{(n)}$ denotes a generalized force vector whose elements are related to the Laplace-Hankel transforms of the mth Fourier harmonic of tractions and fluid displacements of the top and bottom surfaces of the nth layer. The matrices $\mathbf{R}^{(n)}$ and $\mathbf{S}^{(n)}$ in eqns (3.8) are identical to $\mathbf{R}$ and $\mathbf{S}$ defined in eqns (3.6) except that the material properties of the nth layer are used in the definition and $z = z_n$ or z_{n+1}. The vector $\mathbf{C}^{(n)}$ is the arbitrary coefficient vector corresponding to the nth layer.

The eqn (3.8a) can be inverted to express $\mathbf{C}^{(n)}$ in terms of $\mathbf{U}^{(n)}$ and the substitution in eqn (3.8b) yields

$$\mathbf{F}^{(n)} = \mathbf{K}^{(n)}\mathbf{U}^{(n)}, \qquad n = 1, 2, ..., N \tag{3.10}$$

where $\mathbf{K}^{(n)}$ can be considered as an exact stiffness matrix in the Laplace-Hankel transform space describing the relationship between the generalized displacement vector $\mathbf{U}^{(n)}$ and the force vector $\mathbf{F}^{(n)}$ for the nth layer.

The explicit derivation of $\mathbf{K}^{(n)}$ corresponding to an arbitrary Fourier harmonic of a three-dimensional poroelastic problem is extremely complicated and it is impossible to achieve this task manually due to the fact that the inversion of eqn (3.8a) involves a fully populated 8×8 unsymmetric matrix whose elements involve rather complicated expressions. However, this task, which needs to be performed only once, can be achieved by using modern symbolic manipulation packages. In the present study, the author used the computer algebra package *Mathematica* (Wolfram, 1988) to obtain $\mathbf{K}^{(n)}$ explicitly. It should be noted that *Mathematica* results in extremely lengthy and complicated expressions for elements of $\mathbf{K}^{(n)}$ which have to be extensively manipulated and reduced to obtain more simplified expressions to achieve a computationally efficient solution scheme. After lengthy manipulations, it is found that $\mathbf{K}^{(n)}$ is symmetric and its elements can be expressed as

1st Row:

$$k_{11} = \left(\alpha_{2n}^2 + 1\right)\left(d_1\varrho_1 - d_2\varrho_2\right) - 4\alpha_{2n}\left(d_3\varrho_1 - d_4\varrho_3\right) \tag{3.11a}$$

$$k_{12} = 0, \qquad k_{13} = \left(\alpha_{2n}^2 - 1\right)\left(d_1\varrho_1 - d_2\varrho_2\right) + \xi \tag{3.11b}$$

$$k_{14} = \delta_1\left(\alpha_{2n}^2 - 1\right)\left(d_6\varrho_2 - d_5\varrho_1 - 4\alpha_{1n}\alpha_{2n}\varrho_3\right) + \delta_2 k_{11} \tag{3.11c}$$

$$k_{15} = 2d_7\varrho_1 - 2\alpha_{2n}\left(2d_1\varrho_1 - d_2\varrho_2 + d_5\varrho_3\right) \tag{3.11d}$$

$$k_{16} = 0, \qquad k_{17} = 2\left(\alpha_{2n}^2 - 1\right)\left[d_4\varrho_3 - d_3\varrho_1\right] \tag{3.11e}$$

$$k_{18} = 2\delta_1\left[\alpha_{2n}\left(d_2\varrho_1 + d_6\varrho_3\right) - d_7\varrho_2\right] + \delta_2 k_{15} \tag{3.11f}$$

where

$$\alpha_{1n} = e^{-\gamma h_n}, \qquad \alpha_{2n} = e^{-\xi h_n}, \qquad n = 1, 2, ..., N \tag{3.12a}$$

$$d_1 = \left(\alpha_{1n}\alpha_{2n} - 1\right)^2 + \left(\alpha_{1n} - \alpha_{2n}\right)^2, \quad d_2 = \left(\alpha_{1n}\alpha_{2n} - 1\right)^2 - \left(\alpha_{1n} - \alpha_{2n}\right)^2 \tag{3.12b}$$

$$d_3 = \left(\alpha_{1n}\alpha_{2n} - 1\right)\left(\alpha_{2n} - \alpha_{1n}\right), \quad d_4 = \alpha_{2n}\left(\alpha_{1n}^2 - 1\right) \tag{3.12c}$$

$$d_5 = \left(\alpha_{1n}^2 - 1\right)\left(\alpha_{2n}^2 + 1\right), \quad d_6 = \left(\alpha_{1n}^2 + 1\right)\left(\alpha_{2n}^2 - 1\right), \quad d_7 = \alpha_{1n}\left(\alpha_{2n}^2 - 1\right)^2 \tag{3.12d}$$

$$\varrho_1 = \frac{4\mu^2}{\psi}\left(a_4^2 a_5^2 \eta\delta_1\right), \ \varrho_2 = \frac{2\mu}{\xi\psi}\left(2\mu a_4^2 a_5^2 \xi\eta\delta_2 - a_2 a_4 a_5^2\right), \ \varrho_3 = \frac{2\mu}{\psi}\left(a_1 a_4 a_5^2 h_n\right) \tag{3.12e}$$

$$\psi = \left(\alpha_{2n}^2 - 1\right)\left(2d_1 g_1 - d_2 g_2\right) - 4\alpha_{2n}\left(2d_3 g_3 - d_4 g_4\right) \tag{3.13a}$$

$$g_1 = \frac{2\mu a_5 \eta}{\xi}\left[2\mu a_4^2 a_5 \xi\eta\delta_1\delta_2 - a_2 a_4 a_5 \delta_1\right] \tag{3.13b}$$

$$g_2 = \frac{1}{\xi^2}\left[a_2^2 a_5^2 - 4\mu a_4 a_5^2 \eta\left\{a_2\delta_2 - \mu a_4\eta(\delta_1^2 + \delta_2^2)\right\}\right] \tag{3.13c}$$

$$g_3 = 2\mu a_1 a_4 a_5^2 \eta\delta_1 h_n, \qquad g_4 = a_1^2 a_5^2 h_n^2 \tag{3.13d}$$

2nd Row:

$$k_{22} = -\mu\xi\frac{\left(\alpha_{2n}^2 + 1\right)}{\left(\alpha_{2n}^2 - 1\right)}, \qquad k_{26} = \frac{2\mu\xi\alpha_{2n}}{\left(\alpha_{2n}^2 - 1\right)} \tag{3.14a}$$

$$k_{2i} = 0, \qquad i = 1, 3, 4, 5, 7, 8 \tag{3.14b}$$

3rd Row:

$$k_{33} = \left(\alpha_{2n}^2 - 1\right)\left(d_6\varrho_1 - d_5\varrho_2\right) - 4\alpha_{2n} d_4\varrho_3 \tag{3.15a}$$

$$k_{34} = \left(\alpha_{2n}^2 - 1\right)\left\{\delta_1\left(d_1\varrho_2 - d_2\varrho_1\right) + \delta_2\left(d_1\varrho_1 - d_2\varrho_2\right)\right\} - 4\alpha_{2n}\delta_1 d_3\varrho_3 \tag{3.15b}$$

$$k_{35} = -k_{17}, \qquad k_{36} = 0, \qquad k_{37} = 2\alpha_{2n}\left(d_2\varrho_2 + d_5\varrho_3\right) - 2d_7\varrho_1 \tag{3.15c}$$

$$k_{38} = 2\delta_1\left[\alpha_{2n} d_1\varrho_3 - \left(\alpha_{2n}^2 - 1\right)d_3\varrho_2\right] + \delta_2 k_{35} \tag{3.15d}$$

4th Row:

$$k_{44} = \left(\alpha_{2n}^2 + 1\right)\left(2d_1 g_6 - d_2 g_5\right) - \left(\alpha_{2n}^2 - 1\right)d_6 g_7 + 4\alpha_{2n} g_8 \tag{3.16a}$$

$$k_{45} = k_{18}, \qquad k_{46} = 0, \qquad k_{47} = -k_{38} \tag{3.16b}$$

$$k_{48} = 2d_7 g_7 - 2\alpha_{2n}\left(2d_1 g_6 - d_2 g_5 + g_9\right) \tag{3.16c}$$

where

$$g_5 = \frac{2\mu a_5}{\xi\psi}\left[a_2 a_4 a_5\left(\delta_1^2 - \delta_2^2\right) + 2\mu a_4^2 a_5 \xi\eta\delta_2\left(\delta_1^2 + \delta_2^2\right)\right] \tag{3.17a}$$

$$g_6 = \frac{4\mu^2}{\psi}\left(a_4^2 a_5^2 \eta\delta_1\delta_2^2\right), \qquad g_7 = \frac{a_2^2 a_5^2 \delta_1}{\xi^2\eta\psi} \tag{3.17b}$$

$$g_8 = \frac{1}{\eta\delta_1\psi}\left[d_4 g_3\left(\delta_1^2 + \delta_2^2\right) - 2\alpha_{1n}\left(\alpha_{2n}^2 - 1\right)\delta_1\delta_2 g_3 + \alpha_{2n}\left(\alpha_{1n}^2 + 1\right)\delta_1^2 g_4\right] \tag{3.17c}$$

$$g_9 = \frac{1}{\eta\delta_1\psi}\left[d_5 g_3\left(\delta_1^2 + \delta_2^2\right) - 2d_6\delta_1\delta_2 g_3 + 4\alpha_{1n}\alpha_{2n}\delta_1^2 g_4\right] \tag{3.17d}$$

5th Row:

$$k_{55} = k_{11}, \qquad k_{56} = 0, \qquad k_{57} = -k_{13}, \qquad k_{58} = k_{14} \tag{3.18}$$

6th Row:

$$k_{66} = k_{22}, \qquad k_{67} = k_{68} = 0 \tag{3.19}$$

7th Row:

$$k_{77} = k_{33}, \qquad k_{78} = -k_{34} \tag{3.20}$$

8th Row:

$$k_{88} = k_{44} \tag{3.21}$$

The layer stiffness matrix $\mathbf{K}^{(n)}$ is a function of the layer thickness, the layer material properties, the Laplace and Hankel transform parameters s and ξ, respectively. Only negative exponentials that decrease rapidly with increasing ξ, s and h_n are involved in k_{ij}. The relationships between k_{ij}'s [e.g. eqns (3.18)-(3.21)] can also be derived on the basis of the physical behaviour of the system since each k_{ij} represents a component of a generalized force vector due to a generalized displacement vector equals to a unit vector. When compared to the stiffness matrix method proposed by Lysmer and Waas (1972) and Seale and Kausel (1989), the $\mathbf{K}^{(n)}$ obtained from the present method is exact and does not involve any approximations in the derivation.

For the underlying half-space, due to the regularity condition at $z \to \infty$, the general solutions involve only four arbitrary coefficients in the vector $\mathbf{C}^{(N+1)}$, i.e. $B_m^{(N+1)}$, $D_m^{(N+1)}$, $F_m^{(N+1)}$ and $H_m^{(N+1)}$. The stiffness matrix of the bottom half-space can be expressed as

$$\mathbf{F}^{(N+1)} = \mathbf{K}^{(N+1)}\mathbf{U}^{(N+1)} \tag{3.22}$$

where

$$\mathbf{U}^{(N+1)} =< \mathbf{u}^{(N+1)}(\xi, z_{N+1}, s) >^T \tag{3.23a}$$

$$\mathbf{F}^{(N+1)} =< -\mathbf{f}^{(N+1)}(\xi, z_{N+1}, s) >^T \tag{3.23b}$$

$$\mathbf{K}^{(N+1)} = \text{symm.}\left[\tilde{k}_{ij}\right]_{4\times 4} \tag{3.23c}$$

The elements of the half-space stiffness matrix can be expressed as

$$\tilde{k}_{11} = -\frac{2\mu a_4 a_5 \eta}{\beta}, \qquad \tilde{k}_{12} = 0 \tag{3.24a}$$

$$\tilde{k}_{13} = -\frac{\mu a_5 \eta}{\beta} + 2\xi(\delta_1 - \delta_2)\tilde{k}_{11}, \qquad \tilde{k}_{14} = (\delta_2 - \delta_1)\tilde{k}_{11} \tag{3.24b}$$

$$\tilde{k}_{22} = \mu\xi, \qquad \tilde{k}_{23} = \tilde{k}_{24} = 0 \tag{3.24c}$$

$$\tilde{k}_{33} = \tilde{k}_{11}, \qquad \tilde{k}_{34} = -\tilde{k}_{14} \tag{3.24d}$$

$$\tilde{k}_{44} = \frac{a_2 a_5 c\delta_1}{\xi\beta} + c\delta_2 \tilde{k}_{14} \tag{3.24e}$$

where

$$\beta = 2\mu a_4 a_5 \eta^2(\delta_2 - \delta_1) - \frac{a_2 a_5 \eta}{\xi} \tag{3.25}$$

It is noted that exponential terms of ξ and s are not involved in the expression of $\mathbf{K}^{(N+1)}$ and its elements depend on the material properties of the underlying half-space, the Laplace and Hankel transform parameters s and ξ, respectively. The stiffness matrix $\mathbf{K}^{(N+1)}$ of the underlying half-space derived here exactly satisfies all the governing equations. On the other hand, the stiffness matrix scheme proposed by Lysmer and Waas (1972) and Seale and Kausel (1989) is not capable of taking into consideration the influence of an underlying half-space.

3.3 Global Stiffness Matrix

The global stiffness matrix of a multi-layered half-space is assembled by using the layer and half-space stiffness matrices together with the continuity conditions of tractions and fluid flow at layer interfaces. For example, the continuity conditions at the nth interface can be expressed as

$$\mathbf{f}^{(n-1)}(\xi, z_n, s) - \mathbf{f}^{(n)}(\xi, z_n, s) = \mathbf{T}^{(n)} \tag{3.26}$$

where $\mathbf{f}^{(n)}$ is identical to $\mathbf{f}$ defined in eqn (3.2b) with a superscript n denoting the layer number and

$$\mathbf{T}^{(n)} = < T_1^{(n)} \quad T_2^{(n)} \quad T_3^{(n)} \quad \frac{Q^{(n)}}{s} >^T \tag{3.27}$$

in which

$$T_1^{(n)} = \frac{1}{2}\left[\bar{\mathcal{H}}_{m+1}\left(T_{rm}^{(n)} + T_{\theta m}^{(n)}\right) - \bar{\mathcal{H}}_{m-1}\left(T_{rm}^{(n)} - T_{\theta m}^{(n)}\right)\right] \tag{3.28a}$$

$$T_2^{(n)} = \frac{1}{2}\left[\bar{\mathcal{H}}_{m+1}\left(T_{rm}^{(n)} + T_{\theta m}^{(n)}\right) + \bar{\mathcal{H}}_{m-1}\left(T_{rm}^{(n)} - T_{\theta m}^{(n)}\right)\right] \tag{3.28b}$$

$$T_3^{(n)} = \bar{\mathcal{H}}_m\left(T_{zm}^{(n)}\right) \tag{3.28c}$$

$$Q^{(n)} = \bar{\mathcal{H}}_m\left(Q_m^{(n)}\right) \tag{3.28d}$$

where $T_{im}^{(n)}(i = r, \theta, z)$ and $Q_m^{(n)}$ denote the mth Fourier harmonic of the tractions and fluid source applied at the nth interface, respectively.

The consideration of eqn (3.26) at each layer interface together with eqns (3.10) and (3.22) results in the following global equation system.

$$\begin{bmatrix} \mathbf{K}^{(1)} & & & \\ & \ddots & & \\ & & \mathbf{K}^{(N)} & \\ & & & \mathbf{K}^{(N+1)} \end{bmatrix} \begin{Bmatrix} \mathbf{U}^{(1)} \\ \mathbf{U}^{(2)} \\ \vdots \\ \mathbf{U}^{(N)} \\ \mathbf{U}^{(N+1)} \end{Bmatrix} = \begin{Bmatrix} \mathbf{T}^{(1)} \\ \mathbf{T}^{(2)} \\ \vdots \\ \mathbf{T}^{(N)} \\ \mathbf{T}^{(N+1)} \end{Bmatrix} \tag{3.29}$$

The global stiffness matrix of eqn (3.29) is a well-conditioned symmetric matrix and has a band width equal to 8. It is naturally constrained against rigid body displacements due to the presence of $\mathbf{K}^{(N+1)}$. If a half-space is not present at the bottom then the bottom plane at $z = z_N$ has to be restrained to eliminate the rigid body displacements. The number of unknowns in the final equation system, i.e. eqn (3.29) is equal to $4(N+1)$ which is nearly one-half of that corresponding to the classical approach based on the solution of layer arbitrary coefficients $A_m^{(n)}, B_m^{(n)}, ..., H_m^{(n)}$. This reduction of the size of final equation system together with the symmetry makes the present scheme computationally efficient when compared to the conventional scheme (Vardoulakis and Harnpattanapanich, 1986). Furthermore, the eqn (3.29) is invertible and numerically stable for very large values of ξ as shown in Section 3.4.1. Laplace-Hankel transforms of stresses and fluid discharge

at the top and bottom interfaces of a layer can be obtained by using eqns (3.10), (3.29) and (2.8). If displacements and/or pore pressure within points of a layer are required then it is convenient to define a set of fictitious planes through these points and consider these as additional layers. Alternatively, eqn (3.8a) can be used to compute $\mathbf{C}^{(n)}$ for a layer and thereafter compute displacements and pore pressure at arbitrary points within a layer using eqn (3.1a). This, however, may involve the inversion of numerically ill-conditioned matrices such as $\mathbf{R}^{(n)}$ for large values of ξ and consequently loss of precision. If loads and/or fluid sources are applied within a layer then fictitious interfaces are considered at the loading levels.

3.4 Numerical Solutions

3.4.1 Numerical Scheme

A computer code based on the solution procedure described in the preceding sections has been developed to compute the quasi-static Green's functions of a multi-layered poroelastic half-space due to internal loadings and a fluid source. The tasks performed by the computer code can be described as 1) the computation and assembly of stiffness matrices corresponding to each layer and the underlying half-space of a multi-layered poroelastic half-space to establish eqn (3.29) for specified values of ξ and s corresponding to a given numerical Laplace inversion scheme; 2) the solution of eqn (3.29) to obtain the interlayer displacement and pore pressure vectors in the Laplace-Hankel transform space; 3) the evaluation of semi-infinite integrals with respect to ξ defined in eqn (2.8) by direct numerical quadrature discussed in Section 2.5.1 and 4) the evaluation of the time-domain solutions by using the numerical Laplace inversion given by Stehfest [eqn. (2.38)] or Schapery [eqn (2.39)]. It should be noted that the determinant of global stiffness matrix is nonsingular along the integration axis of eqn (2.8) [i.e. real ξ axis for real values of s given by eqns (2.38) and (2.39)]. Although it is impossible to prove this by a rigorous mathematical analysis for an N-layered system, it can be argued that if poles exist in the integrand of eqn (2.8) for real ξ and s values [i.e. singular global stiffness matrix in eqn (3.29)] then by virtue of the application of contour integration method for Laplace inversion yields terms that would increase exponentially with

time. Such behaviour is not admissible in quasi-static problems where the response approaches a finite limit for $t \to \infty$.

The numerical stability and the invertibility of the global stiffness matrix in eqn (3.29) for increasing values of ξ and s can be assessed by computing a condition number of the matrix (Cline *et al.*, 1979). Figure 3.2 presents L_1-condition numbers (The multiplication of the first norm of a matrix and the first norm of its inverse) with respect to ξ for different values of s of the final equation systems corresponding to the present stiffness method [i.e. eqn (3.29)] and the conventional method based on the determination of layer arbitrary coefficients. The results shown in Fig. 3.2 correspond to a layered system consisting of a poroelastic layer of unit thickness ($\nu^{(1)} = 0.25$, $\nu_u^{(1)} = 0.35$ and $B^{(1)} = 0.8$) bonded to a poroelastic half-space ($\nu^{(2)} = 0.2$, $\nu_u^{(2)} = 0.3$ and $B^{(2)} = 0.6$). In addition, $\mu^{(1)}/\mu^{(2)} = 0.5$ and $\kappa^{(1)} = \kappa^{(2)}$. A coefficient matrix of a linear equation system with a small condition number is considered as a well-conditioned system whereas a large condition number indicates ill-conditioning. The numerical results in Fig. 3.2 show that the global stiffness matrix of the present scheme has a smaller condition number which either remains constant or decreases over a wider range of values of transform parameters ξ and s. The condition number of the coefficient matrix corresponding to the conventional method is always higher than that of the global stiffness matrix of eqn (3.29) and becomes extremely large for increasing values of ξ due to the presence of mismatching exponential terms in the coefficient matrix. The numerical stability of the present stiffness matrix approach is clearly demonstrated by the solutions shown in Fig. 3.2.

Table 3.1 presents a comparison of numerical solutions for vertical displacement and vertical stress at the point $(0, a)$ of a homogeneous poroelastic half-space due to a uniform vertical patch load of radius a applied at a depth $z = a$ below the free surface. The half-space is considered to be consisting of 10 layers of equal thickness, $h/a = 0.2$, and an underlying half-space. Solutions obtained from the present stiffness method are compared with the numerical solutions of a homogeneous poroelastic half-space from Chapter 2 to verify the numerical stability and the accuracy of the present matrix scheme. The two solutions are in excellent agreement. Table 3.2 presents a comparison of elastostatic solutions corresponding

to a layer of unit thickness perfectly bonded to a half-space and subjected to uniform vertical pressure of unit total force applied over a circular area of unit radius at the top surface. Exact solutions (computed numerically) provided by Muki and Dong (1980) is used in the comparison with the final solutions ($t \rightarrow \infty$) from the present study. The general accuracy of the solutions obtained from the stiffness matrix method presented in this Chapter is confirmed through these independent comparisons.

3.4.2 Numerical Results for Multi-Layered Poroelastic Half-Spaces

The quasi-static response of a multi-layered poroelastic half-space under a selected set of loadings is investigated in the numerical study. A layered system consisting of two poroelastic layers bonded to an underlying poroelastic half-space is considered in all numerical studies presented in this Chapter. The properties of the first layer are $\nu^{(1)} = 0.25$, $\nu_u^{(1)} = 0.5$ and $B^{(1)} = 1.0$; for the second layer, $\nu^{(2)} = 0.25$, $\nu_u^{(2)} = 0.35$ and $B^{(2)} = 0.8$ and for the underlying half-space, $\nu^{(3)} = 0.2$, $\nu_u^{(3)} = 0.3$ and $B^{(3)} = 0.6$. In addition, $\mu^{(2)}/\mu^{(1)} = 1$; $\mu^{(3)}/\mu^{(1)} = 2$ and applied loadings and fluid discharges are assumed to be uniformly distributed over a circular area of radius a.

3.4.2.1 Displacement Histories under Surface Loadings

Time histories of displacements at the origin ($r = 0, z = 0$) due to uniform patch loadings of intensity f_0 applied at the top surface are studied first. Problems of this nature are useful in the study of consolidation settlement of surface foundations. In the parametric study, the total thickness of the two layers, $h_1 + h_2$, is equal to $2a$ and $\kappa^{(3)}/\kappa^{(2)}$ =0.5. A nondimensional time, $\tau_1[= c^{(2)}t/a^2]$, in the range $10^{-6} \leq \tau_1 \leq 10^4$ is considered in the numerical study. Time histories of nondimensional vertical displacement, $u_{zz}^*[= 2\mu^{(1)}u_z/f_0a]$, at the origin due to a uniform vertical pressure are shown in Figs. 3.3(a) and 3.3(c). Figs. 3.3(b) and 3.3(d) present nondimensional horizontal displacement, $u_{xx}^*[= 2\mu^{(1)}u_x/f_0a]$, at the origin due to a uniform horizontal pressure applied at the top surface. Numerical results presented in Figs. 3.3 indicate that the general trend of the displacement histories is quite similar for both vertical and horizontal loadings as noted in Section

2.5.2 for a homogeneous poroelastic half-space under buried loadings. The influence of permeability on the response is considered in Figs. 3.3(a) and 3.3(b) by setting $\kappa^{(1)}/\kappa^{(2)} = 0.001, 0.01, 0.1, 1.0$ and 10 with $h_1 = h_2 = a$. It can be seen from these two figures that the ratio $\kappa^{(1)}/\kappa^{(2)}$ has a significant influence on the consolidation process of a layered poroelastic half-space. As expected, the consolidation settlement is first noted in the case of $\kappa^{(1)}/\kappa^{(2)} = 10$ whereas, for $\kappa^{(1)}/\kappa^{(2)} = 0.001$, it is observed when $\tau_1 > 0.1$. The earliest final solution is reached for $\kappa^{(1)}/\kappa^{(2)} = 10$ and the latest for $\kappa^{(1)}/\kappa^{(2)} = 0.001$. This behaviour is due to the fact that the first layer is less permeable in the latter case. Comparison of displacement histories in Figs. 3.3(a) and 3.3(b) indicates that the variation of the ratio $\kappa^{(1)}/\kappa^{(2)}$ essentially results in a shift of the response profile in the time scale. The numerical solutions in Figs. 3.3(a) and 3.3(b) show identical initial and final displacements since the material parameters ν, ν_u and μ, and the thicknesses of the two layers are the same for all values of $\kappa^{(1)}/\kappa^{(2)}$.

The influence of layer thickness on the response is studied in Figs. 3.3(c) and 3.3(d) for five different values of the ratio h_1/h_2, i.e. $h_1/h_2 = 0.25, 0.5, 1, 2$ and 4. Note that the total thickness of the two layers is $2a$ and $\kappa^{(1)}/\kappa^{(2)} = 0.001$. The initial displacements for different values of h_1/h_2 are different and their order of magnitude is identical to that of h_1/h_2. This is a consequence of the fact that the undrained behaviour of poroelastic materials is mainly governed by the undrained Poisson's ratio, therefore a higher ratio of h_1/h_2 means a lesser undrained compressibility of the layered system since $\nu_u^{(1)} > \nu_u^{(2)}$. The consolidation settlements in all cases are initiated at almost identical time instants, i.e. after $\tau_1 > 0.1$, and the final settlement is first reached in the case where $h_1/h_2 = 0.25$ (i.e. $h_1/a = 0.4$ and $h_2/a = 1.6$) when $\tau_1 > 100$. It is also found that the time to reach the final solution increases with increasing values of h_1/h_2. These features are consistent with the fact that since $\kappa^{(1)}/\kappa^{(2)} = 0.001$, the layered system becomes more impermeable for a higher ratio of h_1/h_2. Final solutions are identical since elastic properties (drained) of the different layered systems are identical and the consolidation process in all cases is completed for $\tau_1 > 1000$.

3.4.2.2 Displacement and Pore Pressure Histories due to Fluid Sink

The next set of solutions corresponds to problems involving fluid withdrawal from layered poroelastic media. Problems of this nature are useful in the study of settlement due to groundwater withdrawal, energy resource explorations, etc.. A circular fluid sink of uniform intensity q_0 is located at the center of the second layer of the layer system defined previously. The sink is at a depth $z = 10a$ below the free surface. In the numerical study, the permeability of the first layer and the half-space is assumed to be equal, i.e. $\kappa^{(1)} = \kappa^{(3)}$, and the ratio $\kappa^{(2)}/\kappa^{(1)}$ is varied from 1 to 100. In addition, the thickness of the second layer is assumed to vary between a to $4a$. A nondimensional time τ_2, where $\tau_2 = c^{(1)}t/a^2$, is used in the fluid sink problem. Time histories of nondimensional vertical displacement, $u^*_{zq}[= c^{(1)}u_z/q_0a^2]$, at the origin for different values of $\kappa^{(2)}/\kappa^{(1)}$ and h_2 are presented in Figs. 3.4(a) and 3.4(b), respectively, for $10^{-2} \leq \tau_2 \leq 10^4$. It is found that the displacement at this point is higher than that at the point $(0, 10a)$ at all time instants. Similar behaviour was also observed in the numerical solutions shown in Fig. 2.3(c) for the case of a buried patch fluid sink in a homogeneous poroelastic half-space. The solutions presented in Figs. 3.4(a) and 3.4(b) indicate that the surface settlements in all cases are initially zero and increase rapidly with time during the period $1 < \tau_2 < 100$. Final solutions in all cases are reached when $\tau_2 > 1000$.

Figs. 3.4(c) and 3.4(d) show time histories of nondimensional pore pressure, $p^*_q[= c^{(1)}p/2\mu^{(1)}q_0a]$, at the center of the patch sink $(r = 0, z = 10a)$ for different values of $\kappa^{(2)}/\kappa^{(1)}$ and h_2, respectively, for $10^{-3} \leq \tau_2 \leq 10^3$. It is noted that initial pore pressure is zero and suction is subsequently developed at this point. Final values for suction are obtained after $\tau_2 > 100$. It is noted that less suction is developed due to a fluid sink in a more permeable layered system; i.e. for higher values of $\kappa^{(2)}/\kappa^{(1)}$ in Fig. 3.4(c) and for higher values of h_2 in Fig. 3.4(d). It can be argued that higher suction developed in a layered system results in higher stresses in the solid matrix (effective stresses) and consequently larger solid strains. Therefore, the solutions presented in Figs. 3.4(a) and 3.4(b) indicate that the vertical displacement decreases with increasing values of $\kappa^{(2)}/\kappa^{(1)}$ and h_2, respectively.

3.4.2.3 Pore Pressure and Fluid Discharge Profiles along the z-Axis

Nondimensional pore pressure, $p_z^*[= p/f_0]$, along the vertical axis due to a vertical patch load applied at the top surface are shown in Figs. 3.5(a) and 3.5(b) for different values of $\kappa^{(1)}/\kappa^{(2)}$ and h_1/h_2 , respectively, for time instants $\tau_1 = 0.001$ and 1. It is found that no suction is developed along the z-axis due to a vertical surface load and excess pore pressure becomes insignificant for $z > 4a$. The notable feature is that a discontinuity in the slope of the profiles is observed at the interfaces, i.e. at $z/a = 0.4$ for $h_1/h_2 = 0.25$, at $z/a = 1$ for $h_1/h_2 = 1$ and at $z/a = 1.6$ for $h_1/h_2 = 4$. This is due to the fact that since the permeability of the two layers are different a discontinuity exists in the slope of the pore pressure profiles at the interfaces. A small discontinuity also exists at the interface between the second layer and the half-space (i.e. at $z/a = 2.0$) since the permeability of the two media are not the same ($\kappa^{(3)}/\kappa^{(2)} = 0.5$). Initially ($\tau_1 < 0.001$), a very large pore pressure is developed near the top surface resulting in a very high gradient of pressure in the region $0 < z/a < 1$. Pore pressure beneath the first layer decreases with depth in all cases and are nearly identical for $z/a > 2$. As expected, the rate of pore pressure dissipation increases with increasing values of permeability. For example, at $\tau_1 = 1$, excess pore pressure is nearly dissipated in the first layer for $\kappa^{(1)}/\kappa^{(2)} = 10$ whereas appreciable pore pressure is noted in the first layer if $\kappa^{(1)}/\kappa^{(2)} = 0.1$ for all values of h_1/h_2. Excess pore pressure diminishes to negligible level when $\tau_1 > 10$ and 100 for $\kappa^{(1)}/\kappa^{(2)} = 10$ and 0.1, respectively.

Profiles of nondimensional pore pressure, p_q^*, and fluid discharge, $q_{zq}^*[= q_z/q_0]$, along the z-axis due to a patch fluid sink at a depth $z = 10a$ below the free surface are shown in Figs. 3.6(a) and 3.6(b), respectively, for different time instants. Numerical solutions are presented for $8 \leq z/a \leq 12$ and for $\kappa^{(2)}/\kappa^{(1)} = 1$ and 10 when $h_2 = 2a$. Note that $\kappa^{(3)}$ is equal to $\kappa^{(1)}$ in this case. As expected, suction profiles shown in Fig. 3.6(a) indicate that the maximum value of suction is noted at the level of the sink (i.e. $z/a = 10$) for all values of τ_2 and the suction is higher for $\kappa^{(2)}/\kappa^{(1)} = 1$ when compared to $\kappa^{(2)}/\kappa^{(1)} = 10$. Naturally, the pore pressure profiles show a singularity (kink) at $z = 10a$ due to the fluid sink applied at this level. A discontinuity in the slope of the p_q^* profiles is observed at layer interfaces,

i.e. at $z/a = 9$ and 11 for $\kappa^{(2)}/\kappa^{(1)} = 10$. Such a discontinuity does not exist when $\kappa^{(2)} = \kappa^{(1)}$. Final values for suction are attained when $\tau_2 > 1000$. Fluid discharge profiles shown in Fig. 3.6(b) for $\tau_2 = 0.1$ and 1000 indicate that a unit discontinuity exists at the level of applied patch fluid sink ($z = 10a$). A discontinuity in the slope of the discharge profiles is also noted at $z/a = 9$ and 11 when $\kappa^{(2)}/\kappa^{(1)} = 10$ whereas, for $\kappa^{(2)} = \kappa^{(1)}$, discharge profiles are smooth along the z-axis. This behaviour is similar to what observed in Fig. 3.6(a). Initially ($\tau_2 < 0.1$), higher discharge is developed in the case where $\kappa^{(2)}/\kappa^{(1)} = 10$. As time increases, the discharge for $\kappa^{(2)} = \kappa^{(1)}$ increases and reaches a final state when $\tau_2 > 1000$. However, the discharge profile for $\kappa^{(2)}/\kappa^{(1)} = 10$ is nearly time-independent. The fluid discharge corresponding to both values of $\kappa^{(2)}/\kappa^{(1)}$ becomes negligible after $|z/a - 10| > 2$.

3.5 Conclusions

Explicit solutions for stiffness matrices of a layer with a finite thickness and a half-space are presented in the Laplace-Hankel transform space. The present stiffness matrices satisfy exactly all the field equations relevant for a poroelastic medium. These stiffness matrices need to be derived only once and can be applied to study the response of any horizontally layered poroelastic medium. The global equation of a layer system is obtained by assembling the layer matrices on the basis of interface continuity conditions. Accurate time-domain solutions can be obtained by applying the numerical scheme proposed by Stehfest (1970) or Schapery (1962) for Laplace inversion and applying direct numerical quadrature to evaluate the Hankel transform inversion integrals.

The stiffness matrix method presented in this Chapter has the advantage that the size of the final equation system is nearly one-half of that corresponding to the conventional matrix approach based on the determination of layer arbitrary coefficients. In addition, unlike the coefficient matrix of the conventional method, the global stiffness matrix of the present method is symmetric, numerically stable and well-conditioned for the large values of transform parameters and has a band width equal to eight. Selected numerical results presented in this study for different layered systems indicate that the response of a layered poroelastic medium depends

significantly on the poroelastic material parameters and the configuration of layering. The response of a layered system is governed by many parameters (layer thickness, material parameters, etc.) and it is difficult to identify the influence of individual parameters on the response. The present method can be effectively used to compute the kernel functions (Green's functions) required in the application of boundary integral equation methods for a multi-layered poroelastic half-space. It can be also used to verify the accuracy of approximate methods such as the finite element method and other numerical techniques that can be applied to study the consolidation problems involving layered poroelastic media.

Table 3.1: Comparison of vertical displacement and vertical stress due to a vertical patch load applied at depth $z = a$ of a homogeneous poroelastic half-space ($\nu = 0.25, \nu_u = 0.35$ and $B = 0.8$)

t^* (ct/a^2)	$2\mu u_z(0, a, t^*)/f_0 a$			$\sigma_{zz}(0, a^+, t^*)/f_0$		
	Case I	Stiffness Method		Case I	Stiffness Method	
		Stehfest	Schapery		Stehfest	Schapery
10^{-6}	0.9757	0.9757	0.9758	-0.7151	-0.7151	-0.7151
10^{-4}	0.9771	0.9771	0.9775	-0.7154	-0.7154	-0.7155
0.01	0.9891	0.9891	0.9910	-0.7181	-0.7181	-0.7179
0.1	1.0051	1.0051	1.0067	-0.7163	-0.7163	-0.7142
1.0	1.0271	1.0271	1.0291	-0.7059	-0.7059	-0.7068
10	1.0505	1.0505	1.0493	-0.7041	-0.7041	-0.7044
10^4	1.0635	1.0636	1.0635	-0.7040	-0.7040	-0.7040

Case I: Numerical solution from Chapter 2.

Table 3.2: Comparison of vertical displacement due to a vertical patch load applied at the top surface of a layered elastic half-space ($\mu^{(1)}/\mu^{(2)} = 10, \nu^{(1)} = \nu^{(2)} = 0.3$ and $h_1 = 1.0$)

z	$2\mu u_z(0, z)$		r	$2\mu u_z(r, 0)$	
	M & D (1980)†	Stiffness Method		M & D (1980)†	Stiffness Method
0	0.1948	0.1948	0	0.1948	0.1948
1	0.1815	0.1813	1	0.1601	0.1600
2	0.1264	0.1262	2	0.1089	0.1088
6	0.0545	0.0542	5	0.0450	0.0448
11	0.0312	0.0308	10	0.0216	0.0215

† Muki and Dong (1980).

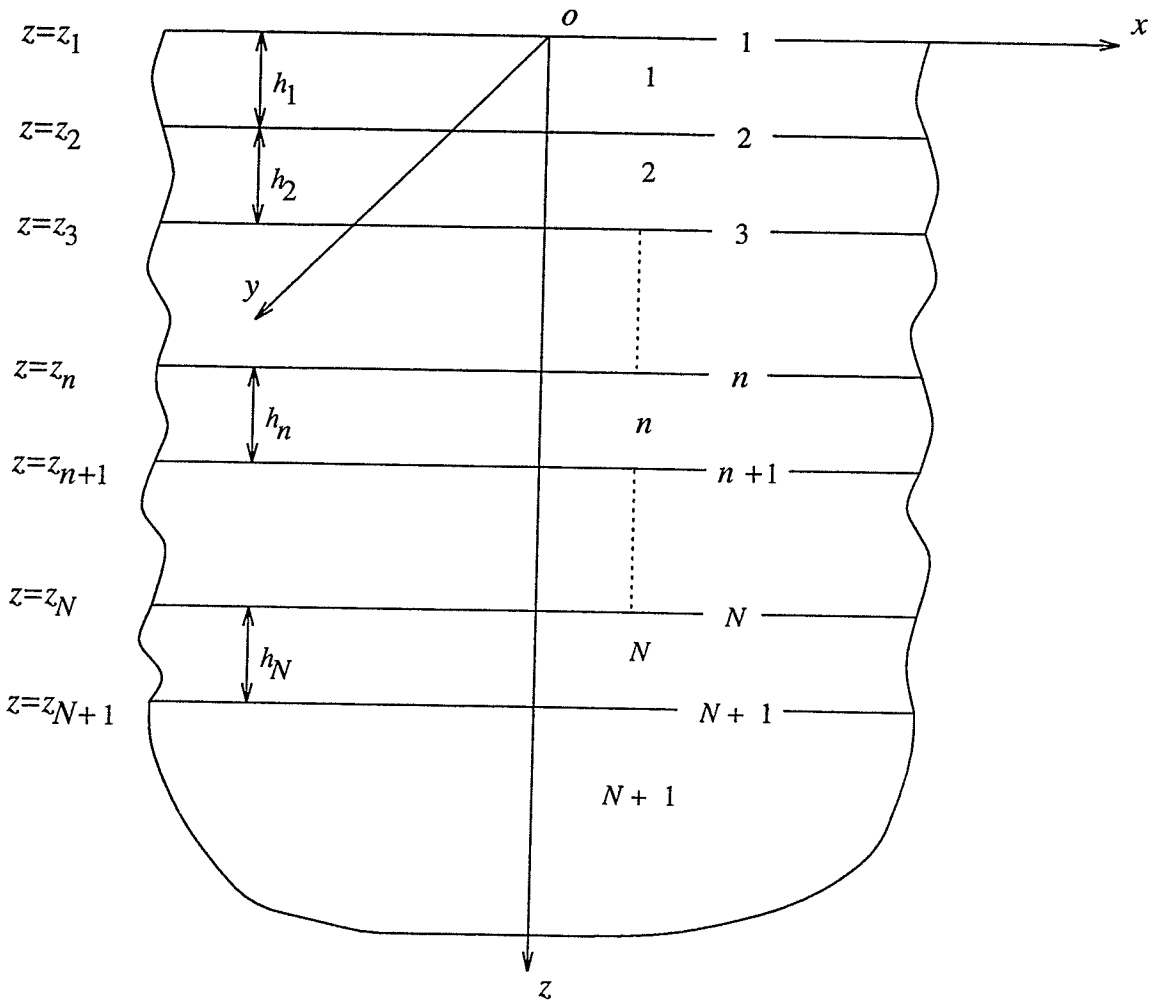

Figure 3.1 Geometry of a multi-layered system

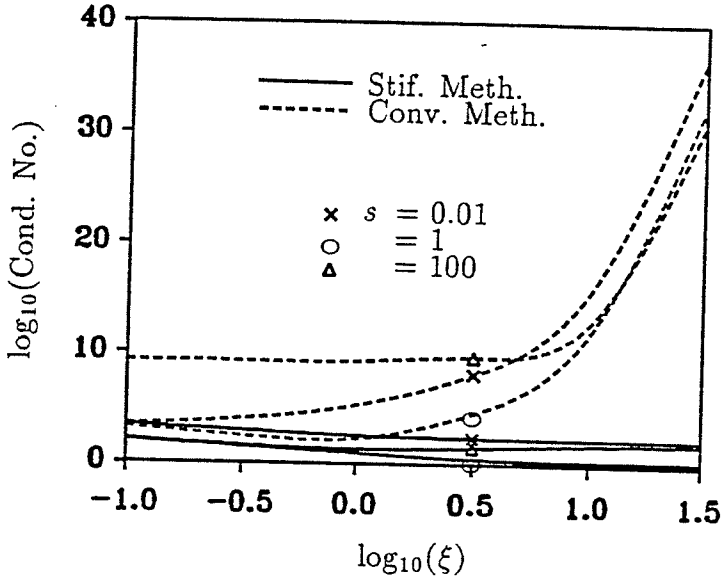

Figure 3.2 Comparison of condition numbers

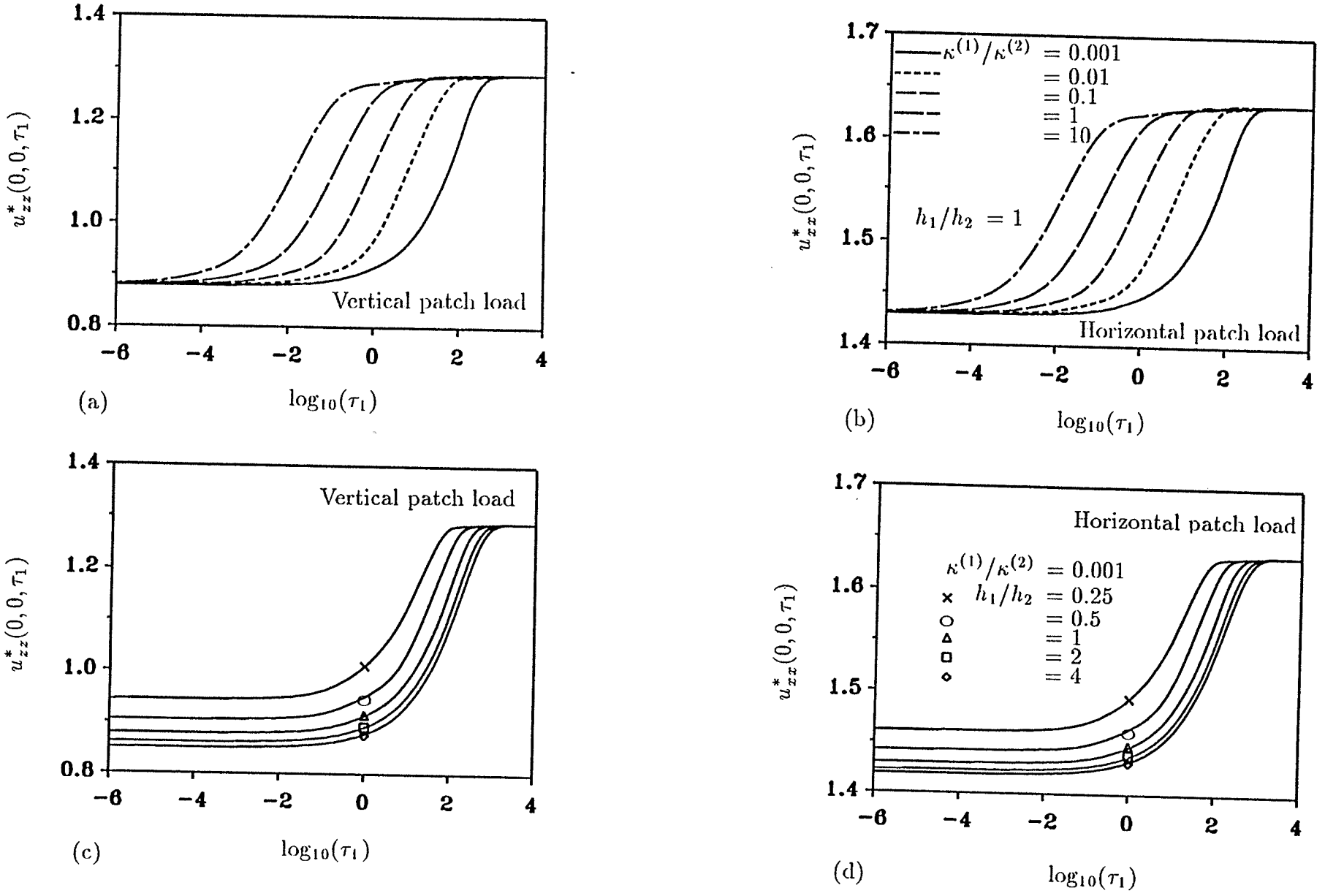

Figure 3.3 Displacement histories under surface loadings

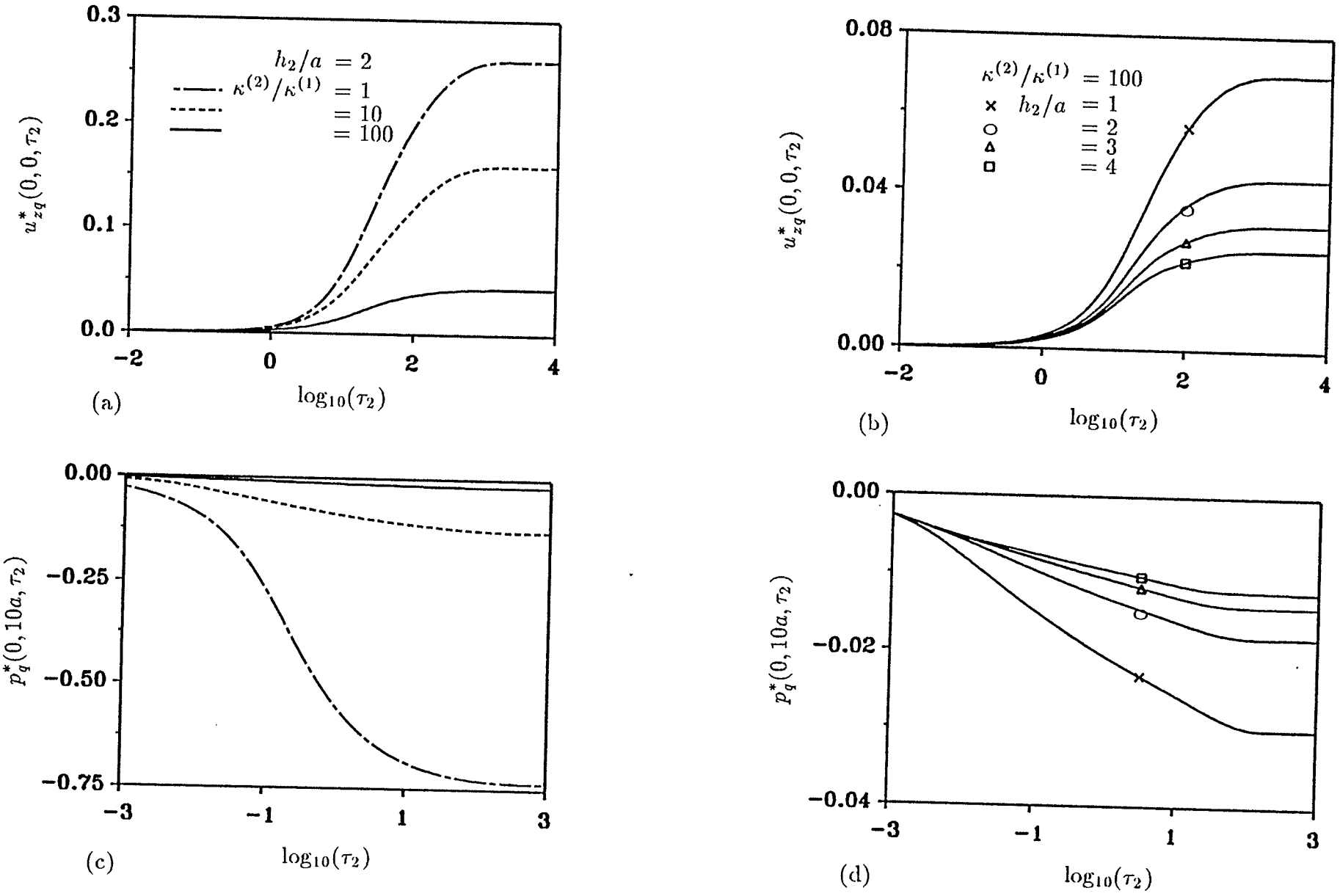

Figure 3.4 Displacement and pore pressure histories due to a patch fluid sink

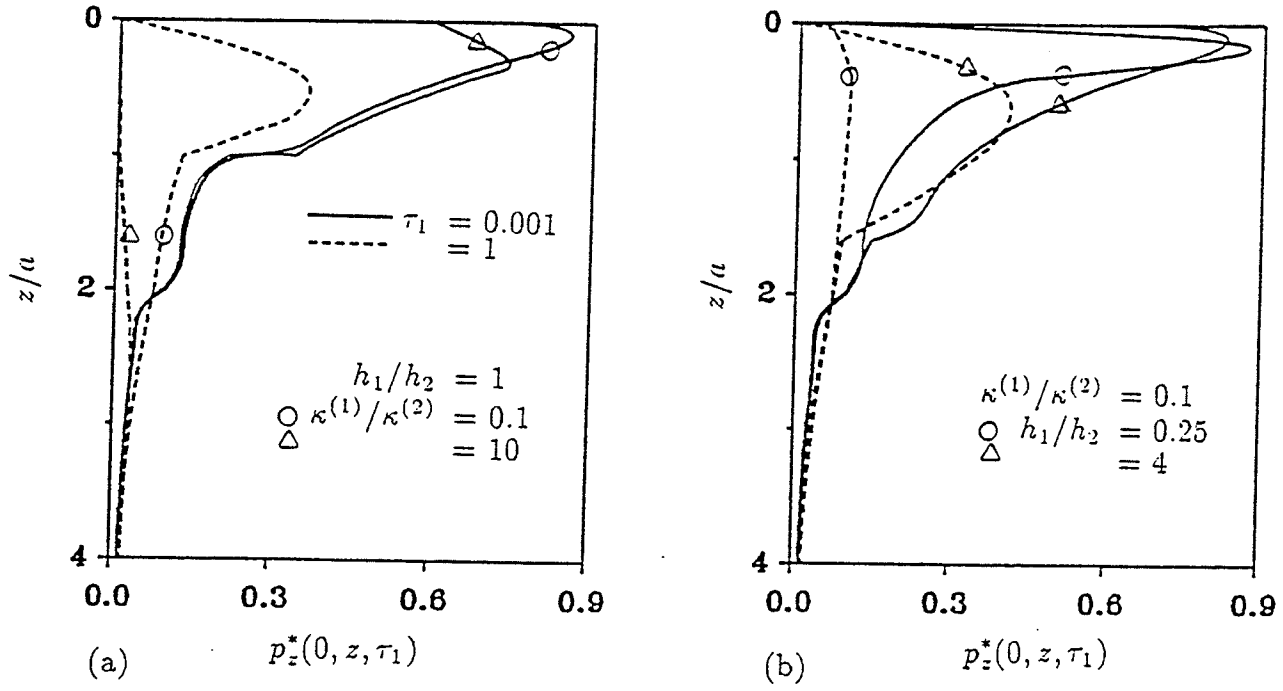

Figure 3.5 Pore pressure along the z-axis due to vertical patch load at the top surface

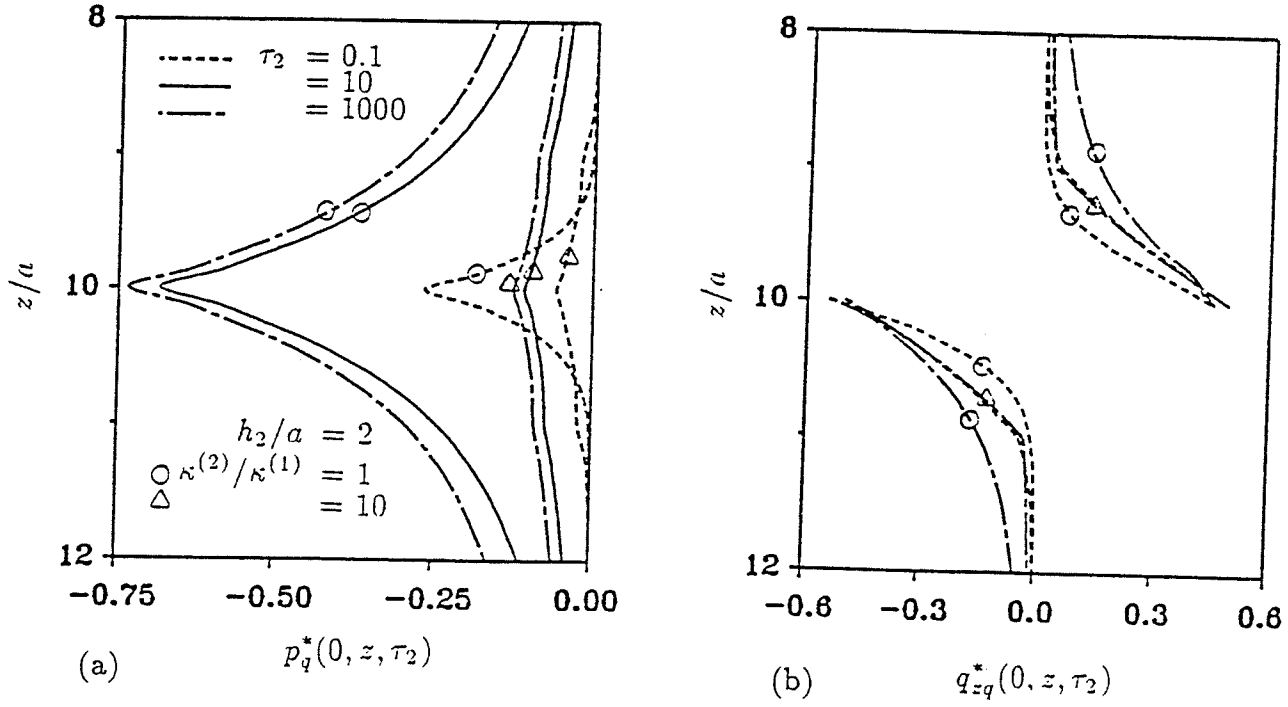

Figure 3.6 Pore pressure and fluid discharge along the z-axis for a patch fluid sink

Chapter 4

2-D DYNAMIC GREEN'S FUNCTIONS

4.1 General

This Chapter is concerned with the derivation of dynamic Green's functions corresponding to time-harmonic and transient loadings and fluid sources applied at a finite depth below the surface of a homogeneous poroelastic half-plane. Biot's equations for dynamic poroelasticity with internal friction are considered. Two-dimensional general solutions for governing equations under time-harmonic excitations can be obtained by applying Helmholtz representation and Fourier integral transforms with respect to the x-coordinate. The Green's functions are presented explicitly in the Fourier transform space for displacements, stresses, excess pore pressure and fluid discharge corresponding to arbitrary distributions of vertical and horizontal loadings and fluid sources (specified discharge and pressure). Solutions corresponding to point and uniformly distributed excitations are also presented. In addition, it is shown that Green's functions corresponding to transient excitations (loadings and fluid sources) can be derived from the time-harmonic solutions through an appropriate change of parameters. An accurate numerical scheme is presented to evaluate poroelastodynamic Green's functions. Selected numerical results for displacements, stresses and pore pressure corresponding to three poroelastic materials and an ideal elastic material are presented to portray the influence of frequency of excitation, poroelastic material properties and types of loadings on the dynamic response of poroelastic half-planes.

4.2 Governing Equations and General Solutions

Consider a poroelastic half-space with a Cartesian coordinate system (x, y, z) defined such that the z-axis is perpendicular to the free surface of the half-space as shown in Fig. 4.1. It is assumed that the deformations are plane strain in the $xz-$plane, i.e. $\epsilon_{xy} = \epsilon_{yy} = \epsilon_{yz} = 0$. The equations of motion in the absence of body forces (solid and fluid) and a fluid source can be written for the present case as

$$\mu\nabla^2 u_x + (\lambda + \alpha^2 M + \mu)\frac{\partial \epsilon}{\partial x} - \alpha M \frac{\partial \zeta}{\partial x} = \frac{\partial^2}{\partial t^2}(\rho u_x + \rho_f w_x) \qquad (4.1a)$$

$$\mu\nabla^2 u_z + (\lambda + \alpha^2 M + \mu)\frac{\partial \epsilon}{\partial z} - \alpha M \frac{\partial \zeta}{\partial z} = \frac{\partial^2}{\partial t^2}(\rho u_z + \rho_f w_z) \tag{4.1b}$$

$$\alpha M \frac{\partial \epsilon}{\partial x} - M \frac{\partial \zeta}{\partial x} = \frac{\partial^2}{\partial t^2}(\rho_f u_x + m w_x) + b\frac{\partial w_x}{\partial t} \tag{4.1c}$$

$$\alpha M \frac{\partial \epsilon}{\partial z} - M \frac{\partial \zeta}{\partial z} = \frac{\partial^2}{\partial t^2}(\rho_f u_z + m w_z) + b\frac{\partial w_z}{\partial t} \tag{4.1d}$$

where

$$\nabla^2 = \frac{\partial^2}{\partial x^2} + \frac{\partial^2}{\partial z^2} \tag{4.2a}$$

$$\epsilon = \frac{\partial u_x}{\partial x} + \frac{\partial u_z}{\partial z} \tag{4.2b}$$

$$\zeta = -(\frac{\partial w_x}{\partial x} + \frac{\partial w_z}{\partial z}) \tag{4.2c}$$

$$\lambda = \frac{2\mu\nu}{1 - 2\nu} \tag{4.2d}$$

In the above equations, $u_i(x, z, t)$ and $w_i(x, z, t)$ $(i = x, z)$, ϵ, ζ, μ, ν, α and M are defined previously in Section 2.2; λ is the Lamé constant of the bulk material; ρ and ρ_f are the mass densities of the bulk material and the pore fluid, respectively, and m is a density-like parameter which depends on ρ_f and the geometry of the pores. In addition, b is a parameter accounting for the internal friction due to the relative motion between the solid matrix and the pore fluid. The parameter b is equal to the ratio between the fluid viscosity and the intrinsic permeability of the medium. If internal friction is neglected then $b = 0$. Note that eqns (4.1) can also be expressed in terms of solid and fluid displacements (Biot, 1956a). Eqns (4.1) are based on the assumptions that the flow of the fluid relative to the solid through the pores is of the Poiseuille type and the thermal and hysteresis effects are negligible. More details of Biot's hypotheses and identification of material parameters are discussed by Biot (1956a), Bourbié *et al.* (1987) and Rasolofosaon (1991).

The motion under consideration is assumed to be time-harmonic with a time factor of $e^{i\omega t}$ where ω is the frequency of the motion and $i = \sqrt{-1}$. For brevity, the term $e^{i\omega t}$ is suppressed henceforth from all expressions. It is important to note that the governing equations, eqns (4.1), do not consist of four independent unknowns. With the aid of eqns (2.1b) and (4.2c), the eqns (4.1) can be reduced to only three independent equations expressed in terms of three unknowns u_x, u_z

and p. The corresponding governing equations can be expressed by using standard indicial notation as

$$\mu u_{i,jj} + (\lambda + \mu) u_{j,ji} + \omega^2 (\rho - \vartheta \rho_f) u_i - (\alpha - \vartheta) p_{,i} = 0 \tag{4.3a}$$

$$p_{,ii} + \frac{\rho_f \omega^2}{\vartheta M} p + \frac{\rho_f \omega^2 (\alpha - \vartheta)}{\vartheta} u_{i,i} = 0 \tag{4.3b}$$

where

$$\vartheta = \frac{\rho_f \omega^2}{(m\omega^2 - ib\omega)} \tag{4.4}$$

The field equations for dynamic thermoelasticity in the absence of body forces and a heat source can be expressed in the frequency domain as

$$\mu u_{i,jj} + (\lambda + \mu) u_{j,ji} + \rho \omega^2 u_i - \gamma \Theta_{,i} = 0 \tag{4.5a}$$

$$\Theta_{,ii} + \frac{i\omega}{\kappa} \Theta + i\omega\eta u_{i,i} = 0 \tag{4.5b}$$

where Θ denotes the temperature increment and γ, κ and η are parameters given by Nowacki (1975). It is evident from eqns (4.3) and (4.5) that there exists an analogy between poroelasticity and thermoelasticity in the frequency domain (Bonnet, 1987 and Cheng *et al.*, 1991).

In view of the analogy between poroelasticity and thermoelasticity in the frequency domain it is possible to obtain a poroelastic Green's function from a corresponding thermoelastic Green's function through the change of relevant parameters. Bonnet (1987) and Cheng *et al.* (1991) obtained poroelastic Green's functions for a full plane from the solutions given by Kupradze *et al.* (1979) and Nowacki (1975), respectively, for thermoelasticity. However, Green's functions for a poroelastic half-plane subjected to internal excitations cannot be derived by using the analogy between poroelasticity and thermoelasticity since the thermoelastic Green's functions for an internally loaded half-plane are not available in the literature. Therefore, a formal solution of the corresponding boundary value problems with the aid of general solutions of eqns (4.1) is necessary.

At this stage, the half-width of a loading strip denoted by a is selected to nondimensionalize all length parameters including the coordinate frame. Stresses and pore pressure are nondimensionalized with respect to shear modulus μ of the

half-plane. All variables will be replaced by appropriate nondimensional variables, but the foregoing notations will be used for convenience.

The equations of motion, eqns (4.1), can be solved by introducing the following displacement decompositions based on Helmholtz representation of a vector field.

$$u_x(x,z,t) = \frac{\partial \phi_1(x,z,t)}{\partial x} + \frac{\partial \psi_1(x,z,t)}{\partial z} \tag{4.6a}$$

$$u_z(x,z,t) = \frac{\partial \phi_1(x,z,t)}{\partial z} - \frac{\partial \psi_1(x,z,t)}{\partial x} \tag{4.6b}$$

$$w_x(x,z,t) = \frac{\partial \phi_2(x,z,t)}{\partial x} + \frac{\partial \psi_2(x,z,t)}{\partial z} \tag{4.6c}$$

$$w_z(x,z,t) = \frac{\partial \phi_2(x,z,t)}{\partial z} - \frac{\partial \psi_2(x,z,t)}{\partial x} \tag{4.6d}$$

where ϕ_i and ψ_i $(i = 1, 2)$ in eqns (4.6) are scalar and vector fields, respectively.

Substitution of eqns (4.6) into eqns (4.1) together with the assumption that the motion is time-harmonic yields two sets of partial differential equations for scalar fields ϕ_1, ϕ_2 and vector fields ψ_1, ψ_2 as

$$\left[(\lambda_c + 2)\nabla^2 + \delta^2\right]\phi_1 = -\left[\alpha M^* \nabla^2 + \rho^* \delta^2\right]\phi_2 \tag{4.7a}$$

$$\left[\alpha M^* \nabla^2 + \rho^* \delta^2\right]\phi_1 = -\left[M^* \nabla^2 + m^* \delta^2 - ib^* \delta\right]\phi_2 \tag{4.7b}$$

and

$$\left[\nabla^2 + \delta^2\right]\psi_1 = -\rho^* \delta^2 \psi_2 \tag{4.8a}$$

$$\rho^* \delta^2 \psi_1 = -\left[m^* \delta^2 - ib^* \delta\right]\psi_2 \tag{4.8b}$$

where the dimensionless parameters $\lambda_c, M^*, \rho^*, m^*$ and b^* are defined as

$$\lambda_c = \lambda^* + \alpha^2 M^*, \lambda^* = \frac{\lambda}{\mu}, M^* = \frac{M}{\mu},$$

$$\rho^* = \frac{\rho_f}{\rho}, m^* = \frac{m}{\rho} \quad \text{and} \quad b^* = \frac{ab}{\sqrt{\rho\mu}} \tag{4.9a}$$

and the nondimensional frequency, δ, is defined as

$$\delta = \sqrt{\frac{\rho}{\mu}}\omega a \tag{4.9b}$$

The Fourier integral transform (Sneddon, 1951) of a function $f(x,z)$ with respect to the $x-$coordinate is defined by

$$\bar{f}(\xi,z)=\frac{1}{\sqrt{2\pi}}\int_{-\infty}^{\infty}f(x,z)e^{-i\xi x}dx \tag{4.10a}$$

and the inverse relationship is given by

$$f(x,z)=\frac{1}{\sqrt{2\pi}}\int_{-\infty}^{\infty}\bar{f}(\xi,z)e^{i\xi x}d\xi \tag{4.10b}$$

It can be shown that the general solutions of Fourier transforms of ϕ_i and ψ_i $(i=1,2)$ can be expressed as

$$\bar{\phi}_1(\xi,z)=A(\xi,\delta)e^{\gamma_1 z}+B(\xi,\delta)e^{-\gamma_1 z}+C(\xi,\delta)e^{\gamma_2 z}+D(\xi,\delta)e^{-\gamma_2 z} \tag{4.11a}$$

$$\bar{\phi}_2(\xi,z)=\chi_1\Big\{A(\xi,\delta)e^{\gamma_1 z}+B(\xi,\delta)e^{-\gamma_1 z}\Big\}+\chi_2\Big\{C(\xi,\delta)e^{\gamma_2 z}+D(\xi,\delta)e^{-\gamma_2 z}\Big\} \tag{4.11b}$$

$$\bar{\psi}_1(\xi,z)=E(\xi,\delta)e^{\gamma_3 z}+F(\xi,\delta)e^{-\gamma_3 z} \tag{4.11c}$$

$$\bar{\psi}_2(\xi,z)=\chi_3\Big\{E(\xi,\delta)e^{\gamma_3 z}+F(\xi,\delta)e^{-\gamma_3 z}\Big\} \tag{4.11d}$$

where $A(\xi,\delta),B(\xi,\delta),C(\xi,\delta),D(\xi,\delta),E(\xi,\delta)$ and $F(\xi,\delta)$ are arbitrary functions to be determined by using appropriate boundary and/or continuity conditions relevant to a given problem and

$$\chi_i=\frac{(\lambda_c+2)L_i^2-\delta^2}{\rho^*\delta^2-\alpha M^*L_i^2}, \qquad i=1,2 \tag{4.12a}$$

$$\chi_3=\frac{\rho^*\delta^2}{ib^*\delta-m^*\delta^2} \tag{4.12b}$$

$$\gamma_i=\sqrt{\xi^2-L_i^2}, \qquad i=1,2 \tag{4.12c}$$

$$\gamma_3=\sqrt{\xi^2-S^2} \tag{4.12d}$$

Note that the radicals $\gamma_i(i=1,2,3)$ are selected such that $\mathrm{Re}(\gamma)\geq 0$. In addition,

$$L_1^2=\frac{\varpi_1+\sqrt{\varpi_1^2-4\varpi_2}}{2} \tag{4.13a}$$

$$L_2^2 = \frac{\varpi_1 - \sqrt{\varpi_1^2 - 4\varpi_2}}{2} \tag{4.13b}$$

$$S^2 = (\rho^* \chi_3 + 1)\delta^2 \tag{4.13c}$$

$$\varpi_1 = \frac{(m^*\delta^2 - ib^*\delta)(\lambda_c + 2) + M^*\delta^2 - 2\alpha M^* \rho^* \delta^2}{(\lambda^* + 2)M^*} \tag{4.13d}$$

$$\varpi_2 = \frac{(m^*\delta^2 - ib^*\delta)\delta^2 - (\rho^*)^2\delta^4}{(\lambda^* + 2)M^*} \tag{4.13e}$$

where L_1, L_2 and S are the dimensionless complex wave numbers associated with three kinds of dispersive and dissipative body waves, which were denoted by Biot as the dilatational wave of the first kind (*fast* wave), the dilatational wave of the second kind (*slow* wave) and the rotational wave, respectively (Biot, 1956a). In the limiting case of an ideal elastic solid ($M^* = \rho^* = m^* = b^* = \alpha = 0$), only ϕ_1 and ψ_1 are involved in the analysis. The governing equations for ϕ_1 and ψ_1 are eqns (4.7a) and (4.8a), respectively, with the right hand side of these equations being equal to zero and eqns (4.7b) and (4.8b) vanish automatically. It is immediately evident that the resulting solutions for ϕ_1 and ψ_1 are identical to those given by Lamb (1904). In addition, L_1 and S are identical to the wave numbers of pressure (P) and shear (SV) waves propagating in an isotropic ideal elastic solid (Achenbach, 1973).

In view of eqns (2.1), (4.2b)-(4.2d), (4.6) and (4.11), the general solutions for Fourier transforms of displacements u_i and w_i ($i = x, z$), stresses $\sigma_{ij}(i, j = x, z)$ and excess pore pressure p can be expressed as

$$\bar{u}_x(\xi, z) = i\xi\left(Ae^{\gamma_1 z} + Be^{-\gamma_1 z} + Ce^{\gamma_2 z} + De^{-\gamma_2 z}\right) + \gamma_3\left(Ee^{\gamma_3 z} - Fe^{-\gamma_3 z}\right) \tag{4.14a}$$

$$\bar{u}_z(\xi, z) = \gamma_1\left(Ae^{\gamma_1 z} - Be^{-\gamma_1 z}\right) + \gamma_2\left(Ce^{\gamma_2 z} - De^{-\gamma_2 z}\right) - i\xi\left(Ee^{\gamma_3 z} + Fe^{-\gamma_3 z}\right) \tag{4.14b}$$

$$\begin{aligned}\bar{w}_x(\xi, z) =& i\xi\left\{\chi_1\left(Ae^{\gamma_1 z} + Be^{-\gamma_1 z}\right) + \chi_2\left(Ce^{\gamma_2 z} + De^{-\gamma_2 z}\right)\right\} \\ &+ \chi_3\gamma_3\left(Ee^{\gamma_3 z} - Fe^{-\gamma_3 z}\right)\end{aligned} \tag{4.14c}$$

$$\bar{w}_z(\xi, z) = \chi_1\gamma_1\left(Ae^{\gamma_1 z} - Be^{-\gamma_1 z}\right) + \chi_2\gamma_2\left(Ce^{\gamma_2 z} - De^{-\gamma_2 z}\right)$$

$$- i\xi\chi_3\left(Ee^{\gamma_3 z} + Fe^{-\gamma_3 z}\right) \tag{4.14d}$$

$$\bar{\sigma}_{xx}(\xi, z) = \varsigma_1\left(Ae^{\gamma_1 z} + Be^{-\gamma_1 z}\right) + \varsigma_2\left(Ce^{\gamma_2 z} + De^{-\gamma_2 z}\right) + 2i\xi\gamma_3\left(Ee^{\gamma_3 z} - Fe^{-\gamma_3 z}\right) \tag{4.15a}$$

$$\bar{\sigma}_{zx}(\xi, z) = 2i\xi\left\{\gamma_1\left(Ae^{\gamma_1 z} - Be^{-\gamma_1 z}\right) + \gamma_2\left(Ce^{\gamma_2 z} - De^{-\gamma_2 z}\right)\right\}$$

$$+ \varsigma_3\left(Ee^{\gamma_3 z} + Fe^{-\gamma_3 z}\right) \tag{4.15b}$$

$$\bar{\sigma}_{zz}(\xi, z) = \beta_1\left(Ae^{\gamma_1 z} + Be^{-\gamma_1 z}\right) + \beta_2\left(Ce^{\gamma_2 z} + De^{-\gamma_2 z}\right) - 2i\xi\gamma_3\left(Ee^{\gamma_3 z} - Fe^{-\gamma_3 z}\right) \tag{4.15c}$$

$$\bar{p}(\xi, z) = \eta_1\left(Ae^{\gamma_1 z} + Be^{-\gamma_1 z}\right) + \eta_2\left(Ce^{\gamma_2 z} + De^{-\gamma_2 z}\right) \tag{4.16}$$

where

$$\eta_i = (\alpha + \chi_i)M^* L_i^2, \qquad i = 1, 2 \tag{4.17a}$$

$$\varsigma_i = -(2\xi^2 + \lambda^* L_i^2 + \alpha\eta_i), \qquad i = 1, 2 \tag{4.17b}$$

$$\varsigma_3 = (\xi^2 + \gamma_3^2) \tag{4.17c}$$

$$\beta_i = 2\gamma_i^2 - \lambda^* L_i^2 - \alpha\eta_i, \qquad i = 1, 2 \tag{4.17d}$$

The fluid discharge, which is defined by the time derivative of the fluid displacement relative to the solid matrix, can be expressed as

$$q_n = i\delta w_n, \qquad n = x, z \tag{4.18}$$

where q_n is the fluid discharge, nondimensionalized with respect to $\sqrt{\mu/\rho}$, in the n-direction ($n = x, z$).

4.3 Solution of Boundary Value Problems

Boundary value problems for a poroelastic half-plane subjected to buried time-harmonic excitations as shown in Fig. 4.1 are considered in this section to derive the Green's functions. The solutions corresponding to four basic loading configurations, i.e. a vertical load, a horizontal load, a fluid source and applied pore

fluid pressure, which are assumed to be distributed over a strip of width $2a$ at a depth $z = z'$, are presented. The loading is uniform in the y-direction so that the resulting deformations are of plane strain type. A solution to the internally loaded half-plane can be derived by considering it as a two-domain boundary value problem. General solutions for each domain are given by eqns (4.14)-(4.16) and (4.18) with arbitrary coefficients $A_i(\xi,\delta)$ to $F_i(\xi,\delta)$ where a subscript i $(i = 1,2)$ is used to identify the domain number. The domain "1" is bounded by $0 \leq z \leq z'$ and domain "2" by $z' \leq z < \infty$. Note that for domain "2", arbitrary functions $A_2(\xi,\delta), C_2(\xi,\delta)$ and $E_2(\xi,\delta) \equiv 0$ to ensure the regularity of the solutions at infinity. The boundary and continuity conditions corresponding to a poroelastic half-plane subjected to buried loadings/fluid source can be expressed as

$$\sigma_{zn}^{(1)}(x,0) = 0, \qquad n = x,z \tag{4.19a}$$

$$p^{(1)}(x,0) = 0 \tag{4.19b}$$

$$u_n^{(1)}(x,z') - u_n^{(2)}(x,z') = 0, \qquad n = x,z \tag{4.19c}$$

$$p^{(1)}(x,z') - p^{(2)}(x,z') = 0 \tag{4.19d}$$

$$\sigma_{zn}^{(1)}(x,z') - \sigma_{zn}^{(2)}(x,z') = \frac{T_n(x)}{\mu}\big[H(x+a) - H(x-a)\big], \quad n = x,z \tag{4.19e}$$

$$w_z^{(1)}(x,z') - w_z^{(2)}(x,z') = \sqrt{\frac{\rho}{\mu}}\frac{iQ(x)}{\delta}\big[H(x+a) - H(x-a)\big] \tag{4.19f}$$

In the above equations, the superscript i $(i = 1,2)$ is used to denote the domain number and $H(\ )$ denotes the unit step function. The intensity of distributed load acting in the n-direction $(n = x,z)$ over a strip of width $2a$ at depth $z = z'$ and a fluid source applied at $z = z'$ over a width of $2a$ are denoted by $T_n(x)$ $(n = x,z)$ and $Q(x)$, respectively. The boundary and continuity conditions given by eqns (4.19) are consistent with the discussion given by Deresiewicz and Skalak (1963). According to eqns (4.19), a pore pressure discontinuity does not exist at $z = z'$ and the applied load is completely taken by the solid skeleton at $z = z'$. Solutions corresponding to eqns (4.19) are the required Green's functions for boundary element methods when the excitation is represented by a line load and a line fluid source.

The boundary and continuity conditions corresponding to a poroelastic half-plane subjected to applied pore fluid pressure at a depth $z = z'$ can be expressed

as

$$p^{(2)}(x,z') - p^{(1)}(x,z') = \frac{P(x)}{\mu}\big[H(x+a) - H(x-a)\big] \tag{4.20a}$$

$$\sigma_{zz}^{(1)}(x,z') - \sigma_{zz}^{(2)}(x,z') = \frac{\alpha P(x)}{\mu}\big[H(x+a) - H(x-a)\big] \tag{4.20b}$$

$$\sigma_{zx}^{(1)}(x,z') - \sigma_{zx}^{(2)}(x,z') = 0 \tag{4.20c}$$

$$w_z^{(1)}(x,z') - w_z^{(2)}(x,z') = 0 \tag{4.20d}$$

together with the boundary and continuity conditions, given by eqns (4.19a)-(4.19c). In eqns (4.20), $P(x)$ denotes the intensity of distributed fluid pressure applied over a strip of width $2a$. Note that according to eqns (4.20), a discontinuity does not exist in the solid skeleton stress at $z = z'$. This type of loading is not required as the kernel functions of boundary element methods. However, Green's functions corresponding to eqns (4.20) are required to simulate the pore pressure jump that could exist under a buried/surface impermeable foundations by using the integral equation method given by Wong and Luco (1986).

Substitution of general solutions for displacements, stresses, pore pressure and fluid discharge defined by eqns (4.14)-(4.16) and (4.18) in eqns (4.19) and (4.20) yields a set of linear simultaneous equations to determine arbitrary functions corresponding to the two domains. The following solutions are obtained for the non-zero arbitrary functions appearing in the general solutions given by eqns (4.14)-(4.16) and (4.18) for different loading cases.

4.3.1 Arbitrary Functions for Vertical Loading

$$A_1 = \frac{\eta_2 e^{-\gamma_1 z'}}{2\mu N_1}\bar{T}_z(\xi) \tag{4.21a}$$

$$B_1 = \frac{\eta_2\left(\nu_5 e^{-\gamma_1 z'} + 2\xi^2\nu_3 e^{-\gamma_2 z'} - 4\xi^2\varsigma_3\nu_1 e^{-\gamma_3 z'}\right)}{2\mu R N_1}\bar{T}_z(\xi) \tag{4.21b}$$

$$B_2 = B_1 - A_1 e^{2\gamma_1 z'}, \qquad C_1 = -\frac{\eta_1 e^{-\gamma_2 z'}}{2\mu N_1}\bar{T}_z(\xi) \tag{4.21c}$$

$$D_1 = \frac{\eta_1\left(2\xi^2\nu_4 e^{-\gamma_1 z'} - \nu_6 e^{-\gamma_2 z'} + 4\xi^2\varsigma_3\nu_1 e^{-\gamma_3 z'}\right)}{2\mu R N_1}\bar{T}_z(\xi) \tag{4.21d}$$

$$D_2 = D_1 - C_1 e^{2\gamma_2 z'}, \qquad E_1 = \frac{i\xi\nu_1 e^{-\gamma_3 z'}}{2\gamma_3 \mu N_1}\bar{T}_z(\xi) \tag{4.21e}$$

$$F_1 = \frac{i\xi\nu_2\left(\nu_4 e^{-\gamma_1 z'} - \nu_3 e^{-\gamma_2 z'}\right) + i\xi\nu_1\nu_7 e^{-\gamma_3 z'}}{2\gamma_3 \mu R N_1}\bar{T}_z(\xi) \tag{4.21f}$$

$$F_2 = F_1 + E_1 e^{2\gamma_3 z'} \tag{4.21g}$$

where

$$\nu_1 = (\eta_1 - \eta_2), \quad \nu_2 = \eta_1\beta_2 - \eta_2\beta_1, \quad \nu_3 = 4\eta_1\gamma_2\gamma_3, \quad \nu_4 = 4\eta_2\gamma_1\gamma_3 \tag{4.22a}$$

$$\nu_5 = \varsigma_3\nu_2 - \xi^2(\nu_3 + \nu_4), \quad \nu_6 = \varsigma_3\nu_2 + \xi^2(\nu_3 + \nu_4), \quad \nu_7 = \varsigma_3\nu_2 + \xi^2(\nu_3 - \nu_4) \tag{4.22b}$$

$$N_1 = 2\xi^2\nu_1 - \nu_2, \quad R = -\varsigma_3\nu_2 + \xi^2(\nu_3 - \nu_4) \tag{4.22c}$$

It is noted that $A_1(\xi,\delta), B_1(\xi,\delta), B_2(\xi,\delta), C_1(\xi,\delta), D_1(\xi,\delta)$ and $D_2(\xi,\delta)$ are even functions of ξ whereas $E_1(\xi,\delta), F_1(\xi,\delta)$ and $F_2(\xi,\delta)$ are odd functions of ξ if the Fourier integral transform of the applied vertical loading denoted by $\bar{T}_z(\xi)$ is an even function of ξ. In addition, R is the Rayleigh equation corresponding to a poroelastic half-plane. In case of a uniformly distributed vertical load of intensity f_0 applied over a strip of width $2a$,

$$\bar{T}_z(\xi) = \sqrt{\frac{2}{\pi}}\frac{\sin(\xi a)}{\xi} f_0 \tag{4.23a}$$

and for a vertical point load of magnitude F_0,

$$\bar{T}_z(\xi) = \frac{F_0}{\sqrt{2\pi}} \tag{4.23b}$$

The solutions for a vertical load applied in a poroelastic full plane can be derived from the above solutions by taking $B_1(\xi,\delta) = D_1(\xi,\delta) = F_1(\xi,\delta) = 0$ and setting $|z - z'| = |z|$, where the origin of the coordinate system is now defined at the point of application of the load.

It is also useful to identify the wave fields created by the applied vertical load on the basis of the solutions given by eqns (4.14)-(4.16) and (4.21). For example, it is noted that in view of eqns (4.21) the terms A_1, C_1 and E_1, when substituted

in eqns (4.14)-(4.16), represent the Biot's fast and slow waves, and the rotational waves, respectively, propagating in a poroelastic full plane. The influence of the free boundary at $z = 0$ is reflected in the solutions by the terms B_1, D_1 and F_1. The reflected field due to each type of body waves consists of L_1, L_2 and S waves.

4.3.2 Arbitrary Functions for Horizontal Loading

$$A_1 = \frac{i\xi(\chi_2 - \chi_3)e^{-\gamma_1 z'}}{2\gamma_1 \mu N_2}\bar{T}_x(\xi) \tag{4.24a}$$

$$B_1 = \frac{i\xi\Big\{(\chi_2 - \chi_3)\nu_5 e^{-\gamma_1 z'} + 2\xi^2(\chi_1 - \chi_3)\nu_4 e^{-\gamma_2 z'} - (\chi_1 - \chi_2)\varsigma_3\nu_4 e^{-\gamma_3 z'}\Big\}}{2\gamma_1 \mu R N_2}\bar{T}_x(\xi) \tag{4.24b}$$

$$B_2 = B_1 + A_1 e^{2\gamma_1 z'}, \qquad C_1 = \frac{i\xi(\chi_3 - \chi_1)e^{-\gamma_2 z'}}{2\gamma_2 \mu N_2}\bar{T}_x(\xi) \tag{4.24c}$$

$$D_1 = \frac{i\xi\Big\{2\xi^2(\chi_2 - \chi_3)\nu_3 e^{-\gamma_1 z'} - (\chi_1 - \chi_3)\nu_6 e^{-\gamma_2 z'} + (\chi_1 - \chi_2)\varsigma_3\nu_3 e^{-\gamma_3 z'}\Big\}}{2\gamma_2 \mu R N_2}\bar{T}_x(\xi) \tag{4.24d}$$

$$D_2 = D_1 + C_1 e^{2\gamma_2 z'}, \qquad E_1 = \frac{(\chi_2 - \chi_1)e^{-\gamma_3 z'}}{2\mu N_2}\bar{T}_x(\xi) \tag{4.24e}$$

$$F_1 = \frac{4\xi^2\nu_2\Big\{(\chi_3 - \chi_2)e^{-\gamma_1 z'} + (\chi_1 - \chi_3)e^{-\gamma_2 z'}\Big\} - (\chi_1 - \chi_2)\nu_7 e^{-\gamma_3 z'}}{2\mu R N_2}\bar{T}_x(\xi) \tag{4.24f}$$

$$F_2 = F_1 - E_1 e^{2\gamma_3 z'} \tag{4.24g}$$

where

$$N_2 = (\chi_1 - \chi_2)(\xi^2 - \gamma_3^2) \tag{4.25}$$

It is noted that $A_1(\xi,\delta), B_1(\xi,\delta), B_2(\xi,\delta), C_1(\xi,\delta), D_1(\xi,\delta)$ and $D_2(\xi,\delta)$ are odd functions of ξ whereas $E_1(\xi,\delta), F_1(\xi,\delta)$ and $F_2(\xi,\delta)$ are even functions of ξ if $\bar{T}_x(\xi)$ is an even function of ξ where $\bar{T}_x(\xi)$ is the Fourier integral transform of the applied horizontal loading. Appropriate values of $\bar{T}_x$ for a uniform strip load and a concentrated horizontal load are given by eqns (4.23a) and (4.23b), respectively. It should be also noted that in view of eqns (4.24) the terms A_1, C_1 and E_1 are associated with the two dilatational waves and the rotational waves, respectively,

propagating in a poroelastic full plane due to the applied horizontal load. The presence of the free boundary is reflected in the solutions by the terms B_1, D_1 and F_1.

4.3.3 Arbitrary Functions for Fluid Source

$$A_1 = \frac{e^{-\gamma_1 z'}}{2\delta(\chi_1-\chi_2)\gamma_1} i\sqrt{\frac{\rho}{\mu}}\bar{Q}(\xi), \qquad B_1 = \frac{\nu_5 e^{-\gamma_1 z'} + 2\xi^2\nu_4 e^{-\gamma_2 z'}}{2\delta(\chi_1-\chi_2)\gamma_1 R} i\sqrt{\frac{\rho}{\mu}}\bar{Q}(\xi) \quad (4.26a)$$

$$B_2 = B_1 + A_1 e^{2\gamma_1 z'}, \qquad C_1 = \frac{e^{-\gamma_2 z'}}{2\delta(\chi_2-\chi_1)\gamma_2} i\sqrt{\frac{\rho}{\mu}}\bar{Q}(\xi) \quad (4.26b)$$

$$D_1 = \frac{2\xi^2\nu_3 e^{-\gamma_1 z'} - \nu_6 e^{-\gamma_2 z'}}{2\delta(\chi_1-\chi_2)\gamma_2 R} i\sqrt{\frac{\rho}{\mu}}\bar{Q}(\xi), \qquad D_2 = D_1 + C_1 e^{2\gamma_2 z'} \quad (4.26c)$$

$$E_1 = 0, \qquad F_1 = \frac{2\xi\nu_2(e^{-\gamma_1 z'} - e^{-\gamma_2 z'})}{\delta(\chi_2-\chi_1)R}\sqrt{\frac{\rho}{\mu}}\bar{Q}(\xi), \qquad F_2 = F_1 \quad (4.26d)$$

Note that $A_1(\xi,\delta), B_1(\xi,\delta), B_2(\xi,\delta), C_1(\xi,\delta), D_1(\xi,\delta)$ and $D_2(\xi,\delta)$ are even functions of ξ whereas $F_1(\xi,\delta)$ and $F_2(\xi,\delta)$ are odd functions of ξ if $\bar{Q}(\xi)$ is an even function of ξ where $\bar{Q}(\xi)$ is the Fourier integral transform of the applied fluid source. In case of a uniformly distributed fluid source of intensity q_0 over a width of $2a$,

$$\bar{Q}(\xi) = \sqrt{\frac{2}{\pi}}\frac{\sin(\xi a)}{\xi} q_0 \quad (4.27a)$$

and for a line source of strength Q_0,

$$\bar{Q}(\xi) = \frac{Q_0}{\sqrt{2\pi}} \quad (4.27b)$$

It should be noted from the solutions given by eqns (4.26) that the wave fields emanating from a fluid source do not create a rotational wave since $E_1 \equiv 0$. The terms A_1 and C_1 are associated with the two dilatational waves propagating in an infinite poroelastic plane due to a fluid source and the presence of the free surface is reflected in the solutions by the terms B_1, D_1 and F_1. However, the total field in a half-plane consists of a rotational wave due to the reflection of the two dilatational waves at $z = 0$.

The solutions for a fluid source applied in a poroelastic full plane can be derived from the above solutions by taking $B_1(\xi,\delta) = D_1(\xi,\delta) = F_1(\xi,\delta) = 0$ and setting $|z - z'| = |z|$, where the origin of the coordinate system is now defined at the point of application of the source. For example, the substitution of eqns (4.26) in eqn (4.16) with the above conditions yields the following solution for pore pressure due to a line fluid source of strength Q_0 applied in a poroelastic full plane.

$$p(x,z) = \sqrt{\frac{\rho}{\mu}}\frac{iQ_0 a}{2\pi\delta}\int_0^\infty \frac{1}{\chi_1 - \chi_2}\left[\frac{\eta_1}{\gamma_1}e^{-\gamma_1|z|} - \frac{\eta_2}{\gamma_2}e^{-\gamma_2|z|}\right]\cos(\xi x)d\xi \qquad (4.28)$$

The above solution can be written in closed form by considering the following relationships (Erdélyi, 1954)

$$\int_0^\infty \frac{e^{-\beta\sqrt{\xi^2+\eta^2}}}{\sqrt{\xi^2+\eta^2}}\cos(\xi x)d\xi = K_0(\eta\sqrt{\beta^2+x^2}) \qquad (4.29a)$$

and

$$K_0(z) = -\frac{1}{2}i\pi H_0^{(2)}(-iz) \qquad (4.29b)$$

where K_0 and $H_0^{(2)}$ are the modified Bessel function of the second kind of order zero and the Hankel function of the second kind of order zero, respectively (Abramowitz and Stegun, 1972). The substitution of eqns (4.29) in eqn (4.28) results in

$$p(x,z) = \sqrt{\frac{\rho}{\mu}}\frac{Q_0 a}{4\delta(\chi_1 - \chi_2)}\left[\eta_1 H_0^{(2)}(L_1 r) - \eta_2 H_0^{(2)}(L_2 r)\right] \qquad (4.30)$$

where

$$r = \sqrt{x^2 + z^2} \qquad (4.31)$$

It can be shown that the above solution is identical to the complex conjugate of eqn (42) of Cheng *et al.* (1991) which is the pore pressure due to a line fluid source. Note that $H_0^{(1)}$ (Hankel function of the first kind) appears in the expression given by Cheng *et al.* (1991) due to a time factor of $e^{-i\omega t}$ being used whereas in the present study a time factor of $e^{i\omega t}$ is used. The appropriate outgoing waves are represented by $H_0^{(2)}$ in the present case. Therefore, eqn (4.30) has to be identical to the complex conjugate of eqn (42) of Cheng *et al.* (1991) (Eringen and Suhubi, 1975).

4.3.4 Arbitrary Functions for Applied Fluid Pressure:

$$A_1 = -\frac{(\lambda^*+2)L_2^2 e^{-\gamma_1 z'}}{2\mu N_1}\bar{P}(\xi) \tag{4.32a}$$

$$B_1 = -\frac{(\lambda^*+2)\Big\{\nu_5 L_2^2 e^{-\gamma_1 z'} + 2\xi^2\eta_2(\beta_3 e^{-\gamma_2 z'} - \beta_5 e^{-\gamma_3 z'})\Big\}}{2\mu R N_1}\bar{P}(\xi) \tag{4.32b}$$

$$B_2 = B_1 - A_1 e^{2\gamma_1 z'}, \qquad C_1 = \frac{(\lambda^*+2)L_1^2 e^{-\gamma_2 z'}}{2\mu N_1}\bar{P}(\xi) \tag{4.32c}$$

$$D_1 = \frac{(\lambda^*+2)\Big\{\nu_6 L_1^2 e^{-\gamma_2 z'} - 2\xi^2\eta_1(\beta_4 e^{-\gamma_1 z'} + \beta_5 e^{-\gamma_3 z'})\Big\}}{2\mu R N_1}\bar{P}(\xi) \tag{4.32d}$$

$$D_2 = D_1 - C_1 e^{2\gamma_2 z'}, \qquad E_1 = -\frac{i\xi(\lambda^*+2)(L_1^2 - L_2^2)e^{-\gamma_3 z'}}{2\gamma_3\mu N_1}\bar{P}(\xi) \tag{4.32e}$$

$$F_1 = -\frac{i\xi(\lambda^*+2)\Big\{\nu_2(\beta_4 e^{-\gamma_1 z'} - \beta_3 e^{-\gamma_2 z'}) + \nu_7(L_1^2 - L_2^2)e^{-\gamma_3 z'}\Big\}}{2\gamma_3\mu R N_1}\bar{P}(\xi) \tag{4.32f}$$

$$F_2 = F_1 + E_1 e^{2\gamma_3 z'} \tag{4.32g}$$

where

$$\beta_3 = 4\gamma_2\gamma_3 L_1^2, \qquad \beta_4 = 4\gamma_1\gamma_3 L_2^2, \qquad \beta_5 = 2\varsigma_3(L_1^2 - L_2^2) \tag{4.33}$$

It is noted that $A_1(\xi,\delta), B_1(\xi,\delta), B_2(\xi,\delta), C_1(\xi,\delta), D_1(\xi,\delta)$ and $D_2(\xi,\delta)$ are even functions of ξ whereas $E_1(\xi,\delta), F_1(\xi,\delta)$ and $F_2(\xi,\delta)$ are odd functions of ξ if $\bar{P}(\xi)$ is an even function of ξ. In addition, $\bar{P}(\xi)$ is the Fourier integral transform of the applied fluid pressure. In case of the uniformly applied fluid pressure of intensity p_0 over a strip of width $2a$,

$$\bar{P}(\xi) = \sqrt{\frac{2}{\pi}}\frac{\sin(\xi a)}{\xi}p_0 \tag{4.34}$$

The wave fields created by the applied fluid pressure can also be identified on the basis of the solutions given by eqns (4.14)-(4.16) and (4.32). For example, in view of eqns (4.32), the terms A_1, C_1 and E_1, when substituted in eqns (4.14)-(4.16), represent the two dilatational waves and the rotational waves, respectively,

propagating in a poroelastic full plane. The presence of the free surface is reflected in the solutions by the terms B_1, D_1 and F_1 and the reflected field due to each body wave consists of all three types of waves.

4.4 Transient Green's Functions

The Green's functions corresponding to a poroelastic half-plane subjected to internal transient excitations (loadings and fluid sources) are considered in this section. In transient dynamic problems, it is convenient to employ the Laplace transform to remove time dependency. The Laplace-Fourier transform of a function $f(x,z,t)$ with respect to variables t and x, respectively, is defined by (Sneddon, 1951)

$$\bar{f}(\xi,z,s)=\frac{1}{\sqrt{2\pi}}\int_0^\infty\int_{-\infty}^\infty f(x,z,t)e^{-(i\xi x+st)}dxdt \qquad (4.35a)$$

In eqn (4.35a), s and ξ denote the Laplace and Fourier transform parameters, respectively. The inverse relationship is given by

$$f(x,z,t)=\frac{1}{i\sqrt{8\pi^3}}\int_{\varrho-i\infty}^{\varrho+\infty}\int_{-\infty}^\infty \bar{f}(\xi,z,s)e^{(i\xi x+st)}d\xi ds \qquad (4.35b)$$

where the line $\mathrm{Re}(s)=\varrho$ is to the right of all singularities of $\bar{f}$ and $i=\sqrt{-1}$.

It can be shown that the general solutions for Laplace-Fourier transforms of displacements, stresses and excess pore pressure are identical to those given by eqns (4.14)-(4.16) for the time-harmonic case with the following definitions of parameters χ_i and γ_i $(i=1,2,3)$, ϖ_1, ϖ_2 and S^2.

$$\chi_i=-\frac{(\lambda_c+2)L_i^2+s^2}{\rho^*s^2+\alpha M^*L_i^2},\quad i=1,2, \qquad \chi_3=-\frac{\rho^*s^2}{b^*s+m^*s^2} \qquad (4.36a)$$

$$\gamma_i=\sqrt{\xi^2+L_i^2},\quad i=1,2, \qquad \gamma_3=\sqrt{\xi^2+S^2} \qquad (4.36b)$$

$$\varpi_1=\frac{(m^*s^2+b^*s)(\lambda_c+2)+M^*s^2-2\alpha M^*\rho^*s^2}{(\lambda^*+2)M^*} \qquad (4.36c)$$

$$\varpi_2=\frac{(m^*s^2+b^*s)s^2-(\rho^*)^2s^4}{(\lambda^*+2)M^*}, \qquad S^2=(\rho^*\chi_3+1)s^2 \qquad (4.36d)$$

Note that the radicals $\gamma_i(i=1,2,3)$ are selected such that $\mathrm{Re}(\gamma)\geq 0$. In addition, the fluid discharge, nondimensionalized with respect to $\sqrt{\mu/\rho}$, in the n-direction $(n=x,z)$ can be expressed in the present case as

$$\bar{q}_n=s\bar{w}_n, \qquad n=x,z \qquad (4.37)$$

The transient solutions for displacements, stresses, excess pore pressure and fluid discharge corresponding to internal excitations are identical to the solutions given in Section 4.3 for time-harmonic problems with the parameters χ_i, γ_i $(i = 1, 2, 3)$, etc. defined as shown in eqns (4.36). The Fourier transforms of excitations denoted by $\bar{T}_n(\xi)$ $(n = x, z)$ in eqns (4.24) and (4.21), $\bar{Q}(\xi)$ in eqns (4.26) and $\bar{P}(\xi)$ in eqns (4.32) are now replaced by $\bar{T}_n(\xi, s)$ $(n = x, z)$, $\delta\bar{Q}(\xi, s)/is$ and $\bar{P}(\xi, s)$, respectively. Note that $\bar{T}_n(\xi, s)$ $(n = x, z)$, $\bar{Q}(\xi, s)$ and $\bar{P}(\xi, s)$ are the Laplace-Fourier transforms of the intensity of loadings, fluid source and fluid pressure, respectively, applied at the level $z = z'$. Green's functions required in the development of boundary integral equation methods for transient dynamic problems of a poroelastic half-plane are obtained when the excitations are represented by impulsive concentrated loads and fluid source. The values of $\bar{T}_n(\xi, s)$ $(n = x, z)$ and $\bar{Q}(\xi, s)$ corresponding to impulsive loads and fluid source are given by eqns (4.23b) and (4.27b), respectively.

4.5 Numerical Solutions

4.5.1 Numerical Scheme

The development of a numerical solution scheme to evaluate Green's functions corresponding to a poroelastic half-plane subjected to buried loadings and fluid sources is considered in this section. The numerical evaluation of time-harmonic Green's functions is discussed in detail since the solutions for transient problems in the Laplace domain have similar explicit forms. It is expected that time-domain solutions for transient problems can be determined by using an accurate Laplace inversion scheme such as Stehfest formula [eqns (2.38)] as discussed in Section 2.5.1 for quasi-static problems. In Chapter 6, transient Green's functions are computed in boundary element analysis and further details related to the computation of transient Green's functions are given there.

The complete solutions for displacements, stresses, pore pressure and fluid discharge corresponding to time-harmonic problems are given by eqns (4.14)-(4.16) and (4.18) together with the solutions for arbitrary functions, $A_i(\xi, \delta)$ to $F_i(\xi, \delta)$ $(i = 1, 2)$, given by eqns (4.21), (4.24), (4.26) and (4.32). It is found that the solutions for poroelastic field at an arbitrary point appear in terms of semi-infinite

integrals with a complex-valued integrand. Given the complexity of the integrands, it is natural to employ a suitable numerical quadrature scheme to evaluate the integrals as discussed in Section 2.5.1 for quasi-static problems. The singularities of the integrands need to be investigated before the establishment of a numerical integration procedure. The understanding of the singularities of the integrands can be obtained by treating ξ as a complex variable. It is noted that due to the presence of the radicals $\gamma_i (i = 1, 2, 3)$ the Riemann surface of the integrand of each integral has eight sheets. However, the condition $\mathrm{Re}(\gamma_i) \geq 0$, which is required to satisfy regularity conditions at infinity, implies that only the sheet in which radicals $\gamma_i (i = 1, 2, 3)$ have positive real parts everywhere is relevant.

The important singularities of the integrand are the branch points of the radicals $\gamma_i (i = 1, 2, 3)$ as defined by eqns (4.12c) and (4.12d) and poles of the function R defined in eqn (4.22c). For a poroelastic half-plane, the branch points are given by L_1, L_2 and S, i.e. the wave numbers corresponding to three kinds of body waves defined by eqns (4.13a), (4.13b) and (4.13c), respectively, while poles are given by the roots of the following equation which is the Rayleigh equation for a poroelastic half-plane governing the propagation of the surface waves.

$$-b_3 d_2 + \xi^2 (d_3 - d_4) = 0 \tag{4.38}$$

It is noted that the surface wave for a poroelastic medium is also dispersive and dissipative like body waves if internal friction exists (i.e. $b \neq 0$). Eqn (4.38) can be reduced to the classical Rayleigh equation in the case of an isotropic elastic solid. Generally, these branch points and poles are all complex-valued with negative imaginary parts. However, their locations can be on the real axis if the viscous coupling between the solid matrix and the pore fluid is neglected ($b = 0$). It can be shown (Deresiewicz, 1962) that the Rayleigh wave in a poroelastic half-space can be nearly real-valued when the frequency is very low or very high. In this thesis, the dissipative nature of the half-plane is incorporated (i.e. $b \neq 0$) therefore the real ξ axis is free from any singularities.

The dynamic Green's functions are computed by using an adaptive version of extended trapezoidal formula with a sampling interval of $\Delta\xi$. For transient problems, the integrand in the semi-infinite Fourier integrals does not have any

branch points or poles along the real ξ-axis therefore the integral with respect to ξ can be performed on the real ξ-axis. It is also found that a sampling interval of $\Delta\xi = 0.1$, as in the case of quasi-static problems discussed in Section 2.5.1, is accurate enough in the numerical evaluation of Green's functions for transient problems. However, for time-harmonic problems, a smaller integration interval has to be employed since the integrands become nearly singular when the path of integration are in the neighbourhood of the pole. Therefore, $\Delta\xi = 0.005$ for $|\xi - \mathrm{Re}(\xi_R)| < 0.25$ where ξ_R is the pole given by eqn (4.38) and $\Delta\xi = 0.05$ when ξ is outside that region. Note that for the case of a dry elastic material (an ideal elastic material) and a poroelastic material with inviscid pore fluid ($b = 0$) where the branch points and poles are on the real axis, one percent attenuation (material damping) is incorporated in the shear modulus in the numerical evaluation of the integrals (Apsel and Luco, 1983). Alternatively, it is possible to deviate the integration contour initially into the first quadrant of the complex plane to avoid the singularities on the real axis and then fall back to an integration along the real axis. The deviated portion of the contour should be selected in light of the location of singularities of the integrand. It should be noted that the integrands of semi-infinite integrals do not have any singularity in the first quadrant of the complex plane since the response of the half-plane has to be finite for large values of x and z. The integrand of the semi-infinite integrals decays exponentially with the Fourier transform parameter if $z \neq z'$. However, for $z \to z'$, the integrand decays rather slowly. Convergence can be enhanced in this case by investigating the asymptotic behaviour of the integrand and devising a numerical integration scheme that incorporates the asymptotic behaviour of the integrand (Apsel and Luco, 1983 and Rajapakse, 1990). Green's functions corresponding to a line load and a line fluid source are singular at $z = z'$ and $x = 0$. The order of these singularities are identical for half-plane and full plane problems. A rigorous examination of the nature of singularities can be obtained by investigating the closed form solution for a full plane (Cheng *et al.*, 1991).

Table 4.1 presents a comparison of numerical solutions for nondimensional stresses of a homogeneous ideal elastic half-plane under a static line load applied at a depth $z = a$ below the free surface (Melan, 1932). Solutions ob-

tained from the present analysis for the limiting case of an ideal elastic material ($M^* = \rho^* = m^* = b^* = \alpha \equiv 0$) and $\delta = 0.01$ are compared with the numerical solution given by Poulos and Davis (1974) for the Melan's problems to verify the general accuracy of the numerical quadrature scheme used to compute the semi-infinite integrals appearing in the Green's functions. Table 4.2 presents a comparison of elastodynamic solutions corresponding to an ideal elastic half-plane ($M^* = \rho^* = m^* = b^* = \alpha \equiv 0$) given by Rajapakse and Wang (1991) with those obtained from the present study when $\delta = 1.0$. It is evident that the two solutions presented in Tables 4.1 and 4.2 are in excellent agreement including at points which are very close to the point of loading. Table 4.3 presents the solutions for pore pressure of a poroelastic full plane ($\lambda^* = 1.5$, $M^* = 12.2$, $\rho^* = 0.53$, $m^* = 1.1$, $b^* = 2.3$ and $\alpha = 0.97$) subjected to a vertical line load. Comparison of solutions obtained from the numerical integration scheme used in the present study with the closed form solutions given by Cheng *et al.* (1991) confirms that the two solutions are complex conjugate. The overall accuracy of the explicit solutions derived in this study and the numerical integration scheme used in the computation of Green's functions is confirmed by these independent comparisons.

4.5.2 Numerical Results for Internal Excitations

The dynamic response of poroelastic half-planes of different material properties to a selected set of time-harmonic internal loading configurations is considered in this section. Three poroelastic materials identified as materials A, B and C and a dry elastic material (an ideal elastic material) are considered in the numerical study. The properties of these materials are: $\lambda^* = 1.5$, $M^* = 12.0$, $\rho^* = 0.5$, $m^* = 1.1$ and $\alpha = 0.97$. In addition, $b^* = 0, 2.0$ and 10.0 for material A, B and C, respectively. Note that only the nondimensional parameter λ^* is required in the case of a dry elastic material. All numerical results presented hereafter correspond to the case where the excitation is applied uniformly over a strip of width $2a$ located at a depth $z = a$ below the free surface of the half-plane.

Figure 4.2 shows the surface displacement profiles of the three poroelastic half-planes and the dry elastic half-plane under internal time-harmonic excitations. Solutions are given for two frequencies of excitations, $\delta = 0.5$ and 2.0. Nondimensional

vertical displacement, $u^*_{zz}[= \mu u_z/f_0 a]$, of the surface under a uniform vertical loading of intensity f_0 is shown in Fig. 4.2(a). Fig. 4.2(b) shows nondimensional surface displacement in the x-direction, $u^*_{xx}[= \mu u_x/f_0 a]$, due to a uniform horizontal loading of intensity f_0. Fig. 4.2(c) shows the nondimensional vertical displacement, $u^*_{zq}[= \sqrt{\mu/\rho} u_z/q_0 a]$, of the surface due to a time-harmonic fluid sink of intensity q_0. It is evident from these solutions that the response of the half-plane depends very significantly on the frequency of excitation of the loading. Both real and imaginary parts of the displacements shown in Figs. 4.2 vary rapidly with the distance and become more oscillatory as the frequency of excitation increases. Due to the complicated variation of the response it is difficult to identify a clear qualitative relationship between the displacements and frequency.

Comparison of solutions presented in Figs. 4.2 also indicates that the poroelastic properties of the medium has a significant influence on the response. It is noted from Fig. 4.2(a) that the vertical displacements along the surface due to internal vertical loading corresponding to poroelastic materials A and B are quite different from the solutions corresponding to an ideal elastic material. The difference in the response between poroelastic and ideal elastic materials is more substantial in the case of the horizontal displacement along the surface due to an internal loading in the x-direction. Solutions presented in Fig. 4.2(c) corresponding to time-harmonic fluid sink show the largest dependence of the response on poroelastic material properties of the medium. Since poroelastic materials A, B and C have identical material properties except for the material parameter b^* it can be stated that the difference in response noted in Figs. 4.2 reflects basically the influence of b^* on the response. However, as in the case of frequency, the dependence of response on b^* is rather complicated and the trends shown in Figs. 4.2 do not show a clear qualitative relationship.

The influence of the parameter M^* was also investigated by considering plots similar to those shown in Figs. 4.2 for material B with different values of M^*. It was found that the influence of M^* on the surface displacements is negligible in the range of $10 < M^* < 1000$. For $M^* < 10$, the influence of M^* is noticeable but not very significant in the case of applied loading but it is substantially high for the case of applied fluid sink. For example, the vertical displacement along the

free surface due to vertical loading is found to be less than ten per cent different when M^* is increased from 1.0 to 10.0 but, for the case of applied fluid sink, u^*_{zq} with $M^* = 10.0$ could be as high as five times of u^*_{zq} with $M^* = 1.0$ for $x < 2a$. The influence of λ^* is found to be similar to that observed for an ideal elastic solid. However, it is difficult to even qualitatively define the relationship between various material parameters and the response due to the complicated dependence of the response on λ^*, b^*, M^* and δ.

Figure 4.3 shows the nondimensional vertical displacements, u^*_{zz}, u^*_{zq} and $u^*_{zp}[= \mu u_z/p_0 a]$, along the z-axis due to vertical loading of intensity f_0, fluid sink of intensity q_0 and fluid pressure of intensity p_0, respectively. It is found that u_x along the z-axis for a horizontal strip load does not show much deviation from the solutions for an ideal elastic material (Rajapakse and Wang, 1991) and not presented here for brevity. Fig. 4.3 indicates that at low frequency ($\delta = 0.5$) the displacements vary smoothly with the depth whereas at high frequency ($\delta = 2.0$) the variations become oscillatory. The influence of poroelastic properties is relatively more visible on vertical displacements along the z-axis under a vertical load when compared to vertical displacements along the free surface shown in Fig. 4.2(a). In general, the influence of the poroelastic properties of the medium on the solutions shown in Figs. 4.3 is similar to what observed earlier in Figs. 4.2 with the highest influence of poroelasticity noted under applied fluid loadings. A kink exists in the real part of vertical displacement profiles shown in Fig. 4.3(a) at $z = a$ due to the loading applied at this level. However, the imaginary part of the displacement is smooth at this level. In all cases, the amplitude of vertical displacements decreases with increasing z for $z/a > 5.0$ and becomes negligible for $z/a > 10.0$.

Fig. 4.4(a) shows the variation of nondimensional vertical stress, $\sigma^*_{zzz}[= \sigma_{zz}/f_0]$, along the z-axis under the uniform vertical loading defined previously. These solutions also show oscillatory variations with the depth at high frequency ($\delta = 2.0$) while at low frequency ($\delta = 0.5$), the variation of stress with depth is smooth. Due to the loading applied at $z = a$, there is a unit discontinuity in the real part of σ^*_{zzz} at $z = a$. Imaginary part of σ^*_{zzz} is smooth at this level. Comparison of solutions corresponding to different materials indicates that the poroelastic material properties have a significant influence on the vertical stress at high frequencies. The

imaginary part of σ^*_{zzz} corresponding to materials A and B is substantially different from the ideal elastic material when $\delta = 2.0$. At low frequencies ($\delta < 0.5$), σ^*_{zzz} corresponding to material A and the ideal elastic material are nearly identical. Fig. 4.4(b) shows the variation of the nondimensional vertical stress, $\sigma^*_{zzp}[= \sigma_{zz}/p_0]$, along the z-axis under applied fluid pressure of intensity p_0 applied over a strip of width $2a$ located at $z = a$. A discontinuity of magnitude α exists in the real part of σ^*_{zzp} at $z = a$. This is consistent with eqn (4.20b). The influence of poroelastic properties on the real part of σ^*_{zzp} in Fig. 4.4(b) is less than that noted in Fig. 4.4 (a) and the general trend of variation with z is somewhat identical. The imaginary part of σ^*_{zzp} depends significantly on poroelastic material properties as in the case of $\text{Im}[\sigma^*_{zzz}]$ shown in Fig. 4.4(a). The real part of σ_{zz} shown in Figs. 4.4 decreases gradually with z while the imaginary part shows oscillatory variations with decreasing magnitudes.

The profiles of nondimensional pore pressure along the z-axis due to applied vertical loading, $p^*_z[= p/f_0]$, and due to applied fluid pressure, $p^*_p[= p/p_0]$, are shown in Figs. 4.5(a) and 4.5(b), respectively. The nondimensional pore pressure, p^*_z, depends significantly on the frequency and poroelastic material properties. As in the case of σ^*_{zzz}, the variation of pore pressure along the z-axis is quite smooth at low frequencies but becomes oscillatory for $\delta > 1.0$. There is no singularity in the pore pressure profiles due to the applied vertical loading. The magnitude of p^*_z is found to increase with increasing b^* which is consistent with the fact that higher b^* means a more impermeable medium. In addition, Fig. 4.5(a) indicates that significant pore pressure is developed under applied vertical loading. Pore pressure profiles shown in Fig. 4.5(b) have a unit discontinuity in the real part at $z = a$ due to the applied pore pressure at this level. This is consistent with the eqn (4.20a) and no discontinuity exists in the imaginary part of p^*_p. The influence of poroelastic material properties is negligible on $\text{Re}[p^*_p]$ profiles but quite significant on $\text{Im}[p^*_p]$. However, the frequency of excitation has a significant influence on both real and imaginary part of the pore pressure profiles shown in Figs. 4.5(a) and 4.5(b).

4.6 Conclusions

A set of Green's functions is presented for displacements, stresses, pore pressure

and fluid discharge of a poroelastic half-plane subjected to time-harmonic internal excitations applied to the solid and fluid phases. It is also shown that Green's functions corresponding to transient excitations (loadings and fluid sources) can be derived from the time-harmonic solutions through appropriate redefinitions of variables. The solutions appear in terms of complex-valued semi-infinite integrals with an integrand that is oscillatory. Numerical solutions are evaluated by direct numerical integration of the semi-infinite integrals. Comparisons with existing solutions for static and dynamic responses of an ideal elastic half-plane and for dynamic response of a poroelastic full plane confirm the accuracy of the present numerical quadrature scheme used in the evaluation of the Green's functions. Internal strip loadings in the vertical and horizontal directions and internal strip fluid sink/pressure are considered in the numerical study. Numerical results presented in this Chapter indicate that the response of the medium is significantly influenced by poroelastic material constants, b^* and M^*, and the nondimensional Lamé constant λ^*. Numerical results also show a strong dependence of the response on the frequency of excitation. In general, the response shows a higher dependence on poroelastic material properties when the excitation is applied to the fluid when compared to the solid skeleton. Due to the complicated nature of the dependence of the response of the medium on b^*, M^*, λ^* and δ, it is difficult to identify a clear qualitative relationship between governing parameters and the response.

The Green's functions presented in this Chapter confirms the fact that the poroelastic solutions differ substantially from ideal elastic solutions. Therefore, the incorporation of poroelastic behaviour of natural soils is important in the study of dynamic soil-structure interaction problems. Green's functions presented in this Chapter are useful in the analysis of a broad class of problems related to earthquake engineering, geotechnical engineering, geophysics by using the boundary integral equation methods and other techniques. The present solution is also useful in the assessment of accuracy of finite element and other approximate numerical methods that can be used to study dynamic response of poroelastic materials.

Table 4.1: Comparison of vertical stress due to a vertical line load V_0 and shear stress due to a horizontal line load H_0 applied at depth $z = a$ of an ideal elastic half-plane ($\nu = 0.25$)

z/a	$a\sigma_{zz}(0,z)/V_0$		$a\sigma_{zx}(0,z)/H_0$	
	P & D (1974)†	Present study	P & D (1974)†	Present study
0.5	0.2672	0.2672	0.0314	0.0314
0.99	26.3127	26.3126	5.2517	5.2516
1.01	-26.7371	-26.7369	-5.3578	-5.3580
1.5	-0.7028	-0.7027	-0.1426	-0.1425
2.0	-0.4087	-0.4086	-0.0786	-0.0785
2.5	-0.2990	-0.2989	-0.0536	-0.0536
3.0	-0.2387	-0.2386	-0.0398	-0.0398

† Poulos and Davis (1974).

Table 4.2: Comparison of vertical displacement and vertical stress due to a vertical strip load of intensity f_0 applied over a strip of width $2a$ at depth $z = a$ of an ideal elastic half-plane ($\nu = 0.25$ and $\delta = 1.0$)

z/a	$\mu u_z(0,z)/f_0 a$				$\sigma_{zz}(0,z)/f_0$			
	R & W (1991)‡		Present study		R & W (1991)‡		Present study	
	Re	Im	Re	Im	Re	Im	Re	Im
0	-0.0186	-0.5895	-0.0187	-0.5893	0	0	0	0
0.5	-0.0042	-0.5941	-0.0041	-0.5939	0.0873	0.2485	0.0874	0.2484
0.99	0.0151	-0.5417	0.0153	-0.5415	0.2126	0.4179	0.2127	0.4176
1.01	0.0128	-0.5386	0.0131	-0.5385	-0.7826	0.4235	-0.7827	0.4232
1.5	-0.1165	-0.4483	-0.1162	-0.4480	-0.6337	0.5306	-0.6338	0.5302
2.0	-0.2175	-0.3351	-0.2171	-0.3347	-0.4271	0.5851	-0.4271	0.5845
2.5	-0.2765	-0.2145	-0.2761	-0.2141	-0.2171	0.5889	-0.2172	0.5883
3.0	-0.2947	-0.0983	-0.2942	-0.0981	-0.0317	0.5478	-0.0320	0.5472

‡ Rajapakse and Wang (1991).

Table 4.3: Comparison of nondimensional pore pressure (ap/V_0) due to a vertical line load V_0 applied in a poroelastic full plane ($\lambda^* = 1.5, M^* = 12.2, b^* = 2.3, \rho^* = 0.53, m^* = 1.1$ and $\alpha = 0.97$)

z/a	$\delta = 0.5$				$\delta = 2.0$			
	Closed form[§]		Present study		Closed form[§]		Present study	
	Re	Im	Re	Im	Re	Im	Re	Im
0.2	0.0032	-0.0139	0.0031	0.0139	0.0068	-0.0465	0.0069	0.0466
0.5	0.0089	-0.0232	0.0089	0.0232	0.0344	-0.0665	0.0345	0.0665
1.0	0.0181	-0.0290	0.0181	0.0290	0.0753	-0.0540	0.0754	0.0540
1.5	0.0257	-0.0290	0.0257	0.0290	0.0938	-0.0181	0.0939	0.0182
2.0	0.0314	-0.0259	0.0314	0.0259	0.0897	0.0191	0.0898	-0.0191
3.0	0.0372	-0.0160	0.0372	0.0161	0.0457	0.0613	0.0457	-0.0614

[§] Cheng *et al.* (1991).

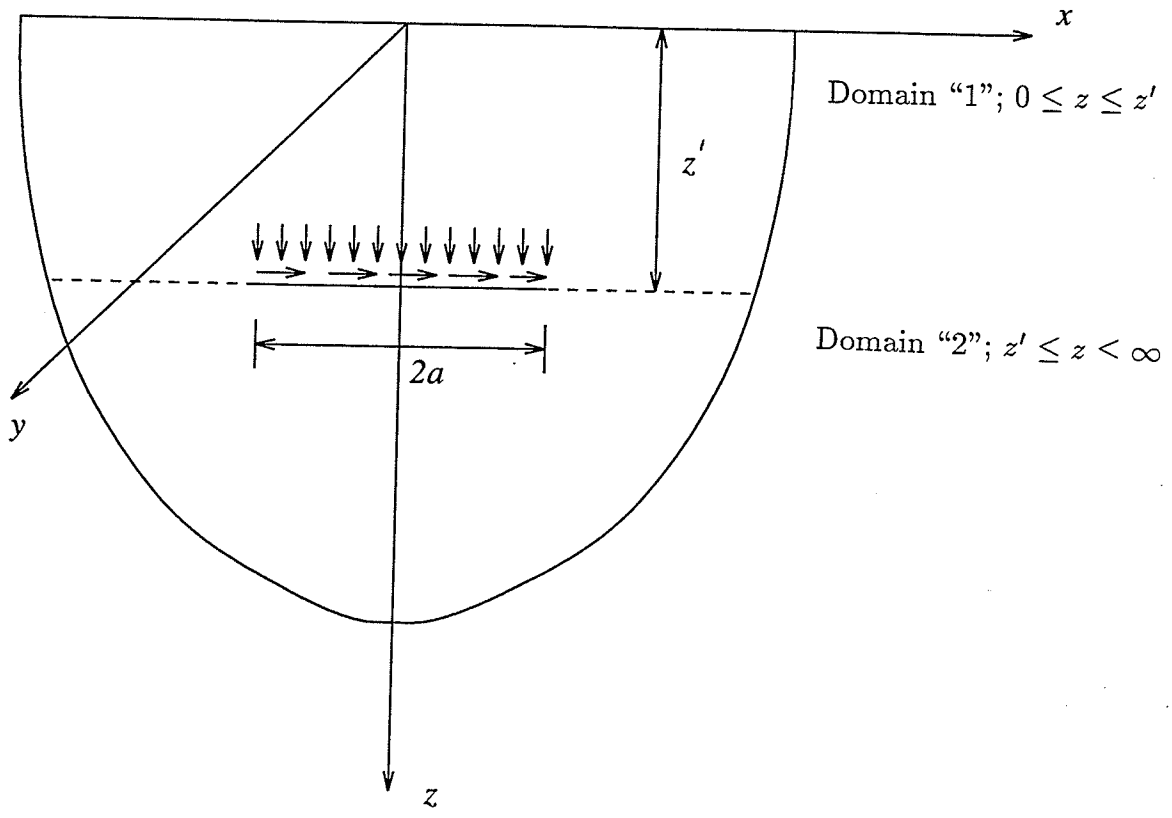

Figure 4.1 Coordinate system and internal loadings

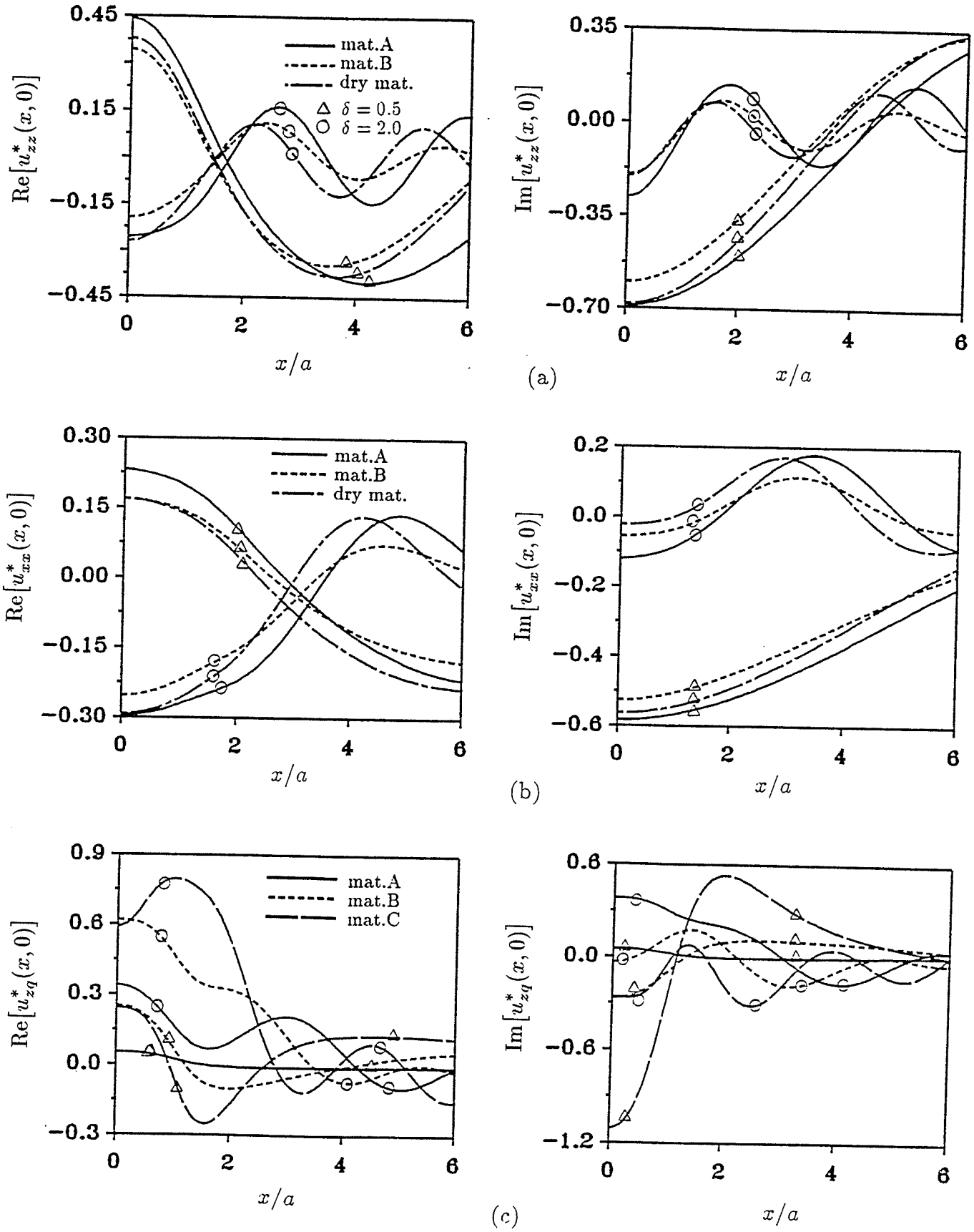

Figure 4.2 Displacements along the free surface for different poroelastic materials subjected to internal excitations ($z' = a$)

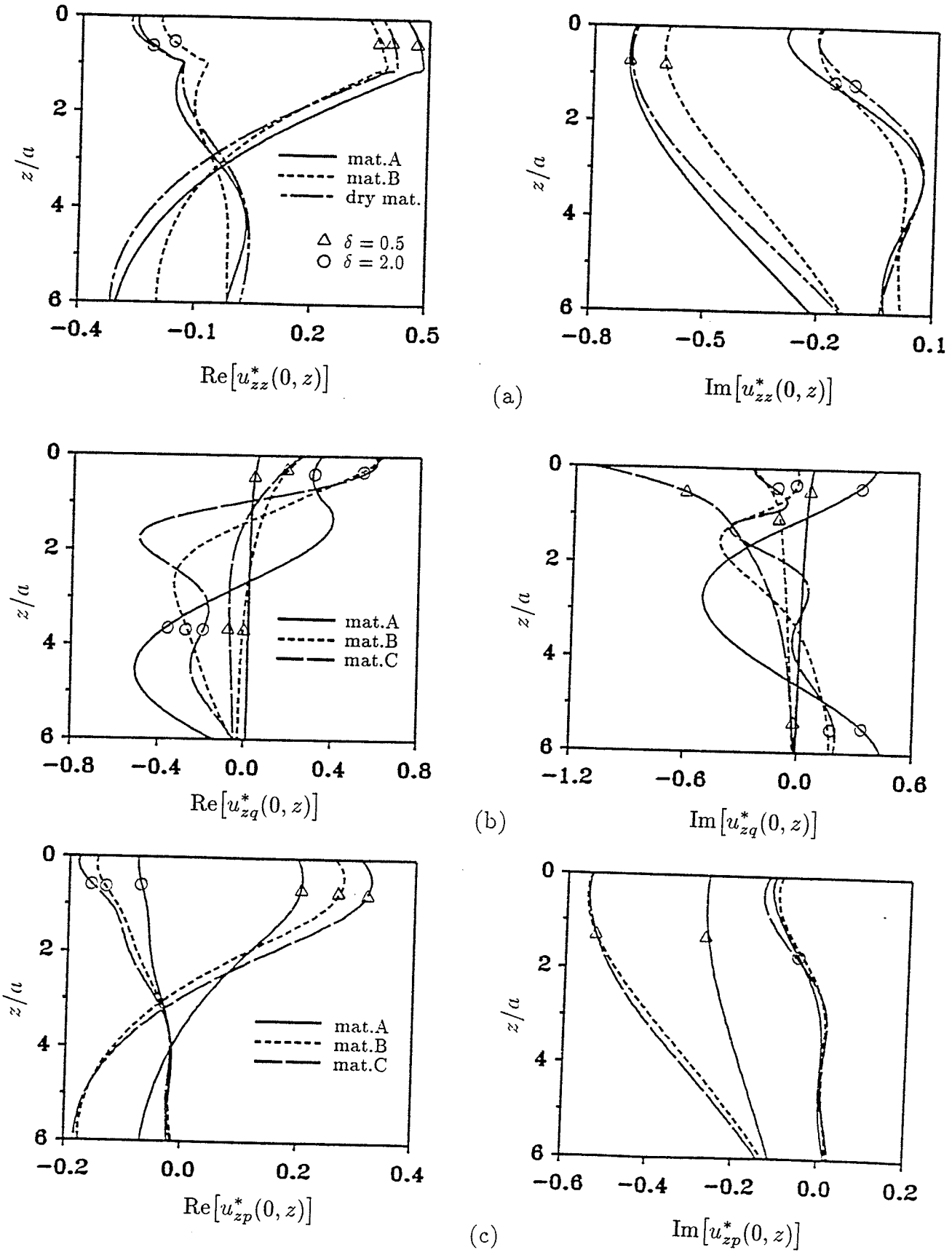

Figure 4.3 Displacements along the z-axis for different poroelastic materials subjected to internal excitations ($z' = a$)

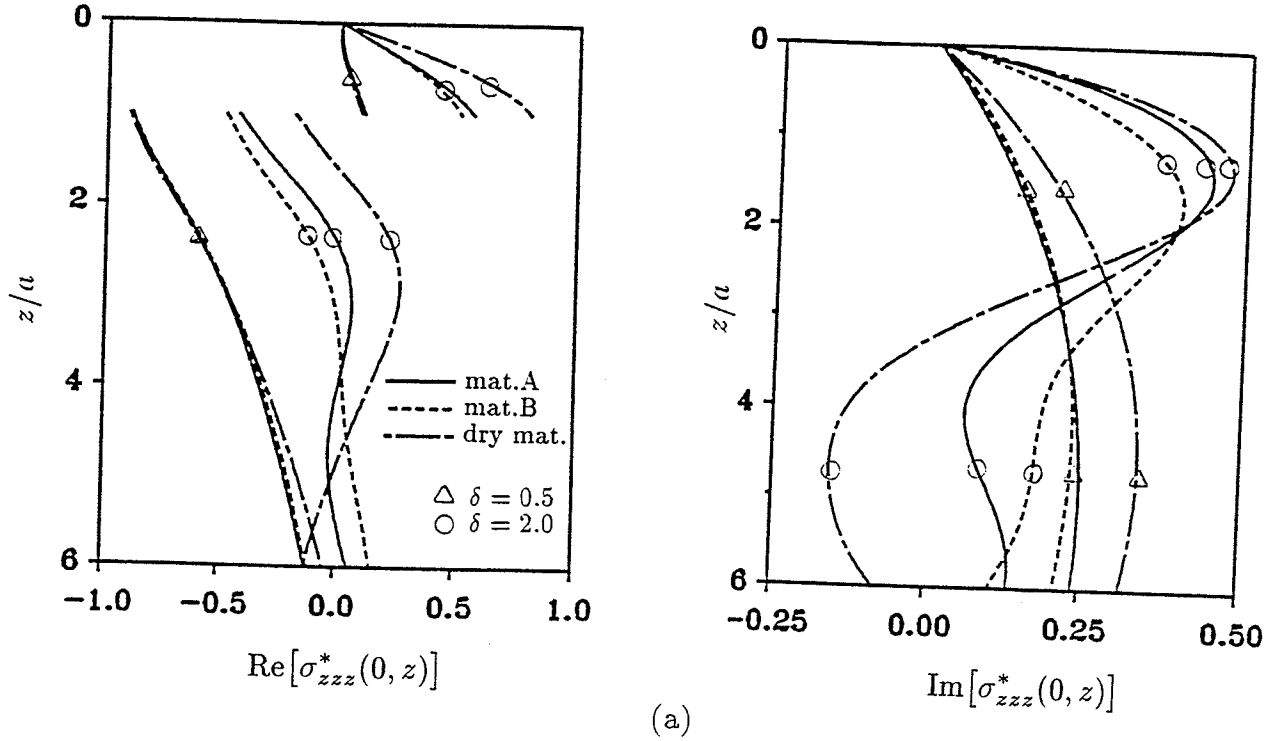

(a)

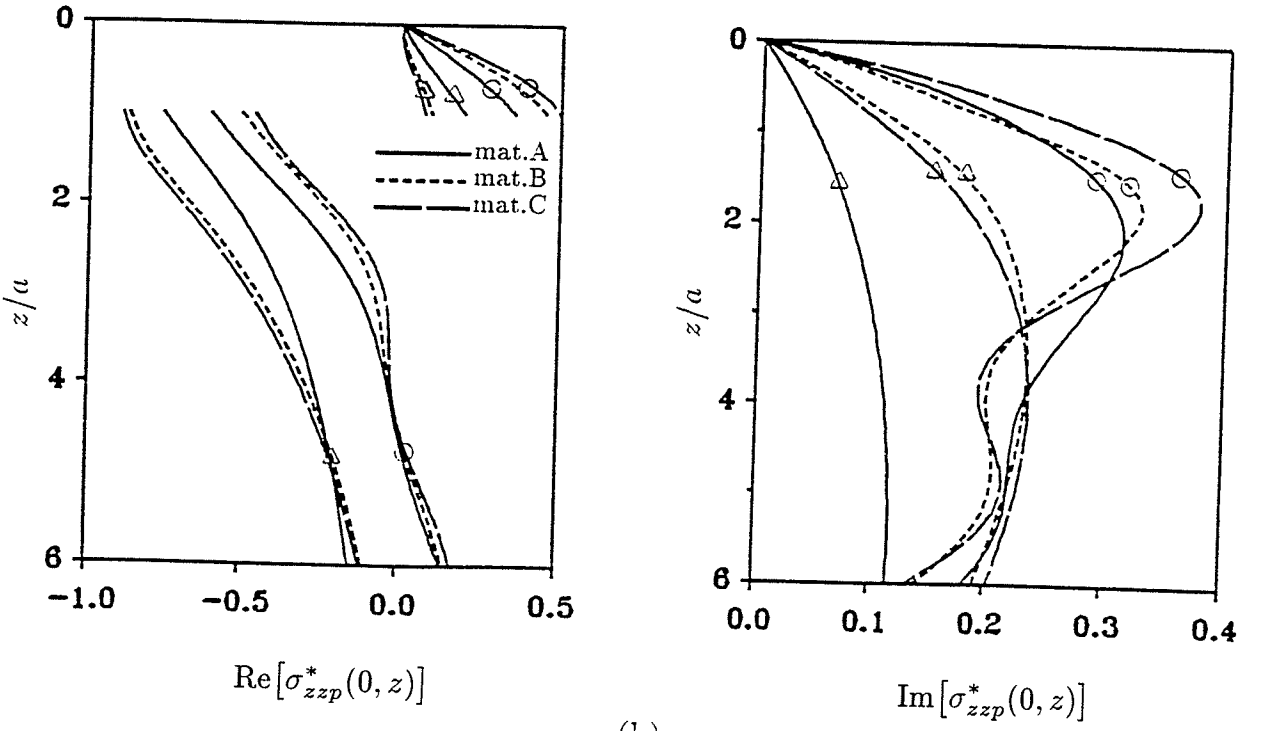

(b)

Figure 4.4 Stresses along the z-axis for different poroelastic materials subjected to internal excitations ($z' = a$)

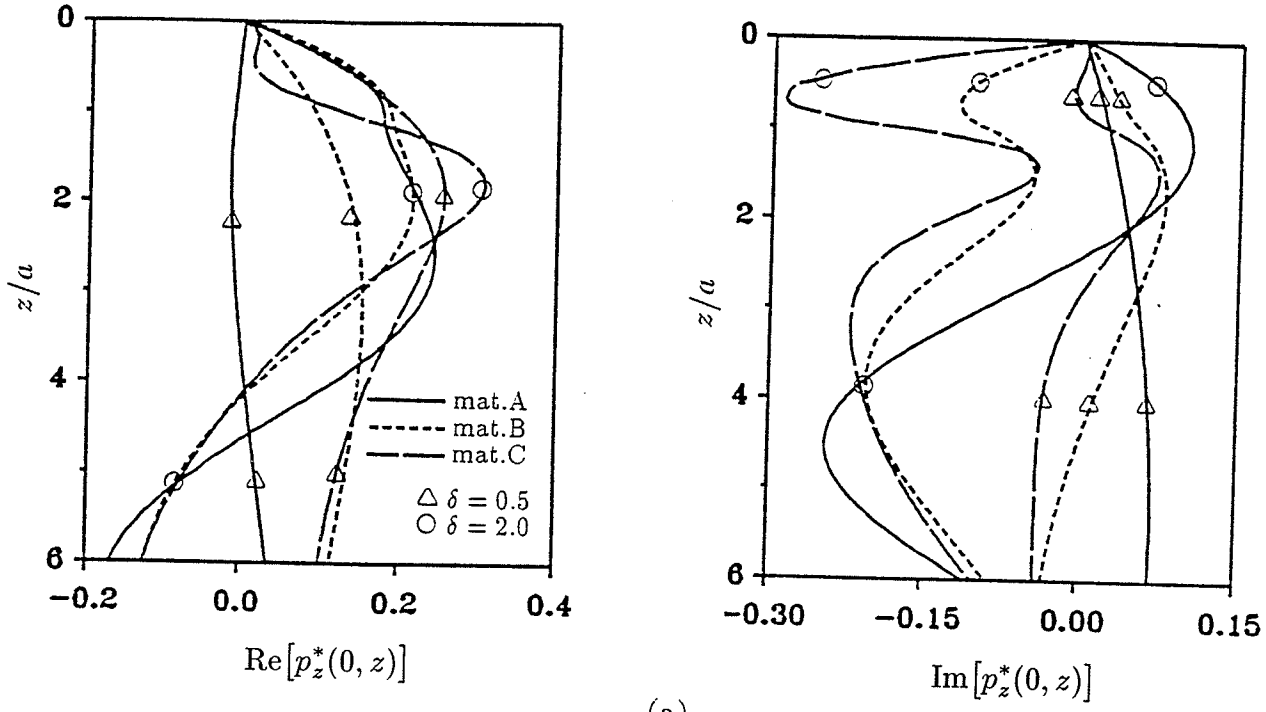

(a)

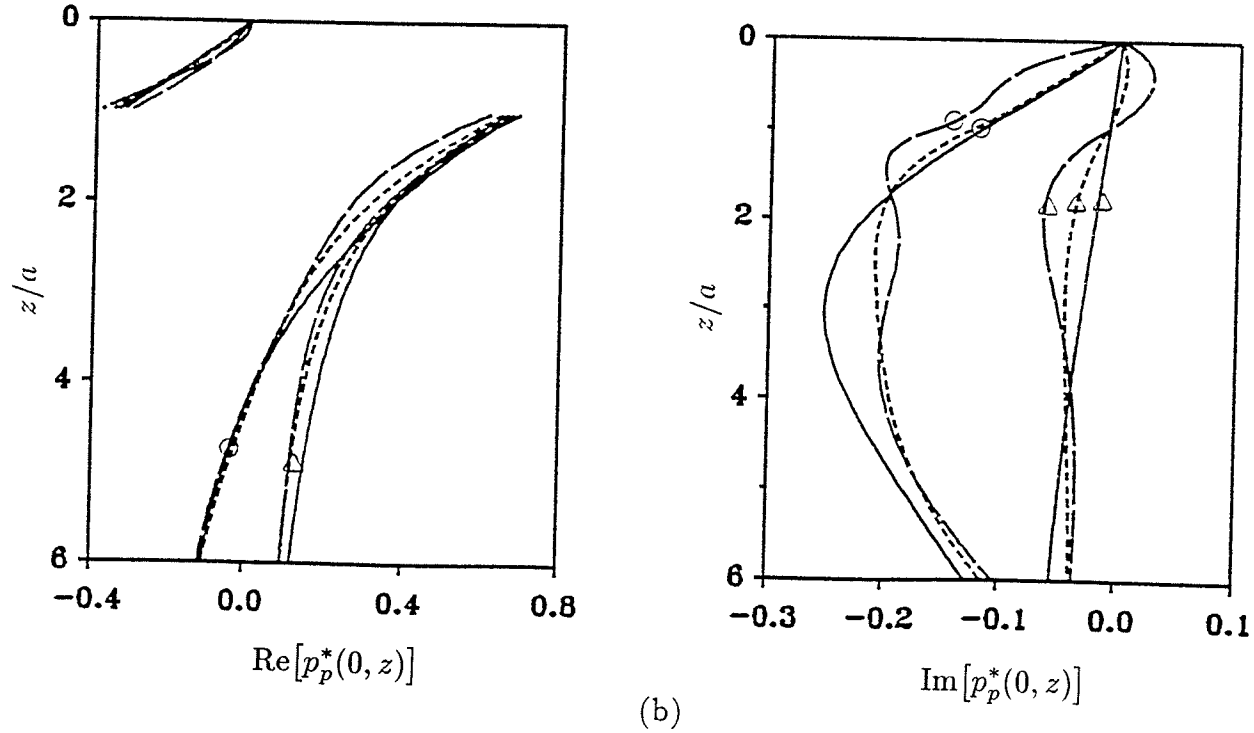

(b)

Figure 4.5 Pore pressure along the z-axis for different poroelastic materials subjected to internal excitations ($z' = a$)

Chapter 5

DYNAMIC GREEN'S FUNCTIONS OF A MULTI-LAYERED POROELASTIC HALF-PLANE

5.1 General

The stiffness matrix scheme presented in Chapter 3 is extended in this Chapter to evaluate Green's functions of a multi-layered poroelastic half-plane due to time-harmonic loads and fluid sources applied in the interior of the layered medium. The system under consideration consists of N layers of different properties and thickness overlying a homogeneous half-plane. Fourier transforms of average displacements of the solid matrix and the pore pressure at layer interfaces are considered as the basic unknowns. Exact stiffness (impedance) matrices describing the relationship between generalized displacement and force vectors of a layer of finite thickness and a half-plane are derived explicitly in the Fourier-frequency space by using exact general solutions given in Chapter 4 for Biot's equations for poroelastodynamics. The global stiffness matrix of a layered system and the global force vector is assembled by considering the continuity of tractions and fluid flow at layer interfaces. The numerical solution of the global equation system for discrete values of Fourier transform parameter together with the application of numerical quadrature to evaluate inverse Fourier transform integrals yield the solutions for poroelastic fields. Selected numerical results for displacements, stresses and pore pressure of multi-layered poroelastic half-planes are presented to demonstrate the influence of layering, material parameters and the frequency of excitation on the dynamic response of a layered poroelastic medium. The significant advantages of the present method for dynamic problems when compared to existing approximate stiffness methods and other methods based on the determination of layer arbitrary coefficients are discussed.

5.2 Stiffness Matrices

Consider a multi-layered system with a total of N poroelastic layers overlying a poroelastic half-space as shown in Fig. 3.1. It is assumed that the deformations are

plane strain in the xz-plane, i.e. $\epsilon_{xy} = \epsilon_{yy} = \epsilon_{yz} = 0$. Following eqns (4.14)-(4.16) and (4.18), general solutions for poroelastic fields governed by eqns (4.1) can be expressed in the Fourier transform space as

$$\mathbf{u}(\xi, z, \omega) = \mathbf{R}(\xi, z, \omega)\mathbf{C}(\xi, \omega) \tag{5.1a}$$

$$\mathbf{f}(\xi, z, \omega) = \mathbf{S}(\xi, z, \omega)\mathbf{C}(\xi, \omega) \tag{5.1b}$$

where

$$\mathbf{u}(\xi, z, \omega) =< i\bar{u}_x \quad \bar{u}_z \quad \bar{p} >^T \tag{5.2a}$$

$$\mathbf{f}(\xi, z, \omega) =< i\bar{\sigma}_{zx} \quad \bar{\sigma}_{zz} \quad \bar{w}_z >^T \tag{5.2b}$$

$$\mathbf{C}(\xi, \omega) =< A \quad B \quad C \quad D \quad E \quad F >^T \tag{5.2c}$$

In the above equations, ξ and ω are the Fourier transform parameter and the frequency of excitation, respectively, and the superposed bar denotes the Fourier transform of quantities with respect to the x-coordinate defined in eqn (4.10a). In addition, the arbitrary functions $A(\xi, \omega), B(\xi, \omega), ..., F(\xi, \omega)$ appearing in $\mathbf{C}(\xi, \omega)$ are to be determined by employing appropriate boundary and/or continuity conditions. The matrices $\mathbf{R}(\xi, z, \omega)$ and $\mathbf{S}(\xi, z, \omega)$ in eqns (5.1) are given by

$$\mathbf{R} = [\mathbf{R}_1 \ \vdots \ \mathbf{R}_2] \tag{5.3a}$$

$$\mathbf{S} = [\mathbf{S}_1 \ \vdots \ \mathbf{S}_2] \tag{5.3b}$$

where

$$\mathbf{R}_1 = \begin{bmatrix} -\xi e^{\gamma_1 z} & -\xi e^{-\gamma_1 z} & -\xi e^{\gamma_2 z} \\ \gamma_1 e^{\gamma_1 z} & -\gamma_1 e^{-\gamma_1 z} & \gamma_2 e^{\gamma_2 z} \\ \eta_1 e^{\gamma_1 z} & \eta_1 e^{-\gamma_1 z} & \eta_2 e^{\gamma_2 z} \end{bmatrix} \tag{5.4a}$$

$$\mathbf{R}_2 = \begin{bmatrix} -\xi e^{-\gamma_2 z} & i\gamma_3 e^{\gamma_3 z} & i\gamma_3 e^{-\gamma_3 z} \\ -\gamma_2 e^{-\gamma_2 z} & -i\xi e^{\gamma_3 z} & -i\xi e^{-\gamma_3 z} \\ \eta_2 e^{-\gamma_2 z} & 0 & 0 \end{bmatrix} \tag{5.4b}$$

$$\mathbf{S}_1 = \begin{bmatrix} -2\mu\xi\gamma_1 e^{\gamma_1 z} & 2\mu\xi\gamma_1 e^{-\gamma_1 z} & -2\mu\xi\gamma_2 e^{\gamma_2 z} \\ \beta_1 e^{\gamma_1 z} & \beta_1 e^{-\gamma_1 z} & \beta_2 e^{\gamma_2 z} \\ \gamma_1\chi_1 e^{\gamma_1 z} & -\gamma_1\chi_1 e^{-\gamma_1 z} & \gamma_2\chi_2 e^{\gamma_2 z} \end{bmatrix} \tag{5.4c}$$

$$\mathbf{S}_2 = \begin{bmatrix} 2\mu\xi\gamma_2 e^{-\gamma_2 z} & i\varsigma_3 e^{\gamma_3 z} & i\varsigma_3 e^{-\gamma_3 z} \\ \beta_2 e^{-\gamma_2 z} & -2i\mu\xi\gamma_3 e^{\gamma_3 z} & 2i\mu\xi\gamma_3 e^{-\gamma_3 z} \\ -\gamma_2\chi_2 e^{-\gamma_2 z} & -i\xi\chi_3 e^{\gamma_3 z} & -i\xi\chi_3 e^{-\gamma_3 z} \end{bmatrix} \tag{5.4d}$$

and

$$\eta_i = (\alpha + \chi_i)ML_i^2, \quad i = 1,2, \qquad \varsigma_3 = \mu(\xi^2 + \gamma_3^2) \tag{5.5a}$$

$$\beta_i = 2\mu\gamma_i^2 - \lambda L_i^2 - \alpha\eta_i, \qquad i = 1,2 \tag{5.5b}$$

$$\chi_i = \frac{(\lambda + \alpha^2 M + 2\mu)L_i^2 - \rho\omega^2}{\rho_f\omega^2 - \alpha M L_i^2}, \quad i = 1,2, \qquad \chi_3 = \frac{\rho_f\omega^2}{ib\omega - m\omega^2} \tag{5.5c}$$

In addition, μ, λ, α, M, ρ, ρ_f, m and b are the poroelastic material constants defined in Sections 2.2 and 4.2 and γ_i $(i = 1,2,3)$ and L_i^2 $(i = 1,2)$ are given in eqns (4.12c), (4.12d) and (4.13a), (4.13b), respectively, with the following definitions of parameters ϖ_i $(i = 1,2)$ and S^2.

$$\varpi_1 = \frac{(m\omega^2 - ib\omega)(\lambda + \alpha^2 M + 2\mu) + \rho\omega^2 M - 2\alpha\rho_f\omega^2 M}{(\lambda + 2\mu)M} \tag{5.6a}$$

$$\varpi_2 = \frac{(m\omega^2 - ib\omega)\rho\omega^2 - {\rho_f}^2\omega^4}{(\lambda + 2\mu)M} \tag{5.6b}$$

$$S^2 = \frac{\omega^2}{\mu}(\rho_f\chi_3 + \rho) \tag{5.6c}$$

For an nth layer $(n = 1,2,...,N)$, let $\mathbf{U}^{(n)}$ denote a vector of generalized coordinates whose elements are the Fourier transforms of displacements and pore pressure of the top and bottom surfaces of the nth layer and $\mathbf{F}^{(n)}$ denote a generalized force vector whose elements are Fourier transforms of tractions and fluid displacements of the top and bottom surfaces of the nth layer. Then,

$$\mathbf{U}^{(n)} = < \mathbf{u}^{(n)}(\xi, z_n, \omega) \quad \mathbf{u}^{(n)}(\xi, z_{n+1}, \omega) >^T \tag{5.7a}$$

$$\mathbf{F}^{(n)} = < -\mathbf{f}^{(n)}(\xi, z_n, \omega) \quad \mathbf{f}^{(n)}(\xi, z_{n+1}, \omega) >^T \tag{5.7b}$$

The vectors $\mathbf{u}^{(n)}$ and $\mathbf{f}^{(n)}$ in eqns (5.7) are identical to $\mathbf{u}$ and $\mathbf{f}$ defined in eqns (5.2a) and (5.2b), respectively, except that the material properties of the nth layer are employed in the definition and $z = z_n$ or z_{n+1}. The above selection of $\mathbf{U}^{(n)}$ and $\mathbf{F}^{(n)}$ satisfies the admissible boundary conditions at the boundaries of a poroelastic layer and those at the interface of two poroelastic materials (Deresiewicz and Skalak, 1963). A relationship between the generalized displacement vector $\mathbf{U}^{(n)}$ and the force vector $\mathbf{F}^{(n)}$ for the nth layer can be established by introducing a stiffness (impedance) matrix $\mathbf{K}^{(n)}$ through the eqn (3.10).

The explicit derivation of $\mathbf{K}^{(n)}$ corresponding to two-dimensional poroelastodynamics is extremely complicated since it involves the manipulation of fully populated 6×6 unsymmetric complex matrices. The algebraic complexity of this task may be the main reason for the emergence of the approximate stiffness matrix method (Lysmer and Waas, 1972 and Waas, 1972) which present a finite element representation for $\mathbf{K}^{(n)}$ based on an approximate displacement field. Similar to the case of three-dimensional quasi-statics presented in Section 3.2, the computer package *Mathematica* is used in the explicit derivation of $\mathbf{K}^{(n)}$. After lengthy manipulations, it is found that $\mathbf{K}^{(n)}$ for elastodynamics is also symmetric and its elements can be expressed as

1st Row:

$$k_{11} = \left(\varsigma_3 - 2\xi^2\right)\left[\left(\alpha_{3n}^2 + 1\right)\phi_1 - \left(\alpha_{3n}^2 - 1\right)\xi^2\phi_3\right] \tag{5.8a}$$

$$k_{12} = \xi\gamma_3\left(\varsigma_3 + 2\xi^2\right)\left[\left(\alpha_{3n}^2 + 1\right)\phi_3 - 4\alpha_{3n}\phi_4\right] - \xi\left(\alpha_{3n}^2 - 1\right)\left[2\gamma_3\phi_1 + \varsigma_3\phi_2\right] \tag{5.8b}$$

$$k_{13} = \xi\left(\varsigma_3 - 2\xi^2\right)\left[4\alpha_{3n}\phi_7 - \left(\alpha_{3n}^2 - 1\right)\phi_5 - \left(\alpha_{3n}^2 + 1\right)\phi_6\right] \tag{5.8c}$$

$$k_{14} = 2\left(\varsigma_3 - 2\xi^2\right)\left[\left(\alpha_{3n}^2 - 1\right)\xi^2\phi_4 - \alpha_{3n}\phi_1\right] \tag{5.8d}$$

$$k_{15} = 2\xi\gamma_3\left(\varsigma_3 - 2\xi^2\right)\xi\gamma_3\left[\alpha_{3n}\phi_3 - \left(\alpha_{3n}^2 + 1\right)\xi^2\phi_4\right] \tag{5.8e}$$

$$k_{16} = 2\xi\left(\varsigma_3 - 2\xi^2\right)\left[\alpha_{3n}\phi_6 - \left(\alpha_{3n}^2 + 1\right)\phi_7 + \left(\alpha_{3n}^2 - 1\right)\phi_8\right] \tag{5.8f}$$

where

$$\alpha_{in} = e^{-\gamma_i h_n}, \qquad i = 1,2,3, \qquad n = 1,2,...,N \tag{5.9a}$$

$$\phi_1 = \frac{\mu\gamma_3}{\varphi}\left[\left(\alpha_{1n}^2 - 1\right)\left(\alpha_{2n}^2 - 1\right)\left(\eta_1\gamma_2 - \eta_2\gamma_1\right)^2 - 4\left(\alpha_{1n} - \alpha_{2n}\right)^2\eta_1\eta_2\gamma_1\gamma_2\right] \tag{5.9b}$$

$$\phi_2 = \frac{\mu\xi^2}{\varphi}\left(\alpha_{1n}^2 - 1\right)\left(\alpha_{2n}^2 - 1\right)\left(\eta_1 - \eta_2\right)^2 \tag{5.9c}$$

$$\phi_3 = \frac{\mu(\eta_1 - \eta_2)}{\varphi}\left[\left(\alpha_{1n}^2 - 1\right)\left(\alpha_{2n}^2 + 1\right)\eta_1\gamma_2 - \left(\alpha_{1n}^2 + 1\right)\left(\alpha_{2n}^2 - 1\right)\eta_2\gamma_1\right] \tag{5.9d}$$

$$\phi_4 = \frac{\mu(\eta_1 - \eta_2)}{\varphi}\left[\alpha_{2n}\left(\alpha_{1n}^2 - 1\right)\eta_1\gamma_2 - \alpha_{1n}\left(\alpha_{2n}^2 - 1\right)\eta_2\gamma_1\right] \tag{5.9e}$$

$$\phi_5 = \frac{(\eta_1 - \eta_2)\xi^2}{\varphi}\left[\left(\alpha_{1n}^2 - 1\right)\left(\alpha_{2n}^2 + 1\right)\gamma_2 - \left(\alpha_{1n}^2 + 1\right)\left(\alpha_{2n}^2 - 1\right)\gamma_1\right] \tag{5.9f}$$

$$\phi_6 = \frac{\gamma_3}{\varphi}\left[\left(\alpha_{1n}^2 - 1\right)\left(\alpha_{2n}^2 - 1\right)\left(\gamma_1 - \gamma_2\right)\left(\eta_1\gamma_2 - \eta_2\gamma_1\right)\right.$$

$$+2\left(\alpha_{1n}-\alpha_{2n}\right)^2\left(\eta_1+\eta_2\right)\gamma_1\gamma_2\Big] \tag{5.10a}$$

$$\phi_7 = \frac{\left(\eta_1-\eta_2\right)}{\varphi}\left(\alpha_{1n}-\alpha_{2n}\right)\left(\alpha_{1n}\alpha_{2n}-1\right)\gamma_1\gamma_2\gamma_3 \tag{5.10b}$$

$$\phi_8 = \frac{\left(\eta_1-\eta_2\right)\xi^2}{\varphi}\Big[\alpha_{2n}\left(\alpha_{1n}^2-1\right)\gamma_2-\alpha_{1n}\left(\alpha_{2n}^2-1\right)\gamma_1\Big] \tag{5.10c}$$

$$\varphi = 2\gamma_3\xi^2\Big[\left(\alpha_{3n}^2+1\right)\phi_3-4\alpha_{3n}\phi_4\Big]-\left(\alpha_{3n}^2-1\right)\left(\gamma_3\phi_1+\xi^2\phi_2\right) \tag{5.10d}$$

2nd Row:

$$k_{22} = \gamma_3\left(\varsigma_3-2\xi^2\right)\Big[\left(\alpha_{3n}^2-1\right)\gamma_3\phi_3-\left(\alpha_{3n}^2+1\right)\phi_2\Big] \tag{5.11a}$$

$$k_{23} = \left(\alpha_{1n}^2-1\right)\eta_1^2\chi_2\psi_1+\left(\alpha_{2n}^2-1\right)\eta_2^2\chi_1\psi_3 - \eta_1\eta_2\left(\chi_1+\chi_2\right)\Big[\left(\alpha_{1n}^2-1\right)\psi_2+\left(\alpha_{2n}^2-1\right)\psi_4+\psi_5\Big] \tag{5.11b}$$

$$k_{24} = -k_{15}, \qquad k_{25} = 2\gamma_3\left(\varsigma_3-2\xi^2\right)\Big[\alpha_{3n}\phi_2-\left(\alpha_{3n}^2-1\right)\gamma_3\phi_4\Big] \tag{5.11c}$$

$$k_{26} = 2\gamma_3\left(\varsigma_3-2\xi^2\right)\Big[\left(\alpha_{3n}^2+1\right)\phi_8-\alpha_{3n}\phi_5-\left(\alpha_{3n}^2-1\right)\phi_7\Big] \tag{5.11d}$$

where

$$\psi_1 = \frac{1}{\varphi}\Big[\left(\alpha_{2n}^2-1\right)\left(\alpha_{3n}^2-1\right)\left(\gamma_2^2\gamma_3^2+\xi^4\right)+2\psi_2\varphi\Big] \tag{5.12a}$$

$$\psi_2 = \frac{\xi^2\gamma_2\gamma_3}{\varphi}\Big[4\alpha_{2n}\alpha_{3n}-\left(\alpha_{2n}^2+1\right)\left(\alpha_{3n}^2+1\right)\Big] \tag{5.12b}$$

$$\psi_3 = \frac{1}{\varphi}\Big[\left(\alpha_{1n}^2-1\right)\left(\alpha_{3n}^2-1\right)\left(\gamma_1^2\gamma_3^2+\xi^4\right)+2\psi_4\varphi\Big] \tag{5.12c}$$

$$\psi_4 = \frac{\xi^2\gamma_1\gamma_3}{\varphi}\Big[4\alpha_{1n}\alpha_{3n}-\left(\alpha_{2n}^2+1\right)\left(\alpha_{3n}^2+1\right)\Big] \tag{5.12d}$$

$$\psi_5 = \frac{\left(\alpha_{3n}^2-1\right)}{\varphi}\Big[\left(\alpha_{1n}^2-1\right)\left(\alpha_{2n}^2-1\right)\xi^4+\gamma_1\gamma_2\gamma_3^2\Big\{\left(\alpha_{1n}^2-1\right)\left(\alpha_{2n}^2-1\right) +2\left(\alpha_{1n}-\alpha_{2n}\right)^2\Big\}\Big] \tag{5.12e}$$

3rd Row:

$$k_{33} = \left(\chi_1-\chi_2\right)\Big[\left(\alpha_{1n}^2+1\right)\eta_1\gamma_1\psi_1-\left(\alpha_{2n}^2+1\right)\eta_2\gamma_2\psi_2\Big]-\left(\alpha_{3n}^2+1\right)\psi_6 \tag{5.13a}$$

$$k_{34} = k_{16}, \qquad k_{35} = -k_{26} \tag{5.13b}$$

$$k_{36} = 2\left(\chi_2-\chi_1\right)\Big[\alpha_{2n}\eta_2\gamma_2\psi_2-\alpha_{1n}\eta_1\gamma_1\psi_1\Big]+2\alpha_{3n}\psi_6 \tag{5.13c}$$

where

$$\psi_6 = \frac{\xi^2\gamma_3}{\varphi}\left(\varsigma_3 - 2\xi^2\right)\Big[2\gamma_1\gamma_2\Big\{\left(\alpha_{1n}^2+1\right)\left(\alpha_{2n}^2+1\right) - 4\alpha_{1n}\alpha_{2n}\Big\} - \left(\alpha_{1n}^2-1\right)\left(\alpha_{2n}^2-1\right)\left(\gamma_1^2+\gamma_2^2\right)\Big] \tag{5.14}$$

4th Row:

$$k_{44} = k_{11}, \qquad k_{45} = -k_{12}, \qquad k_{46} = k_{13} \tag{5.15}$$

5th Row:

$$k_{55} = k_{22}, \qquad k_{56} = -k_{23} \tag{5.16}$$

6th Row:

$$k_{66} = k_{33} \tag{5.17}$$

The element of layer stiffness (impedance) matrix $\mathbf{K}^{(n)}$ is a function of the layer thickness, the layer material properties and the Fourier transform parameter ξ. Only negative exponentials that decrease rapidly with increasing ξ and h_n are involved in k_{ij} as in the case of quasi-statics. The relationships between various k_{ij}'s [e.g. eqns (5.15)-(5.17)] can also be derived on the basis of the physical behaviour of the system since each k_{ij} represents a component of a generalized force vector due to a generalized displacement vector equals to a unit vector. When compared to the scheme of Lysmer and Waas (1972) the $\mathbf{K}^{(n)}$ obtained from the present method is exact and do not involve any approximations in the derivation. The present scheme also result in the stiffness (impedance) matrix of each physical layer of the layered system without further discretization into sub-layers as required in the approximate methods of Lysmer and Waas (1972), Kausel and Peek (1982), etc..

For the underlying half-plane, the stiffness (impedance) matrix are identical to that given by eqn (3.22) with $\mathbf{U}^{(N+1)}$, $\mathbf{F}^{(N+1)}$ and $\mathbf{K}^{(N+1)}$ are now defined as

$$\mathbf{U}^{(N+1)} = < \mathbf{u}^{(N+1)}(\xi, z_{N+1}, \omega) >^T \tag{5.18a}$$

$$\mathbf{F}^{(N+1)} = < -\mathbf{f}^{(N+1)}(\xi, z_{N+1}, \omega) >^T \tag{5.18b}$$

$$\mathbf{K}^{(N+1)} = \text{symm.}\left[\tilde{k}_{ij}\right]_{3\times 3} \tag{5.18c}$$

The elements $\tilde{k}_{ij}$ of the half-plane stiffness matrix $\mathbf{K}^{(N+1)}$ can be expressed as

$$\tilde{k}_{11} = \frac{\mu}{\vartheta}\left(\varsigma_3 - 2\xi^2\right)\left(\eta_1\gamma_2 - \eta_2\gamma_1\right),\ \tilde{k}_{12} = \frac{\mu\xi}{\vartheta}\Big[(\eta_2 - \eta_1)\varsigma_3 + 2\gamma_3(\eta_1\gamma_2 - \eta_2\gamma_1)\Big] \quad (5.19a)$$

$$\tilde{k}_{13} = \frac{\xi}{\vartheta}\left(\varsigma_3 - 2\xi^2\right)\left(\gamma_2 - \gamma_1\right), \quad \tilde{k}_{22} = \frac{\mu\gamma_3}{\vartheta}\left(\eta_1 - \eta_2\right)\left(\varsigma_3 - 2\xi^2\right) \quad (5.19b)$$

$$\tilde{k}_{23} = \frac{1}{\vartheta}\Big[\eta_2\chi_1\left(\gamma_1\gamma_3 - \xi^2\right) - \eta_1\chi_2\left(\gamma_2\gamma_3 - \xi^2\right)\Big] \quad (5.19c)$$

$$\tilde{k}_{33} = \frac{1}{\vartheta}\Big[\gamma_1\chi_1\left(\gamma_2\gamma_3 - \xi^2\right) - \gamma_2\chi_2\left(\gamma_1\gamma_3 - \xi^2\right) + \left(\gamma_1 - \gamma_2\right)\xi^2\chi_3\Big] \quad (5.19d)$$

where

$$\vartheta = \eta_1\left(\gamma_2\gamma_3 - \xi^2\right) - \eta_2\left(\gamma_1\gamma_3 - \xi^2\right) \quad (5.20)$$

It is noted that exponential terms of ξ are not involved in the expression of $\mathbf{K}^{(N+1)}$ and its elements depend on the material properties of the underlying half-plane and the Fourier transform parameter ξ. The stiffness matrix $\mathbf{K}^{(N+1)}$ of the underlying half-plane derived here also satisfies all the governing equations exactly. On the other hand, the matrix schemes proposed by Lysmer and Waas (1972) and Kausel and Peek (1982) are not capable of taking into consideration the influence of an underlying half-plane of a multi-layered system. Therefore, the presence of a rigid base at a finite depth is assumed in the approximate matrix schemes. Oner and Dong (1988) has presented a method to compute the stiffness of the underlying half-plane by using further approximations.

5.3 Global Stiffness Matrix

The global stiffness matrix of a multi-layered half-plane is assembled by using the layer and half-plane stiffness matrices on the basis of continuity of tractions and fluid flow at layer interfaces. The procedure is similar to that described in Section 3.3. The final equation system for determination of interlayer displacement and pore pressure is identical to eqn (3.29) except that the external force vector $\mathbf{T}^{(n)}$ at the nth interface is defined as

$$\mathbf{T}^{(n)} = < i\bar{T}_x^{(n)} \quad \bar{T}_z^{(n)} \quad \frac{\bar{Q}^{(n)}}{i\omega} >^T \quad (5.22)$$

where $\bar{T}_i^{(n)}(i = x, z)$ and $\bar{Q}^{(n)}$ denote the Fourier transforms of the tractions and fluid source applied at the nth interface, respectively.

The global stiffness matrix of eqn (3.29) for a two-dimensional poroelastodynamic problem is a well-conditioned symmetric matrix of order $3(N+1) \times 3(N+1)$ and has a band width equal to 6. When compared to the conventional method based on the determination of layer arbitrary coefficients, the global stiffness matrix involves only numerically stable negative exponential terms of the Fourier transform parameter ξ resulting in a well-conditioned final equation system for all values of ξ as shown in Section 5.4.1. The present scheme also requires less computational effort due to the presence of a banded symmetric global stiffness matrix which is nearly half the size of the unsymmetric coefficient matrix encountered in the conventional schemes based on the determination of layer arbitrary coefficients. In addition, the eigenvalues of the global stiffness matrix can be directly related to the velocities (wave number) of the surface waves in a layered poroelastic medium and the corresponding eigenvectors represent the displacements at layer interfaces for different mode of vibrations.

5.4 Numerical Solutions

5.4.1 Numerical Scheme

This section is concerned with the development of a computer code based on the stiffness matrix scheme to evaluate Green's functions of a multi-layered poroelastic half-plane corresponding to time-harmonic buried loads and fluid source. The tasks performed by the computer code is similar to that described in Section 3.4.1 for quasi-static problems. The program computes the stiffness matrices corresponding to each layer and the underlying half-plane for specified values of Fourier transform parameter ξ and the frequency of excitation ω. These matrices are assembled into the form of eqn (3.29) and the interlayer displacements and pore pressure vectors in Fourier transform space are obtained by solving the global stiffness equation [eqn (3.29)] for each specified value of ξ. Thereafter, the displacement and pore pressure at each interface in the frequency domain are obtained by evaluating the semi-infinite integrals with respect to ξ in eqn (4.10b) by using numerical quadrature as discussed in Section 4.5.1. To ensure that the real ξ-axis is free from singularities, one-percent material attenuation is incorporated into the shear modulus of

the materials in the analysis of dry elastic (ideal elastic) materials and poroelastic materials with b=0. A nondimensional frequency defined as $\delta = \omega a\sqrt{\rho^{(1)}/\mu^{(1)}}$ is used hereafter in the discussion of the numerical results where $\rho^{(1)}$ and $\mu^{(1)}$ are the mass density of the bulk material and the shear modulus of the first layer of a multi-layered half-plane, respectively.

The numerical stability of the global stiffness matrix of a layered system under dynamic excitations is assessed by computing a condition number of the matrix (Cline *et al.*, 1979). Figure 5.1 presents L_1-condition number of the final equation system corresponding to the present stiffness matrix method [i.e. eqn (3.29)] for increasing values of ξ and for different values of δ. The L_1-conditioned number corresponding to the conventional method based on the determination of layer arbitrary coefficients is also shown in Fig. 5.1. The results shown in Fig. 5.1 correspond to a layered system consisting of a poroelastic layer of unit thickness with properties identical to the first layer of the system shown in Table 5.1 bonded to a poroelastic half-plane with properties identical to the second layer of the system shown in Table 5.1. The global stiffness matrix of the present scheme has a much smaller condition number which either remains constant or decreases over a wide range of values of ξ and δ. On the other hand, the condition number of the coefficient matrix corresponding to the conventional method based on the determination of layer arbitrary coefficients is always higher and becomes extremely large for increasing values of ξ due to the presence of mis-matching exponential terms. Similar behaviour is noted in Section 3.4.1 for quasi-static problems. The numerical stability of the present stiffness matrix approach is clearly demonstrated by the solutions shown in Fig. 5.1.

Table 5.2 presents a comparison of numerical solutions for nondimensional vertical stress (σ_{zz}/f_0) due to a static vertical line load f_0 applied at the surface of a homogeneous ideal elastic half-plane (Melan, 1932) and an elastic layer of unit thickness bonded to a rigid base (Poulos, 1966). Solutions obtained from the present stiffness method for the limiting case of an ideal elastic material ($M = \rho_f = m = b = \alpha \equiv 0$) and $\delta = 0.01$ are compared in Table 5.2 with the numerical solutions given by Poulos and Davis (1974) to verify the accuracy of the present solution scheme. The two sets of solutions are in excellent agreement. Table

5.3 presents a comparison of elastodynamic solutions corresponding to an ideal elastic half-plane given by Rajapakse and Wang (1991) with those obtained from the present matrix scheme. The half-plane is considered to be consisting of 10 layers of equal thickness, $h/a = 0.2$, and an underlying half-plane of identical materials. The numerical stability and the general accuracy of the present matrix method are confirmed through these independent comparisons.

5.4.2 Numerical Results for Strip Loadings

In the numerical study, selected results corresponding to two poroelastic layered systems identified as layered systems A and B and a dry elastic (an ideal elastic) layered medium are presented. The configuration of the layered system is shown in Fig. 5.2 and the material properties are given in Table 5.1. Note that only the material parameters μ, λ and ρ are required in the numerical evaluation of dynamic response of dry elastic layer media. It is also noted that for layered system A, where the internal friction is neglected ($b = 0$), and for the dry elastic layered system, one percent attenuation (material damping) is considered in the numerical evaluation to facilitate numerical integration along the real ξ-axis (Apsel and Luco, 1983). All numerical results presented hereafter correspond to the case where vertical and horizontal loads are applied uniformly over a strip of width $2a$ with intensity f_0.

The figure 5.3 shows the nondimensional vertical displacement, $u^*_{zz}(0,z)[= \mu^{(1)} u_z(0,z)/f_0]$, at the center of a vertical strip load applied on the surface ($z'/a = 0.0$) and inside ($z'/a = 1.0$) the layered half-planes. Solutions are presented for the nondimensional frequency range $0.2 \leq \delta \leq 2.6$ since the displacements are arbitrary for $\delta = 0$. It is evident from the figure 5.3 that substantial differences exist between the response of the three layered systems. The variation of u^*_{zz} with δ is quite similar for a surface strip load and a buried strip load although both real and imaginary parts of u^*_{zz} are larger for a surface load. This implies that the half-plane becomes more stiff and damp under a buried load than a surface load. The main difference between the material properties of poroelastic systems A and B exists in the values of b (i.e. internal friction). All materials in the layered system A have zero internal friction ($b = 0$) whereas the system B consists of materials with finite internal friction (Table 5.1). Comparison of u^*_{zz} profiles in Fig. 5.3 indicates that

the presence of finite internal friction in materials makes the layered system more stiff and damp (i.e. smaller real and imaginary values of u^*_{zz}). The influence of b is more pronounced in the frequency range $0.6 < \delta < 1.5$. Comparison of the response of the layered system A and that of the dry elastic layered system also indicates that substantial difference exists in the response when $0.6 < \delta < 1.8$. The real part of u^*_{zz} shown in Fig. 5.3 shows a change in sign within the frequency range $0.8 < \delta < 1.4$ for the three layered systems. The maximum value of the imaginary part of u^*_{zz} occurs when the corresponding real part of the solution is equal to zero. The imaginary part of u^*_{zz} shown in Fig. 5.3 remains negative throughout the frequency range $0.2 \leq \delta \leq 2.6$.

Figure 5.4 shows the variation of $u^*_{xx}(0,z)[= \mu^{(1)} u_x(0,z)/f_0]$ at the center of a horizontal strip load applied on the surface ($z'/a = 0.0$) and inside ($z'/a = 1.0$) the layered half-planes. The behaviour of these solutions is quite different from u^*_{zz} shown in Fig. 5.3. The influence of poroelastic properties on the response is quite smaller when compared to the case of vertical displacement under a vertical loading (Fig. 5.3). The real part of u^*_{xx} corresponding to a surface and a buried load increases initially in the range $0.2 < \delta < 0.5$ and thereafter decreases rapidly with increasing frequency. Re$[u^*_{xx}]$ shows oscillatory variations with frequency for $\delta > 1.4$ but remains positive throughout the frequency range $0.2 \leq \delta \leq 2.6$. The imaginary part of u^*_{xx} remains negative for $0.2 \leq \delta \leq 2.6$ but decreases with δ for all three layered systems reaching its maximum value near $\delta = 0.7$ and thereafter increases with increasing δ. The imaginary part of u^*_{xx} shows relatively more dependence on the poroelastic behaviour of the material than the real part of u^*_{xx}. The solution for u^*_{xx} at the center of a strip is more stiff and damp for a buried horizontal load than a surface load. Similar behaviour was noted for vertical loading.

Figures 5.5(a) and 5.5(b) show the displacements $u^*_{zz}(x,0)$ and $u^*_{xx}(x,0)$ along the surface of a half-plane due to strip loads in the vertical and horizontal directions, respectively. At low frequency ($\delta = 0.3$), the real part of u^*_{zz} and u^*_{xx} decreases gradually with the distance x/a. The imaginary part of the displacements remains nearly constant for the layered system A and the dry elastic layered system whereas a minor linearly increasing variation is noted for the system B. The influence of poroelastic properties is quite negligible on the surface response at low frequencies.

As frequency increases (e.g. $\delta = 1.5$), the surface response of the three layered systems shows increasing differences especially under a vertical loading. The variation of surface displacements with the horizontal distance becomes oscillatory at higher frequencies.

Figure 5.6(a) shows the profiles of nondimensional stress $\sigma^*_{zzz} = \sigma_{zz}/f_0$ along the z-axis due to a vertical strip load applied at $z'/a = 1.0$. At low frequency ($\delta = 0.3$), both the real and imaginary parts of σ^*_{zzz} show negligible dependence on the poroelastic properties as noted previously for displacements. At high frequency ($\delta = 1.5$), profiles of σ^*_{zzz} of poroelastic layered systems A and B are nearly identical but show substantial differences from σ^*_{zzz} of the dry elastic layered system. As expected, the real part of σ^*_{zzz} shows a unit discontinuity at $z/a = 1.0$ due to the loading applied at this level and the imaginary part of σ^*_{zzz} is smooth at this level. The variation of σ^*_{zzz} with the depth is generally smooth within the layers except for the discontinuity in the real part at $z/a = 1.0$ and kinks at the layer interface levels for both real and imaginary parts of σ_{zz}. At low frequency ($\delta = 0.3$), the kinks in the σ_{zz} profiles at the layer interface are not very visible. Solutions for σ_{zz} are negligible for $z/a \geq 6.0$.

Pore pressure profiles along the z-axis (Fig. 5.6(b)) due to a vertical strip load applied at $z'/a = 1.0$ show substantial differences from the vertical stress profiles. Note that the pore pressure in the medium is zero in the case of a dry elastic layered system. The magnitude of real and imaginary parts of p^*_z is generally larger for $\delta = 1.5$ when compared to $\delta = 0.3$. Pore pressure profiles vary smoothly within the layers and show kinks at the layer interfaces. The kinks at layer interfaces are visible for the layered system B at low and high frequencies but are visible for the layered system A only at $\delta = 1.5$. Pore pressure is zero at $z = 0$ due to the imposed boundary condition. Substantial differences in pore pressure observed in Fig. 5.6(b) for poroelastic layered systems A and B indicate that the parameter b quantifying the internal friction has a strong influence on the pore pressure generated in the medium. However, the comparison of pore pressure profiles at different frequencies for layered systems A and B indicate that the dependence of p^*_z on b is very complicated and does not show a clear trend for a layered system. Pore pressure profiles along the z-axis due to vertical loading do not have any discontinuity at the loading level due

to the continuity conditions considered in the analysis. This essentially means that the loading is applied to the solid skeleton resulting in equal discontinuities in the total stress and the effective stress. On the other hand, it is possible to consider loadings applied directly to the fluid, i.e. a discontinuity equal to p_0 in the fluid pressure at an interface which results in a discontinuity of the total stress equal to αp_0. Under this condition, the effective stress at the loading level is continuous.

5.5 Conclusions

The exact stiffness matrix method presented in Chapter 3 is extended to compute Green's functions of a multi-layered poroelastic half-plane due to buried time-harmonic loads and fluid sources. In contrast to the approximate methods (Lysmer and Waas, 1972 and Waas, 1972) reported in the literature the present matrix method rigorously satisfy all the equations governing the dynamic response of a poroelastic medium and is also capable of modelling rigorously the influence of an underlying half-space in a layered system. Furthermore, the present method does not require the discretization of each material layer into thin sub-layers resulting in a much smaller global stiffness equation system. The global stiffness matrix of the present scheme is symmetric and its elements do not involve mis-matching exponential terms. The condition number of the global stiffness equation system is much smaller than that of the equation system corresponding to methods based on the determination of layer arbitrary coefficients and remains nearly constant with increasing values of the Fourier transform parameter. This behaviour confirms the superior numerical stability of the present scheme over the existing schemes. In addition, the present global stiffness matrix [e.g. $3(N+1) \times 3(N+1)$ for the system shown in Fig. 3.1] is nearly one-half the size of the unsymmetric matrix [$(6N+3) \times (6N+3)$ for the system shown in Fig. 3.1] corresponding to conventional methods based on the determination of layer arbitrary coefficients.

The numerical accuracy of the present exact stiffness matrix method is confirmed through existing solutions for an elastic medium subjected to static and dynamic loadings. Selected numerical results for displacements of layered systems presented in this paper indicate that the poroelastic properties and the frequency of excitation have a significant influence on the response. It is also found that the

material parameter b related to internal friction of the porous medium has a significant influence on vertical displacements and pore pressure due to vertical loading. The influence of b on horizontal displacements due to horizontal loading is relatively smaller. The present matrix scheme can be used directly to compute Green's functions required in the application of boundary integral equation methods for multi-layered poroelastic media and in the analysis of a variety of problems encountered in geomechanics, earthquake engineering and geophysics. It can be also used to verify the accuracy of approximate numerical methods such as the scheme by Bougacha *et al.* (1993b). The stiffness method presented in this Chapter can be extended to study transient response of layered poroelastic media by appropriate redefinition of vectors $\mathbf{u}$ and $\mathbf{f}$, and matrices $\mathbf{R}$ and $\mathbf{S}$ in eqns (5.1).

Table 5.1: Material properties of layered systems

	$\mu^{\dagger}$	$\lambda^{\dagger}$	$M^{\dagger}$	$\rho^{\ddagger}$	$\rho_f^{\ddagger}$	$m^{\ddagger}$	$b^{\S}$	α
first layer	2.5	5.0	25.0	2.0	1.0	3.0	1.5	0.95
second layer	1.25	1.88	18.8	1.6	1.0	1.8	0.75	0.98
half-plane	10.0	10.0	20.0	2.4	1.0	4.8	4.5	0.9

$\dagger$ $\times 10^8$ N/m^2.

$\ddagger$ $\times 10^3$ kg/m^3.

§ $\times 10^6$ N-s/m^4 for layered system B; for layered system A, $b^{(1)} = b^{(2)} = b^{(3)} = 0$.

Table 5.2: Comparison of vertical stress due to a vertical line load applied at the top surface of an ideal elastic medium ($\nu = 0.0$)

z	Case I		Case II	
	P & D (1974)†	Present study	P & D (1974)†	Present study
0.2	-3.183	-3.187	-3.148	-3.123
0.4	-1.592	-1.592	-1.641	-1.639
0.6	-1.061	-1.061	-1.159	-1.155
0.7	-0.909	-0.909	-1.034	-1.030
0.8	-0.796	-0.796	-0.948	-0.944
0.9	-0.707	-0.707	-0.887	-0.882

Case I: a half plane.

Case II: a finite layer with rigid base.

$\dagger$ Poulos and Davis (1974).

Table 5.3: Comparison of vertical displacement and vertical stress due to a vertical strip load applied at depth $z = a$ of an ideal elastic half-plane ($\nu = 0.25$ and $\delta = 1.0$)

z/a	$\mu u_z(0,z)/f_0 a$				$\sigma_{zz}(0,z)/f_0$			
	R & W (1991)‡		Present study		R & W (1991)‡		Present study	
	Re	Im	Re	Im	Re	Im	Re	Im
0	-0.0186	-0.5895	-0.0187	-0.5893	0	0	0	0
0.5	-0.0042	-0.5941	-0.0041	-0.5939	0.0873	0.2485	0.0874	0.2484
0.9	0.0108	-0.5546	0.0110	-0.5544	0.1914	0.3914	0.1915	0.3912
1.1	0.0119	-0.5242	0.0120	-0.5241	-0.7605	0.4472	-0.7606	0.4470
1.5	-0.1165	-0.4483	-0.1162	-0.4480	-0.6337	0.5306	-0.6338	0.5302
2.0	-0.2175	-0.3351	-0.2171	-0.3347	-0.4271	0.5851	-0.4271	0.5845
3.0	-0.2947	-0.0983	-0.2942	-0.0981	-0.0317	0.5478	-0.0320	0.5472

‡ Rajapakse and Wang (1991).

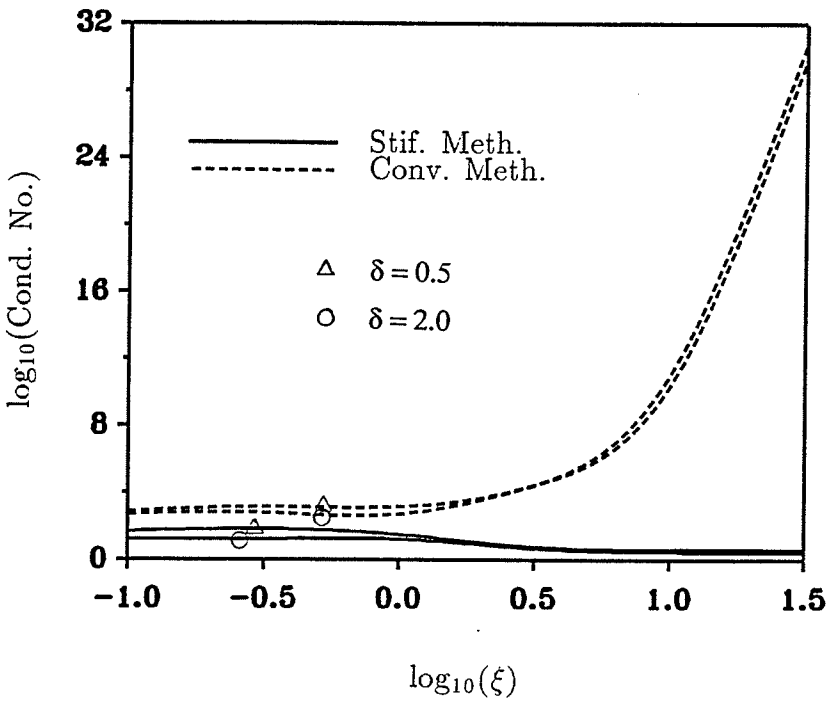

Figure 5.1 Comparison of condition numbers

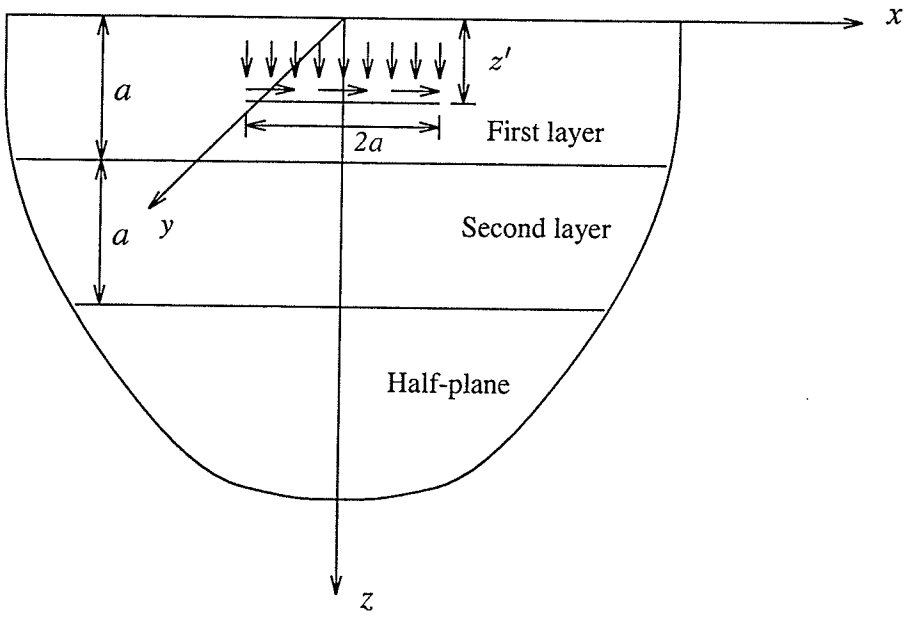

Figure 5.2 A multi-layered half-plane considered in the numerical study

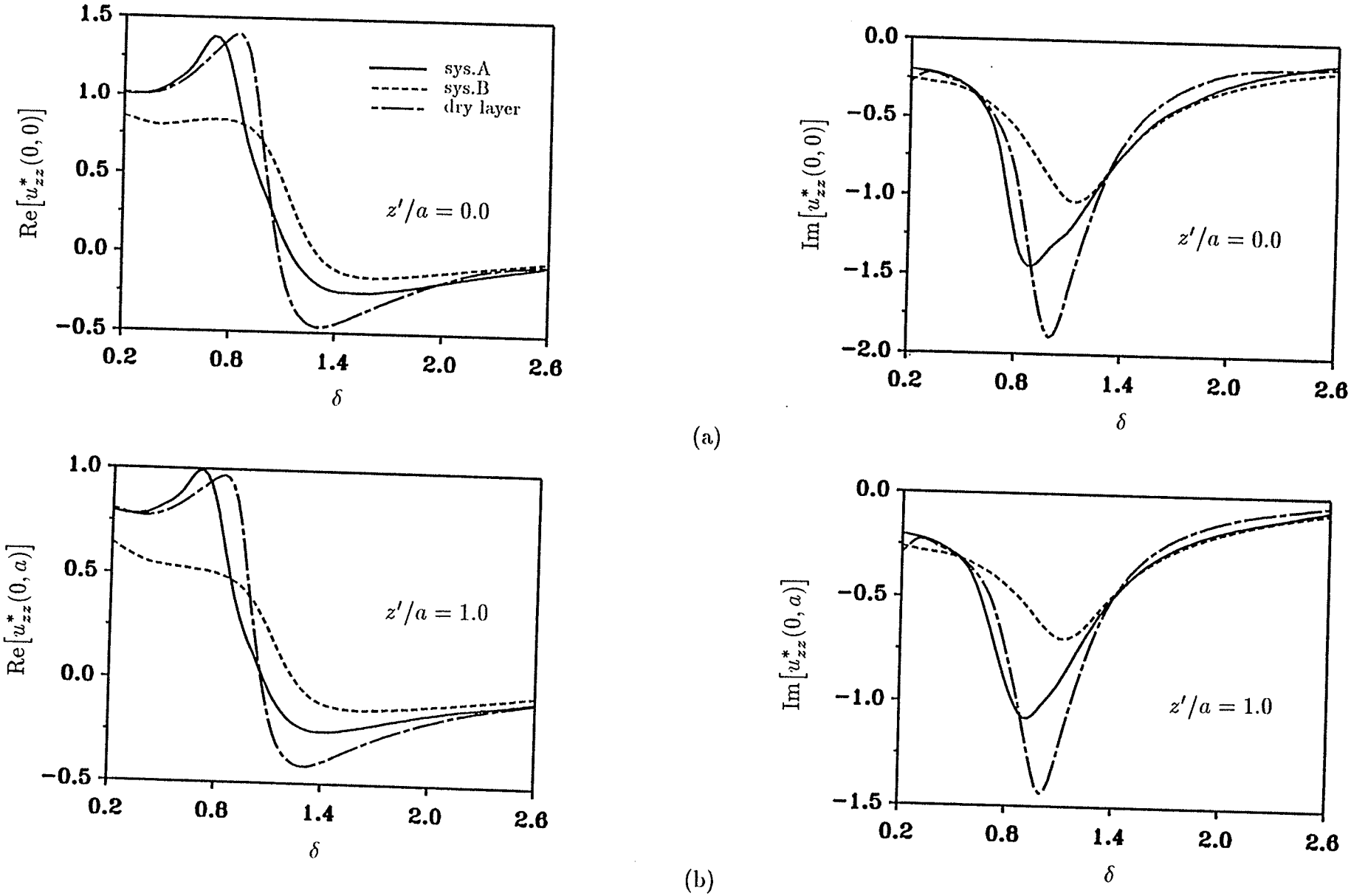

Figure 5.3 Vertical displacements due to vertical strip loads

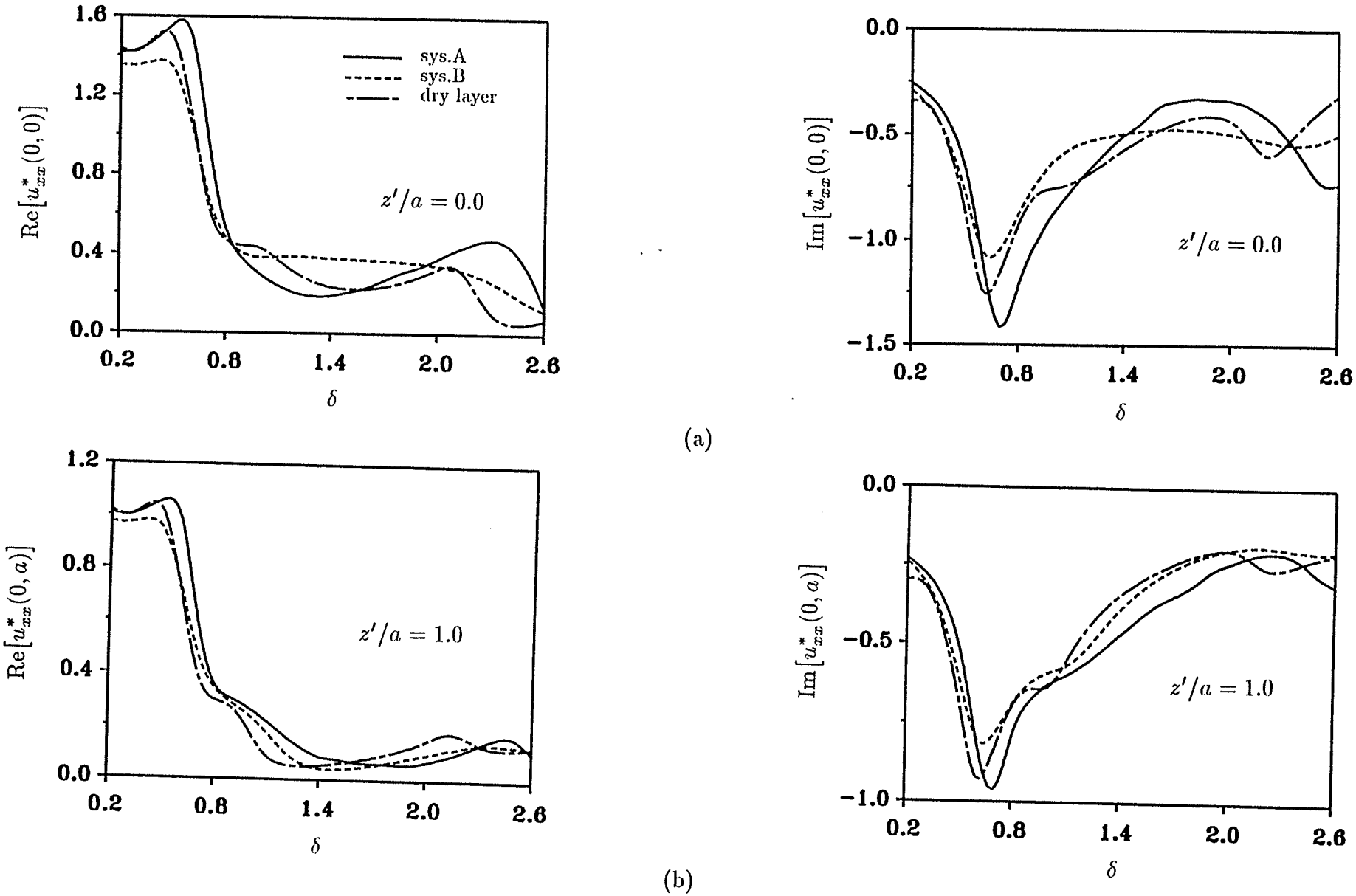

Figure 5.4 Horizontal displacements due to horizontal strip loads

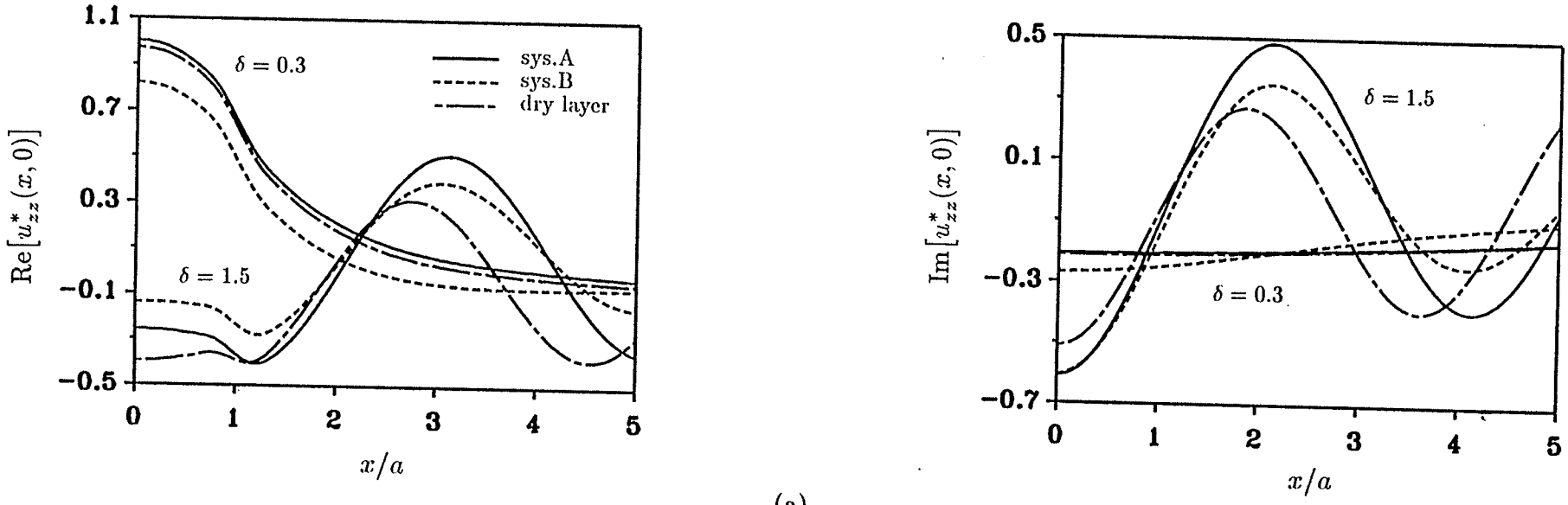

(a)

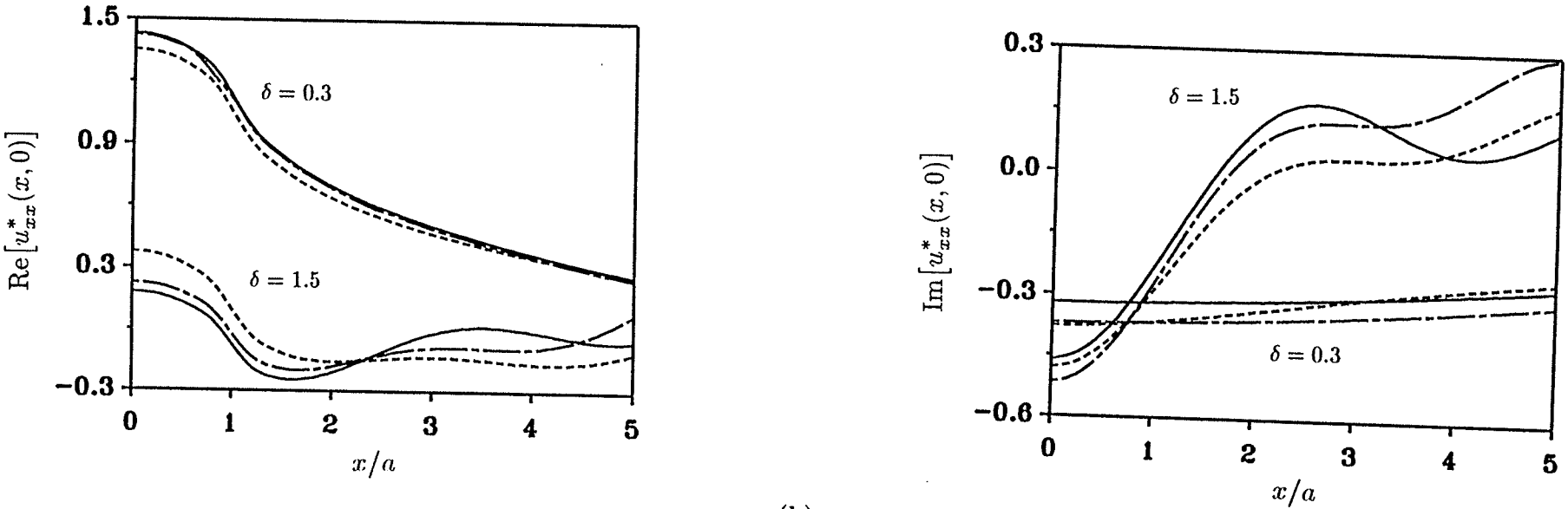

(b)

Figure 5.5 Displacements along the surface due to strip loads at $z'/a = 0.0$

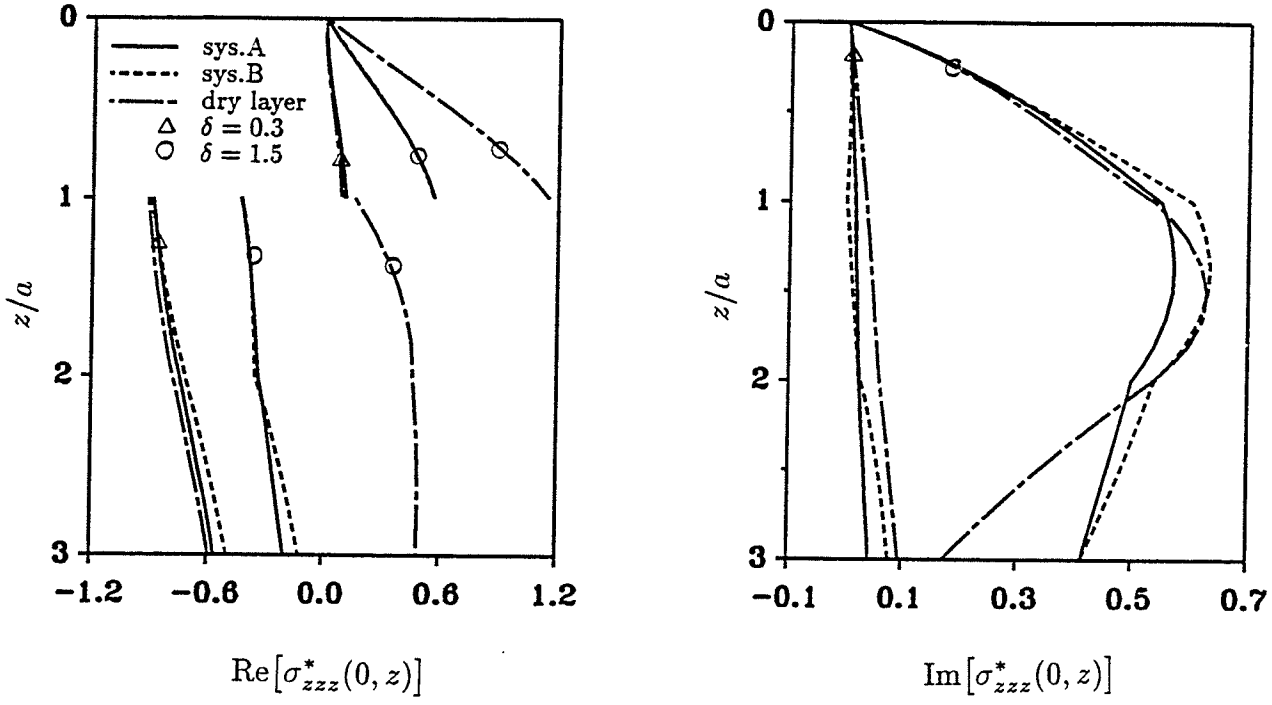

(a)

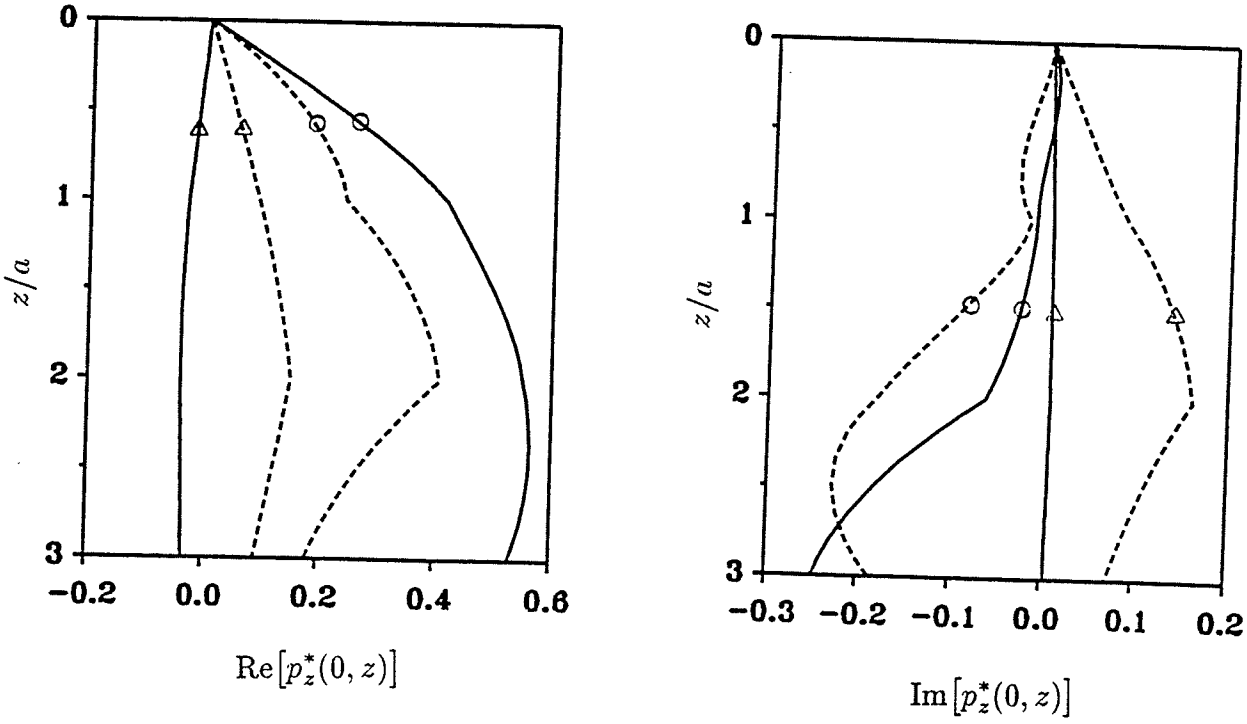

(b)

Figure 5.6 Vertical stress and pore pressure along the z-axis due to a vertical strip load at $z'/a = 1.0$

Chapter 6

INDIRECT BOUNDARY INTEGRAL EQUATION METHOD

6.1 General

The development of computer codes based on an indirect boundary integral equation method is considered in this Chapter for the analysis of quasi-static, time-harmonic and transient boundary value problems involving semi-infinite and infinite poroelastic media. Formulations are presented in the Laplace domain for quasi-static and transient problems and in the frequency domain for time-harmonic problems, respectively. The kernel functions of the integral equation correspond to an appropriate set of Green's functions derived in Chapters 2 and 4 for a homogeneous domain and in Chapters 3 and 5 for a layered system, respectively. The numerical implementation of the integral equation is also discussed. The convergence and numerical stability of the present scheme are investigated by considering two-dimensional and three-dimensional cavity expansion problems under quasi-static, time-harmonic and transient loadings. In addition, the versatility and applicability of the present scheme are demonstrated by presenting the solutions for axial stiffness of a spheroidal anchor embedded in a poroelastic medium, and investigating the dynamic response of a semi-circular tunnel with a rigid wall in a poroelastic medium.

6.2 Indirect Boundary Integral Equation Scheme

Consider a poroelastic domain Ω with a volume V bounded by a surface S with a Cartesian coordinate system (x, y, z) defined as shown in Fig. 6.1. It is assumed that a set of admissible boundary conditions are specified on the surface S. For example, if u_i $(i = x, y, z)$ is specified on S then such a problem is known as a displacement boundary value problem whereas a problem with specified T_i $(i = x, y, z)$ on S is called a traction boundary value problem. In addition, the pore pressure p or the fluid discharge q_n normal to the surface S has to be specified. The surface S is called a fully permeable surface when p is equal to zero on S whereas a fully impermeable surface corresponds to the case where $q_n = 0$ on S.

Generally, the solution of the governing equations for domain Ω [e.g. eqn (2.4) in Section 2.3 for quasi-static deformations] subjected to the boundary condition specified on S by using analytical methods is possible only in a very few special cases such as in the case of a vertically loaded rigid sphere in an infinite poroelastic medium (De jong, 1957). In view of this, the development of computational methods such as boundary integral equation methods have received increasing attentions over the past decade (Cheng and Liggett, 1984a,b; Cheng and Detournay, 1988; Nishimura and Kobayashi, 1989; Cheng *et al.*, 1991 and Dominguez, 1992). As mentioned in Chapter 1, one of the main objectives of this thesis is to present an indirect boundary integral equation scheme with non-singular kernels for analysis of quasi-static, time-harmonic and transient boundary value problems involving semi-infinite and infinite poroelastic domains.

The indirect boundary integral equation method presented herein follows the concepts used by Ohsaki (1973) for the case of ideal elastic media. The present scheme is based on the consideration of an equivalent problem defined with respect to an undisturbed poroelastic medium. For example, consider a poroelastic domain $\bar{\Omega}$ with a volume $\bar{V}$ bounded by a surface $\bar{S}$ identical to S in Fig. 6.1. It is assumed that a set of unknown forces with magnitude $f_i(\mathbf{r}', t')$ with $i = x, y, z$ and a fluid source $\Gamma(\mathbf{r}', t')$ are applied on an auxiliary surface S' defined interior to $\bar{S}$ as shown in Fig. 6.2. Hence, the displacement $u_i(\mathbf{r}, t)$, traction $T_i(\mathbf{r}, t)$, pore pressure $p(\mathbf{r}, t)$ and fluid discharge in the direction of unit normal $\mathbf{n}$ to an arbitrary plane, denoted by $q_n(\mathbf{r}, t)$, at any point with position vector $\mathbf{r}$ in $\bar{V}$ can be expressed as

$$u_i(\mathbf{r},t) = \int_0^t \int_{S'} G_{ij}(\mathbf{r}, t-t'; \mathbf{r}') f_j(\mathbf{r}', t') dS' dt' + \int_0^t \int_{S'} G_{iq}(\mathbf{r}, t-t'; \mathbf{r}') \Gamma(\mathbf{r}', t') dS' dt', \qquad \mathbf{r}' \in S'; \quad i,j = x,y,z \quad (6.1a)$$

$$T_i(\mathbf{r},t) = \int_0^t \int_{S'} H_{ij}(\mathbf{r}, t-t'; \mathbf{r}') f_j(\mathbf{r}', t') dS' dt' + \int_0^t \int_{S'} H_{iq}(\mathbf{r}, t-t'; \mathbf{r}') \Gamma(\mathbf{r}', t') dS' dt', \qquad \mathbf{r}' \in S'; \quad i,j = x,y,z \quad (6.1b)$$

$$p(\mathbf{r},t) = \int_0^t \int_{S'} H_{pj}(\mathbf{r}, t-t'; \mathbf{r}') f_j(\mathbf{r}', t') dS' dt' + \int_0^t \int_{S'} H_{pq}(\mathbf{r}, t-t'; \mathbf{r}') \Gamma(\mathbf{r}', t') dS' dt', \qquad \mathbf{r}' \in S'; \quad j = x,y,z \quad (6.1c)$$

$$q_n(\mathbf{r},t) = \int_0^t \int_{S'} G_{qj}(\mathbf{r},t-t';\mathbf{r}')f_j(\mathbf{r}',t')dS'dt'$$
$$+ \int_0^t \int_{S'} G_{qq}(\mathbf{r},t-t';\mathbf{r}')\Gamma(\mathbf{r}',t')dS'dt', \qquad \mathbf{r}' \in S'; \quad j = x,y,z \qquad (6.1d)$$

In the above equations, $G_{ij}(\mathbf{r},t;\mathbf{r}')$ and $G_{iq}(\mathbf{r},t;\mathbf{r}')$ denote displacements in the i-direction ($i = x,y,z$) at point $\mathbf{r}$ due to an impulsive force in the j-direction ($j = x,y,z$) and an impulsive fluid source, respectively, at point $\mathbf{r}'$ at $t = 0$; $G_{qj}(\mathbf{r},t;\mathbf{r}')$ and $G_{qq}(\mathbf{r},t;\mathbf{r}')$ denote fluid discharge in the direction of a vector $\mathbf{n}$ at point $\mathbf{r}$ due to an impulsive force in the j-direction ($j = x,y,z$) and an impulsive fluid source, respectively, at point $\mathbf{r}'$ at $t = 0$. For example, if $\mathbf{n} = \{0\ 0\ 1\}^T$ then $G_{qx}(\mathbf{r},t;\mathbf{r}')$ is the fluid discharge in the z-direction at point $\mathbf{r}$ due to an impulsive force in the x-direction applied at $\mathbf{r}'$ at $t = 0$. $H_{ij}(\mathbf{r},t;\mathbf{r}')$ and $H_{iq}(\mathbf{r},t;\mathbf{r}')$ denote tractions in the i-direction ($i = x,y,z$) at point $\mathbf{r}$ due to an impulsive force in the j-direction ($j = x,y,z$) and an impulsive fluid source, respectively, at point $\mathbf{r}'$ at $t = 0$; $H_{pj}(\mathbf{r},t;\mathbf{r}')$ and $H_{pq}(\mathbf{r},t;\mathbf{r}')$ denote excess pore pressure at point $\mathbf{r}$ due to an impulsive force in the j-direction ($j = x,y,z$) and an impulsive fluid source, respectively, at point $\mathbf{r}'$ at $t = 0$. It is important to note here that the kernel functions G_{ij}, G_{iq}, H_{ij}, etc. in eqns (6.1) are non-singular since $\mathbf{r} \neq \mathbf{r}'$ in the present scheme. In the case of ideal elasticity, only eqns (6.1a) and (6.1b) are involved in the analysis with the second integrals in those equations being equal to zero. In addition, for ideal elastic problems under static loadings, the convolution integrals with respect to the time parameter t' do not exist, and eqns (6.1a) and (6.1b) reduce to the forms given by Ohsaki (1973).

The Green's functions (kernel functions) are not available explicitly in the time domain for half-space/plane problems. It is computationally more efficient in the case of linear problems (especially for transient problems) to develop a formulation in the Laplace transform domain (Badmus *et al.*, 1993). Applying Laplace transform to the time variable in eqns (6.1) yields

$$\bar{u}_i(\mathbf{r},s) = \int_{S'} \bar{G}_{ij}(\mathbf{r},s;\mathbf{r}')\bar{f}_j(\mathbf{r}',s)dS' + \int_{S'} \bar{G}_{iq}(\mathbf{r},s;\mathbf{r}')\bar{\Gamma}(\mathbf{r}',s)dS' \qquad (6.2a)$$

$$\bar{T}_i(\mathbf{r},s) = \int_{S'} \bar{H}_{ij}(\mathbf{r},s;\mathbf{r}')\bar{f}_j(\mathbf{r}',s)dS' + \int_{S'} \bar{H}_{iq}(\mathbf{r},s;\mathbf{r}')\bar{\Gamma}(\mathbf{r}',s)dS' \qquad (6.2b)$$

$$\bar{p}(\mathbf{r},s) = \int_{S'} \bar{H}_{pj}(\mathbf{r},s;\mathbf{r}')\bar{f}_j(\mathbf{r}',s)dS' + \int_{S'} \bar{H}_{pq}(\mathbf{r},s;\mathbf{r}')\bar{\Gamma}(\mathbf{r}',s)dS' \qquad (6.2c)$$

$$\bar{q}_n(\mathbf{r},s) = \int_{S'} \bar{G}_{qj}(\mathbf{r},s;\mathbf{r}')\bar{f}_j(\mathbf{r}',s)dS' + \int_{S'} \bar{G}_{qq}(\mathbf{r},s;\mathbf{r}')\bar{\Gamma}(\mathbf{r}',s)dS' \qquad (6.2d)$$

where the superposed bar in eqns (6.2) denotes the Laplace transform of quantities with respect to the time coordinate and s is the Laplace transform parameter.

It should be noted that in the case of quasi-static problems the Green's functions for impulsive loads and an impulsive fluid source are obtained by considering the governing equations in the absence of inertia terms as shown in eqns (2.4). However, the quasi-static Green's functions presented in Chapter 2 are derived on the basis of applied loadings and fluid source with time histories identical to a step function $H(t)$. This means that for quasi-static problems the relevant Green's functions can be obtained directly by multiply the Green's functions given in Chapter 2 by a factor "s". However, for transient dynamic problems, Green's functions are derived on the basis of field equations with appropriate inertia terms as presented in Chapter 4 for two-dimensional problems.

In the case of time-harmonic problems where the motion is assumed to be time-harmonic with a time factor of $e^{i\omega t}$, the analysis can be performed directly in the frequency domain. The pertinent integral equations in the frequency domain can be expressed as

$$u_i(\mathbf{r},\omega) = \int_{S'} G_{ij}(\mathbf{r},\omega;\mathbf{r}')f_j(\mathbf{r}',\omega)dS' + \int_{S'} G_{iq}(\mathbf{r},\omega;\mathbf{r}')\Gamma(\mathbf{r}',\omega)dS' \qquad (6.3a)$$

$$T_i(\mathbf{r},\omega) = \int_{S'} H_{ij}(\mathbf{r},\omega;\mathbf{r}')f_j(\mathbf{r}',\omega)dS' + \int_{S'} H_{iq}(\mathbf{r},\omega;\mathbf{r}')\Gamma(\mathbf{r}',\omega)dS' \qquad (6.3b)$$

$$p(\mathbf{r},\omega) = \int_{S'} H_{pj}(\mathbf{r},\omega;\mathbf{r}')f_j(\mathbf{r}',\omega)dS' + \int_{S'} H_{pq}(\mathbf{r},\omega;\mathbf{r}')\Gamma(\mathbf{r}',\omega)dS' \qquad (6.3c)$$

$$q_n(\mathbf{r},\omega) = \int_{S'} G_{qj}(\mathbf{r},\omega;\mathbf{r}')f_j(\mathbf{r}',\omega)dS' + \int_{S'} G_{qq}(\mathbf{r},\omega;\mathbf{r}')\Gamma(\mathbf{r}',\omega)dS' \qquad (6.3d)$$

where the quantities $u_i(\mathbf{r},\omega)$, $G_{ij}(\mathbf{r},\omega;\mathbf{r}')$, $f_j(\mathbf{r}',\omega)$, etc. are defined as similar to eqns (6.1) with the understanding that the analysis is performed in the frequency domain.

If the domain Ω is an infinite medium Green's functions corresponding to a full space/plane are obtained from Chapters 2 and 4. On the other hand, for the case where Ω is a semi-infinite medium, Green's functions corresponding to a half-space/plane are used. For layered media, the relevant kernels in eqns (6.2) and (6.3) are obtained from Chapters 3 and 5.

The unknown quantities, $\bar{f}_j(\mathbf{r}', s)$ and $\bar{\Gamma}(\mathbf{r}', s)$ in eqns (6.2) for quasi-static and transient problems and $f_j(\mathbf{r}', \omega)$ and $\Gamma(\mathbf{r}', \omega)$ in eqns (6.3) for time-harmonic problems, are determined by imposing boundary conditions on $\bar{S}$ which are identical to those prescribed on S. Since the nature of integral equations represented by eqns (6.2) and (6.3) are identical, the numerical implementation of eqns (6.2) is presented as an example with understanding that the solution scheme can be readily extended to eqns (6.3). Equation (6.2) represents a set of Fredholm integral equations of the first kind for unknown fields $\bar{f}_j$ and $\bar{\Gamma}$. In view of the complexity of the kernel functions $\bar{G}_{ij}$, $\bar{H}_{ij}$, $\bar{G}_{qj}$, etc. eqns (6.2) can be solved only by applying numerical techniques. The numerical solution is obtained by considering N and N' node points on $\bar{S}$ and S', respectively. Let $\mathbf{F}$ denote a vector whose elements correspond to the unknown quantities (i.e. forces $\bar{f}_j$ and fluid source $\bar{\Gamma}$) at node points on S' and defined in the following form

$$\mathbf{F} =< \mathbf{f}_1 \quad \mathbf{f}_2 \quad \mathbf{f}_3 \quad ... \quad \mathbf{f}_{N'} >^T \tag{6.4a}$$

where

$$\mathbf{f}_i =< \bar{f}_x(\mathbf{r}_i, s)\ \bar{f}_y(\mathbf{r}_i, s)\ \bar{f}_z(\mathbf{r}_i, s)\ \bar{\Gamma}(\mathbf{r}_i, s) >, \qquad i = 1, 2, ..., N' \tag{6.4b}$$

Then, a discrete version of eqns (6.2) with respect to N and N' node points on $\bar{S}$ and S', respectively, can be expressed as

$$\mathbf{QF} = \mathbf{B} \tag{6.5}$$

where the elements of the vector $\mathbf{B}$ correspond to the specified boundary conditions at node points on $\bar{S}$ and the elements of the matrix $\mathbf{Q}$ are expressed in terms of Green's functions. For example, consider the case where displacement $\bar{u}_i(\mathbf{r}, s)$ $(i = x, y, z)$ and fluid discharge $\bar{q}_n(\mathbf{r}, s)$ on the surface $\bar{S}$ are specified as equal to $u_i^*(\mathbf{r}, s)$ $(i = x, y, z)$ and $q_n^*(\mathbf{r}, s)$, respectively. Then,

$$\mathbf{B} =< \mathbf{u}_1 \quad \mathbf{u}_2 \quad \mathbf{u}_3 \quad ... \quad \mathbf{u}_N >^T \tag{6.6a}$$

$$\mathbf{Q} = [\mathbf{G}(\mathbf{r}_i, s; \mathbf{r}'_j)]_{4N \times 4N'}, \qquad i = 1, 2, ..., N;\ j = 1, 2, ..., N' \tag{6.6b}$$

where

$$\mathbf{u}_i =< u_x^*(\mathbf{r}_i, s)\ u_y^*(\mathbf{r}_i, s)\ u_z^*(\mathbf{r}_i, s)\ q_n^*(\mathbf{r}_i, s) >, \qquad i = 1, 2, ..., N \tag{6.7a}$$

$$\mathbf{G}(\mathbf{r}_i, s; \mathbf{r'}_j) = \Delta S'_j \begin{bmatrix} \bar{G}_{xx} & \bar{G}_{xy} & \bar{G}_{xz} & \bar{G}_{xq} \\ \bar{G}_{yx} & \bar{G}_{yy} & \bar{G}_{yz} & \bar{G}_{yq} \\ \bar{G}_{zx} & \bar{G}_{zy} & \bar{G}_{zz} & \bar{G}_{zq} \\ \bar{G}_{qx} & \bar{G}_{qy} & \bar{G}_{qz} & \bar{G}_{qq} \end{bmatrix} \tag{6.7b}$$

and $\Delta S'_j$ denotes the tributary area corresponding to the j-th node point on S'.

In the above formulations, single node boundary elements with a constant value over a tributary area are used. However, there are more advanced elements (e.g. linear or quadratic) which account for variation of Green's functions within the element length thereby reducing the number of nodes required in the discretization and also enhancing the accuracy.

Another example is the case where traction $\bar{T}_i(\mathbf{r}, s)$ $(i = x, y, z)$ and pore pressure $\bar{p}(\mathbf{r}, s)$ on the surface $\bar{S}$ are specified as equal to $T_i^*(\mathbf{r}, s)$ $(i = x, y, z)$ and $p^*(\mathbf{r}, s)$, respectively. Then,

$$\mathbf{B} = < \mathbf{t}_1 \quad \mathbf{t}_2 \quad \mathbf{t}_3 \quad ... \quad \mathbf{t}_N >^T \tag{6.8a}$$

$$\mathbf{Q} = [\mathbf{H}(\mathbf{r}_i, s; \mathbf{r'}_j)]_{4N \times 4N'}, \qquad i = 1, 2, ..., N; \; j = 1, 2, ..., N' \tag{6.8b}$$

where

$$\mathbf{t}_i = < T_x^*(\mathbf{r}_i, s) \; T_y^*(\mathbf{r}_i, s) \; T_z^*(\mathbf{r}_i, s) \; p^*(\mathbf{r}_i, s) >, \qquad i = 1, 2, ..., N \tag{6.9a}$$

$$\mathbf{H}(\mathbf{r}_i, s; \mathbf{r'}_j) = \Delta S'_j \begin{bmatrix} \bar{H}_{xx} & \bar{H}_{xy} & \bar{H}_{xz} & \bar{H}_{xq} \\ \bar{H}_{yx} & \bar{H}_{yy} & \bar{H}_{yz} & \bar{H}_{yq} \\ \bar{H}_{zx} & \bar{H}_{zy} & \bar{H}_{zz} & \bar{H}_{zq} \\ \bar{H}_{px} & \bar{H}_{py} & \bar{H}_{pz} & \bar{H}_{pq} \end{bmatrix} \tag{6.9b}$$

A least square solution of eqn (6.5) yields

$$\mathbf{F} = \left[\mathbf{Q}^T \mathbf{Q}\right]^{-1} \mathbf{Q}^T \mathbf{B} \tag{6.10}$$

Once $\mathbf{F}$ is known, the complete poroelastic fields on the boundary S as well as at points in Ω can be computed directly from eqns (6.2). In a similar manner, the solution for time-harmonic problems can be obtained by using the procedure described in eqns (6.4)-(6.10) with the appropriate forms of $\mathbf{F}$, $\mathbf{B}$ and $\mathbf{Q}$.

In the case of axially symmetric domains, it is natural to employ the cylindrical polar coordinate system (r, θ, z) defined as shown in Fig. 6.3 in the analysis. This

type of problems can be analyzed by applying Fourier expansion with respect to the circumferential coordinate θ to the field variables as shown in Chapter 2. Due to the orthogonality of trigonometric terms, the boundary value problems can be analyzed seperately for each Fourier harmonic. In the case of problems involving an axially symmetric boundary surface $\bar{S}$ and a corresponding source surface S', the integral equation can be expressed in terms of the correponding generating curves $\bar{L}$ and L' in the rz-plane (see Fig. 6.4). For example, the formulations corresponding to the mth Fourier harmonic can be expressed as

$$\bar{u}_{im}(\mathbf{r},s) = \int_{L'} \bar{G}^m_{ij}(\mathbf{r},s;\mathbf{r}')\bar{f}_{jm}(\mathbf{r}',s)r'dL' + \int_{L'} \bar{G}^m_{iq}(\mathbf{r},s;\mathbf{r}')\bar{\Gamma}_m(\mathbf{r}',s)r'dL', \qquad \mathbf{r}\in\bar{L}; \quad i,j=r,\theta,z \quad (6.11a)$$

$$\bar{T}_{im}(\mathbf{r},s) = \int_{L'} \bar{H}^m_{ij}(\mathbf{r},s;\mathbf{r}')\bar{f}_{jm}(\mathbf{r}',s)r'dL' + \int_{L'} \bar{H}^m_{iq}(\mathbf{r},s;\mathbf{r}')\bar{\Gamma}_m(\mathbf{r}',s)r'dL', \qquad \mathbf{r}\in\bar{L}; \quad i,j=r,\theta,z \quad (6.11b)$$

$$\bar{p}_m(\mathbf{r},s) = \int_{L'} \bar{H}^m_{pj}(\mathbf{r},s;\mathbf{r}')\bar{f}_{jm}(\mathbf{r}',s)r'dL' + \int_{L'} \bar{H}^m_{pq}(\mathbf{r},s;\mathbf{r}')\bar{\Gamma}_m(\mathbf{r}',s)r'dL', \qquad \mathbf{r}\in\bar{L}; \quad j=r,\theta,z \quad (6.11c)$$

$$\bar{q}_{nm}(\mathbf{r},s) = \int_{L'} \bar{G}^m_{qj}(\mathbf{r},s;\mathbf{r}')\bar{f}_{jm}(\mathbf{r}',s)r'dL' + \int_{L'} \bar{G}^m_{qq}(\mathbf{r},s;\mathbf{r}')\bar{\Gamma}_m(\mathbf{r}',s)r'dL', \qquad \mathbf{r}\in\bar{L}; \quad j=r,\theta,z \quad (6.11d)$$

In the above equations, a subscript m is used to identify the mth Fourier harmonic of displacements, tractions, pore pressure and fluid discharge. A superscript m is used in the Green's functions to imply that the circumferential dependence of loadings and fluid sources used in the derivation of Green's functions is given by either $\cos m\theta$ or $\sin m\theta$ type variation. In addition, Green's functions in eqns (6.11) correspond to forces and a fluid source applied over a circular ring of radius r' (Fig. 6.4). It is noted that when both geometry and loadings are axially symmetric the corresponding solutions can be obtained by considering eqns (6.11) with only $m = 0$.

6.3 Numerical Solutions

6.3.1 Numerical Scheme

In this section, the development of computer codes based on the indirect boundary element algorithms outlined in Section 6.2 is considered. The numerical evaluation of Green's functions (i.e. matrix $\mathbf{Q}$) is already discussed in Section 2.5.1 for three-dimensional quasi-static problems and Section 4.5.1 for two-dimensional dynamic (time-harmonic and transient) problems, respectively. Since the analysis is conducted in the Laplace domain for quasi-static and transient problems and the integral equations are solved numerically, Laplace inversion schemes proposed by Schapery [eqn (2.39)] and Stehfest [eqns (2.38)] are used to obtain time-domain solutions. In addition, single node boundary elements based on an average value of a nodal quantity over a tributary area is used in all numerical examples. In ensuing sections, the accuracy and applicability of the present boundary element scheme are demonstrated by considering a set of boundary value problems for which analytical solutions are available.

6.3.2 Numerical Verification of Boundary Element Scheme

6.3.2.1 Spherical Cavity under Quasi-Static Loadings

The convergence, stability and accuracy of the numerical solutions obtained from the present scheme are established by considering the problem of a permeable spherical cavity of radius a in an infinite poroelastic medium under uniform normal traction $f_0H(t)$ applied at the cavity wall [Fig. 6.5(a)] where $H(t)$ denotes a unit step function. This problem is axially symmetric with respect to geometry and loading and the response is a function of only spherical coordinate R (see Fig. 6.3). The solution corresponding to this problem can be obtained analytically and it is found to be identical to the ideal elastic solution. This implies that no excess pore pressure is developed in the medium.

The Green's functions required in the analysis of the spherical cavity problem correspond to impulsive ring loads and fluid source applied in a poroelastic full space and are obtained by multiplying full space Green's functions (without inertia

effects) given in Section 2.4 corresponding to $m = 0$ by a factor "s". These Green's functions are expressed in terms of Lipschitz-Hankel type semi-infinite integrals involving products of Bessel functions and their numerical evaluation is discussed in Section 2.5.1. The numerical Laplace inversion formula proposed by Schapery [eqn (2.39)] is employed in this case to obtain the time-domain solutions for quasi-static problems due to the fact that it requires less computational effort than Stehfest scheme [eqns (2.38)]. Comparison of boundary element solutions for quasi-static problems based on both Laplace inversion schemes indicates negligible difference between the two solutions.

A discretization as shown in Fig. 6.4 is used to obtain the boundary element solutions from eqn (6.11). The influence of the number of nodes N and N' used to discretize the generating curves $\bar{L}$ and L' and the location of source curve L' with respect to $\bar{L}$ denoted by Δa are examined by evaluating the displacement u_R at the cavity wall with the analytical solution given by Saada (1974) for a spherical cavity in an ideal elastic medium. Table 6.1 shows the nondimensional displacement $2\mu u_R/f_0 a$ at the cavity surface for different values of $N, N', \Delta a$ and t^*. A nondimensional time $t^* = ct/a^2$, in which c is the generalized consolidation coefficient defined in eqn (2.5c), is used in Table 6.1 and hereafter in the discussion of quasi-static solutions. Comparison of numerical solutions presented in Table 6.1 with the corresponding nondimensional analytical solution of 0.5 (Saada, 1974) indicates that the present solutions show good convergence and stable behaviour. The maximum error is about two percent and the boundary element solutions also confirm the absence of a consolidation process in this case.

The case of a spherical cavity of radius a in an infinite poroelastic medium subjected to fluid pressure $p_0 H(t)$ applied at the cavity wall [Fig. 6.5(b)] is considered next. In this case, the response is time dependent and the displacement at the cavity surface is zero. Two boundary element meshes for different values of N and N', i.e. $N = 16, N' = 8$ and $N = 20, N' = 10$, respectively, with $\Delta a = 0.15$ (see Fig. 6.4) are used in the numerical evaluation of displacement u_R and pore pressure p in a poroelastic medium ($\nu = 0.2, \nu_u = 0.33$ and $B = 0.62$). Figures 6.6(a) and 6.6(b) show comparisons between analytical solution and boundary element solutions for displacement $2\mu u_R/p_0 a$ and pore pressure p/p_0 respectively, at spherical surfaces

of radius $R/a = 1.5$ and 3.0 inside the medium. The solutions presented in Figs. 6.6(a) and 6.6(b) indicate that the indirect boundary element scheme proposed in this study results in numerically stable and accurate solutions. A small discrepancy between the analytical and boundary element solutions for pore pressure is observed at early times ($t^* < 1.0$). This could be due to the numerical nature of the Laplace inversion which involves the computation of very rapidly decaying integrals for small values of t^* (i.e. large values of s).

6.3.2.2 Axial Stiffness of Rigid Anchors

A class of displacement boundary value problems with a fully impermeable surface [eqns (6.8)] is studied next. First, an impermeable rigid sphere of radius a embedded in a poroelastic medium subjected to a vertical point load F_0 [Fig. 6.7(a)] is considered. An exact analytical solution for this problem is available (De jong, 1957) for a poroelastic material with incompressible constituents ($\nu_u = 0.5, B = 1.0$). Tables 6.2 and 6.3 show comparisons of time histories of vertical displacements between analytical solutions and boundary element solutions for different values of N, N', and Δa, respectively. The two sets of solutions are in excellent agreement and the maximum difference is about two percent. In addition, the variation of numerical solutions for different values of N, N', and Δa in Tables 6.2 and 6.3, respectively, is less than two percent. The numerical convergence and stability of the present scheme for quasi-static problems are clearly established by the solutions presented in Tables 6.1-6.3 and Figs. 6.6.

To demonstrate the applicability of the boundary element code for analysis of more complicated problems, the case of an impermeable rigid spheroidal anchor in a poroelastic medium [Fig. 6.7(b)] is considered next. An exact analytical solution given by Selvadurai (1976) for an anchor in an ideal elastic medium is compared with the final solutions ($t \rightarrow \infty$) obtained from the present scheme for different values of N, N' and Δa in Tables 6.4 and 6.5, respectively. The accuracy of present solutions are once again confirmed through these comparisons.

Figure 6.8 shows time histories of vertical displacement $2\mu a_v u_z/F_0$ of a vertically loaded rigid sphere ($a_v/a_h = 1.0$), an oblate ($a_v/a_h = 0.5$) and a prolate

spheroid ($a_v/a_h = 2.0$ and 3.0) embedded in a poroelastic medium. Three different poroelastic materials, namely, a material with incompressible constituents, Ruhr Sandstone and Westerly Granite, are considered in the numerical study. The properties of these materials are given in Section 2.5.2. The solutions presented in Figs. 6.8(a) and 6.8(b) for vertical displacement of an anchor show similar behaviour to those shown in Figure 2.3 for the case of a buried vertical patch load in a poroelastic half-space, i.e. the initial displacements are governed by the undrained Poisson's ratio (ν_u) whereas the final response depends only on the drained Poisson's ratio (ν). Therefore, an anchor in a poroelastic medium with incompressible constituents has the lowest initial solution followed by anchors in Westerly Granite and Ruhr Sandstone, respectively. The nondimensional final displacements of anchors in a material with incompressible constituents and Westerly granite are identical due to identical drained Poisson's ratio of these materials. The numerical results indicate that the vertical displacement of an anchor increases slowly when $0 < t^* < 0.1$ and more rapidly during the period $0.1 < t^* < 100$ reaching their final values when $t^* > 1000$ for all spheroidal anchors. It is also noted that the difference between the initial and final displacements of an anchor is less than fifteen, ten and five percent of final displacements for anchors in a material with incompressible constituents, Ruhr Sandstone and Westerly Granite, respectively.

6.3.2.3 Cylindrical Cavity under Time-Harmonic Loading

The accuracy of the present boundary element scheme for time-harmonic problems is investigated in this section. A plane strain traction boundary value problem involving a fully permeable cylindrical cavity of radius a in a poroelastic infinite space subjected to time-harmonic radial traction of uniform intensity f_0 is considered (Fig. 6.9). The analytical solutions in the frequency domain for radial displacement u_r, hoop stress $\sigma_{\theta\theta}$ and pore pressure p can be expressed as

$$\frac{\mu u_r(r)}{f_0 a} = \frac{L_1 K_1(L_1 r) + L_2 \Phi K_1(L_2 r)}{\beta_1 L_1^2 + \beta_2 L_2^2 \Phi} \tag{6.12a}$$

$$\begin{aligned}\frac{\sigma_{\theta\theta}(r)}{f_0} =& \frac{1}{\beta_1 L_1^2 + \beta_2 L_2^2 \Phi}[L_1^2 K_2(L_1 r) + L_2^2 \Phi K_2(L_2 r) - \{1 + \lambda^* + \alpha M^*(\alpha + \chi_1)\} \\ & \times L_1^2 K_0(L_1 r) - \{1 + \lambda^* + \alpha M^*(\alpha + \chi_2)\} L_2^2 \Phi K_0(L_2 r)]\end{aligned} \tag{6.12b}$$

$$\frac{p(r)}{f_0} = -(\alpha+\chi_1)M^*L_1^2K_0(L_1r) - (\alpha+\chi_2)M^*L_2^2\Phi K_0(L_2r) \qquad (6.12c)$$

where

$$\beta_i = [1+\lambda^*+\alpha M^*(\alpha+\chi_i)]K_0(L_i) + K_2(L_i), \quad i=1,2 \qquad (6.13a)$$

$$\Phi = -\frac{(\alpha+\chi_1)L_1^2K_0(L_1)}{(\alpha+\chi_2)L_2^2K_0(L_2)} \qquad (6.13b)$$

The nondimensional parameters $\lambda^*, \alpha, M^*, L_i$ and χ_i $(i=1,2)$ are defined in Section 4.2 and K_m is the modified Bessel function of the second kind of order m (Watson, 1944).

Figure 6.10 shows the discretization used in boundary element analysis of two-dimensional cavity expansion problems. The number of nodes on the curves $\bar{S}$ and S' are N and N', respectively, and the distance between the two curves is denoted by Δa. It should be noted that in the analysis of circular cavity problem one can use symmetry conditions and consider only one-quarter of the cavity wall. This results in a much smaller matrix $\mathbf{Q}$ since only one-fourth of the node points shown in Fig. 6.10 is required in the discretization. In the present study, the symmetric conditions are not considered in order to check the numerical stability of large size $\mathbf{Q}$ matrices encountered in the solution of more complicated problems and to check the overall accuracy in the numerical evaluation of Green's functions. The Green's functions required in this case are given in Section 4.3 and correspond to time-harmonic concentrated loads and fluid source applied in a poroelastic full plane. These Green's functions appear in terms of semi-infinite Fourier integrals and their numerical evaluation is discussed in Section 4.5.1. Closed form Green's functions for this problem are also obtainable by using the analogy between thermoelasticity and poroelasticity in the frequency domain (Bonnet, 1987 and Cheng *et al.*, 1991). However, closed form Green's functions are not available for semi-infinite and multi-layered poroelastic media. Therefore, it is useful to apply Green's functions in the integral form to examine the accuracy and numerical stability of the present solution scheme.

A poroelastic medium with $\lambda^* = 1.0, \alpha = 0.95, M^* = 15, \rho^* = 0.5, m^* = 1.2$ and $b^* = 5.0$ is considered in the numerical study. A nondimensional frequency, δ,

as defined by eqn (4.9b) is also used. In addition, $N = 42, N' = 24$ and $\Delta a = 0.3$ are used in the boundary discretization (see Fig. 6.10). Figure 6.11 presents comparison between solutions for radial displacement and hoop stress at the cavity surface ($r = a$) obtained from the present study with the analytical solutions given in eqns (6.12). It is evident from Figs. 6.11(a) and 6.11(b) that the present scheme yields accurate numerical solutions with less than one percent error for both real and imaginary parts. Numerical results also indicate that the radial symmetry is satisfied at all node points with one percent accuracy. Since such high accuracy exists in the solutions obtained from the present scheme using Green's functions expressed in the integral form, it should be also possible to obtain accurate boundary element solutions for time-harmonic problems involving semi-infinite and layered poroelastic media by using Green's functions presented in Chapters 4 and 5, respectively.

6.3.2.4 Impedances of Rigid Semi-Circular Tunnel

The applicability of the present scheme for practical problems is demonstrated by investigating the dynamic response of a massless semi-circular tunnel with a rigid wall in a poroelastic medium under time-harmonic loadings (Fig. 6.12). It is assumed that the tunnel wall is fully impermeable and perfectly bonded to the surrounding medium along the contact surface S. The tunnel is subjected to time-harmonic vertical, horizontal and moment loadings $V_0 e^{i\omega t}$, $H_0 e^{i\omega t}$ and $M_0 e^{i\omega t}$, per unit length respectively. The displacements of the tunnel, under the applied loadings, can be expressed in terms of vertical displacement $\triangle_V e^{i\omega t}$, horizontal displacement $\triangle_H e^{i\omega t}$ and rotation $\phi_0 e^{i\omega t}$ about the y-axis of a point O $(x = 0, z = 0)$ as shown in Fig 6.12.

The displacement at a point (x, z) on the contact surface S can be expressed in terms of $\triangle_V, \triangle_H$ and ϕ_0 as

$$u_x(x, z) = \triangle_H - z\phi_0 \tag{6.14a}$$

$$u_z(x, z) = \triangle_V + x\phi_0 \tag{6.14b}$$

The resultant forces and moment acting on the massless tunnel can be expressed in terms of traction components $T_i(x, z)$ $(i = x, z)$ as

$$V_0 = \int_S T_z dS \tag{6.15a}$$

$$H_0 = \int_S T_x dS \tag{6.15b}$$

$$M_0 = \int_S (T_x z - T_z x) dS \tag{6.15c}$$

Figure 6.13 shows the discretization used in the boundary element analysis for this problem. A solution for unknown quantities (i.e. forces f_j and fluid source Γ) at node points on S' can be obtained in terms of $\triangle_V, \triangle_H$ and ϕ_0 by using eqn (6.10) with $\mathbf{B}$ and $\mathbf{Q}$ being defined in the forms of eqns (6.6a) and (6.6b), respectively. Thereafter, solutions for nodal tractions are expressed in terms of $\triangle_V, \triangle_H$ and ϕ_0 from eqn (6.3b). Substitution of the solutions for nodal tractions in a discrete version of eqns (6.15) written with respect to node points on S yields a relationship between applied forces and displacements $\triangle_V, \triangle_H$ and ϕ_0.

The response of a rigid semi-circular tunnel is characterized by the following nondimensional impedance matrix

$$\begin{Bmatrix} V_0 \\ H_0 \\ M_0 \end{Bmatrix} = \pi\mu \begin{bmatrix} K_V & 0 & 0 \\ 0 & K_H & K_{HM} \\ 0 & K_{MH} & K_M \end{bmatrix} \begin{Bmatrix} \triangle_V \\ \triangle_H \\ a\phi_0 \end{Bmatrix} \tag{6.16}$$

where $K_V, K_H, K_{HM}(= K_{MH})$ and K_M are the vertical, horizontal, coupled and rocking impedances, respectively, and a is the radius of a semi-circular tunnel.

Figure 6.14 shows the vertical, horizontal, coupled and rocking impedances of a rigid massless semi-circular tunnel of radius a in different poroelastic media. Solutions are presented for the nondimensional frequency range $0.1 \leq \delta \leq 2.0$, where δ is defined in eqn (4.9b), since the displacements are arbitrary for $\delta = 0$. Three poroelastic materials identified as materials A, B and a dry elastic material (an ideal elastic material) are considered in the numerical study. The properties of these materials are identical to that given in Section 6.3.2.3 except that $b^* = 0$ and 5.0 for materials A and B, respectively. In addition, only the nondimensional Lamé constant λ^* is required in the case of a dry material. A discretization represented by $N = 36, N' = 24$ and $\Delta a = 0.1$ is used in the boundary element analysis (see Fig. 6.13). Comparison of numerical solutions presented in Fig. 6.14 indicates that both real and imaginary parts of impedances of a tunnel in material B are larger than those in material A. This implies that the presence of finite internal friction

makes a medium more stiff and damp since material A has zero internal friction ($b^* = 0$) whereas $b^* = 5$ for material B. The influence of b is more pronounced when $0.5 < \delta < 2.0$. The real part of K_V, K_H and K_{HM} of a tunnel in material A ($b^* = 0$) increases in the range $0.1 < \delta < 0.5$ and thereafter decrease sgradually with increasing δ whereas, for tunnels in poroelastic material B and in a dry material, the real part of these impedances shows less dependence on the frequency in the range $0.1 \leq \delta \leq 2.0$. The real part of the rocking impedance K_M is found to decrease gradually with the frequency for all tunnels. Numerical results presented in Fig. 6.14 also indicate that the highest radiation damping occurs in a tunnel in material B when $0.1 \leq \delta \leq 2.0$ due to the fact that the maximum value of the imaginary part of the impedances is found in this case. The imaginary part of the impedances for all tunnels shows nearly linear variation with the frequency and remains positive throughout the frequency range $0.1 \leq \delta \leq 2.0$.

6.3.2.5 Cylindrical Cavity under Transient Loadings

The application of the present boundary element scheme to transient problems is considered in this section. To the best of author's knowledge, a numerical implementation of boundary integral equation methods for transient elastodynamic problems together with numerical examples has not been reported in the literature. A two-dimensional cavity expansion problem due to radial traction $f_0\phi(\tau)$ (Fig. 6.15) is considered to verify the accuracy of the present scheme for transient problems. A nondimensional time $\tau = (t/a)\sqrt{\mu/\rho}$ is used in the transient solutions and two different types of time histories for $\phi(\tau)$, i.e. a gradually applied step pulse [Fig. 6.16(a)] and a triangular pulse [Fig. 6.16(b)] are considered in the numerical study. The analytical solution given by Senjuntichai and Rajapakse (1993) is used in the comparison with boundary element solutions.

The boundary discretization used in this problem is shown in Fig. 6.10. Once again, the complete geometry was considered in the numerical analysis. The transient Green's functions required in this problem correspond to the case where impulsive loads and fluid source are applied in a poroelastic full plane. Exact closed form Green's functions in this case can not be obtained by using the analogy between

thermoelasticity and poroelasticity as in the case of time-harmonic problems. However, it is possible to obtain transient Green's functions in closed form (Wiebe and Antes, 1991) when the internal friction between the solid skeleton and the pore fluid is neglected (i.e. $b = 0$). In this study, the internal friction is taken into account ($b \neq 0$) and the corresponding Green's functions in the Laplace domain are given in Section 4.3. These Green's functions are presented in terms of semi-infinite Fourier integrals and the numerical evaluation of the integrals is discussed in Section 4.5.1. Since the present analysis is conducted in the Laplace domain for transient problems, a numerical Laplace inversion formula is used to obtain time-domain solutions. The numerical inversion of Laplace transform for transient problems requires more computational effort when compared to the case of quasi-static problems. Simple scheme such as Schapery's scheme cannot be used for transient dynamic problems. Therefore, the Laplace inversion formula proposed by Stehfest [eqns (2.38)] is employed in this case. The main advantage of Stehfest's scheme when compared to other schemes (e.g. Hosono, 1979) is that it involves sampling of the Laplace transform solutions only at real values of the transform parameter.

Figures 6.17(a) and 6.17(b) present comparisons of time histories of radial displacement and hoop stress at the cavity surface obtained from the boundary element scheme and the analytical solution (Senjuntichai and Rajapakse, 1993). The boundary element solutions are obtained from a discretization with $N = 48, N' = 28$ and $\Delta a = 0.3$ (see Fig. 6.10). A poroelastic material with properties $\lambda^* = 2.0, \alpha = 0.98, M^* = 20, \rho^* = 0.5, m^* = 1.25$ and $b^* = 10$ is considered in the numerical study. In addition, the eqns (2.38) with $L = 10$ is used to obtain time-domain solutions. Comparison of solutions presented in Figs. 6.14(a) and 6.14(b) clearly shows the high accuracy of the transient solutions obtained from the present boundary element scheme. Numerical results for displacement and hoop stress under the two loading cases indicate that the analytical and boundary element solutions agree very well in both ascending and descending parts of the response. Furthermore, the radial symmetry is satisfied at all node points within a two percent error.

6.4 Conclusions

Following the concepts of Ohsaki (1973) for ideal elastic media, an accurate

indirect boundary integral formulation is presented to analyze quasi-static, time-harmonic and transient boundary value problems related to semi-infinite and infinite poroelastic media. The kernel functions of the integral equations are non-singular and correspond to Green's functions derived explicitly in Chapter 2 for quasi-static problems and Chapter 4 for time-harmonic and transient problems, respectively. In the case of layered poroelastic media, the relevant kernel functions are directly obtained from Chapters 3 and 5. Single node boundary elements with a uniform distribution over a tributary area are found to yield accurate solutions. It is also found that accurate time-domain solutions can be obtained by applying Laplace inversion schemes proposed by Schapery (1962) and Stehfest (1970) for quasi-static and transient problems, respectively. The numerical examples have demonstrated the high accuracy and numerical stability of the present scheme in analyzing a variety of problems involving poroelastic media by using Green's functions expressed in the integral forms. In the case of semi-infinite and layered media, the relevant Green's functions are always expressed in the integral forms. In view of the high accuracy obtained from the present scheme by using infinite space Green's functions in the integral forms, it can be concluded that the Green's functions presented in Chapters 3 and 5 can be effectively used in the present boundary element scheme to analyze complicated boundary value problems involving layered poroelastic half-spaces.

Table 6.1: Convergence of displacement $2\mu u_R/f_0 a$ of a pressurized spherical cavity in an infinite poroelastic medium with N, N', Δa and t^*

(N, N')	$t^* = 0.01$			$t^* = 100$		
	$\Delta a = 0.2$	$\Delta a = 0.25$	$\Delta a = 0.3$	$\Delta a = 0.2$	$\Delta a = 0.25$	$\Delta a = 0.3$
16,8	0.488	0.490	0.496	0.490	0.492	0.498
18,10	0.490	0.492	0.497	0.496	0.498	0.499
20,10	0.497	0.495	0.498	0.499	0.499	0.500
20,12	0.498	0.499	0.499	0.499	0.500	0.500
24,12	0.499	0.499	0.500	0.499	0.500	0.500

Table 6.2: Convergence and comparison of vertical displacement of a rigid spherical anchor in an infinite poroelastic medium with N and N' ($\Delta a = 0.15, \nu = 0.25, \nu_u = 0.5$ and $B = 1.0$)

t^* (ct/a^2)	$2\mu a u_z/F_0$					
	Analytical Solution†	Present Study with different (N, N')				
		(20,12)	(24,12)	(24,14)	(28,14)	(28,16)
0.001	0.106	0.106	0.105	0.106	0.106	0.106
0.1	0.108	0.109	0.109	0.109	0.109	0.109
10.0	0.121	0.120	0.120	0.120	0.120	0.120
1000	0.123	0.123	0.123	0.124	0.123	0.124
∞	0.124	0.124	0.123	0.124	0.124	0.124

† De jong (1957).

Table 6.3: Convergence of vertical displacement of a rigid spherical anchor in an infinite poroelastic medium with Δa ($N = 20$ and $N' = 12$)

t^* (ct/a^2)	$2\mu a u_z/F_0$			
	$\Delta a = 0.08$	$\Delta a = 0.1$	$\Delta a = 0.15$	$\Delta a = 0.2$
0.001	0.108	0.107	0.106	0.105
0.1	0.110	0.109	0.109	0.109
10.0	0.121	0.120	0.120	0.120
1000	0.124	0.124	0.123	0.123
∞	0.124	0.124	0.124	0.124

Table 6.4: Convergence and comparison of vertical displacement of rigid spheroidal anchors in an ideal elastic medium with N and N' ($\Delta a = 0.1$ and $\nu = 0.25$)

a_v/a_h	$2\mu a_v u_z/F_0$				
	Analytical Solution‡	Present Study with different (N, N')			
		(18,10)	(20,10)	(20,12)	(24,14)
0.5	0.142	0.141	0.143	0.143	0.145
1.5	0.165	0.162	0.167	0.163	0.163
2.0	0.198	0.197	0.201	0.193	0.196
3.0	0.250	0.258	0.253	0.254	0.254

‡ Selvadurai (1976).

Table 6.5: Convergence of vertical displacement of rigid spheroidal anchors in an ideal elastic medium with Δa ($N = 20$ and $N' = 12$)

a_v/a_h	$2\mu a_v u_z/F_0$			
	$\Delta a = 0.08$	$\Delta a = 0.1$	$\Delta a = 0.15$	$\Delta a = 0.2$
0.5	0.145	0.143	0.149	0.150
1.5	0.164	0.163	0.163	0.164
2.0	0.193	0.193	0.197	0.196
3.0	0.249	0.254	0.249	0.243

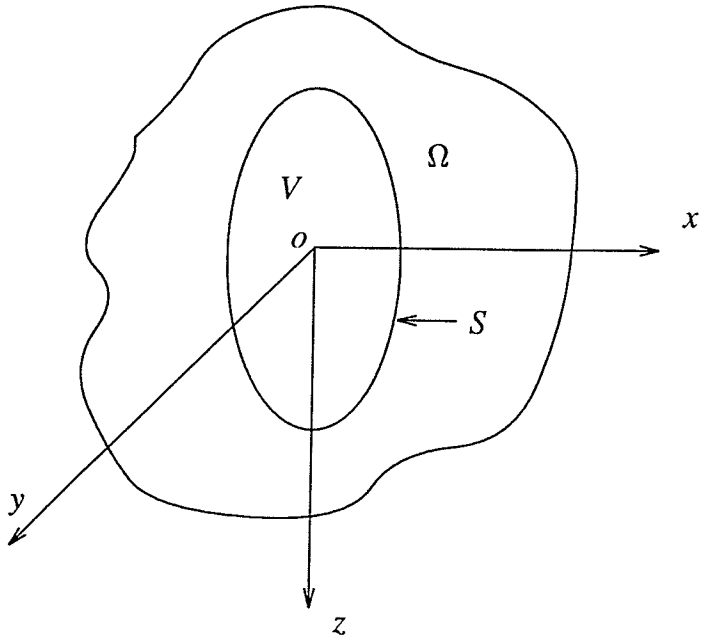

Figure 6.1 Domain and surface related to boundary value problems

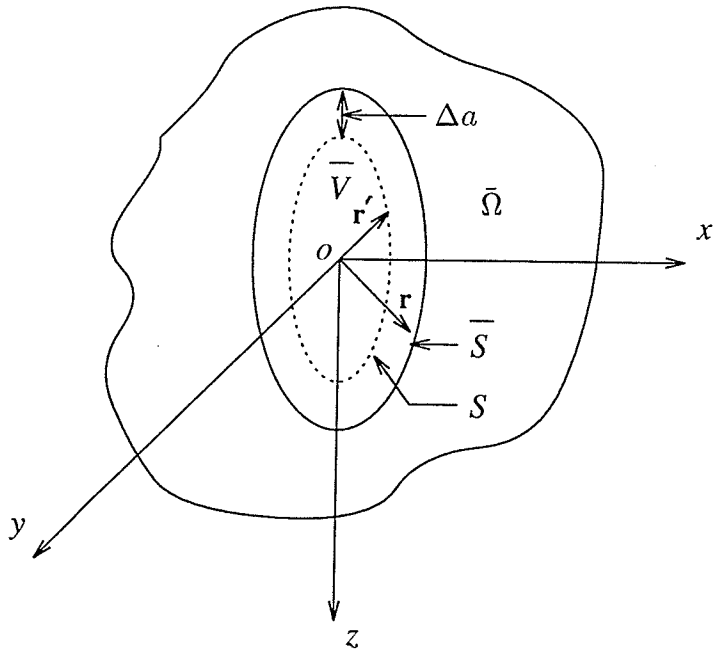

Figure 6.2 Equivalent domain considered in the indirect boundary integral equation method

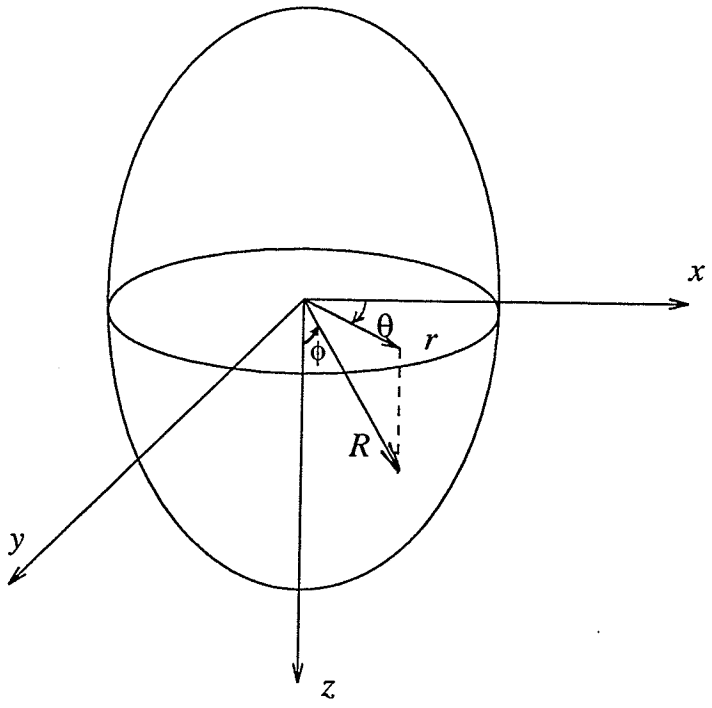

Figure 6.3 Axially symmetric domain with different coordinate systems

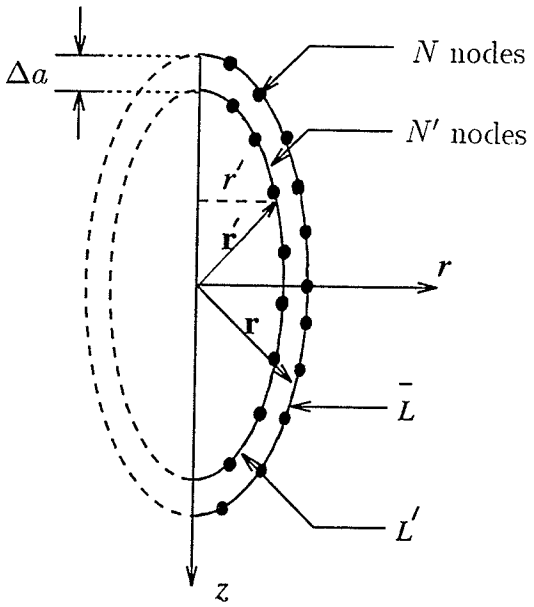

Figure 6.4 Generating curves $\bar{L}$ and L' with discretization considered in axially symmetric problems

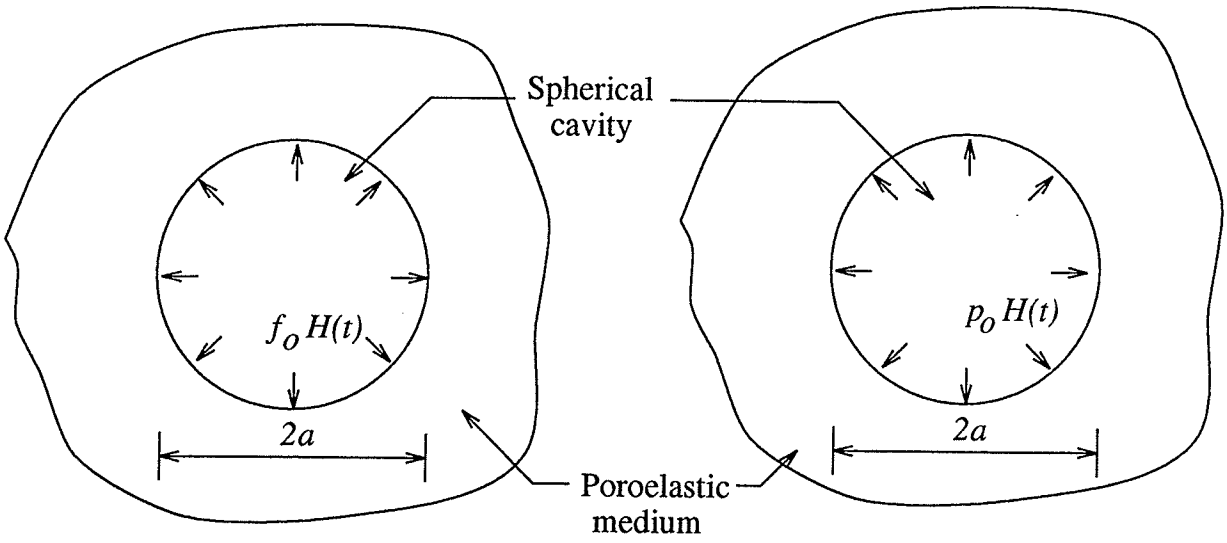

(a) Applied radial traction

(b) Applied fluid pressure

Figure 6.5 Three-dimensional cavity problems considered in the numerical study

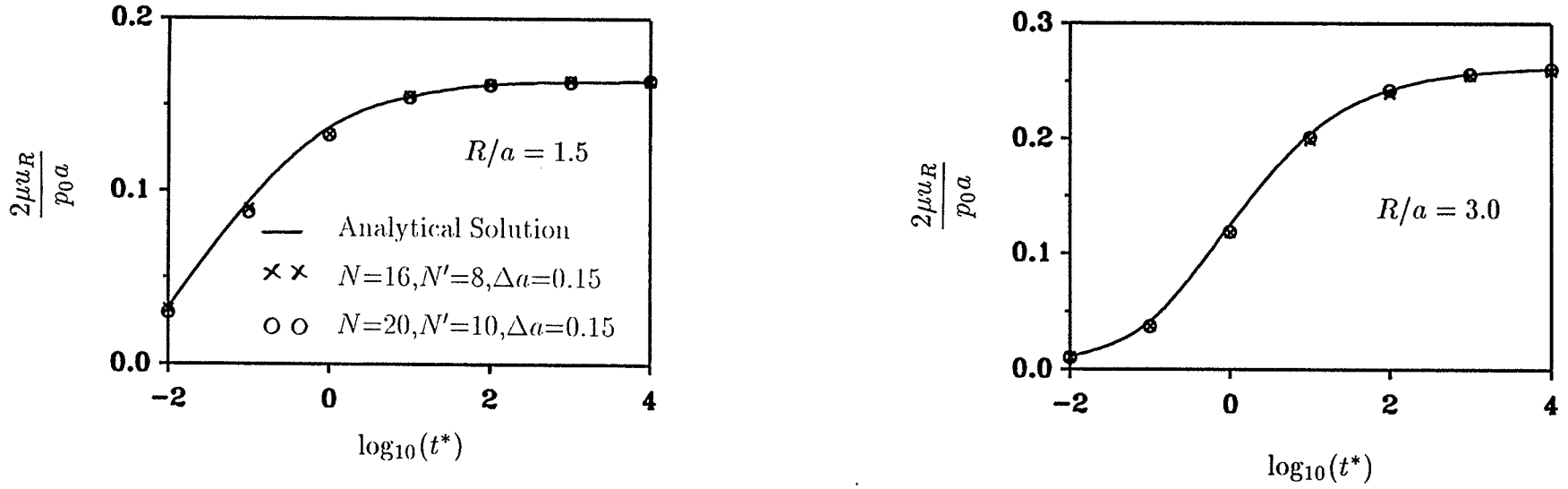

(a)

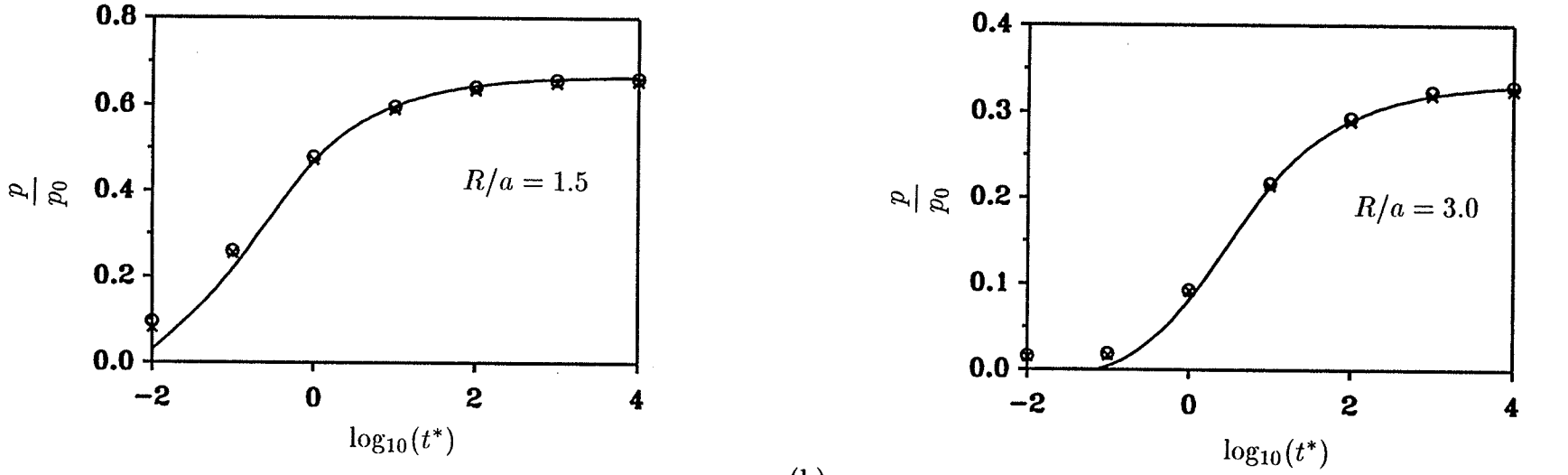

(b)

Figure 6.6 Comparison of displacement and pore pressure histories for a spherical cavity subjected to fluid pressure

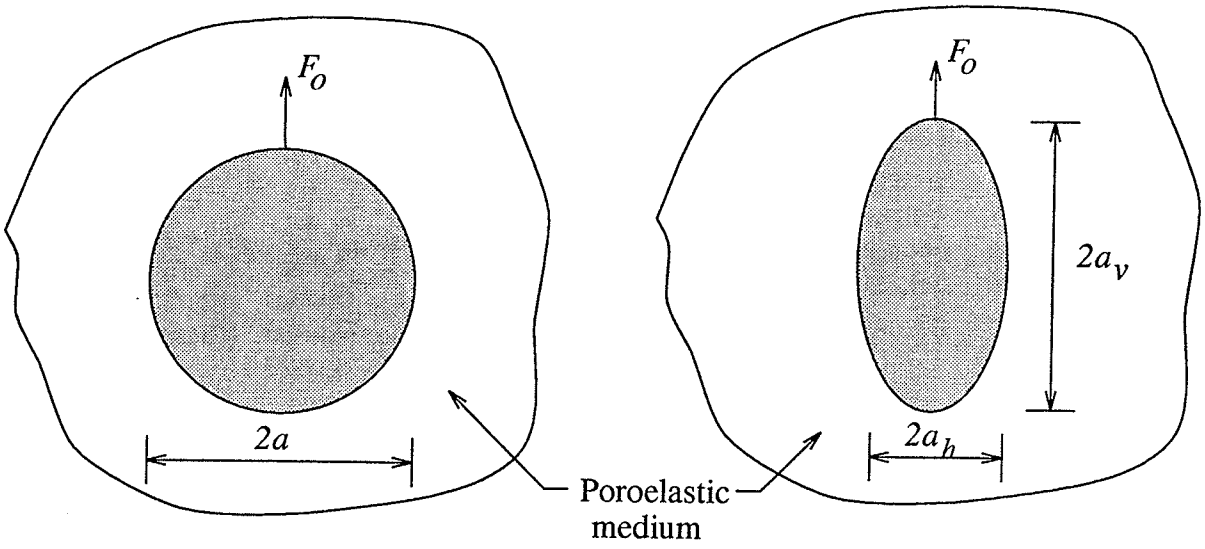

(a) Spherical anchor

(b) Spheroidal anchor

Figure 6.7 Axially loaded rigid anchors with different geometries considered in the numerical study

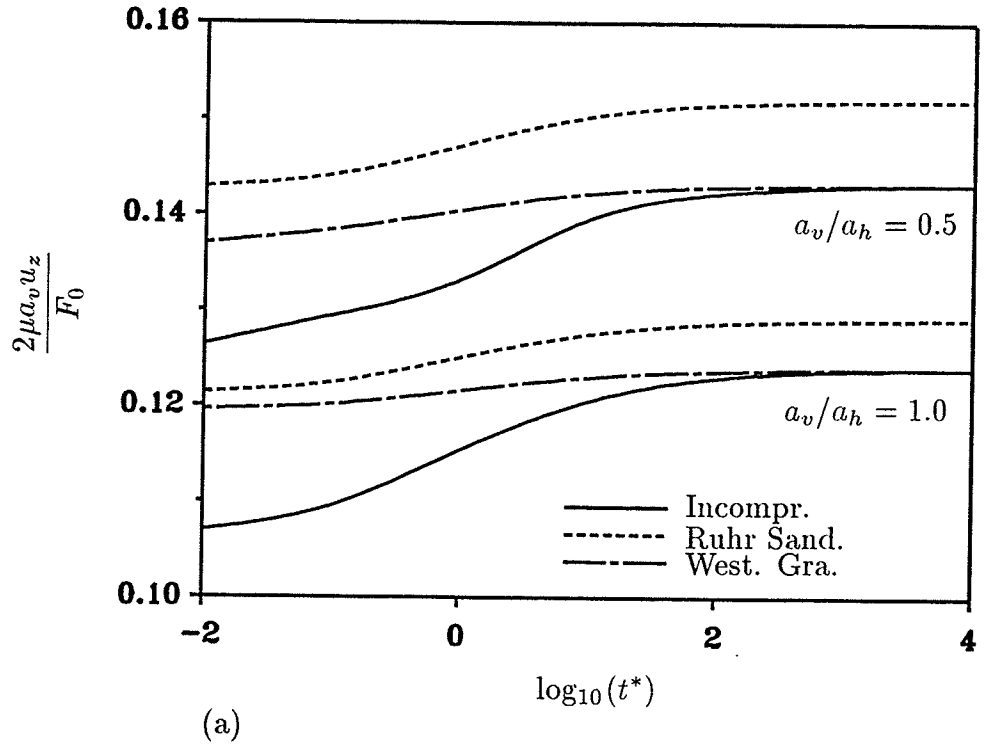

(a)

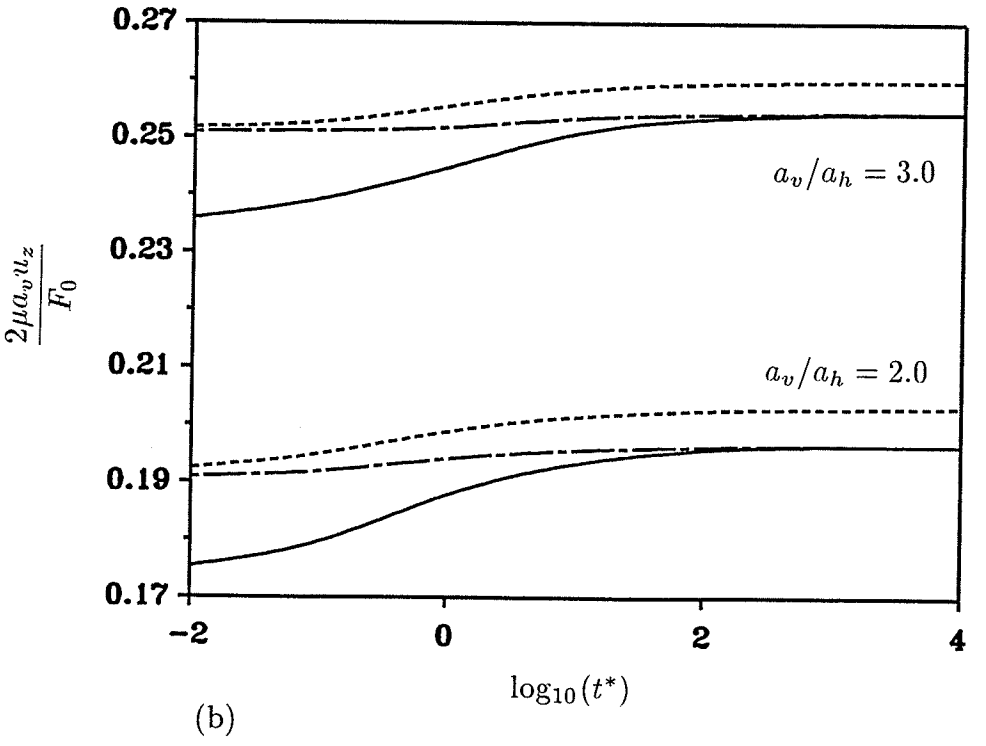

(b)

Figure 6.8 Time histories of vertical displacement of spheroidal anchors in poroelastic media

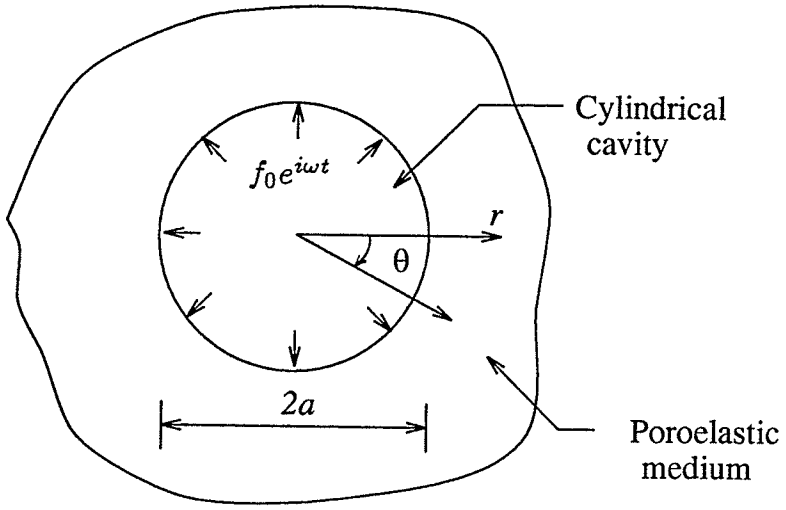

Figure 6.9 Two-dimensional cavity expansion problems under time-harmonic loading

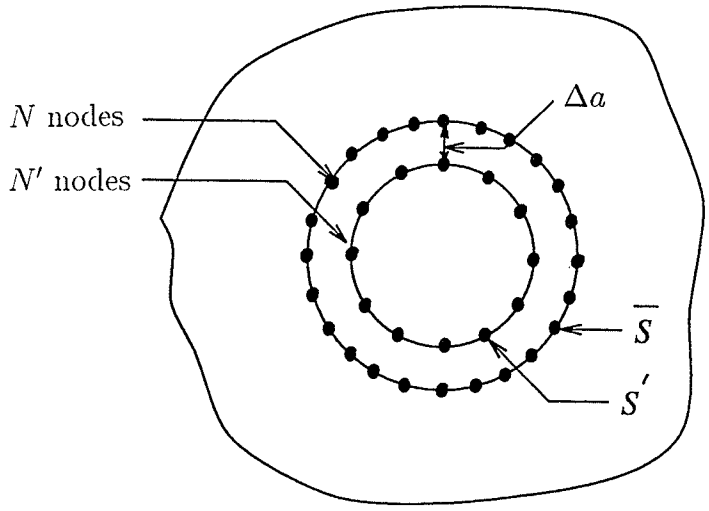

Figure 6.10 Boundary discretization for two-dimensional cavity expansion problems

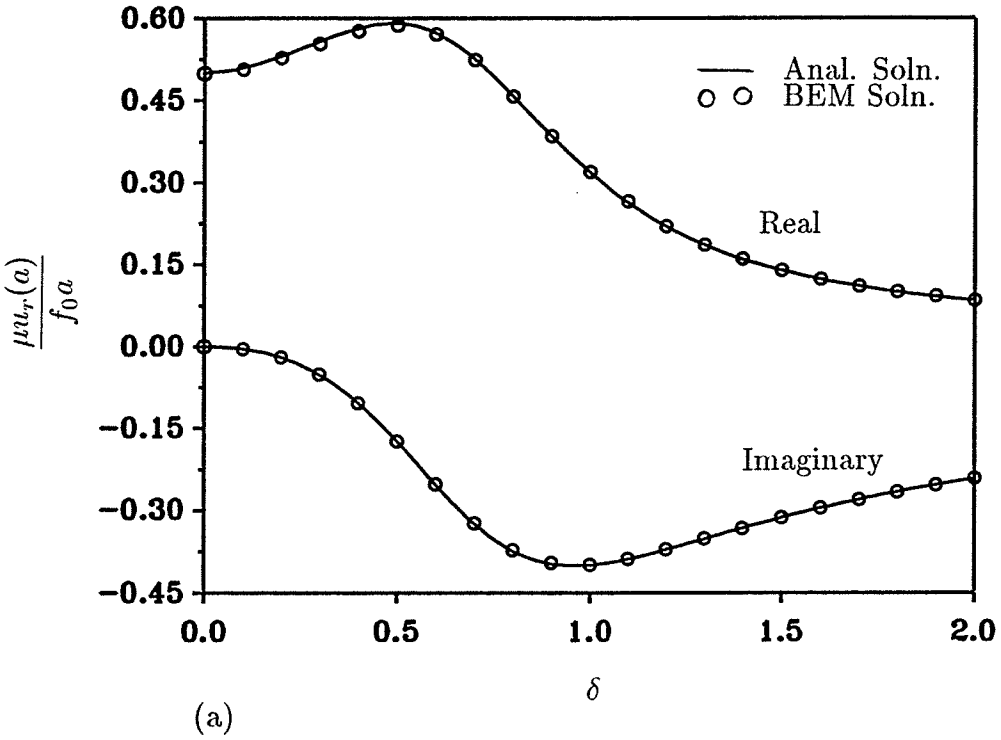

(a)

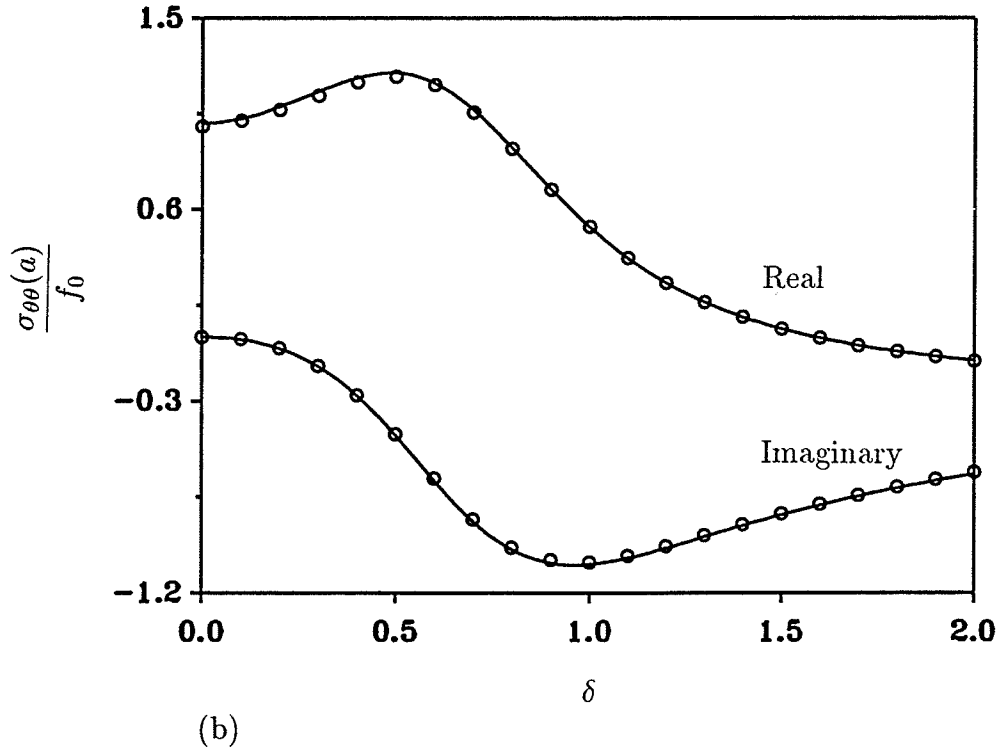

(b)

Figure 6.11 Comparison of radial displacement and hoop stress of a cylindrical cavity under time-harmonic loading

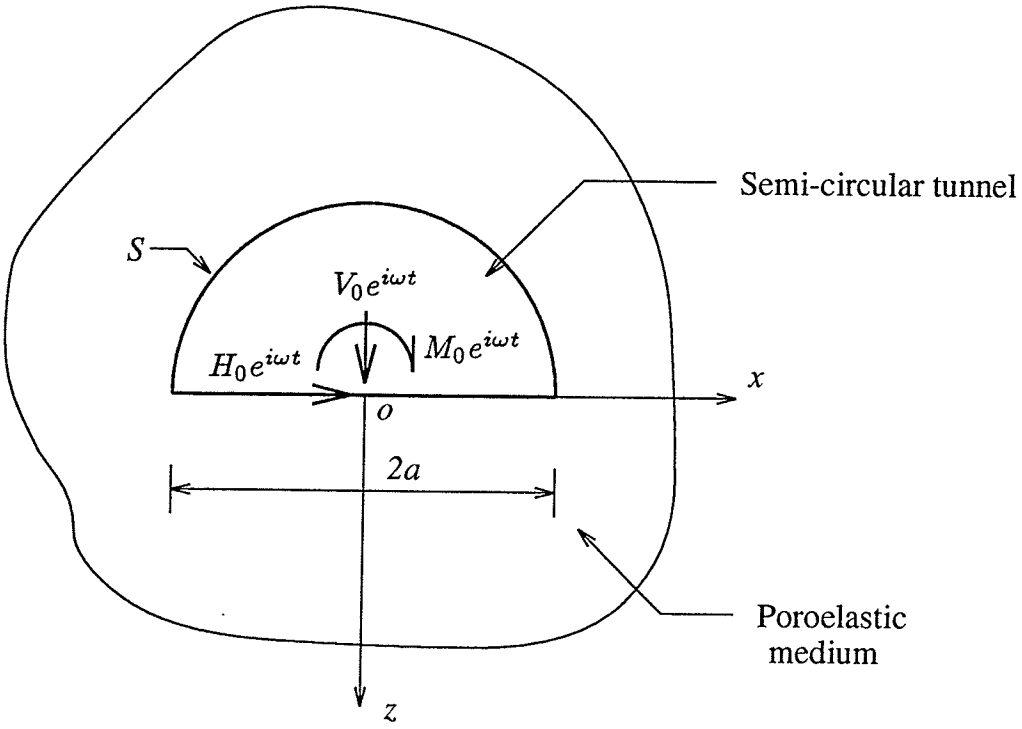

Figure 6.12 Semi-circular tunnel with a rigid wall under time-harmonic loadings

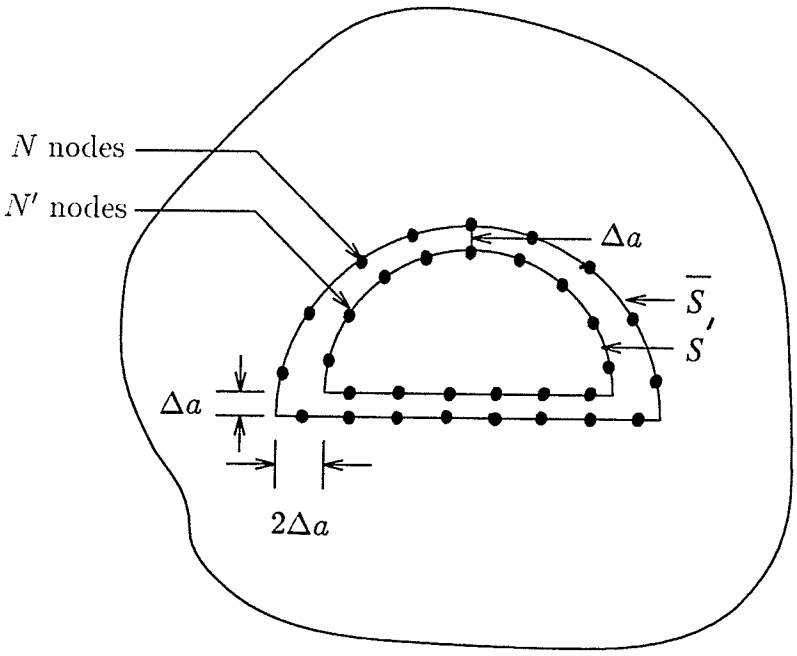

Figure 6.13 Boundary discretization for rigid semi-circular tunnel problem

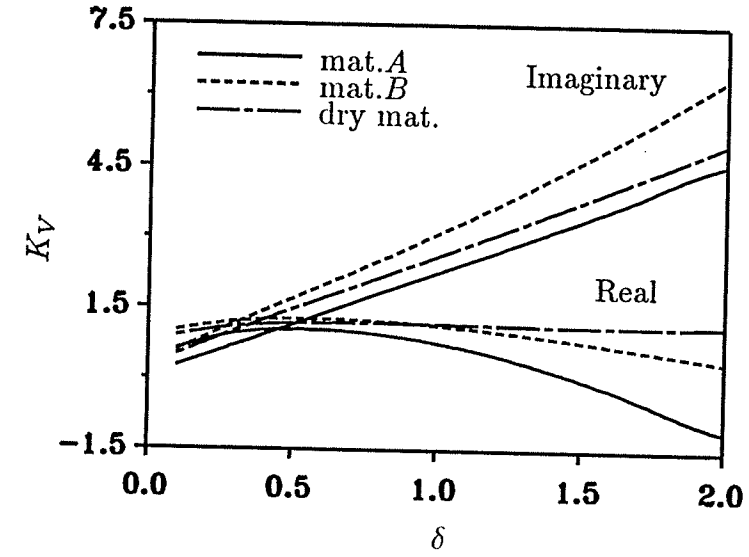

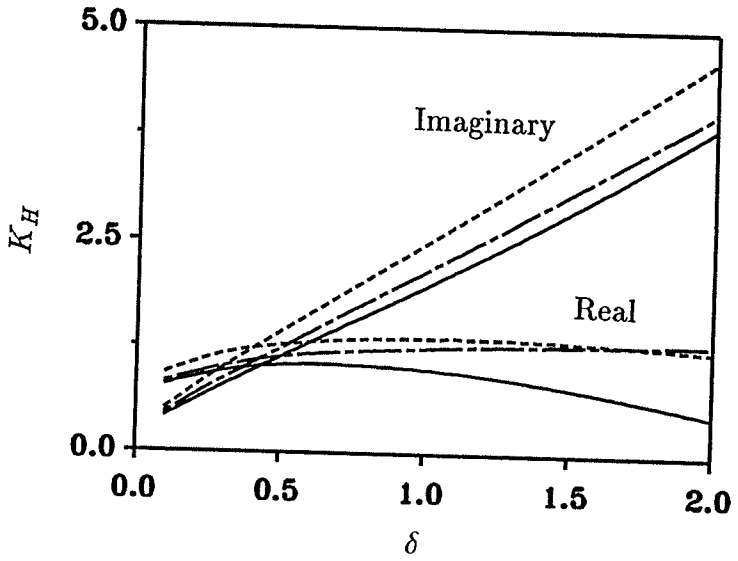

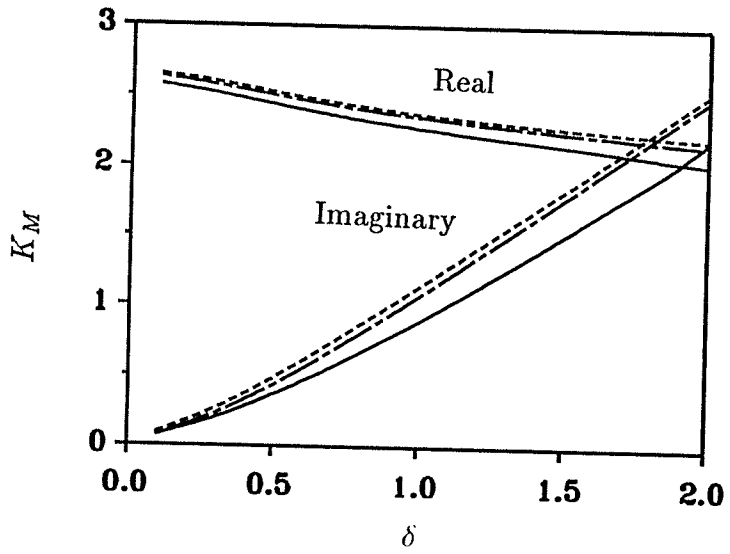

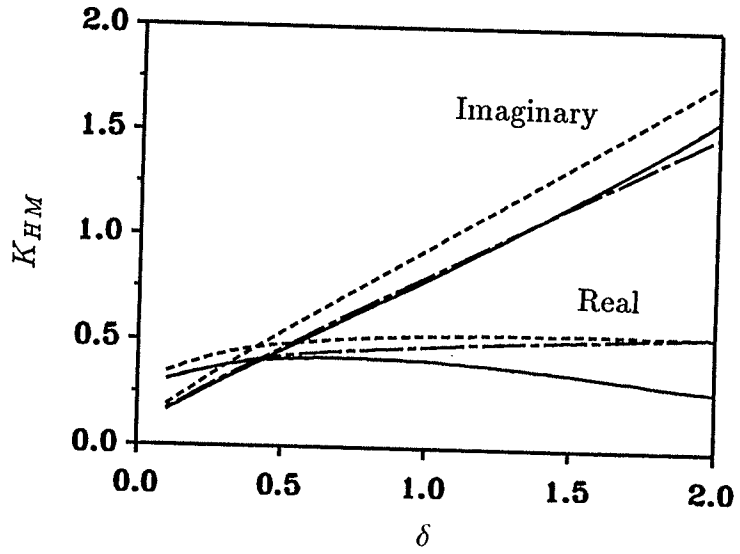

Figure 6.14 Impedances of a rigid semi-circular tunnel

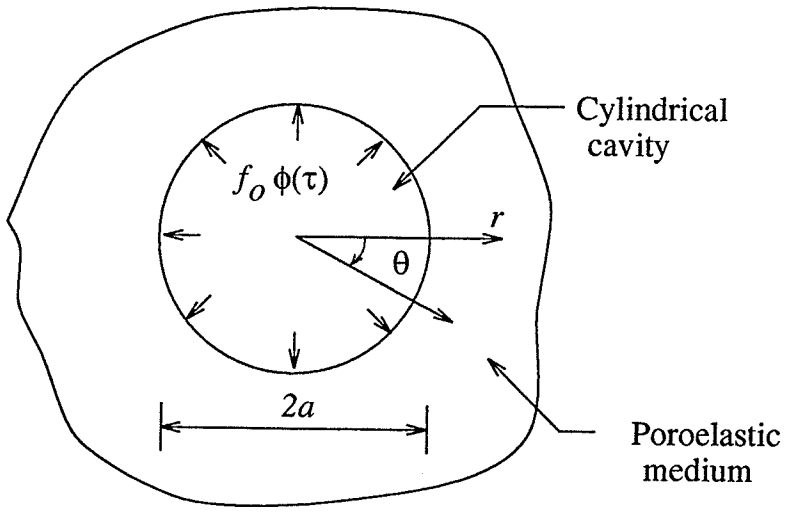

Figure 6.15 Two-dimensional cavity expansion problems under transient loadings

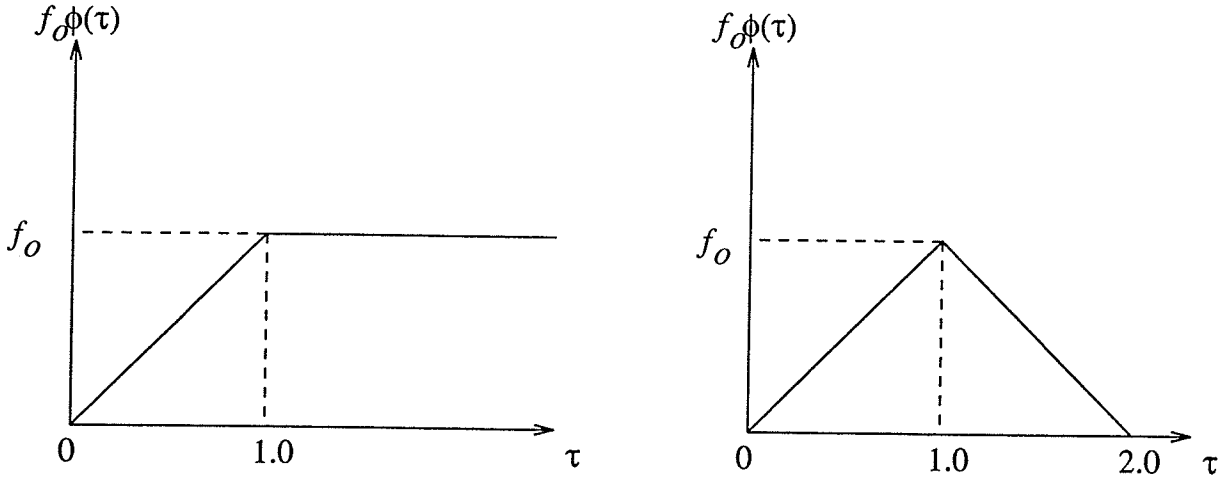

(a) Gradually applied step load

(b) Triangular pulse

Figure 6.16 Time histories of loadings considered in transient problems

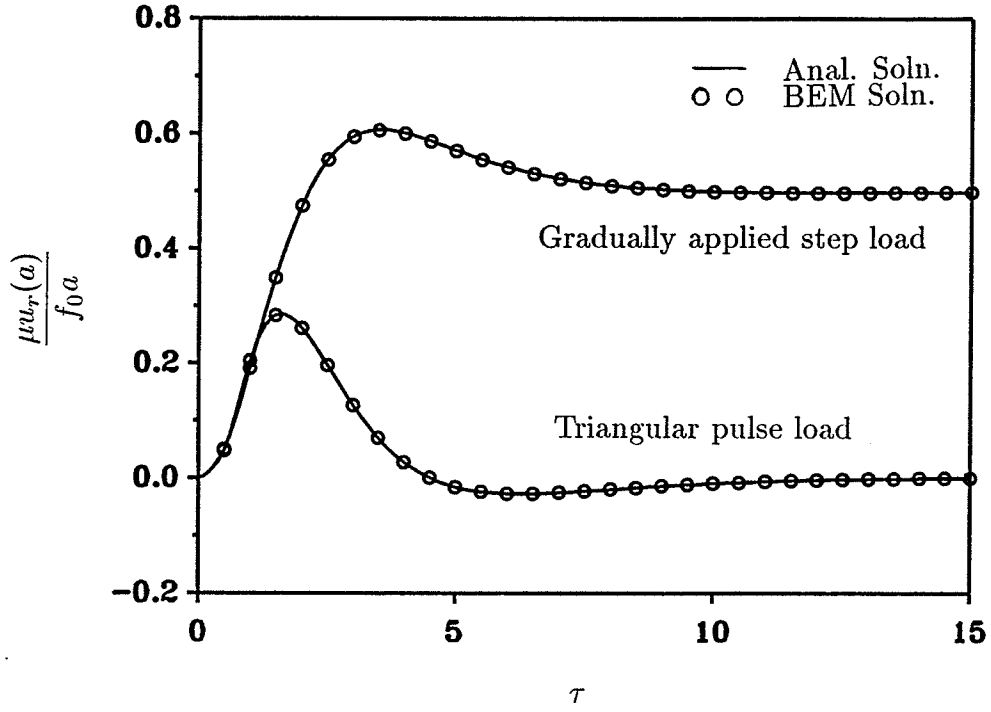

(a)

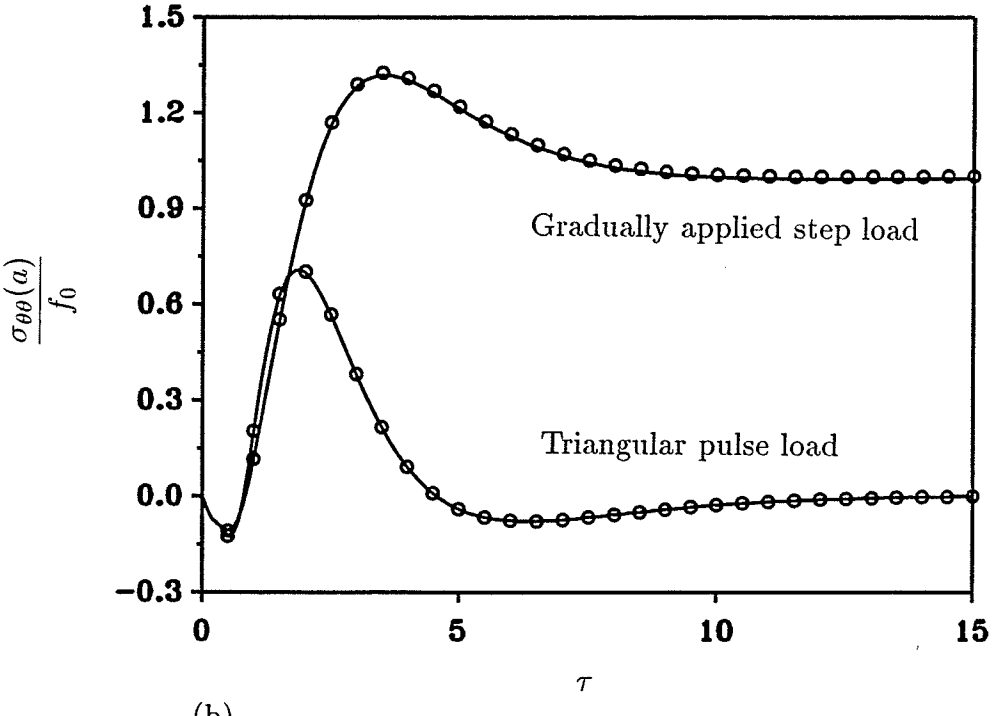

(b)

Figure 6.17 Comparison of radial displacement and hoop stress of a cylindrical cavity under transient loadings

Chapter 7

CONCLUDING REMARKS

7.1 Conclusions

The main conclusions of this thesis are summarized in this Chapter. Separate conclusions are presented at the end of Chapters 2-6 based on the analysis and numerical results presented in those Chapters. The followings are the major findings and conclusions of the present study.

1) Green's functions corresponding to quasi-static and dynamic loads and fluid sources applied at a finite depth below the surface of a homogeneous half-space can be obtained explicitly in terms of semi-infinite integrals.
2) The integrands of semi-infinite integrals appearing in the Green's functions of a homogeneous half-space are very complicated and cannot be evaluated analytically. The application of direct numerical quadrature such as the extended trapezoidal rule is the appropriate way to compute these Green's functions. For quasi-static problems, it is found that time-domain solutions can be obtained with high accuracy by using Laplace inversion schemes proposed by Schapery (1962) and Stehfest (1970). In the case of time-harmonic problems, the path of integration is free from any singularity due to the dissipative nature of the medium. However, a smaller integration interval is required in the vicinity of the singularities of the integrands.
3) The exact stiffness method presented in this study results in a computationally efficient and numerically stable scheme to evaluate Green's functions for multi-layered poroelastic media. When compared to the conventional methods based on the determination of layer arbitrary coefficients, the present scheme involves matrices consisting of only negative exponential terms of the integral transform parameters and requires less computational effort due to the presence of a banded symmetric matrix which is nearly half the size of that encountered in the conventional scheme. When compared to the approximate stiffness methods reported in the literature, the present stiffness scheme exactly satisfies all the governing equations of the medium and is also capable of rigorously accounting

for the presence of an underlying half-space. In addition, the present scheme does not require the discretization of physical layers into further sub-layers.

4) Numerical solutions presented in this study for homogeneous poroelastic media indicate that in the case of quasi-static problems the initial response is mainly governed by the undrained Poisson's ratio whereas the final response depends only on the drained Poisson's ratio. Numerical solutions corresponding to time-harmonic excitations indicate that the response is governed by a complicated combination of nondimensional parameters b^*, M^*, λ^* and the frequency of excitation. A clear qualitative relationship between the governing parameters and the response cannot be identified in the case of layered poroelastic media.

5) It is found that an indirect boundary integral equation method similar to that presented by Ohsaki (1973) for ideal elasticity can be developed for poroelasticity. The indirect boundary element scheme is developed for the analysis of quasi-static, time-harmonic and transient problems involving semi-infinite and infinite poroelastic media. The accuracy and the numerical stability of the present algorithms for quasi-static, time-harmonic and transient problems are confirmed by solving a set of boundary value problems for which analytical solutions are available. Full space Green's functions expressed in the integral forms have been used in all example problems analyzed by using the boundary element method. The fact that highly accurate numerical results are obtained from the boundary element method based on Green's functions computed by using numerical integration scheme indicates that the half-space and layered media Green's functions presented in this thesis can be effectively used in boundary element analysis of more complicated problems involving poroelastic media.

7.2 Recommendations for Future Work

In author's opinion, there are two main aspects to be considered in any future extension of this work. The first one is the derivation of 3-D dynamic Green's functions for homogeneous and multi-layered poroelastic half-spaces. Secondly, in this thesis, only a few types of problems are considered in the boundary element analysis since the main objectives are to develop the indirect boundary element algorithm

and verify its accuracy. Given the fact that Chapters 2-5 present the necessary Green's functions for both homogeneous and multi-layered media, it is very useful to employ the boundary element scheme presented herein to study practical problems such as the dynamics of embedded foundations, quasi-statics of a single pile and pile groups, scattering of seismic waves by cavities, canyons, etc. in poroelastic media and investigate in detail the influence of poroelastic effects.

REFERENCES

Abramowitz, M. and Stegun, I. A. (1972). *Handbook of Mathematical functions.* Dover, New York.

Achenbach, J. D. (1973). *Wave Propagation in Elastic Solids.* North-Holland Publishing Co., Amsterdam, The Netherlands.

Apsel, R. J. (1979). "Dynamic Green's functions for layered media and applications to boundary-value problems." *Ph.D. Thesis*, University of California, San Diego.

Apsel, R. J. and Luco, J. E. (1983). "On the Green's functions for a layered half space. Part II." *Bull. Seism. Soc. Am.*, **73,** 931-951.

Badmus, T., Cheng, A. H.-D. and Grilli, S. (1993). "A Laplace-transform-based three-dimensional BEM for poroelasticity." *Int. J. Numer. Meth. Eng.*, **36,** 67-85.

Beskos, D. E. (1987). "Boundary element methods in dynamic analysis." *Appl. Mech. Reviews*, **40,** 1-23.

Biot, M. A. (1941a). "General theory of three-dimensional consolidation." *J. Appl. Phys.*, **12,** 155-164.

Biot, M. A. (1941b). "Consolidation settlement under a rectangular load distribution." *J. Appl. Phys.*, **12,** 426-430.

Biot, M. A. (1955). "Theory of elasticity and consolidation for a porous anisotropic solid." *J. Appl. Phys.*, **26,** 182-185.

Biot, M. A.. (1956a). "Theory of propagation of elastic waves in a fluid-saturated porous solid,I, low frequency range." *J. Acoust. Soc. Am.*, **28,** 168-178.

Biot, M. A.. (1956b). "Theory of propagation of elastic waves in a fluid-saturated porous solid,II, high frequency range." *J. Acoust. Soc. Am.*, **28,** 179-191.

Biot, M. A. (1962). "Mechanics of deformation and acoustic propagation in porous media." *J. Appl. Phys.*, **33,** 1482-1498.

Biot, M. A. and Clingan, F. M. (1941). "Consolidation settlement of a soil with impervious top surface." *J. Appl. Phys.*, **12,** 578-581.

Biot, M. A. and Clingan, F. M. (1942). "Bending settlement of a slab resting on a consolidation foundation." *J. Appl. Phys.*, **13,** 35-40.

Biot, M. A. and Willis, D. G. (1957). "The elastic coefficients of theory of consolidation." *J. Appl. Mech.*, Trans. ASME, **79,** 594-601.

Bonnet, G. (1987). "Basic singular solutions for a poroelastic medium in the dynamic range." *J. Acoust. Soc. Am.*, **82,** 1758-1762.

Bougacha, S., Roësset, J. M. and Tassoulas, J. L. (1993a). "Dynamic stiffness of foundations on fluid-filled poroelastic stratum." *J. Eng. Mech.*, ASCE, **119,** 1648-1662.

Bougacha, S., Tassoulas, J. L. and Roësset, J. M. (1993b). "Analysis of foundations on fluid-filled poroelastic stratum." *J. Eng. Mech.*, ASCE, **119,** 1632-1648.

Bourbié, T., Coussy, O. and Zinszner, B. E. (1987). *Acoustics of Porous Media.* Gulf, Houston, Texas.

Boutin, C., Bonnet, G. and Bard, P. Y. (1987). "Green functions and associated sources in infinite and stratified poroelastic media." *Geophys. J. R. astr. Soc.*, **90,** 521-550.

Bowen, R. M. (1976). "Theory of mixtures." *Continuum Physics*, A. C. Eringen eds., **3,** Academic Press, New York, 1-127.

Bowen, R. M. (1982). "Compressible porous media models by use of the theory of mixtures." *Int. J. Eng. Sci.*, **20,** 697-735.

Burridge, R. and Vargas, C. A. (1979), "The fundamental solution in dynamic poroelasticity." *Geophys. J. R. astr. Soc.*, **58,** 61-90.

Cheng, A. H.-D. (1981). "Boundary integral equation formulation for porous-elasticity with applications in soil mechanica and geophysics." *Ph.D. Thesis*, Cornell University.

Cheng, A. H.-D., Badmus, T. and Beskos, D. E. (1991). "Integral equation for dynamic poroelasticity in frequency domain with BEM solution." *J. Eng. Mech.*, ASCE, **117,** 1136-1157.

Cheng, A. H.-D. and Detournay, E. (1988). "A direct boundary element method for plane strain poroelasticity." *Int. J. Numer. Anal. Meth. Geomech.*, **12,** 551-572.

Cheng, A. H.-D. and Liggett, J. A. (1984a). "Boundary integral equation method for linear poroelasticity with applications to soil consolidation." *Int. J. Numer. Meth. Eng.*, **20,** 255-278.

Cheng, A. H.-D. and Liggett, J. A. (1984b). "Boundary integral equation method for linear poroelasticity with applications to fracture propagation." *Int. J. Numer. Meth. Eng.*, **20,** 279-296.

Cheng, A. H.-D. and Predeleanu, M. (1987). "Transient boundary element formulation for poroelasticity." *Appl. Math. Modelling*, **11,** 285-290.

Cleary, M. P. (1977). "Fundamental solutions for a fluid-saturated porous solid." *Int. J. Solid Structures*, **13,** 785-806.

Cline, A. K., Moler, C. B., Stewart, G. W. and Wilkinson, J. H. (1979). "An estimate for the condition number of a matrix." *SIAM J. Numer. Analysis*, **16,** 368-375.

Dargush, G. F. and Banerjee, P. K. (1989). "A time domain boundary element method for poroelasticity." *Int. J. Numer. Meth. Eng.*, **28,** 2423-2449.

De Josselin De Jong, G. (1957). "Applications of stress functions to consolidation problems." *Proc. 4th Int. Conf. Soil Mech. Found. Eng.*, London, **1,** 320-323.

Deresiewicz, H. (1962). "The effect of boundaries on wave propagation in a liquid-filled porous solid: IV Surface waves in a half-space." *Bull. Seism. Soc. Am.*, **52,** 627-638.

Deresiewicz, H. and Rice, J. T. (1962). "The effect of boundaries on wave propagation in a liquid-filled porous solid: III Reflection of plane waves at a free plane boundary (general case)." *Bull. Seism. Soc. Am.*, **52,** 595-625.

Deresiewicz, H. and Skalak, R. (1963). "On uniqueness in dynamic poroelasticity." *Bull. Seism. Soc. Am.*, **53,** 783-788.

Detournay, E. and Cheng, A. H.-D. (1988). "Poroelastic response of a borehole in a non-hydrostatic stress field." *Int. J. Rock Mech. Min. Sci. and Geomech. Abstr.*, **25,** 171-182.

Detournay, E., Cheng, A. H.-D., Roegiers, J.-C. and Mclennan, J. D. (1989). Poroelastic consideration in *in situ* stress determination by hydraulic fracturing. *Int. J. Rock Mech. Min. Sci. and Geomech. Abstr.*, **26,** 507-513.

Dominguez, J. (1991). "An integral formulation for dynamic poroelasticity." *J. Appl. Mech.*, **58,** 588-591.

Dominguez, J. (1992). "Boundary element approach for dynamic poroelastic problems." *Int. J. Numer. Meth. Eng.*, **35,** 307-324.

Dong, S. B. and Nelson, R. B. (1972). "On natural vibrations and waves in laminated orthotropic plates." *J. Appl. Mech.*, **94,** 739-745.

Erdélyi, A. (1954). *Tables of Integral Transforms.* Bateman manuscript project, Cal. Inst. of Tech., McGraw-Hill, New York.

Eringen, A. C. and Suhubi, A. S. (1975). *Elastodynamics.* Vol. 2, Academic Press, New York.

Gazetas, G. (1983). "Analysis of machine foundation vibrations: state of the art." *Soil Dynamics and Earthquake Engineering*, **2,** 2-42.

Geertsma, J. and Smith, D. (1961). "Some aspect of elastic wave propagation in a fluid-saturated porous solid." *Geophys.*, **26,** 169-181.

Ghaboussi, J. and Wilson, E. L. (1973). "Flow of compressible flow in porous elastic solids." *Int. J. Numer. Meth. Eng.*, **5,** 419-442.

Gibson, R. E. (1974). "The analytical methods in soil mechanics." *Geotechnique*, **24,** 115-140.

Gilbert, F. and Backus, G. E. (1966). "Propagator matrices in elastic wave and vibration problems." *Geophysics*, XXXI, 326-332.

Green, A.E. and Naghdi, P. M. (1965). "A dynamical theory of interacting continua." *Int. J. Eng. Sci.*, **3,** 231-341.

Gurtin, M. (1964). "Variational principles for linear elastodynamics." *Arch. Rational Mech. Anal.*, **16,** 34-50.

Halpern, M. R. and Christiano, P. (1986a). "Response of poroelastic halfspace to steady-state harmonic surface tractions." *Int. J. Numer. Anal. Meth. Geomech.*, **10,** 609-632.

Halpern, M. R. and Christiano, P. (1986b). "Steady-state harmonic response of a rigid plate baring on a liquid-saturated poroelastic halfspace." *Earthquake Engineering and Structural Dynamics*, **14,** 439-454.

Harnpattanapanich, T. and Vardoulakis, I. (1987). "Numerical Laplace-Fourier transform inversion technique for layered-soil consolidation problems; II. Gibson soil layer." *Int. J. Numer. Anal. Meth. Geomech.*, **11,** 103-112.

Haskell, N. A. (1953). "The dispersion of surface waves on multilayered media." *Bull. Seism. Soc. Am.*, **43,** 17-34.

Haskell, N. A. (1960). "Crustral reflection of plane *SH* waves." *J. Geophys. Res.*,

65, 4147-4150.

Haskell, N. A. (1962). "Crustral reflection of plane P and SV waves." *J. Geophys. Res.*, **67,** 4751-4767.

Hosono, T. (1979). *Trans. Inst. Elect. Eng. Jpn.*, **54,** 44.

Hwang, C. T., Morgenstern, N. R. and Murray, D. W. (1971). "On solution of plane strain consolidation problems by finite element methods." *J. Can. Geotech.*, **8,** 109-118.

Jones, J. P. (1961). "Rayleigh waves in porous elastic fluid saturated solid." *J. Acoust. Soc. Am.*, **33,** 959-962.

Kanok-Nukulchai, W. and Chau, K. T. (1990). "Point sink fundamental solutions for subsidence prediction." *J. Eng. Mech.*, ASCE, **116,** 1176-1182.

Kanok-Nukulchai, W. and Suaris, V. W. (1982). "An efficient finite element scheme for elastic porous media." *Int. J. Solids Structures*, **18,** 37-49.

Karasudhi, P. (1990). *Foundation of Solid Mechanics.* Kluwer Academic Publishers, The Netherlands.

Katsube, N. and Carroll, M. M. (1987a). "The modified mixture theory for fluid-filled porous materials: theory." *J. Appl. Mech.*, **54,** 35-40.

Katsube, N. and Carroll, M. M. (1987b). "The modified mixture theory for fluid-filled porous materials: applications." *J. Appl. Mech.*, **54,** 41-46.

Kausel, E. and Peek, R. (1982). "Dynamic loads in the interior of a layered stratum: an explicit solution." *Bull. Seism. Soc. Am.*, **72,** 1459-1481.

Kausel, E., Roesett, J. M. and Waas, G. (1975). "Dynamic analysis of circular foundation." *J. Eng. Mech. Div.*, ASCE, **101,** 679-693.

Kausel, E. and Seale, S. H. (1987). "Static loads in layered halfspaces." *J. Appl. Mech.*, **54,** 403-408.

Kennett, B. L. N. (1974). "Reflections, rays, and reverberations." *Bull. Seism. Soc. Am.*, **64,** 1685-1696.

Kobayashi, S. (1984)."Fundamentals of boundary integral equation methods in elastodynamics." *Topics in Boundary Element Research*-2, C. A. Brebbia eds., Springer-Verlag, Berlin, 1-54.

Knopoff, L. (1964). "A matrix method for elastic wave problems." *Bull. Seism. Soc. Am.*, **54,** 431-438.

Krause, G. (1978). "Finite element schemes for porous elastic media." *J. Eng. Mech. Div.*, ASCE, **104,** 605-620.

Kreider, D. L., Kuller, R. G., Ostberg, D. R. and Perkins, F. W. (1966). *An Introduction to Linear Analysis.* Addison-Wesley Publishing Company, Massachusetts.

Kupradze, V. D., Gezelia, T. G., Basheleishvili, M. O. and Burchuladze, T. V. (1979). *Three-Dimensional Problems of the Mathematical Theory of Elasticity and Thermoelasticity.* North-Holland, Amsterdam, The Netherlands.

Lamb, H., (1904). "On the propagation of tremors over the surface of an elastic solid," *Phil. Tran. R. Soc. Lond.*, Series A, **203,** 1-42.

Liggett, J. A. and Liu, P. L.-F. (1983). *The Boundary Integral Equation Method for Porous Media Flow.* George Allen & Unwin (Publishers) Ltd., London.

Luco, J. E. (1982). "Linear soil-structure interaction: a review." *Earthquake Ground Motion and Its Effects on Structures,* AMD-Vol. 53, S. K. Datta eds., ASME, New York, 41-57.

Luco, J. E. and Apsel, R. J. (1983). "On the Green's functions for a layered half space. Part I." *Bull. Seism. Soc. Am.*, **73,** 909-929.

Lysmer, J. and Waas, G. (1972). "Shear waves in plane infinite structures." *J. Eng. Mech. Div.*, ASCE, **98,** 85-105.

Mandel, J. (1953). "Consolidation des sols (étude mathématique)." *Geotechnique*, **3,** 287-299.

Manolis, G. and Beskos, D. E. (1989). "Integral formulation and fundamental solutions of dynamic poroelasticity and thermoelasticity." *Acta Mech.*, **76,** 89-104, also "Errata." (1990). *Acta Mech.*, **83,** 223-226.

McNamee, J. and Gibson, R. E. (1960a). "Displacement functions and linear transforms applied to diffusion through porous elastic media." *Q. J. Mech. App. Math.*, **13,** 98-111.

McNamee, J. and Gibson, R. E. (1960b). "Plane strain and axially symmetric problems of the consolidation of a semi-infinite clay stratum." *Q. J. Mech. App. Math.*, **13,** 210-227.

Melan, E. (1932). "Der spanning zustand der durch eine einzelkraft im innern beanspruchten halbschiebe, Z. Angew.." *Math. Mech.*, **12.**

Mindlin, R. D. (1936). "Force at a point in the interior of a semi-infinite solid." *Physics*, **7**, 195-202.

Morlands, L. W. (1972). "A simple constitutive theory for fluid saturated porous solids." *J. Geophys. Res.*, **77**, 890-900.

Mossessian, T. K. and Darvinski, M. (1989). "Scattering of elastic waves by three-dimensional surface topographies." *Wave motions*, **11**, 579-592.

Muki, R. (1960). "Asymmetric problems of the theory for a semi-infinite solid and a thick plate." *Progress in Solid Mechanics*, I. N. Sneddon and R. Hill eds., North Holland, Amsterdam, **1**, 399-439.

Muki, R, and Dong, S. B. (1980). "Elastostatic far-field behavior in a layered half space under surface pressure." *J. Appl. Mech.*, **47**, 504-512.

Nishimura, N. (1987). "Boundary integral equation methods for consolidation problems." *Topics in Boundary Element Research*-4, C. A. Brebbia eds., Springer-Verlag, Berlin, 76-95.

Nishimura, N. and Kobayashi, S. (1989). "A boundary integral equation method for consolidation problems." *Int. J. Solid Structures*, **25**, 1-21.

Norris, A. N. (1985). "Radiation from a point source and scattering theory in a fluid-saturated porous solid." *J. Acoust. Soc. Am.*, **77**, 2012-2023.

Nowacki, W. (1975). *Dynamic Problems of Thermoelasticity.* Noordhoff, Leyden, The Netherlands.

Ohsaki, Y. (1973). "On movement of a rigid body in semi-infinite elastic medium." *Proc. of Japan Earthquake Eng. Symp.*, Japan, 245-252.

Oner, M. and Dong, S. B. (1988). "Analysis of on-plane waves in layered half-space by global-local finite element method." *Soil Dynamics and Earthquake Engineering.*, **7**, 2-8.

Paul, S. (1976a). "On the displacement produced in a porous elastic half-space by an impulsive line load (non-dissipative case)." *Pure Appl. Geophys.*, **114**, 605-614.

Paul, S. (1976b). "On the disturbance produced in a semi-infinite poroelastic medium by a surface load." *Pure Appl. Geophys.*, **114**, 615-627.

Philippacopoulos, A. J. (1988a). "Lamb's problem for fluid-saturated, porous media." *Bull. Seism. Soc. Am.*, **78**, 908-923.

Philippacopoulos, A. J. (1988b). "Waves in partially saturated medium due to surface loads." *J. Eng. Mech.*, ASCE, **114,** 1740-1759.

Philippacopoulos, A. J. (1989). "Axisymmetric vibration of disk resting on saturated layered half-space." *J. Eng. Mech.*, ASCE, **115,** 2301-2322.

Piessens, R. (1975). "Bibliography on numerical inversion of the Laplace transform and applications." *J. Comp. Appl. Math.*, **1,** 115-126.

Poulos, H. G. (1966). "Stresses and displacements in an elastic layer underlain by a rough rigid base." *Civ. Eng. Res. Rep.*, **R63,** University of Sydney, Australia.

Poulos, H. G. and Davis, E. H. (1974). *Elastic Solutions for Soil and Rock Mechanics.* John Wiley & Sons, Inc., New York.

Predeleanu, M. (1968). "Reciprocal theorem in the consolidation theory of porous media." *Anal. Univ. Bucuresti, Seria Stiintele Naturii, Matematica, Mechanica,* **17,** 75-79.

Predeleanu, M. (1981). "Boundary integral method for porous media." *Boundary Element Methods.*, C. A. Brebbia eds., Springer-Verlag, 325-334.

Puswewala, U. G. A. and Rajapakse, R. K. N. D. (1988). "Axisymmetric fundamental solutions for a completely saturated porous elastic solid." *Int. J. Eng. Sci.*, **26,** 419-436.

Rajapakse, R. K. N. D. (1990) "Response of an axially loaded elastic pile in a Gibson soil." *Geotechnique*, **40,** 237-249.

Rajapakse, R. K. N. D. (1993). "Stress analysis of borehole in poroelastic medium." *J. Eng. Mech.*, ASCE, **119,** 1205-1227.

Rajapakse, R. K. N. D. and Shah, A. H. (1988). "Hybrid modelling of semi-infinite media." *Int. J. Solids and Structures*, **26,** 833-849.

Rajapakse, R. K. N. D. and Wang, Y. (1991) "Elastodynamic Green's functions of orthotropic half plane." *J. Eng. Mech.*, ASCE, **117,** 588-604.

Rasolofosaon, P. N. J. (1991) "Plane acoustic waves in linear viscoelastic porous media: Energy, particle displacement, and physical interpretation." *J. Acoust. Soc. Am.*, **89,** 1532-1550.

Rice, J. R. and Cleary, M. P. (1976). "Some basic stress-diffusion solutions for fluid saturated elastic porous media with compressible constituents." *Rev. Geophys. Space Phys.*, **14,** 227-241.

Rizzo, F. J. (1967). "An integral equation approach to boundary value problems of classical elastostatics." *Q. Appl. Math.*, **25,** 83-95.

Rudnicki, J. W. (1986a). "Fluid mass sources and point forces in linear elastic diffusive solid." *Mechanics of Materials*, **5,** 383-393.

Rudnicki, J. W. (1986b). "Slip on an impermeable fault in a fluid-saturated rock mass." *Earthquake Source Mechanics*, Das, J., Boatwright, J., and Scholz, C. H., eds., American Geophysical Union, Geophysical Monograph 37, 81-89.

Rudnicki, J. W. (1987). "Plane strain dislocations in linear elastic diffusive solids." *J. Appl. Mech.*, **54,** 545-552.

Saada, A. S. (1974). *Elasticity: Theory and Application.* Pergamon Press, Oxford.

Sandhu, R. S. (1968). "Fluid flow in saturated porous elastic media." *Ph.D. Thesis*, University of California, Berkeley.

Sandhu, R. S. and Wilson, E. L. (1969). "Finite element analysis of seepage in elastic media." *J. Eng. Mech. Div.*, ASCE, **95,** 641-652.

Schapery, R. A. (1962). "Approximate methods of transform inversion for viscoelastic stress analysis." *Proc. 4th U.S. Nat. Congress on Appl. Mech.*, **2,** 1075-1085.

Schiffman, R. L. and Fungaroli, A. A. (1965). "Consolidation due to tangential loads." *Proc. 6th Int. Conf. Soil Mech. and Found. Engng.*, 188-192.

Schwab, F. (1970). "Surface-wave dispersion computations: Knopoff's method." *Bull. Seism. Soc. Am.*, **60,** 1491-1520.

Seale, S. H. and Kausel, E. (1989). "Point loads in cross-anisotropic, layered halfspaces." *J. Eng. Mech.*, ASCE, **115,** 509-524.

Selvadurai, A. P. S. (1976). "The load-deflexion characteristics of a deep rigid anchor in an elastic medium." *Geotechnique*, **26,** 603-612.

Selvadurai, A. P. S. (1979). *Elastic Analysis of Soil-Foundation Interaction.* Elsevier Scientific Publishing, Amsterdam.

Senjuntichai, T. and Rajapakse, R. K. N. D. (1993). "Transient response of a circular cavity in a poroelastic medium." *Int. J. Numer. Anal. Meth. Geomech.*, **17,** 357-383.

Skempton, A. W. (1954). "The pore pressure coefficients A and B." *Geotechnique*, **4,** 143-147.

Sneddon, I. N. (1951). *Fourier Transforms.* McGraw-Hill, New York.

Stehfest, H. (1970). "Numerical inversion of Laplace transforms." *Communs. Ass. Comput. Mach.*, **13,** 47-49.

Terzaghi, K. (1923). "Die Berechnung der Durchassigkeitsziffer des Tones aus dem Verlauf der hydrodynamischen Spannungsercheinungen." *Sitzungsber. Akad. Wiss. Wien. Math.-Naturwiss. Kl., Abt. 2A*, **132,** 105-124.

Thomson, W. T. (1950). "Transmission of elastic waves through a stratified solid medium." *J. Appl. Phys.*, **21,** 89-93.

Truesdell, C. and Toupin, R. A. (1960). "The classical field theories." *Handbuck der Physik*, 1/3, S. Flügge eds., Springer, New York, 360-363.

Vardoulakis, I. and Harnpattanapanich, T. (1986). "Numerical Laplace-Fourier transform inversion technique for layered-soil consolidation problems: I. Fundamental solutions and validation." *Int. J. Numer. Anal. Meth. Geomech.*, **10,** 347-365.

Waas, G. (1972). "Linear two-dimensional analysis of soil dynamic problems in semi-infinite layered media." *Ph.D. Thesis*, University of California, Berkeley.

Waas, G. (1980). "Dynamisch Belastete Fundamente auf Geschichtetem Baugrund." VDI *Berichte*, **381,** 185-189.

Wang, Y. and Rajapakse, R. K. N. D. (1990). "Asymmetric boundary-value problems for a transversely isotropic elastic medium." *Int. J. Solids Structures*, **26,** 833-849.

Watson, G. N. (1944). *A Treatise on the Theory of Bessel Functions.* University Press, Cambridge.

Watson, T. H. (1970). "A note on fast computation of Rayleigh wave dispersion in the multi-layered elastic half space." *Bull. Seism. Soc. Am.*, **60,** 161-166.

Wiebe, Th. and Antes, H. (1991). "A time domain integral formulation of dynamic poroelasticity." *Acta Mech.*, **90,** 125-137.

Wolf, J. P. (1985). *Dynamic Soil-Structure Interaction.* Prentice-Hall, Englewood Cliffs, New Jersey.

Wolfram, S. (1988). *Mathematica: A system for doing mathematics by computer.* Addison-Wesley Publishing Company, Inc.

Wong, H. L. and Luco, J. E. (1986). "Dynamic interaction between rigid foundations in a layered half-space." *Soil Dynamics and Earthquake Engineering*, **5,**

149-158.

Yew, C. H. and Jogi, P. N. (1978). " The determination of Biot's parameters for sandstones." *Exp. Mech.*, **18,** 167-172.

Yew, C. H., Jogi, P. N. and Gray, K. E. (1979). "Estimation of the mechanical properties of fluid-saturated rocks using the measured wave motions." *J. Energy Res. Tech.*, **101,** 112-116.

Yokoo, Y., Yamagate, K. and Nagaonka, H. (1971a). "Finite element method applied to Biot's consolidation theory." *Soils and Foundations*, (Japanese Society of Soil Mechanics and Foundation Engineering), **11,** 29-46.

Yokoo, Y., Yamagate, K. and Nagaonka, H. (1971b). "Finite element analysis of consolidation following undrained deformation." *Soils and Foundations*, (Japanese Society of Soil Mechanics and Foundation Engineering), **11,** 37-58.